Simulating Action Potential Initiation and Propagation in Physically Detailed Damaged and Healthy Neurons

—Benjamin Barlow—

Thesis submitted to the University of Ottawa
in partial fulfillment of the requirements for the
Doctorate in Philosophy degree in Physics

Department of Physics
Faculty of Science
University of Ottawa

uOttawa

Statement of Originality

All work presented as my own in this thesis is, to the best of my knowledge, new and original. Thanks to the diligent proofreading of my supervisors, Professors Béla Joós and André Longtin, I made multiple improvements to the text that would not have occurred without their irreplaceable feedback. The papers in this thesis were written in collaboration with my supervisors, and for greater precision, each publication in the main text is preceded by a *Statement of Originality* pertaining specifically to it.

To James and Eleanore

Part I

Front Matter

Abstract

This thesis presents single-compartment and multi-compartmental neuron models. We simulated injury-induced pathological spiking patterns, as well as heterogeneous ion channel distributions in the axon initial segment (AIS) and their impact on backpropagation. In neurons, voltage-gated sodium and potassium ion channels (Na_Vs and K_Vs, respectively) regulate ionic currents across the cell membrane in the production of action potentials (APs). As such, channel dynamics feature throughout this thesis. The starting point was the Coupled *left-shift* (*CLS*) model of cellular damage, wherein the gating properties of Na_Vs are thrown "out of tune" by injury (*left-shift*, *LS*), such that the subpopulation of affected channels (*AC*) no longer responds correctly to homeostatic membrane potentials. We simulated a single-compartment neuron with *CLS*-type damage and systematically mapped out its excitability regimes in the *LS*–*AC* plane. Next, we added temperature sensitivity to the Na_V and K_V gating kinetics and maximal conductances, the Nernst potentials, and the Na^+/K^+ pump. We compared the neuron's ability to cope with *CLS* damage when temperature effects were added one by one, to the case where all effects act together as they would in nature. The former "knock-in/knock-out" simulations revealed the importance of (i.e. model sensitivity to) each temperature-driven change in the ionic currents that govern excitability. Our multicompartmental pyramidal cell models indicate that the pattern of ion channels in the AIS affects feedback sent to synapses in the soma and dendrites. Inserting a set of hypothetical Na_V distributions into the AIS, we found that the impact of Na_V subtypes on the neuron's backpropagation threshold depends on the mode of stimulation (orthodromic or antidromic). Both modes are used by experimentalists, and our results should inform comparative studies as well as the design of neural prosthetics, as the AIS is a logical target for multielectrode arrays used in brain-computer interfaces. Coupled *left-shift* in the AIS produced axonal hypersensitivity, decoupled the somatic backpropagation threshold from the AP threshold, and modified backpropagation in a manner resembling polarity reversal of the AIS sodium channel pattern. Below the ectopic threshold, *CLS* may interfere with homeostatic intracellular signalling and learning via the putative role of spike-timing-dependent plasticity in the dendrites.

Acknowledgements

I am sincerely grateful to my supervisors, Professors Béla Joós and André Longtin, for their guidance, insight, integrity, and support. Thank you for staying the course and seeing past the horizon when I was grappling with the challenges of the present. Thank you also for reading the *roughest* of drafts, when yours truly, having dived into a particular question for weeks without surfacing, inadvertently assumed the reader already knew everything I was going to say.

I also wish to thank Professor Zbigniew M. Stadnik for the fun we had performing live physics demonstrations and later filming them during those years when the University of Ottawa was forced to—temporarily—close its lecture halls.

List of contributions

0.1 Publications in the main text

- Béla Joós, **Benjamin M. Barlow**, and Catherine E. Morris "Calculating the Consequences of Left-Shifted Na_V Channel Activity in Sick Excitable Cells" M. Chahine (ed.), Voltage-gated Sodium Channels: Structure, Function and Channelopathies, Handbook of Experimental Pharmacology 246, October 2017, doi.org/10.1007/164_2017_63
- **B. M. Barlow**, B. Joós, A. K. Trinh, and A. Longtin "Cooling reverses pathological bifurcations to spontaneous firing caused by mild traumatic injury" Chaos: An Interdisciplinary Journal of Nonlinear Science, 28(10): 106328, October 2018, doi.org/10.1063/1.5040288
- **Benjamin S. M. Barlow**, André Longtin, Béla Joós "Impact on backpropagation of the spatial heterogeneity of sodium channel kinetics in the axon initial segment" PLOS Computational Biology, March 15, 2024, doi.org/10.1371/journal.pcbi.1011846

0.2 Additional publications

During the course of my doctoral studies, I wrote and published the following paper under the advisement of my co-supervisor, Béla Joós (in addition to the papers included in the main text)

- **Ben M. Barlow**, Martine Bertrand, and Béla Joós "Relaxation of a simulated lipid bilayer vesicle compressed by an atomic force microscope" Physical Review E, November 2016, doi.org/10.1103/physreve.94.052408,

using molecular dynamics simulation results that I created for my Master's thesis at the University of Ottawa, of small unilamellar vesicles.

The initial manuscript was submitted on the 5^{th} of May 2016. I submitted a revised manuscript addressing reviewers' comments on the 21^{st} of August 2016, including new derivations to account for contemporaneous experimentally observed power spectra of entropic undulations in vesicles (Mell et al. [42]). The paper was published on the 15^{th} of November, 2016 [3].

While I was revising and updating that manuscript for publication, I also presented it as a poster at the 2016 CAP Congress. I won two awards for that presentation (listed under Awards), and as a result, we published the following article as well:

- Feature Article - Best Student Paper, Physics in Canada, Vol. 72, No.3 (2016), pp.120-122: "Relaxation of a Simulated Lipid Bilayer Vesicle Compressed by an AFM" **Ben M. Barlow**, Martine Bertrand, and Béla Joós (https://pic-pac.cap.ca/index.php/Issues/showpdf/issue/v72n3.0.pdf).

Following those publications, my research focus shifted from molecular dynamics to computational neuroscience—the latter being the topic of this thesis. I had long been curious about simulating intracellular signalling in spatially extended neuron models with detailed cell morphology copied from real brain cells, and that was not attainable via coarse-grained molecular dynamics. In both cases, key results came from a time constant that changed with the state of the plasma membrane: A "τ" that was a function of the *tension* in the membrane for the vesicle simulations, and a transmembrane *voltage*-dependent "τ" in the pyramidal neuron models.

0.3 ModelDB entries

To make the simulations available to other researchers for future use, I have contributed model code to the following pages at ModelDB[1].

- Joós, Barlow, and Morris [28]: `https://modeldb.science/234111`
- Barlow, Joós, Trinh, and Longtin [2]: `https://modeldb.science/263193`
- Barlow, Longtin, and Joós [4]: `https://modeldb.science/267088`

0.4 Awards

- Teaching Assistant of the Year - Department of Physics (academic year 2018-2019)
- Best Student Poster Presentation Award, 2nd Prize, 2016 CAP Congress, Canadian Association of Physicists
- DPMB[2] Best Student Poster Presentation Award, First Prize, 2016 CAP Congress, Canadian Association of Physicists

0.5 Conference presentations

- *16th Canadian Neuroscience Meeting, Canadian Association for Neuroscience, May 2023, Montréal, Canada:* **B. Barlow**, A. Longtin, and B. Joós "P3-B-553: The spatial separation of voltage-gated sodium channel subtypes in the axon initial segment can have opposite effects on backpropagation depending on the site of stimulation"

[1] `https://modeldb.science`
[2] Physics in Medicine and Biology Division

(https://can-acn.org/wp-content/uploads/2023/05/CAN-2023-Abstract-BookV2.pdf)

- *Centre for Neural Dynamics Research Spotlight 2022, October 2022, University of Ottawa, Alta Vista Campus (The Ottawa Hospital / L'Hôpital d'Ottawa):* **Benjamin Barlow**, André Longtin, and Béla Joós "Separation of NaV Subtypes in the Axon Initial Segment can Impede or Promote Backpropagation"
- *SIAM Conference on the Life Sciences (LS22), Session CP6 Neuroscience I, Tuesday, July 12, 2022:* **Benjamin Barlow**, André Longtin, and Béla Joós, "Separation of Na_V Subtypes in the Axon Initial Segment Can Impede Or Promote Backpropagation"
(https://meetings.siam.org/sess/dsp_programsess.cfm?SESSIONCODE=74800)
- *Joint 7th Annual Biophysical Society of Canada/IUPAB Ion Channel Biophysics Meeting, May 2022:* **Benjamin Barlow**, André Longtin, and Béla Joós, "Separation of NaV Subtypes in the Axon Initial Segment can Impede or Promote Backpropagation"
(https://event.fourwaves.com/jointbsc2022iupab/abstracts/62230323-a0c8-454c-9450-2f46859cb931)
- *APS March Meeting 2021, Session S12: Physics of Neural Systems I, March 2021:* **Benjamin Barlow**, Béla Joós, and André Longtin "Impact of Sodium Channel Distribution in the Axon Initial Segment on the Initiation and Backpropagation of Action Potentials"
(https://meetings.aps.org/Meeting/MAR21/Event/404772)
- *APS March Meeting 2019, Session P67: Physics of Neural Systems I, March 2019:* **Benjamin Barlow**, Béla Joós, Anh-Khoi Trinh, and André Longtin "Cooling Reverses Pathological Bifurcations to Spontaneous Firing Caused by

Mild Traumatic Injury"

(https://meetings.aps.org/Meeting/MAR19/Session/P67.9)

- *Poster#69, 2016 CAP Congress / Congrès 2016 de l'ACP, June 2016, University of Ottawa:* **Ben Barlow**, Martine Bertrand, and Béla Joós "Relaxation of a Simulated Lipid Bilayer Vesicle Compressed by an AFM"

Contents

List of Figures

[3] `https://commons.wikimedia.org/wiki/File:Blausen_0657_MultipolarNeuron.png#filelinks`

[4] `https://www.blender.org`
[5] `https://docs.blenderneuron.org/index.html`
[6] `https://www.python.org`
[7] `https://h01-release.storage.googleapis.com/landing.html`

[9] https://en.wikipedia.org/wiki/Voltage-gated_sodium_channel

[11] https://commons.wikimedia.org/wiki/File:Giant_Axon_of_Squid_(14356033761).jpg

List of abbreviations and symbols

AIS — Axon Initial Segment

AP — Action Potential

BAP — Backpropagating Action Potential

CLS — Coupled *left-shift* model, see Section 4.2 – *Introduction: CLS model*.

LS — *left-shift*: The hyperpolarizing shift of *activation* and *availability* kinetics of voltage-gated sodium channels in the CLS model, see Section 4.2 – *Introduction: CLS model*.

AC — Affected Channels: fraction of all voltage-gated sodium channels in the membrane that are affected by CLS ($AC \in [0, 1]$), see Section 4.2 – *Introduction: CLS model*.

T-CLS — Coupled *left-shift* model with Temperature modulation, see Section 5.2 – *Introduction: CLS and Temperature (T-CLS)*.

GHK — Goldman-Hodgkin-Katz

HH model — Hodgkin-Huxley model

Na_V — Voltage-gated sodium channel

K_V — Voltage-gated potassium channel

m, kg, s, K, A, V, C, M, mol — Symbols for *SI units*: metre, kilogram, second, kelvin, ampere, volt, coulomb, moles-per-litre, moles,...

$\mathtt{p}$, $\mathtt{n}$, μ, $\mathtt{m}$, $\mathtt{c}$, $\mathtt{k}$, $\mathtt{M}$ — orders of magnitude: $10^{-12}, 10^{-9}, 10^{-6}, 10^{-3}, 10^{-2}, 10^{3}, 10^{6}$... e.g. A length of one micrometer is written "$1\mu\mathsf{m}$".

Å — ångström, $\text{Å} \stackrel{\text{def}}{=} 10^{-10}\mathsf{m}$

$\boldsymbol{e}$ — Euler's number, $\boldsymbol{e} \approx 2.718281828459\ldots$

e — elementary charge (proton charge), $\mathsf{e} \approx 1.602 \times 10^{-19}\mathsf{C}$

$\hbar_{\text{B}}$ — Boltzmann Constant, $\hbar_{\text{B}} = 1.380649 \times 10^{-23}\frac{\mathsf{J}}{\mathsf{K}} \approx 8.617 \times 10^{-5}\mathsf{eV/K}$

T_{Human} — Human body temperature, $\approx 310.15\mathsf{K}$

$\hbar_{\text{B}} T_{Human} \approx 4.2821 \times 10^{-21}\mathsf{J}$

$\mathsf{N_A} \stackrel{\text{def}}{=} 6.02214076 \times 10^{23}$ — Avogadro's number, (molecules-per-mol)

$R = \mathsf{N_A}\hbar_{\text{B}} \approx 8.314\frac{\mathsf{J}}{\mathsf{mol{\cdot}K}}$ — universal gas constant

$F = \mathsf{e}\mathsf{N_A} \approx 96,485\frac{\mathsf{C}}{\mathsf{mol}}$ — Faraday's constant

$[S]$ — Concentration of ion species S: e.g. $[\text{Na}^+]_{\text{in}}$ denotes the intracellular concentration of sodium ions.

- In single-compartment neuron models, also called point-cells (e.g., Chapters 4 and 5), we can write the time-dependent intracellular and extracellular concentrations of S-ions as $[S]_{\text{in}}(t)$ and $[S]_{\text{out}}(t)$, respectively.
- may also write the time-dependent concentration of S-ions at the location in space with coordinates $\vec{r} = (x, y, z)$ as $[S](\vec{r}, t)$.

I_{BP} (nA) — Backpropagation current threshold: amplitude of square injected current pulse with duration $\Delta t_{\text{pulse}} = 1\mathtt{ms}$ (as in Barlow, Longtin, and Joós [4], see Section 6.3)

I_{FP} (nA) — Forwardpropagation current threshold: amplitude of square 1ms injected current pulse [4]

Q_{BP} (pC) — Backpropagation charge threshold, $Q_{BP} = I_{BP}\Delta t_{\text{pulse}}$: charge injected by a square 1ms current pulse

Q_{FP} (pC) — Forwardpropagation charge threshold, $Q_{FP} = I_{FP}\Delta t_{\text{pulse}}$: charge injected by a square 1ms current pulse

$\mathbb{J}$ — Number flux (number of atoms or molecules of a given type per-unit-area per-unit-time)

$\mathbb{E}$ — Electric field strength, $\frac{\text{V}}{\text{m}}$ or equivalently $\frac{\text{N}}{\text{C}}$.

Beyond the notation listed above, various forms of typographic *emphasis* on specific **terms** will be encountered in the main text. Acknowledging that some readers may find the emphasis superfluous—as seen in these examples—its potential to add clarity for a broad audience seemed worth the risk.

Part II

Introduction and Background

Chapter 1

Introduction

1.1 The reader as a galaxy of neurons

Reading begins with photoreceptor neurons excited by photons from the page.

This thesis, in a sense, is about the reader: The contents of these pages will be received by photoreceptor cells at the retina, and make their journey along the optic nerve towards the visual cortex. On the way, signals leading from the left side of each retina will be diverted to the left side of the brain, which perceives the right visual field[1], and vice-versa—see Figure 1.1.

Back of the brain regenerates patterns in the visual field. A vivid analogy to octopus skin imitating the animal's surroundings.

In the cortex, the letters and images on the page will be represented via spiking electrical signals in specialized brain cells. Photons absorbed by the retina trigger action potentials in the surface layers of the brain in what is called a retinotopic map. Initially, the brain activity maps the visual field in space—albeit flipped and spatially distorted (Figure 1.1) owing to the concentration of photoreceptors at the fovea (and other features beyond the present discussion). If, by analogy, we replaced those brain cells with chromatophores (found in the skin of octopuses, cuttlefish and squid[2]), we could imagine the primary visual cortex 'camouflaging' itself to resemble what each eye sees, as if a patch of octopus skin were hidden at the back of the head.

[1] Recall that the lens of the eye focuses the **right** visual field onto the **left** retina (see Figure 1.1).
[2] Squid will return—see *Loligo in the lab*, page# 76.

Beyond perception, the interpretation and understanding of these pages will take place in other parts of the reader's cortex, hippocampus, and other brain regions, recruiting ever more pyramidal cells. All of the cells mentioned in the journey above are neurons, which are the focus of this thesis and constitute the present audience. At nearly one hundred billion neurons per human brain, they compare in number to the stars in our galaxy.

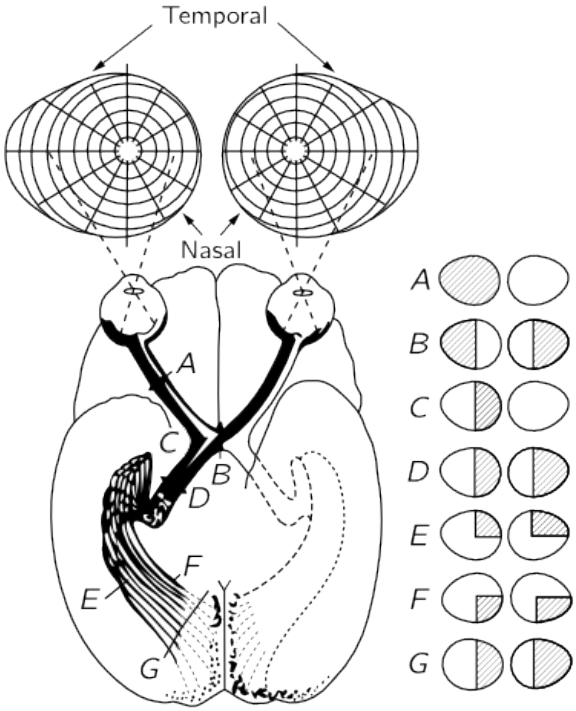

The adult brain appears to be modular in its design, perhaps due to the limited number of synaptic connections that a cortical neuron—such as a pyramidal cell—can maintain with neighbouring cells [5].

Figure 1.1: **Diagram of the connections of the retina to the visual cortex, and corresponding simplified retinotopic map.** It is interesting that the left side of the retina connects to the left hemisphere of the brain (in both eyes), and the right sides connect to the right hemisphere, given that our bodies tend to be wired to the brain on opposite sides: The *left*(*right*) hemisphere controls and senses the *right*(*left*) arm, and so on. However, in the brain's connection to the eyes, somehow evolution has made an exception to said *contralateral organization* of the human nervous system to ensure a contralateral relationship between the brain's visual cortex and the external world (matching, e.g., the sense of touch), counteracting the left-right flip that occurs when focusing light through a lens. (If the eye had two lenses instead of one, would the *left* side of each retina map to the *right* visual cortex, and *vice-versa*?) [Diagram from The Feynman Lectures on Physics, Vol. I: The New Millennium Edition: Mainly Mechanics, Radiation, and Heat. by Richard P. Feynman, Robert B. Leighton, Matthew Sands, copyright ©2011. Reprinted by permission of Basic Books, an imprint of Hachette Book Group, Inc.]

This thesis studies *individual* neurons, e.g., the cells that form computational networks in brain tissue like the visual cortex mentioned above. We will return to the anatomy and biophysics of neurons in Chapters 2 and 3, respectively titled *Background I: Neurons and aqueous ions* (page#11) and *Background II: Action potentials and ion channels* (page#48).

1.2 Biophysical neuron models

Biophysical neuron models are essential tools for understanding the cellular mechanisms, symptoms, and potential cures of neurological diseases.

Biophysical neuron models attempt to accurately simulate processes that occur in living cells. They serve as tools to test existing theories and experimental assumptions as the open-ended project of understanding the brain and the cells that compose it continues. Applications include replicating, predicting, and explaining the results of electrophysiological experiments, elucidating the mechanisms and (often hidden) symptoms of neurological diseases, and assisting the search for effective treatments thereof. They tend to be designed with a specific biological phenomenon in mind—e.g. excitotoxic spiking patterns[3] in injured neurons—and computational efficiency is a constraint rather than an objective of such models.

Simulations that combine biophysics with three-dimensional morphological reconstructions of real cells—to remove assumptions about their structure at the cost of additional parameters—are often called realistic neuron models[4]. By some notions, an ideal realistic model would emulate the full computational function and connectivity of biological neurons of a given type; so that a simulated brain composed of various realistic model neurons would reincarnate, in software, the personality of an animal whose last act was to have their entire brain (successfully) captured by an electron microscope Bostrom 2017 [7].

Whether such a project is destined to remain science fiction is left up to the reader[5], but consider the developments in brain tissue digitization and emulation reported

[3] e.g., Chapters 4 and 5
[4] e.g., Chapters 6 and 7

just this year: Recently, a fruit fly connectome (*Drosophila melanogaster*, Figure 1.2) was successfully digitized at ∼ nm resolution, with every neuron and synapse sorted and labelled (Dorkenwald et al. 2024 [12]). Reportedly, simulations populating this connectome with highly simplified neurons are already reproducing some known functions of the fly brain (Shiu et al. 2024 [50]). A $1\,\mathrm{mm}^3$ sample of human cortex has also recently been scanned with similar fidelity (Shapson-Coe et al. 2024 [49]), though much larger tissue volumes will need to be mapped—presently the mouse brain is an ambitious goal. (At one cubic millimetre, most of the neurites pass through the human sample, their origin and destination being well outside the scanned volume.)

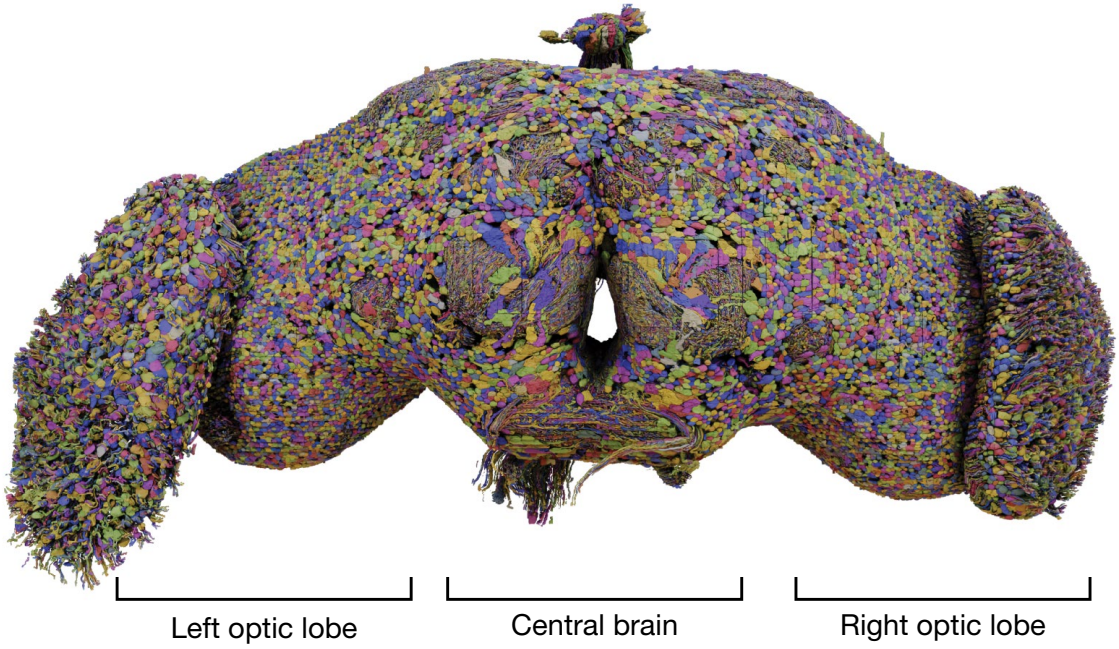

Figure 1.2: **The neurons in the brain of a fruit fly, digitally reconstructed from electron microscopic images.** Adapted from Fig.1**a** of '*Neuronal wiring diagram of an adult brain*', Dorkenwald et al. 2024 [12], licensed under [CC BY 4.0] (https://creativecommons.org/licenses/by/4.0/)

[5]Due to the potential complexity of dendritic morphological and synaptic plasticity, simulating short-term brain dynamics on the order of seconds seems more plausible than any attempt to emulate a living mammalian brain on longer timescales from its connectome scanned at *one point in time*. Nonetheless, brains can do interesting things in well under a second.

1.2.1 An aside: Artificial neural networks vs. biophysical simulations

The past decade has seen compelling progress in the application of neural networks, enabling computers to program themselves to learn new skills. Neural nets are not new, but in the mid-2010s they started working well enough to be useful on a variety of recognition and control tasks that seemed impossibly difficult for humans to program directly.

The neurons we simulate below are not the kind in neural-net software. (See Table 1 on page# 281.)

The architecture of neural nets is based loosely on the biological system whose unique—at that time—property, intelligence, its inventors hoped to recreate: animal brain tissue. Due to the intense interest in artificial neural networks and artificial intelligence (AI) at the time of writing—the 2024 Nobel Prizes in Physics *and* Chemistry[6] both went to AI researchers—I wish to distinguish the mathematical objects called neurons in those models from biophysical simulations of living neurons, as the latter is the focus of this thesis. There is substantial overlap in these related fields' terminology, and Table 1 is included as an appendix[7] on page# 281 to highlight some similarities and differences between them.

AI and biophysical neuron modelling continue to evolve in concert, as they have done practically since their inception. For example, to reconstruct the neural circuitry in the digitized brain volumes mentioned above (Section 1.2), the morphology of each neuron must be traced through stacks of nanometres-thin tissue slices. Without AI, tracing the axons, dendrites, cell bodies, capillaries (or trachea in the fly's case), glial cells and so on through such massive datasets would be impossibly tedious. (See, e.g., Figure 2.12 in *Background I: Neurons and aqueous ions*.)

[6] www.nobelprize.org/all-nobel-prizes-2024/

[7] Appendix A | Table 1: Biophysical neuron models versus nodes in neural nets

1.3 Thesis overview

The papers in this thesis are biophysical neuron models. They were created to study the role of certain membrane proteins—called voltage-gated sodium channels—in excitotoxic disease processes, action potential initiation, and intracellular signalling via the backpropagation[8] of action potentials into the dendritic tree. We used single-compartment and multi-compartmental cell geometries to simulate injury-induced pathological spiking patterns, and the effects of heterogeneous ion channel distributions in the axon initial segment (AIS) on backpropagation in healthy and *CLS*-damaged neurons.

Ahead of the research articles are several sections introducing the relevant concepts, equations, and biophysics—context which is by convention omitted from technical papers—so that this thesis will hopefully be self-contained.

Background

Chapters 2 and 3 cover background material that is a shared foundation for all of the modelling studies included in the thesis. Chapter 2 (page#11) emphasizes the anatomy of neurons and the physics governing the collective motion of ions in water (electrodiffusion), giving rise to biological electric currents and the membrane potential (steady state and equilibrium). Chapter 3 (page#48) builds on the previous sections to introduce axial current in multi-compartmental models, the cable equation, voltage-gated ion channels, and the Hodgkin-Huxley model of space-clamped and propagating action potentials. The biophysics of transmembrane ion currents is further developed in terms of effective permeability and the GHK model (Goldman-Hodgkin-Katz equations), along with electrogenic ion pumps, gating charges in active channels, and other useful material.

[8] In neuroscience, **backpropagation** refers to a phenomenon observed in real neurons, **not to be confused with The Backpropagation Algorithm** famously used in artificial neural networks.

Chapters 4, 5 and 6 present the modelling studies listed under *Publications in the main text* on page#vii (see *List of contributions* above). Each of those chapters contains additional introductory material and a Statement of Originality.

Single-compartment simulations

In Chapter 4 (page#98) we use the Coupled *left-shift* model to simulate ectopic action potentials, where neurons may fire pathologically for long periods of time after injuries to the nervous system. I mapped out spontaneous spiking patterns exhibited by the `CLS` model under a range of damage conditions (Joós, Barlow, and Morris [28]). An introduction to that project begins on page#99, and later sections in Chapter 4 provide supplementary information and analysis of ectopic spiking dynamics with leaky sodium channels, including a primer on dynamical systems theory.

Chapter 5 (page#130) extends the `CLS` model to simulate bifurcations to ectopic spiking caused by interacting effects of *left-shift* and temperature in damaged neurons (Barlow, Joós, Trinh, and Longtin [2]).

Multicompartmental simulations

Chapter 6 (page#149) invokes multicompartmental pyramidal neuron models to study the regulation of backpropagation by sodium channels in the axon initial segment (Barlow, Longtin, and Joós [4]). Section 6.4 (page#180) includes over thirty pages of supporting information on pyramidal cell simulations and other model details. Section 6.5 (page#219) also discusses hidden problems in published model codes, and how to fix them.

Then, Chapter 7 (page#234) expands on the published work from Chapters 4, 5 and 6 by simulating `CLS` in the axon initial segment of a multi-compartmental pyramidal neuron model with GHK currents. The conversion from ohmic Hodgkin-Huxley style currents to GHK equations is detailed in the introduction to Chapter 7.

The key findings of the thesis are brought together in Chapter 8 (page#254), where they are summarized and interpreted. From this outlook, Chapter 9 (page#263) describes opportunities for future research built on the tools developed thus far.

Roadmap

Much of the background (such as the introduction to random walks) was intended to build up the concepts and assumptions underlying biophysical neuron models from basic physics.

- In Chapter 2 '*Background I: Neurons and aqueous ions*' and Chapter 3 '*Background II: Action potentials and ion channels*', I attempt to provide a lively and self-contained introduction to the physics and biology underlying neuron simulations. Readers should *not* feel obligated to cover the entire background (pages 11–98) ahead of the main results in Chapters 4 to 7 (collectively named Part III '*Published Research and Additional Results*').

- Chapters 4, 5 and 6 each conclude with a ***Chapter Synthesis*** that highlights key findings and concepts from the respective paper.

In one sense the material in the introduction is all essential, but that does not mean it is essential that you read it.

- Readers who are eager to reach Part III can skip most of Chapter 2, which focuses on fundamental concepts (e.g. Ohm's law in saline). For example, *Electrodiffusion* (2.3) covers a range of—in my opinion—interesting derivations, but it is not essential to read that material ahead of time. An exception is ***Morphology of neurons*** **(2.2)** with its annotated high-resolution images of human cortical neurons. Without that material, later references to neuronal morphology—especially in Chapters 6 and 7, where *every* simulation has the morphology of a real pyramidal neuron—will be ambiguous at best.

- The *topics* covered in '*Background II: Action potentials and ion channels*' (Chapter 3)—including *The cable equation* (3.1), *Voltage-gated ion channels* (3.2), *The Hodgkin-Huxley equations* (3.3), *Pumps* (3.4), and *Goldman-Hodgkin-Katz (GHK)* (3.5)—form a crucial foundation for the later chapters.

Chapter 2

Background I: Neurons and aqueous ions

2.1 What is a neuron?

Neurons are eukaryotic cells that evolved to send signals rapidly across animals' bodies in the form of electrical impulses. They are nature's solution to the sluggishness and inefficiency of diffusion as a means of intercellular communication over long anatomical distances.

Neurons are eukaryotic cells—as are the cells composing the bodies of all plants and animals. Any eukaryote destined to become an *animal* much larger than a paramecium or an amoeba must divide and become multicellular. As its cells divide, they also differentiate to serve different functions. One way to define **neuron**, in contrast with other eukaryotic cells, is by understanding the problem neurons solve...

An essential function for any animal is the ability to sense its surroundings and to locomote.[1] This requires rapid communication between cells at opposite ends of the body, to coordinate muscle movement for example. Diffusion[2], the means by which chemical signals propagate *passively* in living things, is much too slow for this purpose—as we will now see.

[1] Unlike plants, animals cannot synthesize their food and must instead find it. Animals are said to be *heterotrophic*, and plants are *autotrophic*.

[2] i.e. the tendency of molecules' root-mean-squared displacements, relative to an initial position, to increase with time due to Brownian motion.

Imagine a potassium ion in water being kicked around in a random walk due to Brownian motion (Figure 2.1). Bacteria and unicellular eukaryotes like amoebae or paramecia can send chemical signals across their bodies by releasing a number of molecules at one location and waiting for them to diffuse to their destination.

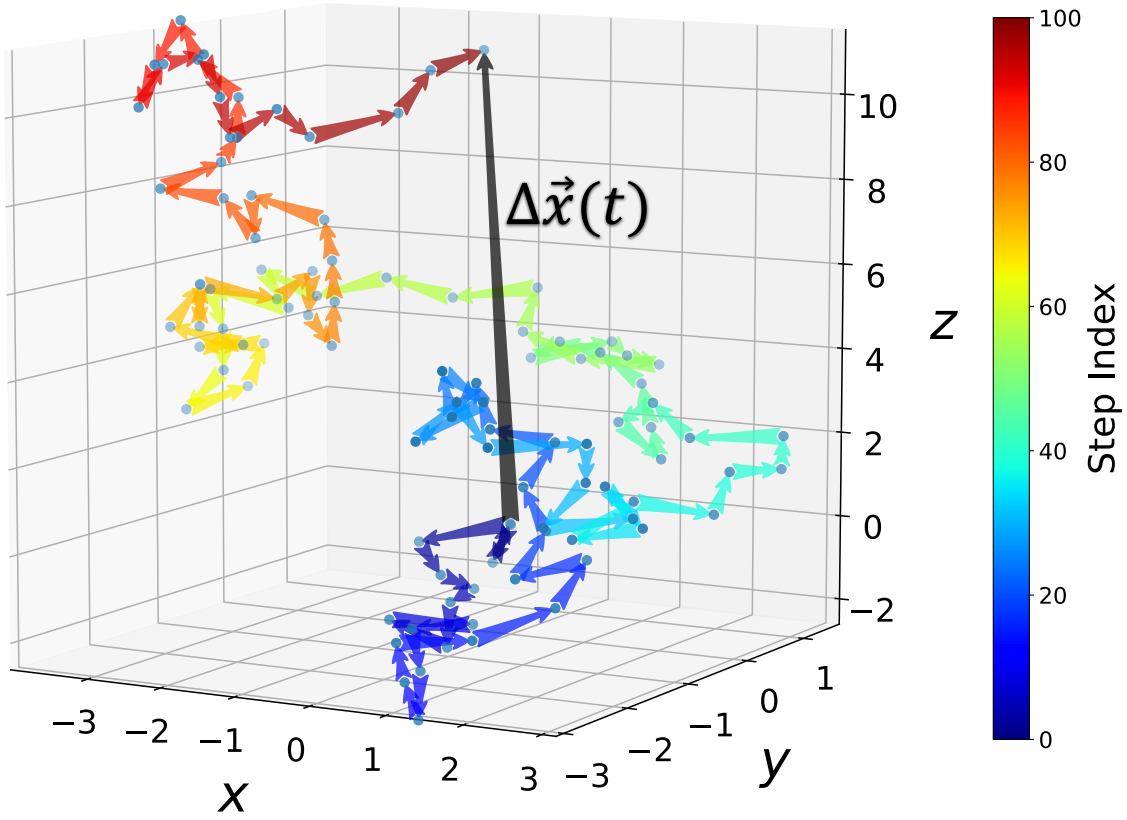

Figure 2.1 visualizes a random walk in three dimensions by adding together randomly oriented vectors tip-to-tail.

Figure 2.1: **Modelling molecular diffusion: A random walk in three dimensions.** Chemical signals diffuse quickly across unicellular eukaryotes, but multicellular animals need *neurons* to coordinate their movement. Here, we plot a single particle's trajectory during a 100-step random walk. Each coloured arrow represents a single step, and in this model, they all have the same length, $\lambda = 1$. (Any apparent length-variability in these arrows results from projecting the 3D path onto two dimensions.)

The black arrow—$\Delta\vec{x} \stackrel{\text{def}}{=} (\Delta x, \Delta y, \Delta z)$—connecting the start and end points in Figure 2.1 is the net displacement of the particle over the duration of the walk.[3] To

Note the mathematical fonts in Figure 2.1: $x \neq x$.

[3] There is nothing mysterious about diffusion that cannot be understood in terms of the random walk of a single particle. The time evolution of concentration gradients that is described by the diffusion equation (see Equation (2.33) in due time) is merely the superposition of many random walks.

see why diffusion becomes prohibitively slow over longer distances, note that the *time taken* (Δt) to traverse the black arrow is proportional to the *length* of the random walk (total number of coloured arrows).

The distance travelled by a chemical signal via diffusion is measured as the root-mean-squared ***displacement*** Δx of a collection of particles relative to the position they began at (Equation (2.1)). That distance grows as the ***square root*** of the elapsed time Δt [43],

Neurons are necessary because diffusion is slow and inefficient

$$\boxed{\Delta x \overset{\text{def}}{=} \sqrt{\langle \Delta \vec{x}^2 \rangle} = \sqrt{6 D \Delta t}}. \tag{2.1}$$

In a random walk, the diffusion coefficient, D, is given by the step size λ and the time interval between steps τ:

$$D = \frac{\lambda^2}{2\tau}. \tag{2.2}$$

The following three plots are intended to illustrate Equation (2.1), and visualize how diffusion results from the individual random walks of particles in a fluid. Figure 2.1 had 100 steps. Below, we introduce a modest *ensemble* of five particles and trace their trajectories as they diffuse for $1,000$ steps (Figure 2.2), $10,000$ steps (Figure 2.3), and $1,000,000$ steps (Figure 2.4).[4]

[4] In nature, the step size is variable, but a fixed step size model is sufficient for our purposes [43].

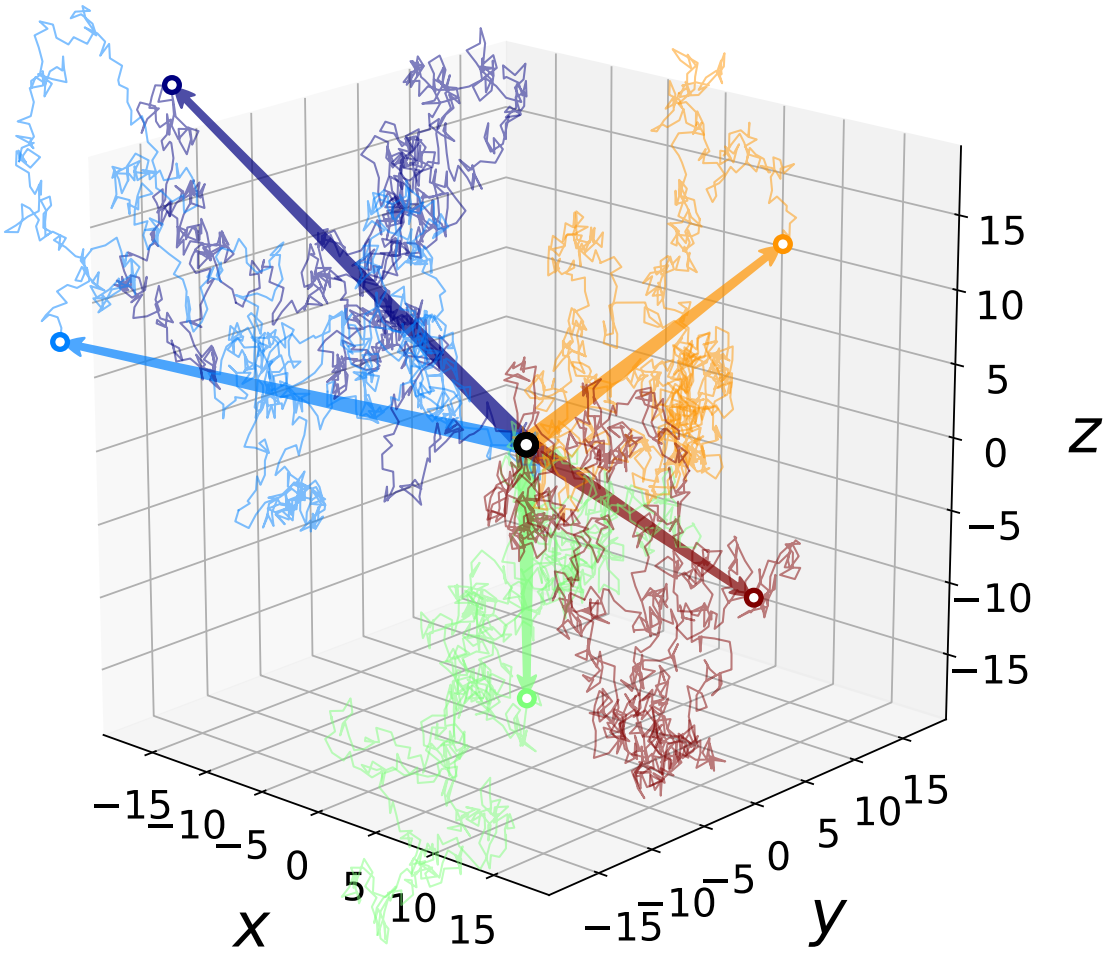

Figure 2.2: **Five random walks, one thousand steps each.** All walks begin at the origin, with an arrow pointing to the final step in the trajectory. Colour is now used to distinguish the walks, whereas previously (Figure 2.1), it indicated the number of steps. Axis limits are scaled to the maximal displacement in each direction. (Dimensionless step length $\lambda = 1$. Arbitrary time step τ.)

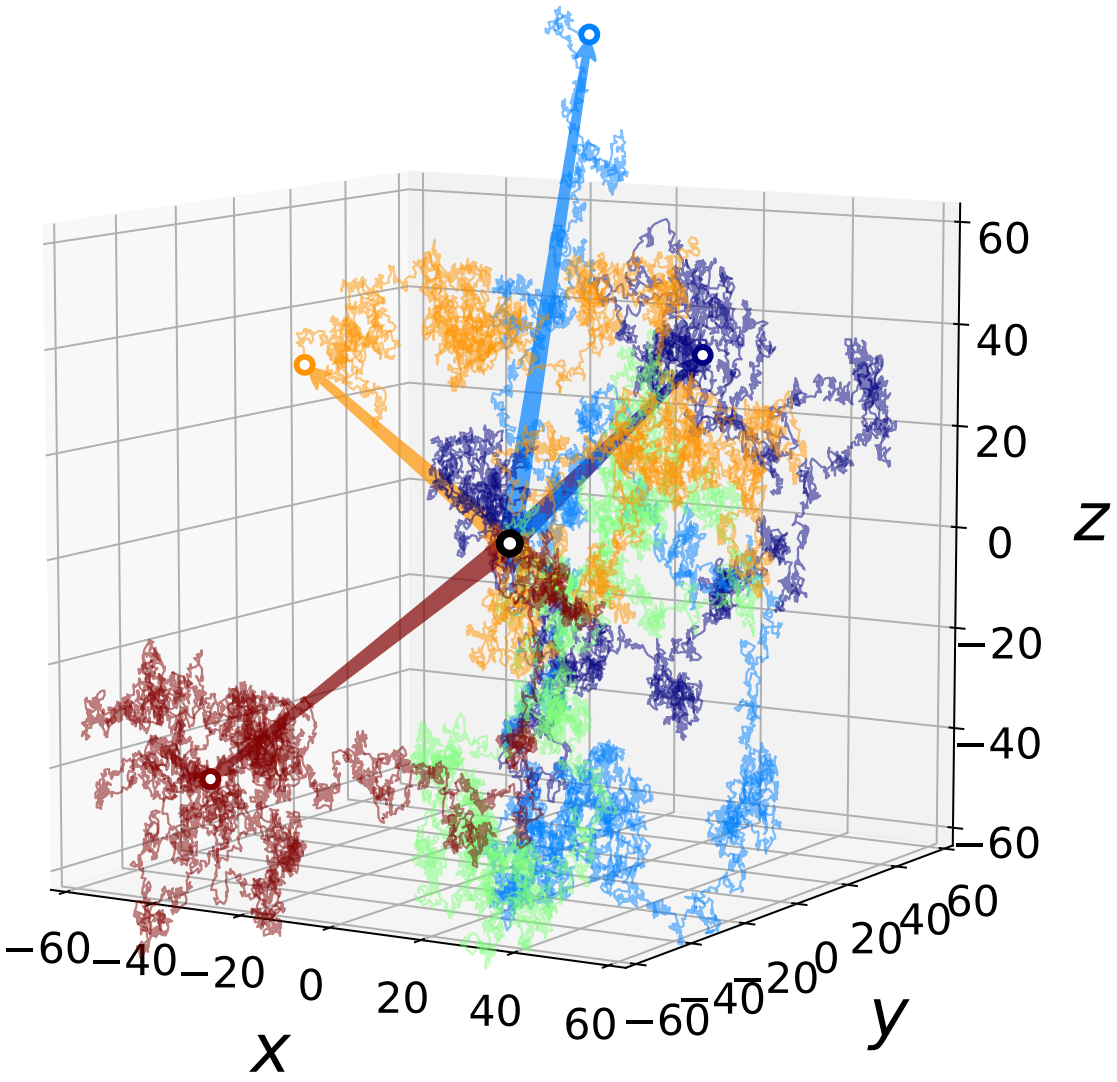

Figure 2.3: **Ten thousand steps in each random walk.** (Dimensionless step length $\lambda = 1$. Arbitrary time step τ.)

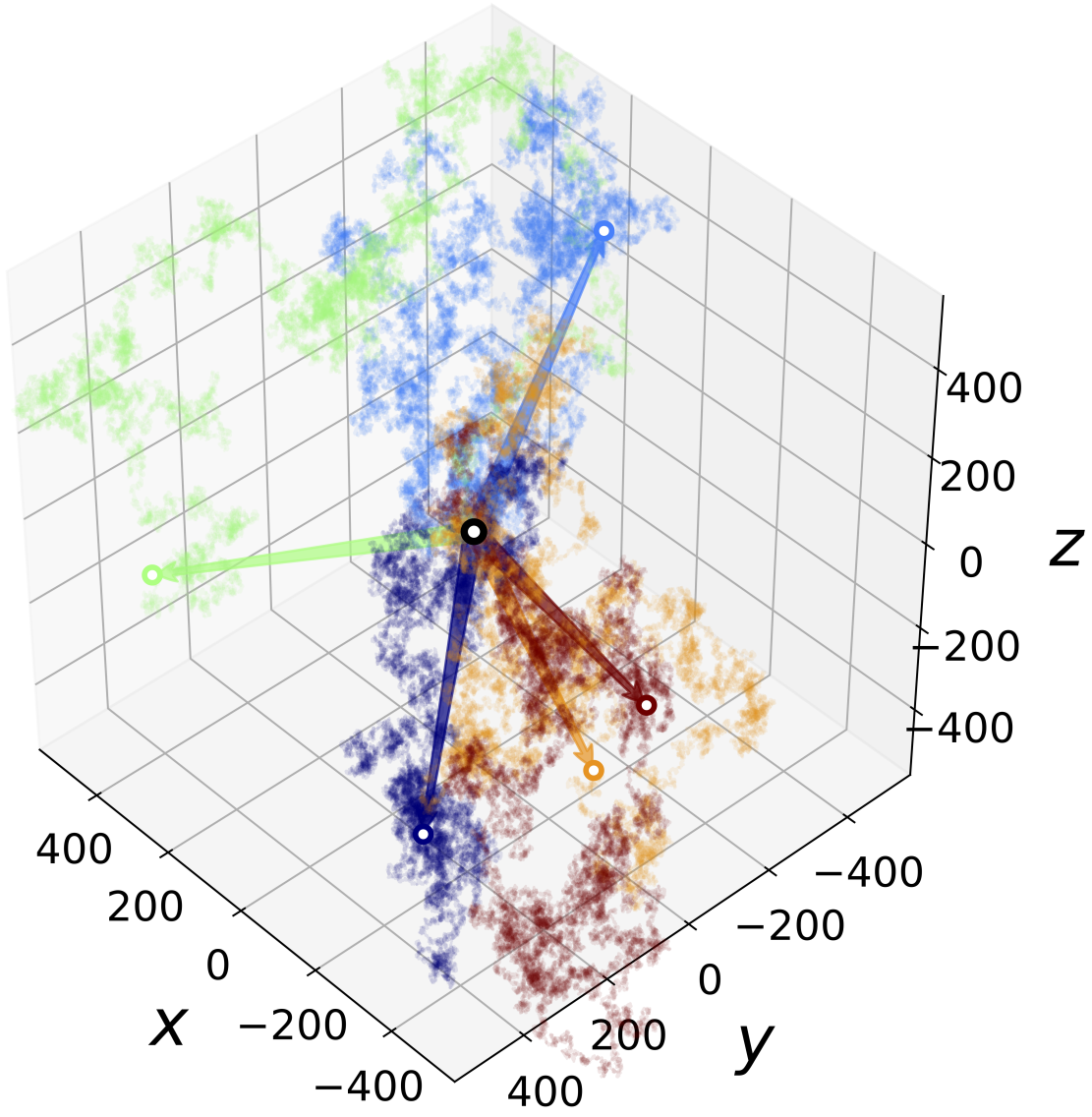

Figure 2.4: **One million steps in each random walk.** At this scale, the trajectories begin to resemble multicoloured translucent smoke. (Dimensionless step length $\lambda = 1$. Arbitrary time step τ.)

Note that in Figures 2.2, 2.3 and 2.4, the axes have been scaled to enclose all five trajectories in each plot. Although the *relation* between the number of steps and the mean-squared displacement must be noisy in such a small ensemble of paths, the axes expand (roughly) as the root of the number of steps—as expected from Equation (2.1).

In Figure 2.5, we plot $\sqrt{\Delta t}$ as a function of time, which is the R.M.S.[5] displacement in the limit of an infinitely large ensemble of trajectories. The slope (speed) is initially quite steep. However, the curve quickly bends toward the horizontal, and diffusion becomes slow over longer distances (many mean-free-path lengths).

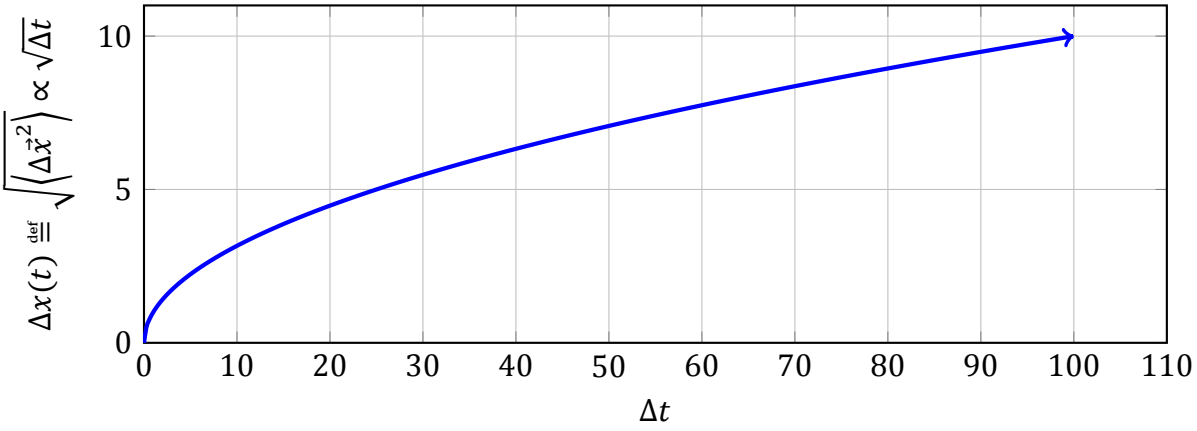

Figure 2.5: **The net displacement (root-mean-square) of a particle or molecule, via diffusion, grows as $\sqrt{\text{time}}$:** Quick over short distances and prohibitively slow over longer distances. See axis limits in Figures 2.1 to 2.4. (In the units of this plot, the diffusion coefficient has been set to $D = 1/6$, so that $\sqrt{\langle \Delta \vec{x}^2 \rangle} = \sqrt{\Delta t}$.)

At longer times, the more one waits, the less additional distance ($\Delta x(t)$) per unit of time one gets from diffusion alone (Figure 2.6). Even in tiny animals, diffusion places a severe constraint on the speed and efficiency of intercellular communication. For example, the brain of a fruit fly (*Drosophila melanogaster*, Figure 1.2 on page#5) has over 100,000 neurons [36]. The distances add up quickly in the network.

[5] "root-mean-squared"

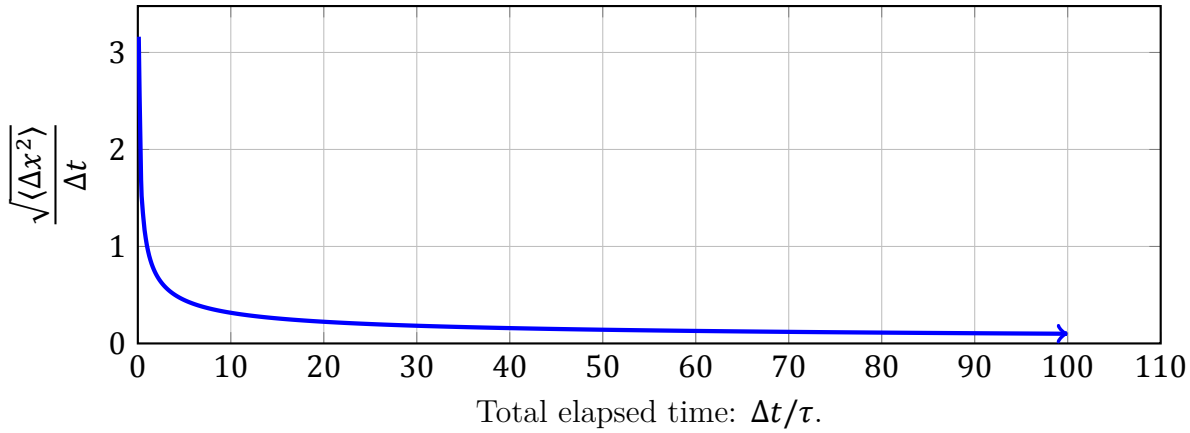

Figure 2.6: **How well diffusion works for sending signals as a function of the size of your body: distance achieved per unit time.** In the units of this plot, the diffusion coefficient has been set to $D = 1/6$, so that $\sqrt{\langle \Delta \vec{x}^2 \rangle} = \sqrt{\Delta t}$. Data is cut off due to the singularity at $\Delta t = 0$. (As usual, the singularity is a falsehood. A more detailed model would converge to a finite molecular velocity from Maxwell-Boltzmann statistics when $\Delta t \lesssim \tau$.)

However, eukaryotes *did* become the larger multicellular animals—including fruit flies and orcas—that we see (and are) today. To sense and navigate their environment, animals needed a mechanism to bypass the limits of diffusion, allowing them to send signals across their bodies rapidly and efficiently.

Neurons are the highest-speed solution (exceeding $100\frac{\text{m}}{\text{s}}$) that animals evolved for this purpose. They interleave short-range intercellular diffusion (neurotransmitter release at synapses) with long-range intracellular electromechanical waves called action potentials (APs) that sustain their speed over distances ranging from micrometres to metres. Neurons' branched morphology allows them to form complex networks, giving rise to neural computation.

That answers what a neuron is, in the sense of ***function***, at a high level. In Background II: Action potentials and ion channels, we complete this story by explaining how neurons generate action potentials and introduce the Hodgkin-Huxley model of

APs.[6] In the meantime, there is also the question of ***structure***: How can one tell that a cell *is* a neuron?

2.2 Structure: faithful images of neurons in brain tissue

What comes to mind when you think of a neuron? Non-biologists like myself might conjure cartoon images resembling Figure 2.7.

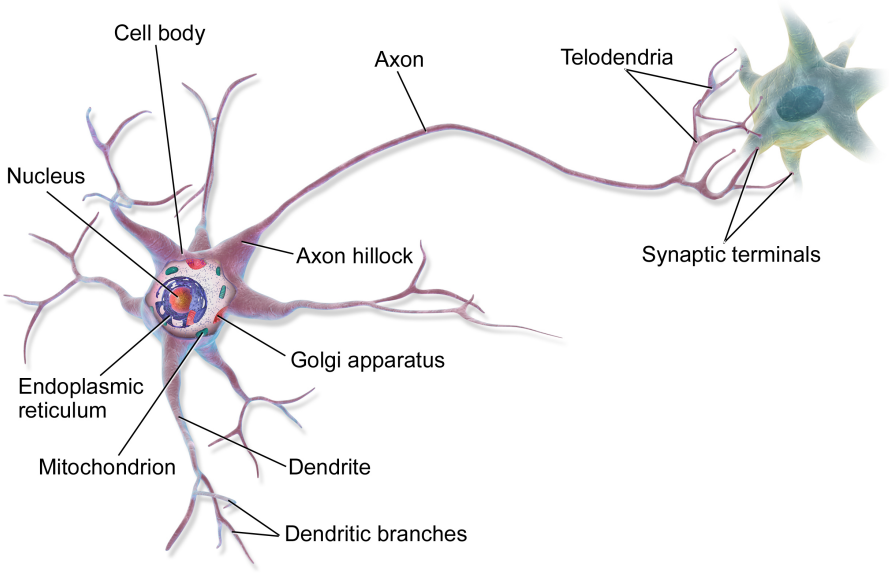

What comes to mind when you think of a neuron?

Figure 2.7: **A familiar depiction of a neuron.** Credit: Wikipedia[7]

The image below is a closer approximation to the genuine article: a digitized pyramidal neuron from cerebral cortex (Figure 2.8).

[6] The work of Hodgkin and Huxley may well be the greatest achievement in all of biophysics.
[7] https://commons.wikimedia.org/wiki/File:Blausen_0657_MultipolarNeuron.png#filelinks
[8] https://www.blender.org
[9] https://docs.blenderneuron.org/index.html
[10] https://www.python.org

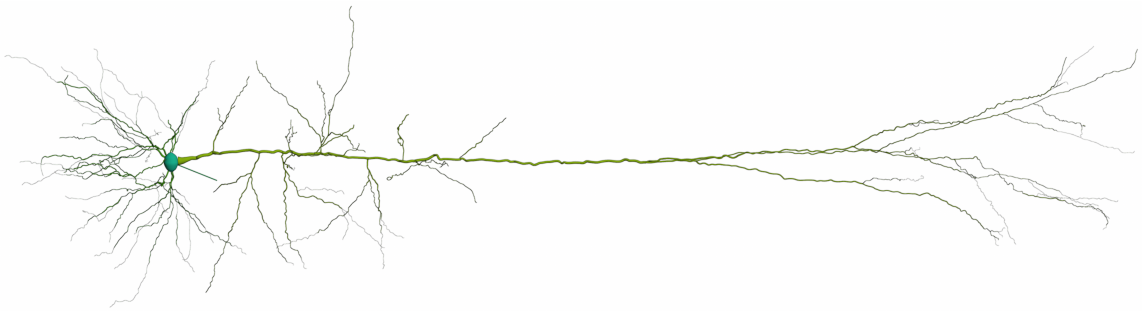

A real neuron, digitized in three dimensions, and lacking finer details such as spines.

Figure 2.8: **Morphology of a rat layer-5b neocortical pyramidal neuron, from Hay et al. [19].** Somatodendritic morphology is digitally reconstructed from a real cell. Image created using blender[8] and the blenderNEURON[9] package in Python[10].

When I thought of neurons, I would naturally imagine a branched structure floating in space, like a fluorescently stained cell in an optical microscope image, or the rendering shown above in Figure 2.8. However, in reality, things are much messier. For one thing, that image omits spines. Figure 2.9 includes spines, which is why the dendrites appear fuzzy compared to Figure 2.8. This figure (below) was captured from a high-resolution 3D rendering of a human L4 pyramidal neuron, compiled from stacks of 30nm thick slices of cortex imaged with an electron microscope (Shapson-Coe et al. [48, 49]).

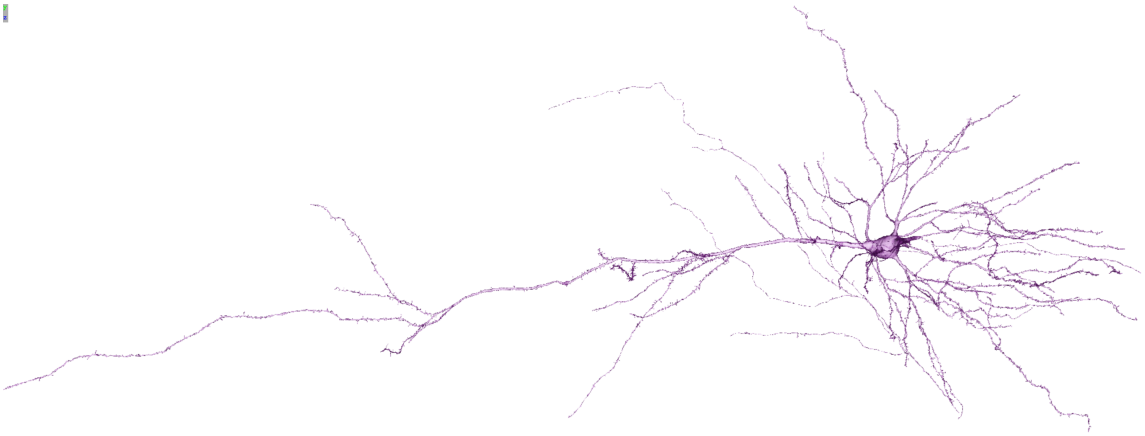

What neurons actually look like. The axon is not so easy to spot. (Hint: It isn't the long, spiny one on the left...)

Figure 2.9: **A Layer-4 pyramidal neuron from human cerebral cortex. Can you spot the axon?**... (Worry not: The axon and other important neuronal processes are annotated below in Figure 2.10.) Render modified from the H01 release via Neuroglancer, Maitin-Shepard et al. [40].

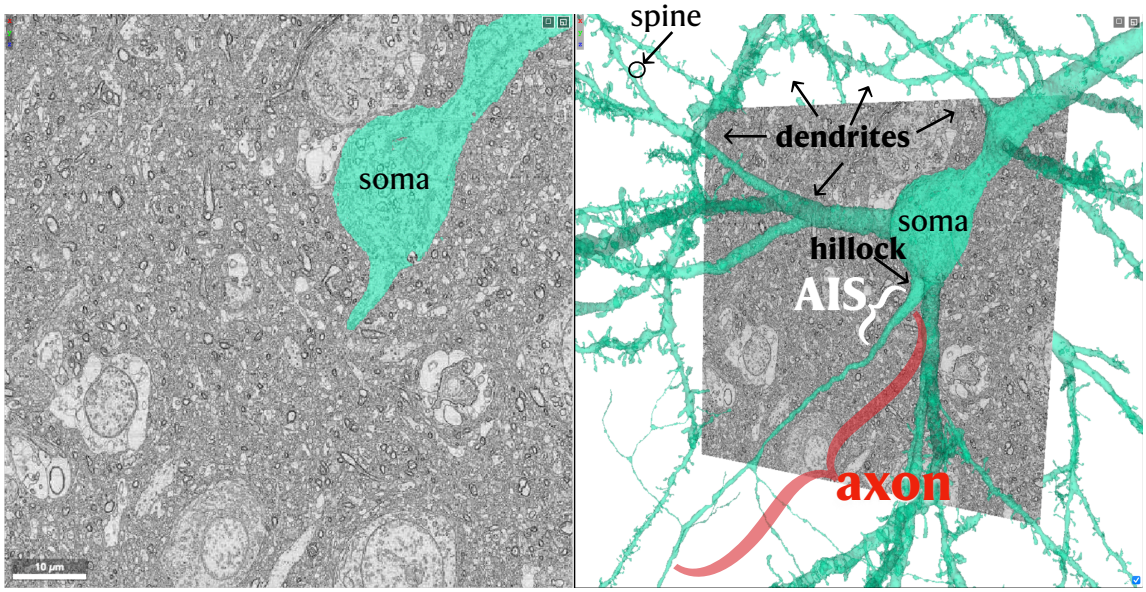

Figure 2.10: **Anatomy of a neuron.** L3 pyramidal cell from human temporal cortex, with Axon visible. Render modified from the H01 release via Neuroglancer, Maitin-Shepard et al. [40].

[11] not shown
[12] https://h01-release.storage.googleapis.com/landing.html

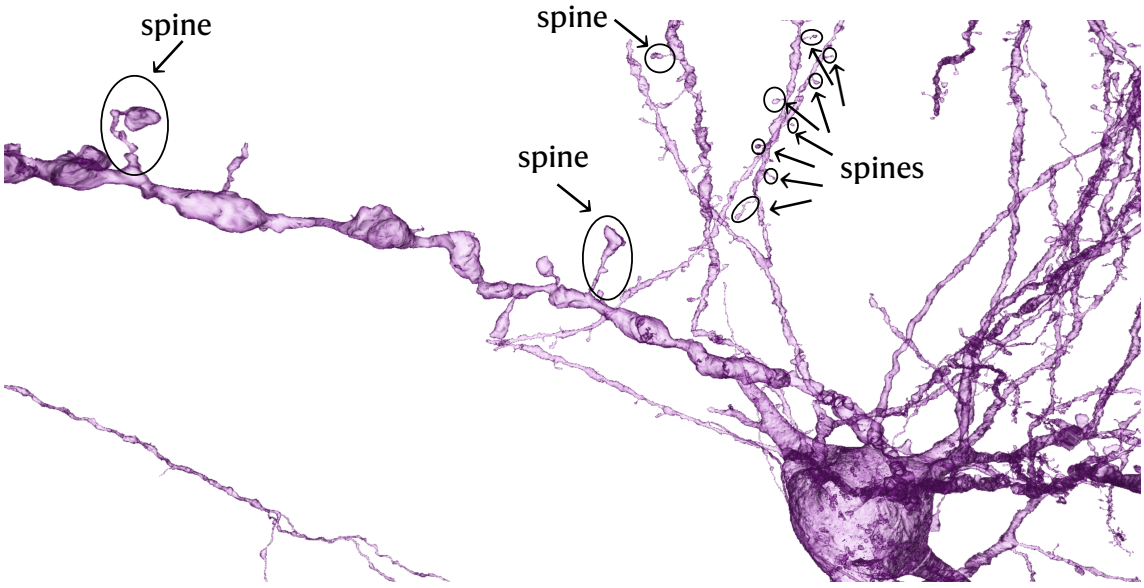

3D-rendered electron microscopy provides connectomic-level detail. That is, down to the synaptic vesicles contained within presynaptic terminals[11] at the spines.

Figure 2.11: **Same neuron as in Figure 2.9, zooming in to show dendritic spines (excitatory synaptic input).** Soma is visible in the bottom right corner. Render modified from the H01 release[12] via Neuroglancer.

Figures 2.9 to 2.11 provide the genuine 3D shape: the membrane of a pyramidal cell imaged at nanometre resolution. But we are still omitting something crucial. The space surrounding the neuron is crammed with the axons and dendrites of other cortical neurons, as well as glial cells, capillaries, etc. This so-called extracellular *space* (ECS) is hardly spacious, with the gaps between most cells being on the order of 40nm [44]. Although brain tissue is approximately 20% ECS by volume, electron microscopy sample preparation techniques can shrink the ECS volume down to 5%, with current methods performing much better [25, 55].

Brain tissue is so densely packed that nearly every square micron of the cell's surface is adjacent to some other cell. Figure 2.12 is an electron microscope image of a cross-section of human association cerebral cortex, alongside the 3D render of a single neuron's soma and dendrites, allowing us to see the myriad cellular processes surrounding and enveloping the neuron.

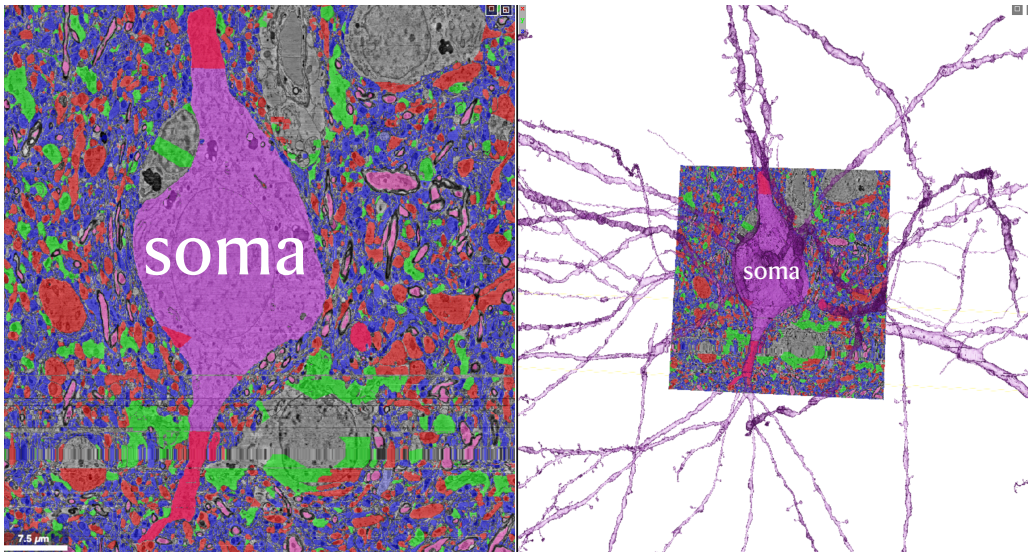

Neurons are utterly surrounded and enveloped by myriad cellular processes, including the axons and dendrites of other neurons.

Figure 2.12: **Left: electron microscopy xy-section from the H01 release. Right: same cross section with three-dimensional morphology of the neuron whose soma is labelled in the plane.** (Modified from Neuroglancer [40]).

a poetic remark

By their appearance, one would almost think that neurons, tired of waiting for random walk after random walk to complete, chose to *become* the walks by instantiating them in their morphology, and thereby expedited the trajectories via electrical signals instead of tedious uncorrelated sequential steps.

Biologists have a variety of tools for staining and tagging cells to identify neurons. In addition to their shape, neurons can be identified via electrophysiological measurements—i.e. by listening for action potentials (see Chapter 3).

2.3 Electrodiffusion

> *"If, in some cataclysm, all of scientific knowledge were to be destroyed, and only one sentence passed on to the next generations of creatures, what statement would contain the most information in the fewest words? I believe it is the atomic hypothesis (or the atomic fact, or whatever you wish to call it) that all things are made of atoms—little particles that move around in perpetual motion, attracting each other when they are a little distance apart, but repelling upon being squeezed into one another. In that one sentence, you will see, there is an enormous amount of information about the world, if just a little imagination and thinking are applied."*—Atoms in Motion, from Feynman, Leighton, and Sands [17]

The world is made of atoms.

The world is made of atoms [17]. Although neurons are measured in microns ($1\mu m = 10^{-6} m$) and can be as long as the animal they inhabit,—whereas atoms are measured in ångströms ($Å \stackrel{\text{def}}{=} 10^{-10} m$)—to understand the currents that govern action potentials we must start at the level of atoms.

Electrical currents in neurons are due to the motion of ions (atoms with a net charge) in water.

Ionic currents are driven by two effects: the drift velocity of ions in saline due to an electrostatic body force, and their diffusion which is driven by concentration gradients and temperature. Here, we will quantify both of these effects to explain the emergent transmembrane voltage of neurons and the currents that flow across the cell membrane. From there, we can introduce the GHK equation for the resting potential in the presence of multiple ion species and move on to the equivalent-circuit model of a neuron, which is an ohmic approximation of the permeability description used in GHK. These derivations follow [53, 43, 17], and [15].

First: GHK, then ohmic approximation, Hodgkin-Huxley.

2.3.1 The electric currents in our cells

Electricity flows in neurons in the form of ionic currents.

You may recall that electricity flows in metallic conductors due to the "sea" of delocalized electrons, which are free to move all over metals. Well, seawater—where our vertebrate ancestors evolved—and the saline fluids filling and surrounding our cells conduct electricity via the "sea" of ions bobbing around in them.

Solvated ions crystallize into salt as seawater evaporates.

If you place a large pot of (clean) seawater on a stove and attempt to boil it all away, a whitish paste will accumulate in the bottom of the pot which, if allowed to dry, will weigh roughly 35g-per-L of seawater. What remains is sea salt—i.e. sodium chloride plus salts of magnesium and calcium, and potassium chloride as well as other hitherto dissolved solids.

The ions that make up the salt crystals were dissociated from one another in the seawater. In air, the Brownian kicks of surrounding gas molecules aren't energetic enough to liberate ions from salt crystals at an appreciable rate, but the situation is different in water. The polar character of H_2O molecules reduces the energy needed to escape the lattice to something easily attainable by the Boltzmann distribution at temperatures much lower than body temperature ($T \approx 310\text{K}$).

Water molecules screen the electric field of ions in solution.

Before the seawater evaporated, the Na^+, K^+, Cl^-, and other ions were diffusing around freely. Aqueous ions are shielded from the electrostatic pull of their oppositely charged counterions by neighbouring water molecules, which orient themselves into hydration shells that "screen" charged particles. Although the ions are shielded from each other's electric fields, they still feel the force of *externally* applied fields. Pure water is an insulator, but even low concentrations of solvated ions allow water to conduct electricity.

Water+dissolved ions = conductor.

2.3.2 Drift current

In the absence of a body force, the average displacement and velocity of a particle undergoing Brownian motion is zero: $\langle x \rangle = \langle \dot{x} \rangle = 0$. When an external electric field $\vec{\mathbb{E}}$ is applied across a saline solution, the ions therein experience a body force,

Electric field induces drift velocity of aqueous ions: an electric current.

$$\vec{F} = q\vec{\mathbb{E}} = ze\vec{\mathbb{E}}, \tag{2.3}$$

where z is the ion's valence and e is the elementary charge. $\vec{F}$ will, on average, drive the ions to follow electric field lines according to their valence (see Figure 2.13).

The instantaneous velocity of an aqueous ion is relentlessly randomized by collisions with water molecules; however, due to the electric field, a collective drift velocity of such ions will emerge, and since ions are charge carriers, the drift velocity produces a net flow of charge—a drift-electric current.

Because the drift velocity creates an electric current, the velocity $\vec{v}_{drift}$ can be inferred by measuring the current between two submerged electrodes if the ion concentration is known (Equation (2.13)).

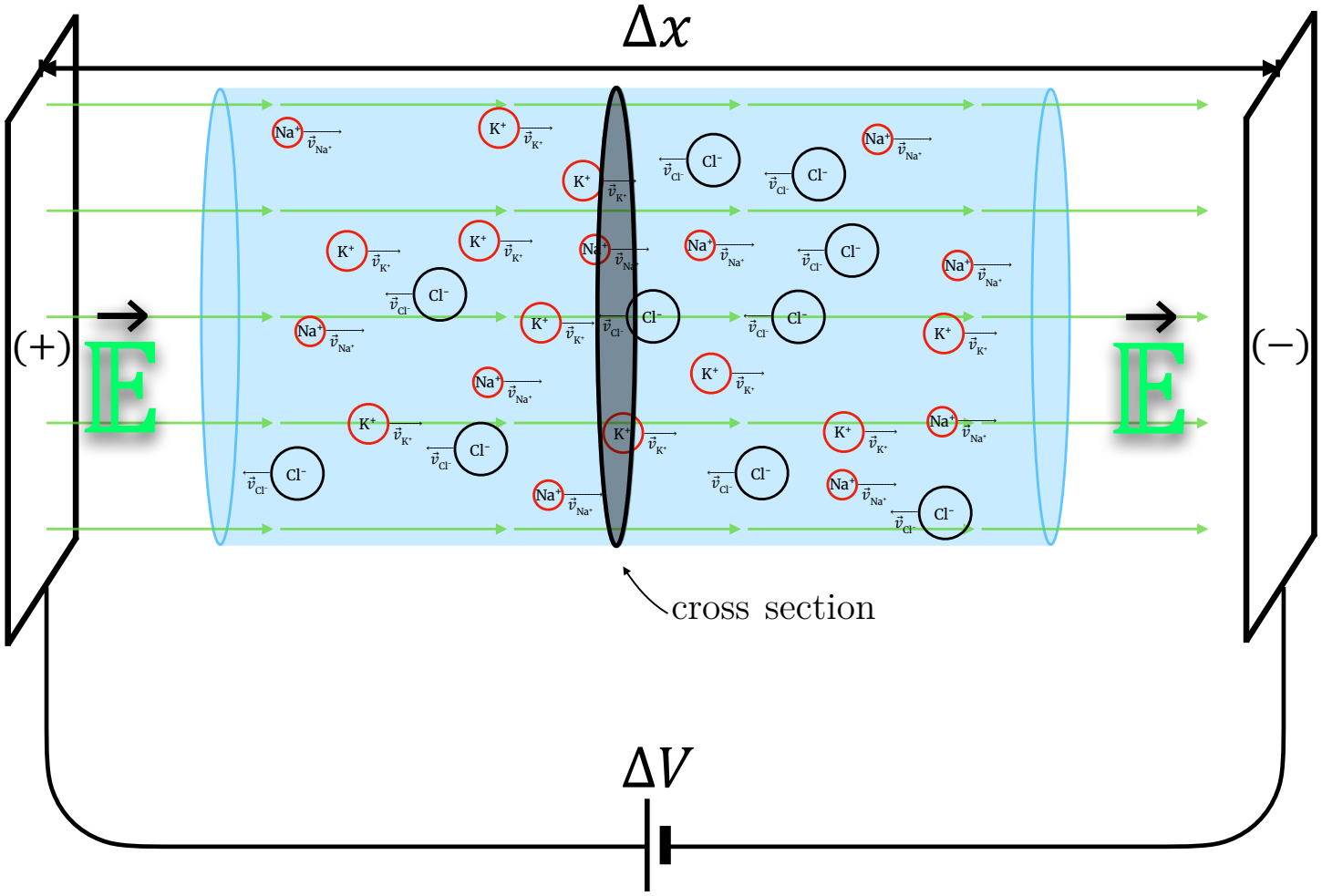

Figure 2.13: **Electrical current in saline (or cytosol) resulting from the bulk motion of ions (drift velocity) in an external electric field $\vec{\mathbb{E}}$.** Arrows attached to ions represent their drift velocities, $\vec{v}_{\text{ion}}$, *not* their stochastic instantaneous velocities. Water molecules are not drawn, and are instead represented by the shaded blue cylinder. Although additional ions may be present in real neurons (e.g. Ca^{2+}, Mg^{2+}), this cartoon could depict the current flowing through a glass pipette electrode, or the axial current along a dendrite or axon, or the current through a pore in the cell membrane, or a gap junction, etc.

Saline, cytosol, and cerebrospinal fluid share a property called *bulk electroneutrality* with other familiar substances. Positive and negative charges balance one another, and hence, these materials do not spontaneously explode. In the presence of an electric field $\mathbb{E}$, H_2O molecules will feel a restoring torque that directs their intrinsic dipole moment into alignment with the field lines. Having zero net charge, the water molecules will *not* experience a net force—aside from the torque—and therefore do not flow in response to $\mathbb{E}$.

However, aqueous ions in the aforementioned fluids will be propelled at a constant average velocity $\vec{v}_{drift}$ that produces a viscous drag force equal and opposite to the body force from the $\vec{\mathbb{E}}$-field.

$$\vec{F}_{\text{viscous·drag}} = -\vec{v}_{drift}\zeta = -ze\vec{\mathbb{E}}. \tag{2.4}$$

In Figure 2.13, the drift velocity of each ion species is denoted $\vec{v}_{\text{ion}}$, where "ion" $\in \{Na^+, K^+, Cl^-\}$. $\vec{v}_{drift}$ is averaged over many ions and is observed on a timescale much longer than the mean-free time between collisions. The viscous force on the ion results from its interactions with water molecules—vastly outnumbering the aqueous ions—during the stochastic collisions it experiences along its path (see Figure 2.1). The viscous drag coefficient ζ has dimensions[13]

$$[\![\zeta]\!] = \frac{\text{mass}}{\text{time}}, \tag{2.5}$$

and is related to the viscosity η and the ionic radius R via Stokes' law

$$\zeta(T) = 6\pi R\eta(T) \quad \Big| \quad \text{Stokes' drag formula.} \tag{2.6}$$

[13]The special square brackets denote: $[\![\text{physical quantity}]\!] \stackrel{\text{def}}{=}$ dimensions of physical quantity.

In the time between collisions, the ions accelerate freely in the electric field. Added to their randomly oriented thermal velocities is a component parallel to $\vec{\mathbb{E}}$. If τ is the average time that an ion, selected at random, will continue along its trajectory before hitting another water molecule, then

$$\vec{v}_{drift} = \overbrace{\left(\frac{\vec{F}_{\vec{\mathbb{E}}}}{m}\right)}^{\vec{a}\Delta t}\tau = \frac{\tau}{m}q\vec{\mathbb{E}} = \tilde{\mu}\vec{F}. \tag{2.7}$$

By symmetry, τ is also the average time *since* a randomly selected ion's previous collision. The mobility $\tilde{\mu}$ is defined as

$$\tilde{\mu} = \frac{\tau}{m}, \tag{2.8}$$

with m being the particle mass. (The tilde "$\sim$" over the mobility $\tilde{\mu}$ indicates that we are using Feynman's definition of mobility [17, Volume I, Chapter 43], which is the reciprocal of ζ. The more commonly used *electrophoretic mobility* μ is defined below in Equation (2.47), they are related via $q\tilde{\mu} = \mu$.)

The drift current density $\mathbb{J}$ is given by the average number of ions of each species that pass through a cross section of the cylinder (shaded region in the centre of Figure 2.13) per unit time—each ion being multiplied by its charge ($\mathsf{e} \times$ valence)—divided by the cross-sectional area A.

The charge that flows through a cross section (area A, see Figure 2.13) during the time interval Δt due to the drift velocity of a given ion species is

$$Q(\Delta t) = qnAv_{drift}\Delta t = \tilde{\mu}q^2nA\mathbb{E}\Delta t. \tag{2.9}$$

Dividing through by $A\Delta t$ gives the current *density* due to the drift velocity,

$$\mathbb{J}_{ion} = \frac{Q}{A\Delta t} = qnv_{drift} = \tilde{\mu}q^2 n\mathbb{E} = \tilde{\mu}q^2 n\frac{\Delta V}{\Delta x}, \tag{2.10}$$

where Δx is the spacing between submerged electrodes in Figure 2.13 and ΔV is the applied voltage.

Since $z_{Na^+} = z_{K^+} = 1$, and $z_{Cl^-} = -1$, we can rewrite the total drift current as

$$\vec{\mathbb{J}}_{drift} = \sum_{ions} \vec{\mathbb{J}}_{ion} = \sum_{ions} (\underbrace{z_{ion}}_{q_{ion}}\mathrm{e}) n_{ion}\vec{v}_{ion} = \mathrm{e}\left(n_{Na^+}\vec{v}_{Na^+} + n_{K^+}\vec{v}_{K^+} - n_{Cl^-}\vec{v}_{Cl^-}\right). \tag{2.11}$$

Writing the drift velocities' magnitudes as $v_{ion} \overset{\text{def}}{=} |\vec{v}_{ion}|$, and the unit vector in the direction of the electric field as $\mathbf{e}_{\mathbb{E}} \overset{\text{def}}{=} \frac{\vec{\mathbb{E}}}{|\vec{\mathbb{E}}|}$, note that

$$\left\{\vec{v}_{Na^+}, \vec{v}_{K^+}, \vec{v}_{Cl^-}\right\} = \left\{v_{Na^+}\mathbf{e}_{\mathbb{E}}, v_{K^+}\mathbf{e}_{\mathbb{E}}, v_{Cl^-}(-\mathbf{e}_{\mathbb{E}})\right\}. \tag{2.12}$$

Because Cl^- is an anion and the other particles are cations, the "$-$" sign in the chloride term on the right of Equation (2.11) is cancelled by its drift velocity being in the opposite direction to that of Na^+ and K^+, thus

$$\boxed{\mathbb{J}_{drift} = \mathrm{e}\left(n_{Na^+}v_{Na^+} + n_{K^+}v_{K^+} + n_{Cl^-}v_{Cl^-}\right)}. \tag{2.13}$$

2.3.3 Ohm's law from $\mathbb{J}_{drift}$

The drift velocity discussed above gives rise to a version of Ohm's law in cytosol and saline solutions in general. Note that both anions and *cations* serve as charge carriers in neurons. Benjamin Franklin's current convention is well suited to neuroscience, where electric currents are ions moving through water (rather than electrons through a

Benjamin Franklin's current convention is true for cations flowing in the cytosol.

crystal[14]) and three out of the four key currents' charge carriers $\{Na^+, K^+, Ca^{2+}, Cl^-\}$ are positive ions.

In metallic conductors like copper—or silver, which is roughly 10% better—we are familiar with Ohm's law,

Units of electrical conductance: $S \stackrel{\text{def}}{=} \frac{1}{\Omega} = \mho$.

$$I = GV, \tag{2.14}$$

where I is the current through a piece of the conducting material, G is its conductance, and V is the voltage drop from one end of the conductor to the other. I has units of amperes (A)—or Coulombs of charge flowing per second—and G, which is the inverse of the resistance R, has units of Siemens which are reciprocal Ohms ($S = \Omega^{-1}$), or "Mho"s ($\mho$) if you prefer.[15]

The conduct*ance* is an extrinsic property which measures how easily electric current flows through a *particular object*, so it varies with the size and shape of the object. In an electronic circuit, the object might be a cylindrical piece of metal wire. In a neuron, it could be a cylindrical volume of cytosol, as in Figure 2.13.

Conductivity of seawater derived from the ionic current between two submerged, charged plates.

To formulate the aqueous Ohm's law, we will make use of intrinsic properties instead, namely the conduct*ivity* g, which is a property of the material and allows us to calculate the conductance of any object given its dimensions:

$$G = g\left(\frac{A}{L}\right). \tag{2.15}$$

If A is the cross section in Figure 2.13, take a cylindrical volume of cytosol with length L and base A as our conductor. The current density in the conductor is

$$\mathbb{J}_{ion} = \frac{I_{ion}}{A}. \tag{2.16}$$

[14] Metals are composed of microscopic crystalline domains called *grains*.
[15] The Mho lives on.

From Equation (2.10), the current is then

$$I_{ion} = A \cdot qnv_{drift} = A \cdot \tilde{\mu} q^2 n \mathbb{E} = \underbrace{\tilde{\mu} q^2 n \left(\frac{A}{L}\right)}_{G} V_L, \tag{2.17}$$

where V_L is the voltage drop across the conductor (i.e. $\left(\frac{V_L}{L}\right) = \mathbb{E}$).

One can see that Equation (2.17) is an Ohm's law for saline by comparing it to Equation (2.14). Each ion species contributes g_{ion}, given by

$$g_{ion} = \tilde{\mu}_{ion} q_{ion}^2 n_{ion}, \tag{2.18}$$

to the total conductivity g. We will make use of this version of Ohm's law in the equivalent circuit model of the axonal membrane (Hodgkin-Huxley style kinetics, see Background II: Action potentials and ion channels).

The fluid filling and surrounding neurons is about ten million times less conductive than silver. This has consequences for signal transmission: the high resistivity of cytosol makes it difficult to send DC electrical signals[16] along the lengths of neurons. Instead, they use a form of AC signal called an action potential, which we will see later on in Chapter 3.

[16] A common remark in neuroscience is that "neurons are terrible wires". Yes, but they *are not mere wires*. Would we prefer that our axons were made of metal? Have you ever cut an electrical wire only to watch it grow back and find its old connection?

2.3.4 Diffusive current - Fick's laws

Here I will introduce the diffusive current following [43, 17]. In 1855, Adolph Fick empirically demonstrated that salt ions in water diffuse according to the same equation that describes the diffusion of heat and electricity in conducting materials [18].

Concentration gradients drive the diffusive flow of aqueous ions: another electric current

Let $n(x, y, z)$ denote the concentration—e.g. number of Na^+ ions per unit volume—as a function of position. **Fick's first law** states that the diffusive flux $\mathbb{J}$—the net number of ions per unit area that traverse a cross section of fluid per unit time—is proportional to the gradient of the concentration:

$$\boxed{\vec{\mathbb{J}} = -D\vec{\nabla}n}. \tag{2.19}$$

As defined here, $\mathbb{J}$ is also known as a number flux.

D is the diffusion coefficient, which we will ignore for the moment.

Although Fick's first law is empirical, the following derivation may provide some intuition to accompany it. In the case of longitudinal diffusion along the x–axis, Equation (2.19) can be simplified to

$$\mathbb{J} \propto -\frac{\partial n}{\partial x}. \tag{2.20}$$

The aim here is to show that the number flux (or diffusive current density) due to the thermal motion of particles suspended in a fluid should be proportional to the concentration gradient. The particles could be salt ions in water, or hydrocarbon molecules diffusing in air, et cetera.

In Figure 2.14, we sketch an idealized version of the random motion of Na^+ ions diffusing in water in one dimension. It is assumed that the density of ions, $n(x)$, is small compared to the number density of the fluid, and there is no net body force

acting on the particles to bias their macroscopic motion. We want to know the number of particles that cross the surface (area "A") per unit time.

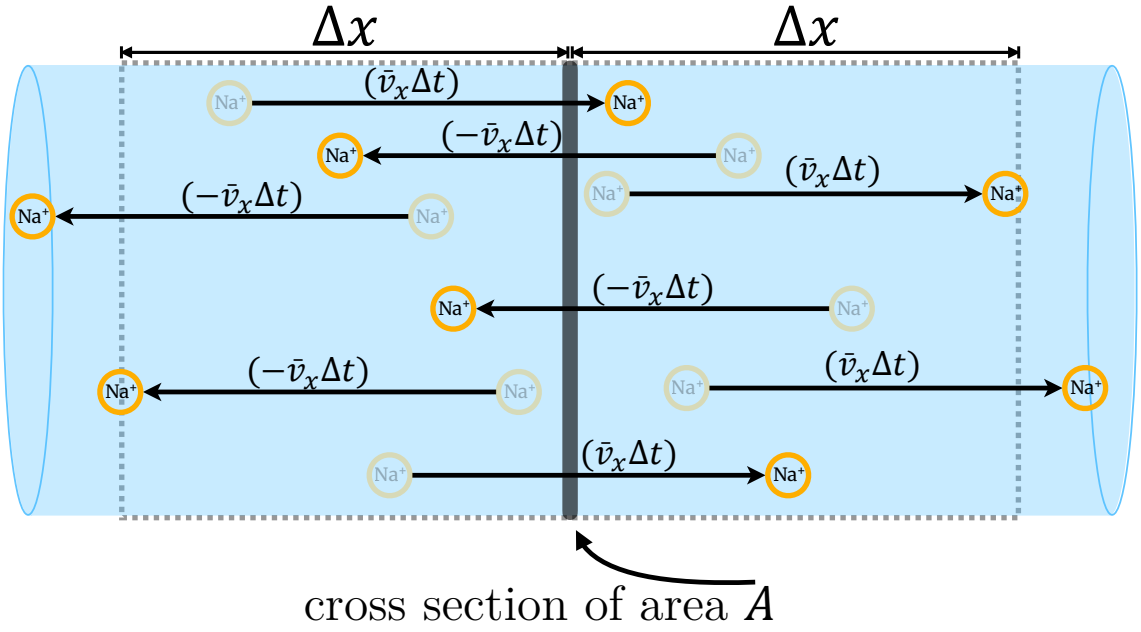

Figure 2.14: **Conceptual sketch of Fick's first law in one dimension** (See [43, 17]). Arrows point toward ions' positions at time $t = (t_0 + \Delta t)$. The faded images of ions at arrows' tails indicate their previous position, i.e. at time $t = t_0$. The root-mean-square velocity of the ions due to their thermal motion is denoted $\bar{v}_x$, not to be confused with their average velocity, which is zero, nor the much slower drift velocity. Note that in this figure, the distance the ions travel (length of the arrows) represents a kind of ensemble average, since statistical mechanics tells us that at any instant the ions' velocities will be randomly distributed around $\bar{v}_x$. (Counterions are omitted to reduce visual clutter.)

Let N_+ denote the number of particles that were initially in the box to the left of A at time $t = 0$ that subsequently crossed A (moving left to right) by the time $t = \Delta t$. Likewise, N_- denotes the number of particles that crossed A *from the right* during the same period. Using this sign convention, the *net* number of particles that diffused across the surface A during Δt is

$$N = (N_+ - N_-), \tag{2.21}$$

where positive N corresponds to a current (or number flux) in the positive x–direction.

If we choose Δx on the order of the mean free path, λ, of the diffusing particles, we can approximate the number density as being uniform in the boxes to the left and right of A in Figure 2.14. Let $n(x)$ denote the number density in the left box, and $n(x + \Delta x)$ in the box on the right.

Since the average velocity $\langle v_x \rangle$ due to Brownian motion (a random walk) is zero, half the particles in either box will be travelling toward A. The other half will be travelling away from $\overbrace{\text{that cross section}}^{A}$, so we include a factor of $\frac{1}{2}$ in the expressions below:

$$\begin{cases} N_+ \propto \frac{n(x)}{2} A v \Delta t, \text{ and} \\ N_- \propto \frac{n(x+\Delta x)}{2} A v \Delta t, \end{cases} \tag{2.22}$$

where v is the thermal speed of the particles—i.e. the effective speed at which they travel between collisions—since in Figure 2.14 we are keeping $\Delta t \lesssim \tau$:

$$\bar{v}_x = \sqrt{\langle v_x^2 \rangle} = \sqrt{\frac{k_B T}{m}}. \tag{2.23}$$

Combining Equation (2.21) and Equation (2.22), the diffusive current density $\mathbb{J}_x$ is

$$\mathbb{J}_x = \frac{N}{A\Delta t} \propto \Big(n(x) - n(x + \Delta x) \Big) \bar{v}_x = \frac{-1}{2} \bar{v}_x \frac{dn}{dx} \Delta x. \tag{2.24}$$

If we treat diffusion as a random walk where all memory of a particle's past trajectory is erased with each collision, the appropriate value for Δx is the step size of the random walk, i.e. the mean free path λ. Writing $\bar{v} = \frac{\lambda}{\tau}$, Equation (2.24) becomes

$$\boxed{\mathbb{J}_x \propto -\frac{\lambda^2}{2\tau} \frac{dn}{dx}}, \tag{2.25}$$

which is convenient since (1) it recovers Equation (2.19) *and* (2) the diffusion coefficient for a random walk is defined as

$$D = \frac{\lambda^2}{2\tau}, \tag{2.26}$$

see [43].

This is *not* entirely satisfying since we have not explained *why* Δx and Δt cannot be made *much* smaller than λ and τ. Scaling Δx and Δt by some positive number $\varepsilon << 1$ *should* be permissible in the above derivation, but it would change the value of $\mathbb{J}_x$ in Equation (2.24).

But why did we resort to hiding Δx and Δt inside a constant?

The above derivation began with Figure 2.14, which is missing something crucial: There is nothing in that figure that captures the *irreversibility* of the diffusion process [see 45, Section 15.3]. That is why we invoked Equation (2.26) to *impose* the correct choice of Δx and Δt by tucking them neatly inside the mathematical definition of D. However, choosing Δx as the mean free path *does* make physical sense: On the right-hand side of Equation (2.24), we see that a particle with a longer mean free path will diffuse more rapidly.

Explanation: The limitations of the above derivation.

In reality, D is a coefficient that is determined experimentally via measurements of $\mathbb{J}_x$ and $\frac{dn}{dx}$, or other direct observations. The above derivation does, however, satisfy the goal stated at the outset: we have shown that $\mathbb{J}_x \propto -\frac{\partial n}{\partial x}$ (i.e. the diffusive flux is proportional to the gradient of $n(x)$, Equation (2.20)), which becomes Equation (2.19) in three dimensions.

In Figure 2.15, we obtain the time-derivative of the concentration from Fick's first law (Equation (2.19)).

Diffusion is a directly measured and perpetually observed experimental fact, and Fick's law describes it accurately. The semi-derivation above connects Fick's law—which is really a mathematically expressed observation—to our intuitions about atoms in thermal motion.

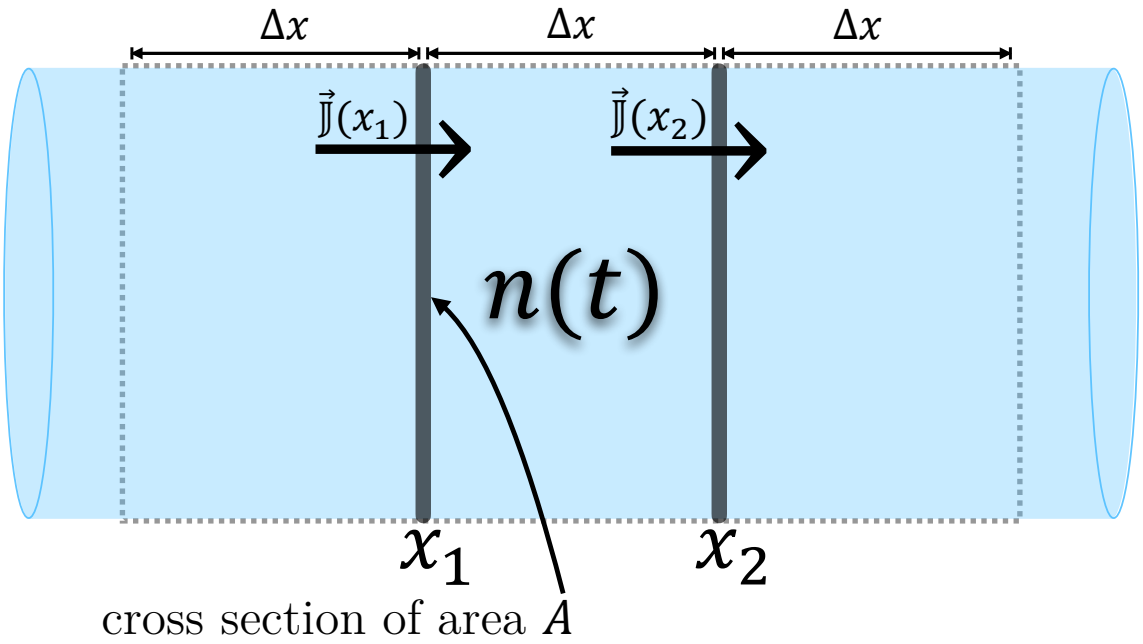

Figure 2.15: **Conceptual Sketch for Fick's second law, also known as the diffusion equation.** In this figure and the equations below, $n(t)$ is the number density of some ion species in the box bounded by the cross sections at x_1 and x_2. Horizontal arrows piercing the cross sections indicate the direction of positive diffusive flux; however, $\mathbb{J}(x_1)$ and $\mathbb{J}(x_2)$ can be positive or negative.

Again restricting ourselves to one spatial dimension, let n denote the number density of an ion species at the box in the middle of Figure 2.15. The change in n per unit time is given by the diffusive flux across the two cross sections on either side of the middle box:

$$\frac{\partial n}{\partial t} = \frac{1}{Vol}\Big(\mathbb{J}_x(x_1)A_1 - \mathbb{J}_x(x_2)A_2\Big). \tag{2.27}$$

Letting each cross section have the same area ($A_1 = A_2 = A$), we have

$$\longrightarrow \frac{\partial n}{\partial t} = \frac{1}{\underbrace{A\Delta x}_{Vol}}\Big(\mathbb{J}_x(x_1)A - \mathbb{J}_x(x_2)A\Big), \tag{2.28}$$

$$= \frac{1}{\Delta x}\Big(\mathbb{J}_x(x_1) - \mathbb{J}_x(\underbrace{x_1 + \Delta x}_{(x_2)})\Big). \tag{2.29}$$

For small Δx we can use the derivative of $n(x)$, as before,

$$\longrightarrow \frac{\partial n}{\partial t} \cong \frac{1}{\Delta x}\left(\mathbb{J}_x(x_1) - \left[\mathbb{J}_x(x_1) + \frac{\partial \mathbb{J}_x}{\partial x}\Delta x\right]\right). \tag{2.30}$$

Finally, we invoke Equation (2.19) to write the flux in terms of the gradient,

$$\text{Equation (2.30)} \Longrightarrow \frac{\partial n}{\partial t} = -\frac{\partial \mathbb{J}_x}{\partial x} = -\frac{\partial}{\partial x}\left(-D\frac{\partial n}{\partial x}\right), \tag{2.31}$$

$$\therefore \frac{\partial n}{\partial t} = D\frac{\partial^2 n}{\partial x^2}. \tag{2.32}$$

In three dimensions, Equation (2.32) becomes[17]

$$\boxed{\frac{\partial n}{\partial t} = D\nabla^2 n}, \tag{2.33}$$

which is known as Fick's second law, or the diffusion equation.

The Laplacian of a function $\varphi(x, y, z)$ in Cartesian coordinates is written

$$\nabla^2\varphi \overset{\text{def}}{=} \vec{\nabla}\cdot\vec{\nabla}\varphi = \left(\frac{\partial}{\partial x}, \frac{\partial}{\partial y}, \frac{\partial}{\partial z}\right)\cdot\left(\frac{\partial \varphi}{\partial x}, \frac{\partial \varphi}{\partial y}, \frac{\partial \varphi}{\partial z}\right) = \frac{\partial^2\varphi}{\partial x^2} + \frac{\partial^2\varphi}{\partial y^2} + \frac{\partial^2\varphi}{\partial z^2}. \tag{2.34}$$

Since ∇^2 measures the local curvature of $n(x, y, z)$, Equation (2.33) tells us that diffusion flattens out variations in the local ion concentrations, and drives the system toward a state where all diffusing particles are homogeneously distributed in the solvent.

[17] Assuming D is isotropic.

2.3.5 Einstein's relation

Returning to Equation (2.7), we now write the number flux of some ion S with number density $[S](x)$ and valence z_S in terms of the drift velocity in aqueous solution under an external electric field $\vec{\mathbb{E}}$.

Starting with the drift velocity,

$$\left|\vec{v}_{drift}\right| = \left|\tilde{\mu}\vec{F}\right| = \left|\tilde{\mu} z_S \mathrm{e} \vec{\mathbb{E}}\right|, \tag{2.35}$$

the flux due to drift can be written as

$$\left|\vec{J}_{drift}\right| = [S]\left|\vec{v}_{drift}\right| \Longrightarrow J_{drift} = [S]\tilde{\mu} z_S \mathrm{e}\mathbb{E}, \tag{2.36}$$

with $\mathbb{E} = -\frac{dV}{dx}$.

For a system in thermodynamic equilibrium, the drift flux cancels the diffusive flux

$$J_{drift} = -\mathbb{J}_x \Longrightarrow \boxed{[S]\tilde{\mu} z_S \mathrm{e}\mathbb{E} = D\frac{d[S]}{dx}}, \tag{2.37}$$

and the Boltzmann distribution also applies

$$[S](x) = const \cdot \overbrace{e^{-U(x)/k_B T}}^{e^{-\left(\frac{z_S \mathrm{e} V(x)}{k_B T}\right)}} \Longrightarrow \boxed{D\frac{d[S]}{dx} = -D \cdot [S]\frac{z_S \mathrm{e}}{k_B T}\overbrace{\left(\frac{dV}{dx}\right)}^{-\mathbb{E}}}, \tag{2.38}$$

where $U(x) = -z_S \mathrm{e} V(x)$ is the potential energy of the ion.

By combining Equations (2.37) and (2.38), we can eliminate the force and concentration from both sides

$$\cancel{[S]}\,\tilde{\mu} z_S \mathrm{e}\mathbb{E} = \cancel{[S]}\, D\frac{z_S \mathrm{e}}{k_B T}\,\mathbb{E}, \tag{2.39}$$

which gives Einstein's relation

$$\therefore \boxed{D = \tilde{\mu} k_B T}. \tag{2.40}$$

The above derivation is based on Feynman et al. [17, Volume I, Chapter 43].

If we prefer to use the electrophoretic mobility μ, then Equation (2.35) is written

$$v_{drift} = \mu \mathbb{E}, \tag{2.41}$$

and Einstein's relation (2.40) becomes

$$\boxed{z_S e D = \mu k_B T}. \tag{2.42}$$

Stokes-Einstein

Stokes' viscous drag formula (Equation (2.6)) lets us connect the drift velocity to the electric field strength—without invoking the mobility—via the effective radius of the hydrated ion R_S and the viscosity η:

$$\left| z_S e \vec{\mathbb{E}} \right| = \left| \vec{F}_{\text{viscous·drag}} \right| = v_{drift} \zeta \Longrightarrow \mathbb{E} = \frac{v_{drift} \cdot 6\pi\eta R_S}{z_S e}. \tag{2.43}$$

Plugging Equation (2.41) into (2.43) gives a new expression for the mobility

$$\mathbb{E} = \mu \frac{\mathbb{E} \cdot 6\pi\eta R_S}{z_S e} \Longrightarrow \mu = \frac{z_S e}{6\pi\eta R_S}, \tag{2.44}$$

which, when combined with Equation (2.42), gives the Stokes-Einstein relation

$$\boxed{D = \frac{k_B T}{6\pi R_S \eta} \qquad \Leftrightarrow \qquad D\zeta = k_B T}. \tag{2.45}$$

From the boxed expressions above (2.45), we can see the interconnected temperature-dependence of the viscous-drag coefficient $\zeta = \zeta(T)$ (reciprocal mobility), the diffusion coefficient $D = D(T)$, and the viscosity $\eta = \eta(T)$.

2.3.6 The Nernst-Planck equation

The Nernst-Planck equation combines the effects of diffusion (Equation (2.19)) and drift (Equation (2.10)) to obtain the total flux of ions, hence the term electrodiffusion:

$$\boxed{\mathbb{J}_x = \overbrace{-D_x \frac{\partial [C]}{\partial x}}^{\text{diffusion}} - \overbrace{\mu [C] \underbrace{\left(\frac{\partial V}{\partial x} \right)}_{\mathbb{E}}}^{\text{drift}}}. \tag{2.46}$$

(Ion concentrations are often denoted with square brackets, e.g. $[\mathrm{K}^+]_{\mathrm{in}}$ is the intracellular concentration of potassium ions. We have switched to this notation, writing $[C] = [C](x)$ instead of using $n(x)$ for the number density.)

As mentioned above (see Equation (2.42)), the electrophoretic mobility μ is defined in terms of the diffusion coefficient using Einstein's relation [15]

$$\mu = \frac{qD}{k_{\mathrm{B}}T} = \frac{z_{\mathrm{ion}}\mathrm{e}D}{k_{\mathrm{B}}T}, \tag{2.47}$$

and one can rewrite the Nernst-Planck equation (2.46) as

$$\mathbb{J}_x = -\mu \left(\frac{k_{\mathrm{B}}T}{q} \frac{\partial [C]}{\partial x} + z_{\mathrm{ion}} [C] \frac{\partial V}{\partial x} \right) = -D \left(\frac{\partial [C]}{\partial x} + \frac{z_{\mathrm{ion}}\mathrm{e}}{k_{\mathrm{B}}T} [C](x) \frac{\partial V}{\partial x} \right). \tag{2.48}$$

This equation describes the *bulk* motion of charged molecules or ions in solution under an electric field, and it is the physical basis for much that follows. In Section 2.4.1 we use it to derive the reversal potential, and in Section 3.5.3 it gives rise to the Goldman-Hodgkin-Katz equations.

2.4 The Nernst potential

Here I will follow the approach in [43, 15, 53] to introduce the Nernst potential.

Associated with each permeant ion species (e.g. Na^+, K^+, Cl^-, Ca^{2+}...) is a value of the transmembrane voltage V_m called the *Nernst potential* and denoted E_{ion}. It is also called the *reversal potential* because as V_m crosses E_{ion}, the flow of ions of that particular species—through channels in the membrane that are permeable to it—will reverse, i.e. the transmembrane current of an ion flips sign at E_{ion} (see Figure 3.15).

The current is driven by diffusion (temperature), which pushes the system toward greater entropy by reducing the concentration gradient across the pore. E_{ion} is the voltage that produces an electric field in the pore sufficient to counteract the diffusive current of that ion species when inner and outer concentrations are unequal.

2.4.1 Deriving E_{Nernst} from the Nernst-Planck equation

The transmembrane voltage at which the diffusive current of a given ion species is cancelled by its electrical drift current—resulting in an equilibrium with zero net flux of said ions across the membrane—is called the Nernst potential. If multiple ion species are present, each will have its own Nernst potential.

Below, $[C]$ denotes the concentration (or number density) of a given ion having valence z, flowing through a pore in the cell membrane. The concentration as a function of position along the pore's axis is denoted by $[C](x)$. Following [15], we derive the Nernst potential by setting $\mathbb{J}_x = 0$ in Equation (2.48):

$$0 = -\mu\left(\frac{k_B T}{q}\frac{\partial[C]}{\partial x} + z[C](x)\frac{\partial V}{\partial x}\right)\Bigg|_{V_m = E_{\text{Nernst}}}, \tag{2.49}$$

$$\Longrightarrow \frac{-k_B T}{qz}\frac{1}{[C](x)}\frac{\partial[C]}{\partial x} = \frac{\partial V}{\partial x}. \tag{2.50}$$

Next, we integrate Equation (2.50) along the length of the pore to get the transmembrane voltage at which this equilibrium condition is achieved:

$$\int_{x_{\text{out}}}^{x_{\text{in}}} dx\,\frac{\partial V}{\partial x} = \int_{x_{\text{out}}}^{x_{\text{in}}} dx\,\frac{-k_B T}{qz}\frac{1}{[C](x)}\frac{\partial[C]}{\partial x}, \tag{2.51}$$

$$\Longrightarrow \underbrace{(V_{\text{in}} - V_{\text{out}})}_{E_{\text{Nernst}}} = \frac{-k_B T}{qz}\ln\big([C](x)\big)\Big|_{x_{\text{out}}}^{x_{\text{in}}}, \tag{2.52}$$

$$\therefore \boxed{E_{\text{Nernst}} = \frac{-k_B T}{q_{ion}}\ln\left(\frac{[C]_{\text{in}}}{[C]_{\text{out}}}\right)}. \tag{2.53}$$

If the inner and outer concentrations of an ion are known, then E_{Nernst} is the value of the membrane potential at which that ion will have zero transmembrane current.

2.4.2 Nernst potential from Boltzmann

We can use the Boltzmann distribution to obtain the Nernst potential in surprisingly few steps. This is done by treating the concentration as a probability and starting from the experimental fact that cells have a nonzero transmembrane voltage,

$$\Delta V \neq 0. \tag{2.54}$$

For the moment, we will not associate ΔV with V_{rest}; it is just the voltage across some membrane.

Consider a single ion in a volume of fluid that encloses a patch of cell membrane (Figure 2.16). Since the Nernst potential (Equation (2.53)) is calculated from the *ratio* of inner and outer concentrations, it is not necessary to specify $[\text{Z}]_{\text{in}}$ and $[\text{Z}]_{\text{out}}$. Instead, to compute E_{Z}, it is sufficient to know the relative probability of the ion being inside versus outside the cell as a function of ΔV.

The Boltzmann distribution gives the likelihood of a particle being in a state i, having energy U_i, as

$$p(U_i) \propto e^{-\beta U_i} \quad ; \quad \beta \stackrel{\text{def}}{=} \frac{1}{k_{\text{B}} T}, \tag{2.55}$$

with all states having the same constant of proportionality[18]. This probability $p(U_i)$—also denoted p_i—is also called the Boltzmann factor of the state i.

[18]The constant of proportionality normalizes the sum of the probabilities to unity.

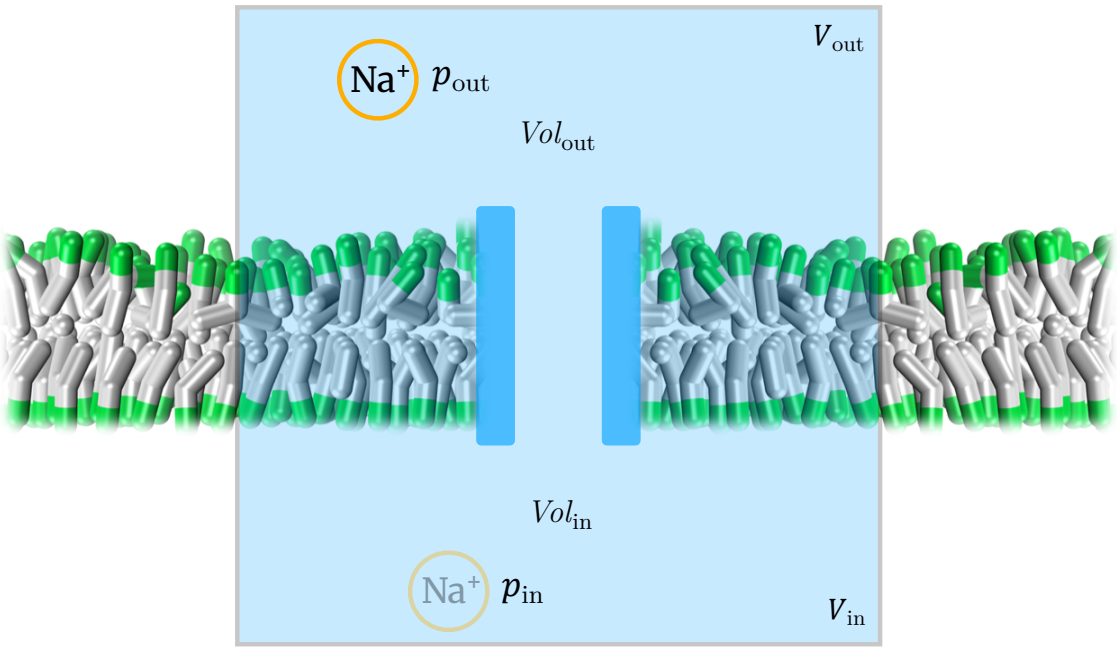

Inner and outer ion concentrations map to probabilities in a two-state system.

Figure 2.16: **The probability of an ion (in this case, sodium) being on either side of the membrane is indicated by its opacity.** The inner and outer volumes enclosed in this figure are equal, i.e. $Vol_{out} = Vol_{in}$. (Note: This figure is for conceptual purposes; it is not to scale. The ion concentrations—or probability of finding an ion within a given volume—are not uniform when this close to the membrane.)

We can treat the ion (say Na^+), which may be inside or outside the cell, as a two-state system. This is because bulk electroneutrality dictates that, beyond a thin depletion region on either side of the cell membrane with a thickness on the order of the Debye screening length[19]

Charge screening makes $V(r)$ flat outside the depletion layers. There is a skin of charge at the surfaces of the membrane. Nelson et al. [43] shows concentration differences cause ΔV.

$$\lambda_D = \sqrt{\frac{\varepsilon_r \varepsilon_0 k_B T}{2e^2 N_A [C](\infty)}}, \tag{2.56}$$

the electric potential inside and outside the cell does not change as a function of distance to the membrane. The screening length is $\lambda_D \sim \mathrm{nm}$ for neurons.[20] Notation: $[C]_\infty$ is the concentration of ions at an infinite distance from the membrane (charged surface).

Hence, the two states are "inside" or "outside", with energies $U_{\text{in}} = q_{Na^+} V_{\text{in}}$ and $U_{\text{out}} = q_{Na^+} V_{\text{out}}$, respectively, and $q_{Na^+} = e$. The probability of the Na^+ ion being on the intracellular side of the membrane can be converted to a concentration:

$$[Na^+]_{\text{in}} \propto \frac{p_{\text{in}}}{Vol_{\text{in}}}. \tag{2.57}$$

Likewise, the ratio of the concentrations is the ratio of the Boltzmann factors:

$$\frac{[Na^+]_{\text{out}}}{[Na^+]_{\text{in}}} = \frac{p_{\text{out}}}{p_{\text{in}}} = \frac{e^{-\beta q_{Na^+} V_{\text{out}}}}{e^{-\beta q_{Na^+} V_{\text{in}}}} = e^{\beta q_{Na^+}(V_{\text{in}} - V_{\text{out}})} = e^{\beta q_{Na^+} \Delta V}. \tag{2.58}$$

Now, with a few more steps...

$$\ln\left(\frac{[Na^+]_{\text{out}}}{[Na^+]_{\text{in}}}\right) = \beta q_{Na^+} \Delta V = \frac{q_{Na^+}}{k_B T} \Delta V, \tag{2.59}$$

[19] This formula assumes monovalent ions. A more reliable formula replaces $[C](\infty)$ with the *ionic strength*, defined as $I = \sum_{\text{ions}} z_{\text{ion}}^2 [\text{ion}](\infty)$.

[20] This is due to charge screening, a crucial phenomenon governing electrostatic interactions in aqueous media [43].

...we obtain the membrane potential in terms of the inner and outer concentrations:

$$\Delta V = -\frac{k_B T}{q_{Na^+}} \ln\left(\frac{[Na^+]_{in}}{[Na^+]_{out}}\right). \tag{2.60}$$

Writing "E_Z" instead of ΔV in Equation (2.60) (and q_Z instead of q_{Na^+}), we have again the Nernst potential, derived directly from Boltzmann:

$$\boxed{E_Z = -\frac{k_B T}{q_Z} \ln\left(\frac{[Z]_{in}}{[Z]_{out}}\right)}.^{21} \tag{2.61}$$

The Nernst potential is the voltage needed to counteract diffusion in the presence of a transmembrane ionic concentration gradient.

[21] This equation is equivalent to Equation (2.53).

Chapter 3

Background Ⅱ: Action potentials and ion channels

We mentioned in What is a neuron? that neurons evolved to overcome the limits of diffusion so that animals can send signals rapidly over long anatomical distances in the form of electrical impulses called action potentials (APs). The discussion paused on page#18, and it resumes here.

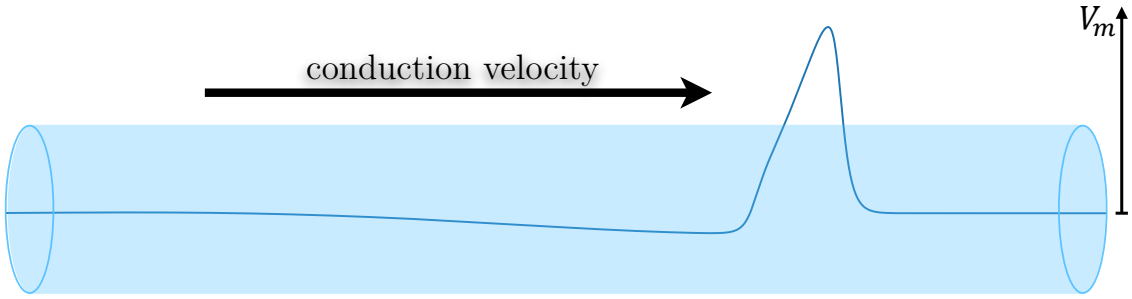

Neurons create a fast-moving longitudinal electrical wave via a series of short-range transmembrane electrodiffusion events.

Figure 3.1: **Sketch of a Hodgkin-Huxley action potential[1] travelling from left to right, superimposed on a cylindrical unmyelinated axon.** The axis of the cylinder intersects $V_\mathrm{m} = 0\,\mathrm{mV}$ on the voltage (vertical) axis. • In this graphic, the peak of the AP pierces the cartoon membrane in the (approximate) regime where V_m becomes *positive*. The significance of this overshoot is to the discovery by Hodgkin and Huxley that, beyond *net* permeability changes that happen during the AP, the *ions* to which the membrane is permeable must be changing as well [21].

[1] The action potential was simulated in Python using NEURON, with standard Hodgkin-Huxley parameters.

It is not entirely accurate to say that neurons overcome the limits of diffusion. They make use of the speed of diffusion over short distances—via transmembrane ion currents—to create a longitudinal wave of depolarization that travels without attenuation. The structure of the axon converts the short-range motion of ions into a crisp, rapidly moving long-range electrical signal (Figure 3.3).

Below the action potential threshold, the response of the neuron's membrane potential to stimulation is linear. The amplitude of the depolarization decays rapidly with distance, and is proportional to the strength of the stimulus even at locations on the axon that are distant from the stimulation site. With suprathreshold stimulation, the shape of the response (an AP) is independent of the stimulus strength, except nearby the stimulating electrode.

3.1 The cable equation

An action potential is a highly dissipative chain reaction [43]. The chain reaction is generated via voltage-gated ion channels in the membrane, which were added to the cable equation by Hodgkin and Huxley [21], as discussed in Section 3.3. The dissipative aspect of signal conduction along the axon is captured by the *passive* cable equation, derived here. Passive properties of the axon are those parameters which do not change with the membrane potential.

This section is based on Nelson et al. [43] and Sterratt [53]. To derive the cable equation, we take the axon in Figure 3.11 and slice it into a stack of cylindrical discs, like a roll of coins, as depicted in Figure 3.2.

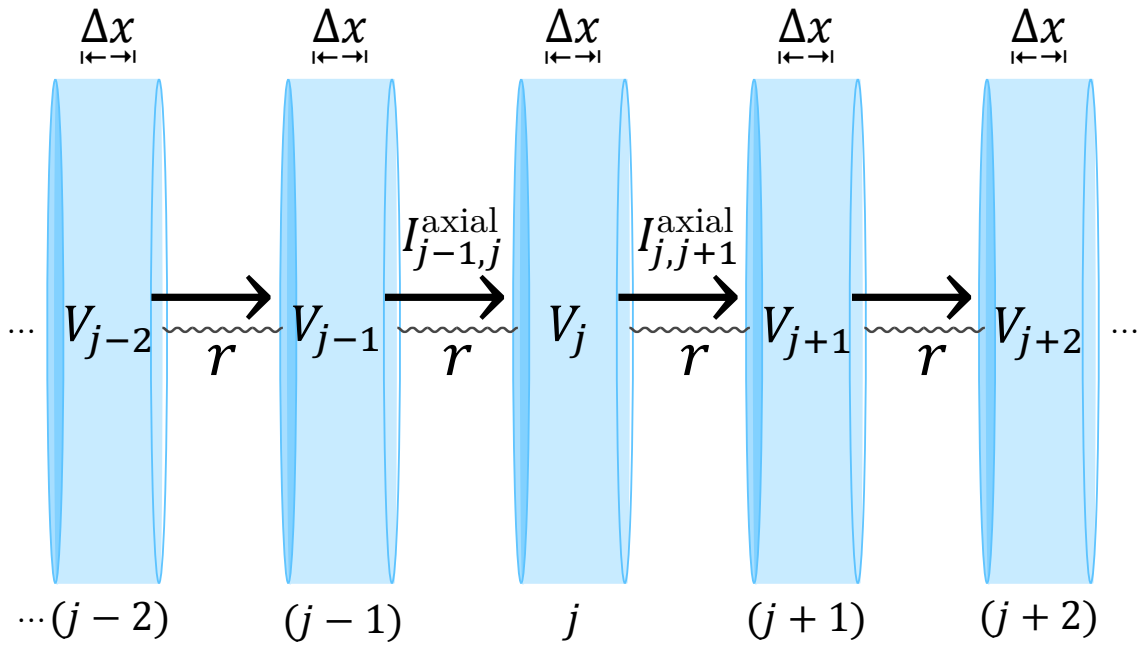

"Cylinder", "slice", and "segment" are used interchangeably to describe a compartment belonging to the axon.

Figure 3.2: **Spatial discretization of the cable equation for multicompartmental models.** The long continuous cylindrical unmyelinated axon in Figures 3.1, 3.3, 3.7 and 3.11 is diced into short isopotential segments of length Δx and radius a. Each segment has its own set of currents (ionic and capacitive) so that the axon is a series of coupled copies of the equivalent circuit detailed in Figure 3.6. There is an extracellular axial resistance that accompanies the intracellular resistance R_a, but the former is negligible relative to R_a and is usually ignored. It is somewhat misleading to place the resistors between the cylinders in this figure since, in reality, the axial resistance is a property of the cylindrical slices.

We analyze the total current at the j^{th} segment in terms of the current flowing to and from its neighbouring segments—to which it is resistively coupled via Ohm's law—and its own transmembrane current. The current from neighbouring segments is longitudinal, called the axial current.

If Δx is allowed to be arbitrarily small, the position of segment j in Figure 3.2 is $x = x_j = j\Delta x$. We can write the axial current $I^{\text{axial}}(x,t)$ at compartment j as

$$I^{\text{axial}}(x,t) = I_j^{\text{net·axial}} = \underbrace{I_{j-1,j}^{\text{axial}} - I_{j,j+1}^{\text{axial}}}_{\substack{\text{net axial current} \\ \text{into } j^{\text{th}} \text{ slice}}}, \tag{3.1}$$

where the subscript notation on I^{axial} is: $I_{(\text{from here}),\,(\text{to there})}$.

The net radial *outward* current through the membrane of the j^{th} slice (segment), including capacitive current[2], is

$$I_j^{\text{radial}} = 2\pi a \Delta x \left(i_{\text{m},j} - i_{\text{inj},j}\right), \tag{3.2}$$

where i_m denotes membrane current density (i.e. current per unit membrane area). The two currents must balance at every compartment to ensure that no charge builds up in any of the cylinders (slices), thus

$$I_{j-1,j}^{\text{axial}} - I_{j,j+1}^{\text{axial}} = I_j^{\text{radial}}. \tag{3.3}$$

That is, charge conservation requires that the axial current entering any segment matches the membrane current leaving it (and vice-versa), i.e.

[2] Although charge does not cross the capacitor, the current into and out of the capacitor flows *as if* it were an outward current through the membrane.

$$I^{\text{axial}}_{j-1,j} - I^{\text{axial}}_{j,j+1} = \underbrace{2\pi a \Delta x \left(i_{\text{m},j} - i_{\text{inj},j}\right)}_{I^{\text{radial}}_j}. \tag{3.4}$$

Dividing by $2\pi a \Delta x$ yields

$$\boxed{\frac{1}{2\pi a \Delta x}\left(I^{\text{axial}}_{j-1,j} - I^{\text{axial}}_{j,j+1}\right) = i_{\text{m},j} - i_{\text{inj},j}}. \tag{3.5}$$

Since the axial current is ohmic, we can write the left-hand side of Equation (3.5) in terms of the voltage as

$$\frac{1}{2\pi a \Delta x}\left(\frac{V_{j-1} - V_j}{r} - \frac{V_j - V_{j+1}}{r}\right). \tag{3.6}$$

The total axial resistance of each compartment is

$$r = \frac{R_{\text{a}} \Delta x}{\pi a^2}, \tag{3.7}$$

which allows us to write the axial current term of Equation (3.5) as the discretized second spatial derivative of V:

$$\frac{a}{2R_{\text{a}}}\left(\left(\frac{V_{j+1} - V_j}{\Delta x^2}\right) - \left(\frac{V_j - V_{j-1}}{\Delta x^2}\right)\right). \tag{3.8}$$

That is, as Δx vanishes Equation (3.8) becomes the axial current in the continuous cable equation

$$\frac{a}{2R_{\text{a}}}\left(\frac{\left(\frac{V_{j+1} - V_j}{\Delta x}\right) - \left(\frac{V_j - V_{j-1}}{\Delta x}\right)}{\Delta x}\right) \xrightarrow{\Delta x \to dx} \frac{a}{2R_{\text{a}}}\frac{\partial^2 V}{\partial x^2}. \tag{3.9}$$

Writing the capacitive and ion current terms explicitly, the membrane current in Equation (3.5) is

$$i_{\mathrm{m}}(x,t) = C_{\mathrm{m}}\frac{dV_j}{dt} + \sum_{\mathrm{ion}} g_{\mathrm{ion}}(V - E_{\mathrm{ion}}). \tag{3.10}$$

Therefore, with ohmic ion currents, the cable equation in its discretized and continuous forms are (respectively)

$$C_{\mathrm{m}}\frac{dV_j}{dt} = \frac{a}{2R_{\mathrm{a}}}\left(\left(\frac{V_{j+1}-V_j}{\Delta x^2}\right) - \left(\frac{V_j - V_{j-1}}{\Delta x^2}\right)\right) - \sum_{\mathrm{ion}} g_{\mathrm{ion},\,j}(V_j - E_{\mathrm{ion}}) + i_{\mathrm{inj},\,j}, \tag{3.11}$$

and

$$C_{\mathrm{m}}\frac{\partial V}{\partial t} = \frac{a}{2R_{\mathrm{a}}}\frac{\partial^2 V}{\partial x^2} - \sum_{\mathrm{ion}} g_{\mathrm{ion}}(V - E_{\mathrm{ion}}) + i_{\mathrm{inj}}(x,t). \tag{3.12}$$

Equation (3.11) is the fundamental equation of multicompartmental models [53]. The analytical solutions to Equation (3.12) for the passive cable's response to a step current are exponential saturation/relaxation curves [15].

In an action potential, a focal suprathreshold depolarization of $V(x)$ is amplified by active currents—flowing through local Na_V channels that opened in response to the perturbation—and then propagates *passively* to neighbouring as-yet unexcited membrane via the longitudinal (axial) conductivity of the axoplasm. Via the latter *passive propagation of axial current*, the neighbouring membrane then depolarizes beyond *its threshold*, and its voltage $V_{\mathrm{m}}(x+dx)$ is in turn amplified by its own local set of Na_V channels.

$V(x)$ is the membrane potential at x; and V_j is the potential at $x_j = j\Delta x$.

The *local inactivation of Na_V channels that immediately follows* their initial amplifying contribution to the AP keeps the spike travelling forward—rather than two APs travelling in opposite directions—by temporarily preventing membrane that has recently spiked from being re-excited by the passive longitudinal current in the same manner as is described above. This is true at locations distant from the axon initial segment (AIS),

which is where APs are initiated in vertebrate neurons. When the AIS initiates an action potential, the wave *can* travel in both directions, and the depolarization leaving the AIS toward the soma and dendrites is called a *backpropagating* AP (BAP).

Backpropagation is a form of intracellular signalling, putatively involved in synaptic plasticity and learning, that we modelled in [4]. (Also, if an axon is stimulated at some point *between* its AIS and its terminals—as can be done artificially with a microelectrode—one can indeed initiate two APs at a single location, with one AP travelling away from the electrode antidromically toward the soma, and the other AP propagating orthodromically.)

3.1.1 Conduction velocity ϑ

We can estimate the conduction velocity ϑ via dimensional analysis using the membrane's time and length constants (τ_m and λ_m respectively). Because the action potential's *shape and amplitude are conserved as it travels* along the axon, the time (τ_m) taken for the amplitude to decay by $\frac{1}{e}$ as recorded at a given fixed position, and conversely, the distance (λ_m) over which the amplitude decays by $\frac{1}{e}$ along a space plot of the membrane potential at a given fixed time, are directly connected via the propagation speed (conduction velocity) ϑ [43, 15]:

$$\vartheta \sim \frac{\lambda_m}{\tau_m} = \sqrt{\frac{a}{2r_m r_L C_m^2}} = \sqrt{\frac{a\kappa g_{\text{total}}}{2C_m^2}} \leftarrow \begin{cases} \lambda_m = \sqrt{\frac{ar_m}{2r_L}} = \sqrt{\frac{a\kappa}{2g_{\text{total}}}}, \\ \tau_m = r_m C_m = \frac{C_m}{g_{\text{total}}}. \end{cases} \tag{3.13}$$

Dayan and Abbott [11, pp. 210-211] provide a more accurate estimate of the velocity from the passive spread of depolarization following a current pulse: $\vartheta \sim \frac{2\lambda_m}{\tau_m}$. Plugging in the parameters for the squid giant axon (Section 3.3.8) gives:

$$\frac{2\lambda_m}{\tau_m} \approx 12 \frac{\text{m}}{\text{s}}, \tag{3.14}$$

whereas the measured speed is closer to $20\frac{\mathrm{m}}{\mathrm{s}}$ [43].

The velocity is, of course, affected by active membrane properties. More accurate estimates of the conduction velocity can be obtained via numerical methods (e.g. simulating the Hodgkin-Huxley model) and ideally via electrophysiological recordings.

3.1.2 Point-cell models (point neurons)

If we are not interested in modelling the propagation of signals within the neuron, we can instead treat the entire cell as a *single* compartment. This is also appropriate under whole-cell clamp conditions, where the membrane potential is controlled by aspirating a patch of the membrane into a glass-pipette electrode and then applying sufficient suction to open the membrane, thereby removing the barrier between the saline solution in the electrode and the cytosol. The membrane can also be punctured by a sharp electrode.

Point cells—or single-compartment simulations—are efficient for modelling *temporal* patterns of spiking activity in neurons, such as bursting or tonic ectopic action potentials, if the spatiotemporal details of initiation and spread of each spike within the cell are not required.

3.2 Voltage-gated ion channels

Ion channels generate the active currents, first described by Hodgkin and Huxley [21], that give rise to action potentials (Section 3.3). Conceptually, we can think of a voltage-gated ion channel as a valve with filters at each end, inserted perpendicular to the cell membrane. A valve—rather than an open pipe—because the channel actively opens and closes to start and stop the flow of current depending on the membrane potential, and filters because ion channels are selective as to which ion species can pass through them. Filters at each end, because the channel (e.g. K_V) may not have the same affinity for its namesake ions on its intracellular side as on its extracellular end.

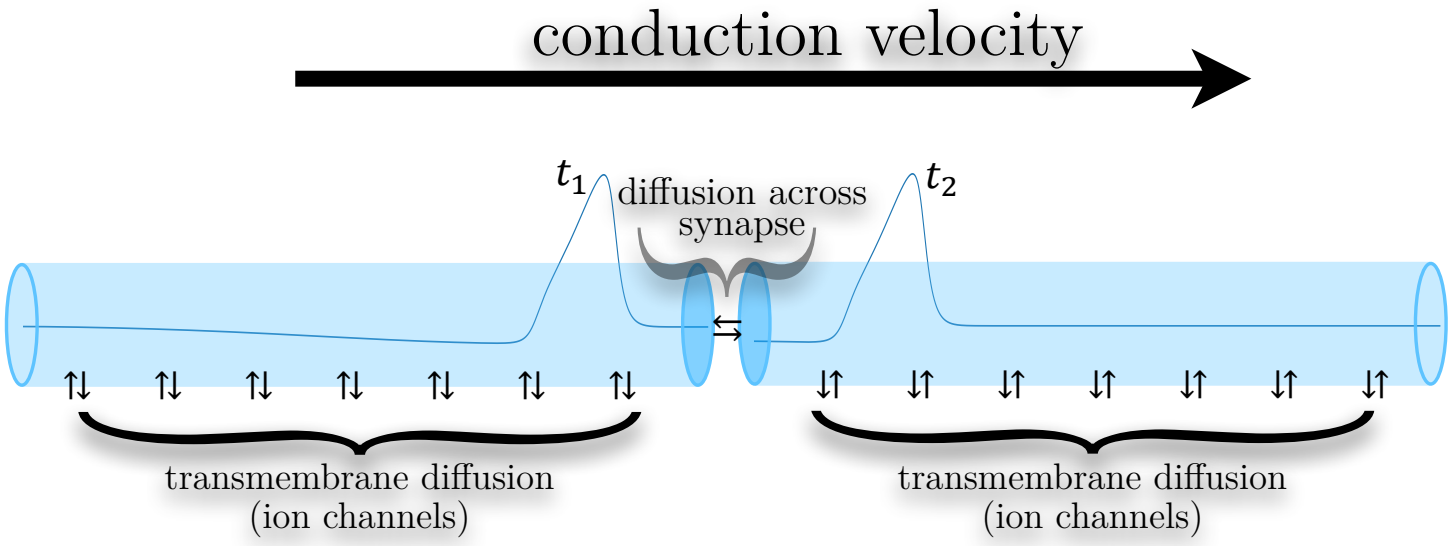

Figure 3.3: **Sketch: Neurons convert short-range transmembrane electrodiffusion into long-range intracellular electrical signals (APs).** A sequence of fast, short-range diffusion events creates the long-range electrical signal called an action potential. The opening and closing of Na_V channels is depicted in Figure 3.11. Neurons don't overcome diffusion; they *use* it at every step. Centre of figure: The action potentials are interspliced with intercellular diffusion of neurotransmitters across $\sim$ 10nm synapses (intercellular signalling).

A single voltage-gated sodium channel has a conductance of roughly 25pS [43] which gives a current of $\sim 3\text{pA}$ per open Na_V channel at $V = V_{\text{rest}}$, assuming $E_{\text{Na}^+} \approx 50\text{mV}$ and $V_{\text{rest}} \approx -70\text{mV}$.

When Hodgkin and Huxley (HH) constructed their equivalent circuit model of the axon ([21], Figure 3.6, Equation (3.31)), voltage-gated ion channels had not yet been discovered. It was clear that the axon was able to control its permeability to different ion species in response to changes in the membrane potential. HH also inferred that the mechanism responsible for these permeability changes—and therefore the excitability of the axon—was contained in the cell membrane (Figure 3.11).

Voltage-gated ion channels were unknown at the time that HH discovered the sodium and potassium permeability changes that produce action potentials.

Because the voltage-gated sodium current of the squid axon generated positive feedback when the membrane was depolarized by more than $\approx 15\text{mV}$ above V_{rest}, HH knew they could not determine the kinetics of the ion currents that give rise to action potentials by adjusting the amplitude of current pulses injected by a standard electrode (see Figures 3.12 and 3.13). Instead, their voltage-clamp apparatus supplied negative feedback via analog electrical circuits to counteract the physiological transmembrane currents and thereby hold V_{m} fixed at a preset voltage.

A voltage-clamp is a device that allows experimenters to control the membrane potential. Space-clamping is the condition where V_m is constant over a given length of the axon. Hodgkin and Huxley's voltage clamp maintained both of these conditions via long electrodes inserted lengthwise inside the axon.

They inserted a long electrode, with two helically wound wires, inside their giant axon specimens. One wire served to inject current, and the other measured the membrane potential. The injected current and membrane potential were both recorded for later analysis, and were also used for live feedback to control V_{m} during the voltage-clamp experiments. Their electrode also flattened the membrane potential along the axon by shorting the intracellular resistance of the cytosol, which is orders of magnitude less conductive than metallic conductors. That way, axial current was eliminated in the portion of axon under study, and its membrane current was identical to the electrode current [53].

By stepping the membrane potential, they could measure the *membrane current* I_{m} as a function of V_{m} across the full range of voltages traversed during action potentials (and beyond) since that current is matched by (cancelled out) the known current supplied by the voltage-clamp electrode which was placed inside the axon. Under voltage-clamp conditions, the capacitive current—which varies as $\frac{\partial V}{\partial t}$ (Equations 3.12, 3.28)—disappears, leaving only the ionic currents to be cancelled by the feedback current at steady state. By voltage-clamping the squid giant axon, HH were able to directly measure the ionic currents for the first time [20].

Using a tool that resembled a miniature rolling pin, which they rolled along open sections of axons that they had removed from squid, HH extruded the contents of the axon, creating a hollow tubular membrane. Maintaining the proper inner and outer ion concentrations in solution, HH confirmed experimentally that the bedraggled, hollowed-out axons generated action potentials all the same. From that observation, they concluded that action potentials must be generated by some mechanism in the membrane, which we now know to be the families of voltage-gated sodium and potassium channels denoted Na_V and K_V.

The "action" happens in the membrane. The lumen maintains homeostasis over longer time scales.

[3] https://en.wikipedia.org/wiki/Voltage-gated_sodium_channel

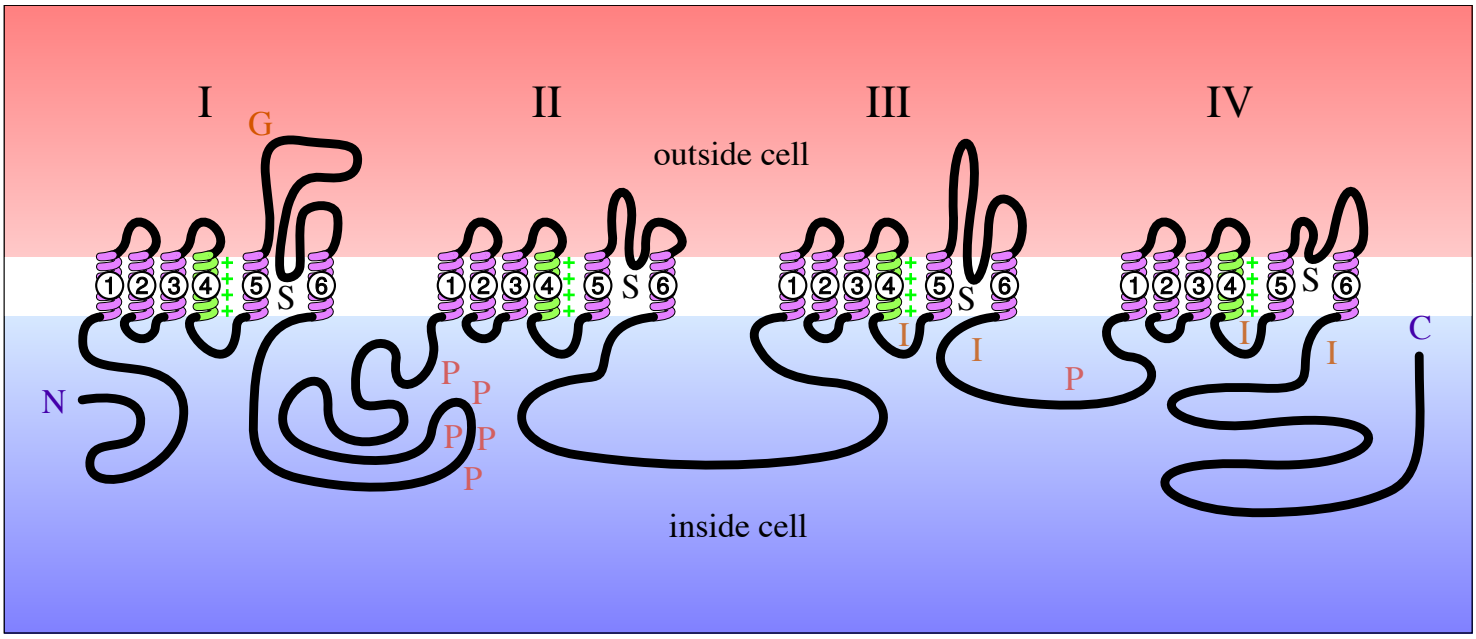

Figure 3.4: **Exploded-view: α-subunit of a voltage-gated sodium ion channel.** This protein is knitted into the membrane and forms the pore of the Na_V channel. Charged regions (indicated with green "+" signs) are pushed and pulled by the local electric field, driving conformational changes that open and close the channel. (Source: Wikipedia[3])

3.2.1 Gating charges and their Boltzmann statistics

Voltage-gated ion channels contain positive charges (gating charges) in the regions of the protein called the "voltage-sensor" [20] (see Figure 3.4). Depolarization—positive deviations of the membrane potential above V_{rest}—forces the gating charges outward, which induces conformational changes in the channel protein that *open* it.

The gating particles *also* obey the Boltzmann equation, and so our friend "$e^{-(\text{potential energy})/k_B T}$" returns yet again, to give the ratio of the open and closed states' probabilities at equilibrium

$$\boxed{\frac{P(\text{open})}{P(\text{closed})} = e^{-\left(\frac{w - z_g \mathrm{e} V_{\mathrm{m}}}{k_B T}\right)}}, \tag{3.15}$$

wherein each *ion channel* is being treated as a two-state system. (The effective valence of the ion channel due to its gating charge is denoted by z_g, e is the fundamental

electric charge, as always, and $\mathbb{E} = -V_{\mathrm{m}} / l$ is the electric field strength with l being the effective thickness of the plasma membrane.)

The electric field in the membrane is quite strong since the bilayer is so thin:

$$\frac{\text{milliVolts}}{\text{nanometres}} = \text{MegaVolts-per-metre.} \tag{3.16}$$

As explained in [20, Chapter 2], there are two terms in the channel protein's energy change ΔU that are associated with moving the protein's voltage sensor from its "closed" position—on the inner leaflet of the membrane—to its "open" position on the outer leaflet:

1. When the gating charges—that form the voltage sensor—move, they necessarily distort the (membrane-bound) channel protein to which they belong. As the channel opens, there is an energy cost, denoted w, associated with said conformational change, which is independent of the membrane potential:

$$\underbrace{w = \left(\begin{array}{l}\text{Required energy to change the}\\ \text{conformation of the channel pro-}\\ \text{tein, from its closed to open state}\\ \text{when } V_{\mathrm{m}} = 0 \text{ (i.e. no } \mathbb{E}\text{-field).}\end{array}\right)}_{\text{“}w\text{arping energy”}} \tag{3.17}$$

   As a mnemonic, one might call w the channel protein's "*warping* energy".

2. The second term is the change to the gating charges' electrical potential energy when they traverse the electric field in the membrane during the channel's transition from "closed" to "open":

$$-z_g \mathrm{e} V. \tag{3.18}$$

Since probabilities sum to unity, we write

$$\frac{P(\text{closed})}{P(\text{open})} + 1 = \frac{P(\text{closed}) + P(\text{open})}{P(\text{open})} = \frac{1}{P(\text{open})}, \tag{3.19}$$

and from Equation (3.15), the ratio of open channels as a portion of all channels in the membrane is

$$P(\text{open}) = \left(1 + \frac{P(\text{closed})}{P(\text{open})}\right)^{-1} \Longrightarrow \boxed{P(\text{open}) = \frac{1}{1 + e^{\left(\frac{w - z_g eV}{k_B T}\right)}}}, \tag{3.20}$$

also known as the *open probability* or steady-state *activation* for that channel type at $V(x,t) = V_{\text{m}}$.

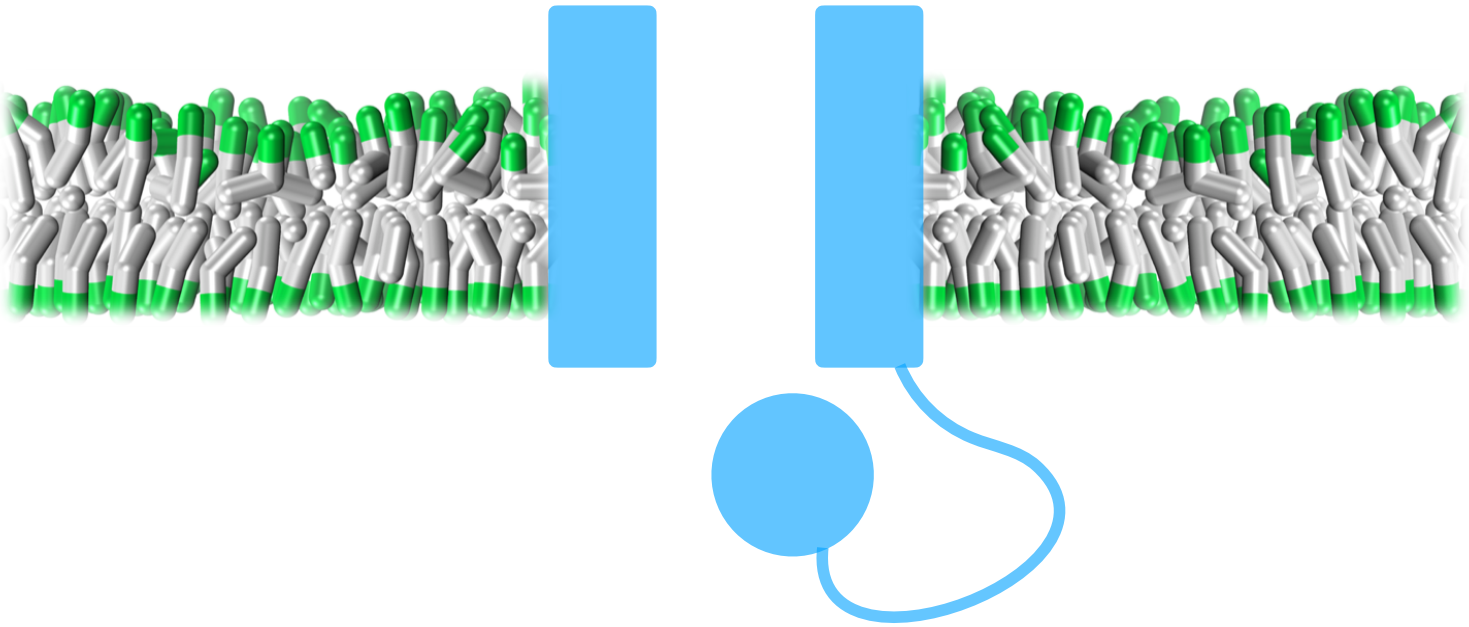

Figure 3.5: **Conceptual sketch of an open ion channel with a single inactivation gate, akin to the Na_V channels from the Hodgkin-Huxley model [21].** (The bilayer on either side is a snapshot from coarse-grained molecular dynamics simulations of a liposome[3].)

3.3 The Hodgkin-Huxley equations

Neurons (and all eukaryotic cells) have a resting potential, a target transmembrane voltage that they will naturally relax toward in the exponential saturation that is modelled by RC circuits. The resting potential results from the separation of charges at the inner and outer membrane surfaces (the membrane acts as a capacitor).

The thin inner and outer sheets of charge separated across the membrane (capacitor) are themselves a result of the selective permeability of the cell membrane combined with transmembrane concentration gradients of various permeant ions (intracellular concentration $\neq$ extracellular concentration) interacting with large, negatively charged macromolecules (impermeant anions) trapped inside the cell.

Various ion currents—involving the movement of permeant ions through openings in the cell membrane—determine the resting potential. These currents, which are perpetually leaking in the direction that reduces their Nernst potentials (Equation (2.61)), like a battery passively draining its charge, are balanced by active transport via ion pumps that maintain the concentrations gradients[4] (see Section 3.4).

Neurons exhibit passive and active responses to perturbations away from the resting potential. In the former, when stimulation is below a certain threshold, the cell will relax back to the resting potential as mentioned above (see Figure 3.12). In the latter case, when stimulation is sufficiently strong, positive feedback ensues (Figure 3.13).

If we ignore ion pumping for the moment, the resting potential can be calculated from permeant ions' Nernst potentials and their conductances, akin to a centre-of-mass equation:

$$V_{\text{rest}} \cong \frac{\sum g_{\text{ion}} E_{\text{ion}}}{\sum g_{\text{ion}}}. \tag{3.21}$$

[4] Na^+/K^+ pumps "trickle charge" the neuron[43].

Sodium channels trigger APs, but there is more to the story. The sequence of events that produces action potentials was discovered and described by Hodgkin and Huxley[21] in a series of experiments, biophysical modelling, and hand-cranked differential equation solving that earned them the Nobel Prize.

3.3.1 Brief outline

The HH model began from the theoretical assumption (paraphrasing [21]) that:

$$\text{(membrane current)} = \underbrace{\text{(capacity current)}}_{C_\text{m}\frac{\partial V}{\partial t}} + \text{(ionic current)} \tag{3.22}$$

- Capacity current involves a change in the density of ions at the inner and outer surfaces of the cell membrane (Debye length: $\lambda_D \sim \mathtt{nm}$, see Equation (2.56)).
- Ionic current I_ion involves the movement of charged particles through the membrane.

The HH sign convention for the membrane current I_m is:

$$I_\text{m} = C_\text{m}\frac{\partial V}{\partial t} + I_\text{ion}. \tag{3.23}$$

Hodgkin and Huxley used voltage-clamp experiments to measure the transmembrane ionic current. In their setup, V_m was held constant by a feedback circuit that continuously monitored the membrane potential and injected a current I_inj into the axon via an intracellular electrode. I_inj was automatically adjusted to keep V_m at the preset value, and since

$$\frac{\partial V}{\partial t} = 0, \tag{3.24}$$

it follows from Equation (3.23) that $I_{\text{inj}} = I_{\text{m}} = I_{\text{ion}}$. That is, by clamping the membrane potential at a fixed voltage along the length of a section of axon (space clamp), the ionic current can be measured directly.

3.3.2 Prelude: gating variables

The Hodgkin-Huxley model is defined, fundamentally, by ***gating variables*** which we can denote

$$u(V,t). \tag{3.25}$$

A gating variable u is a **probability** that evolves with time in response to the conditions of the membrane (e.g. $V = V_{\text{m}}$). It represents a component, or a step, in the opening or closing of an ion channel.

Through their experiments on squid axons, Hodgkin and Huxley found that in order to fit their data, the elements embedded in the cell membrane that were responsible for ion-selective permeability changes (known today as voltage-gated channels) had to be modelled as exponential saturations raised to the power of the number of "gates" involved. Hence, *each channel is modelled as the combined state of independent gates*, all of which need to be in their own "open" state for the ion channel to be open.

The probability of a channel—chosen at random from a thermodynamic ensemble of many channels like it—to be in its open state is, therefore, the compound probability of all the independent gates belonging to said channel being in their open states simultaneously. If a potassium channel has four activation gates, its open probability is $u^4(V,t)$, with $u \in [0,1]$. (The variable name "n" is used for potassium channels' gates.)

*Let $u_j = u_j(V,t)$ be our **shorthand** way of referring to a member of the set of gating variables featured in the HH model: $u_j \in \{m,h,n\}$ or, for that matter, $\{\text{gating variables}\}$ belonging to any other Hodgkin-Huxley-style model.*

The equations describing the membrane current depend on the experimental setup. Voltage-and-Space-Clamp produces a counterintuitive expression.

The HH model is a nonlinear system, and its gating variables evolve according to their steady-states and "time constants"—denoted $(\text{gating variable})_\infty(V)$ and $\tau_{\text{gating variable}}(V)$ respectively—that are *functions* of the membrane potential.[5]

In their notation, the voltage-gated-conductance density $g(V,t)$ in the membrane to ion S, due to channels having k-activation gates $u(V,t)$ and ℓ-inactivation gates $h(V,t)$ is

$$g(V,t) = \bar{g}u^k h^\ell, \tag{3.26}$$

where $\bar{g}$ is the maximal conductance density, which corresponds to the area-density of channels embedded in the membrane. It is assumed that the voltage-gated channels are only permeable to one type of ion, denoted "S". The current-per-unit-membrane-area due to said channels is

$$I_S(V,t) = g_S(V,t)\Big(V - E_S\Big). \tag{3.27}$$

The details of voltage-gated channels in the HH model are discussed in Section 3.3.5.

3.3.3 HH model for propagating action potentials

Hodgkin and Huxley [21] provided a cable equation with active currents describing the electrical excitability of the axon (Equation (3.28)) including propagating action potentials. In absence of an externally applied (injected) electrode current, there are

[5] Your potential objection to the notion of a variable "time constant" is noted. We could strain the language further by distinguishing a so-called "constant time constant" from a time constant that is a function, but we will not. Instead, for expediency, we agree to call $\tau_u(V)$ the voltage-sensitive time constant of the gating variable $u(V,t)$.

four terms, two active and two passive:

$$\overbrace{\frac{a}{2R_\mathrm{i}}\frac{\partial^2 V}{\partial x^2}}^{\text{axial current}} = \underbrace{C_\mathrm{m}\frac{\partial V}{\partial t} + g_\mathrm{leak}\left(V - E_\mathrm{leak}\right)}_{\text{passive}} + \underbrace{\overbrace{g_{K_V}(V,t)\left(V - E_{\mathrm{Na}^+}\right)}^{\text{negative feedback}} + \overbrace{g_{Na_V}(V,t)\left(V - E_{\mathrm{K}^+}\right)}^{\text{positive feedback}}}_{\text{active (voltage-gated)}}. \tag{3.28}$$

The passive currents in Equation (3.28) are due to the intrinsic capacitance C_m of the phospholipid bilayer, the axon's intracellular conductivity $\kappa_\mathrm{i} = \frac{1}{R_\mathrm{i}}$, and the component of the membrane conductance—or permeability to ions—that is *independent* of the membrane potential (g_leak).

The active currents—the last two terms on the right in Equation (3.28)—are where the *gating variables* reside. They model the variable conductance of the membrane to potassium and sodium ions ($g_{K_V}(V,t)$, $g_{Na_V}(V,t)$) due to voltage-gated ion channels embedded in the bilayer that are responsible for the positive and negative feedback cycle that produces action potentials.

The voltage-gated channels (denoted K_V and Na_V, respectively) combined with the free energy stored in the imbalance of inner and outer concentrations of Na^+ and K^+ ions render the axon an excitable medium: The membrane will amplify perturbations of its voltage above a certain threshold[6] (see Figures 3.12 and 3.13).

Noting that—when recording a propagating action potential—the time-series of $V(t)$ at some fixed position x resembles the space-plot of $V(x)$ in a snapshot at time t, Hodgkin and Huxley introduced a wave equation [21] to define a conduction velocity ϑ (or speed of action potential propagation):

$$\frac{\partial^2 V}{\partial x^2} = \frac{1}{\vartheta^2}\frac{\partial^2 V}{\partial t^2}. \tag{3.29}$$

[6] The threshold may vary with experimental conditions, and a variety of other factors including the recent history of the membrane potential (refractory period) can also affect the threshold [43].

There is some handwaving to ignore here, because space plots are notoriously challenging to observe—every point on the curve at a given time must be simultaneously recorded by a dedicated electrode. HH may have relied on their physical intuition for this observation. The conduction velocity (Equation (3.29)) allowed them to rewrite Equation (3.28) as

$$\frac{1}{\vartheta^2}\left(\frac{a}{2R_\mathrm{i}}\right)\frac{d^2V}{dt^2} = C_\mathrm{m}\frac{dV}{dt} + g_\mathrm{leak}\Big(V - E_\mathrm{leak}\Big) + g_{K_V}(V,t)\Big(V - E_{\mathrm{Na}^+}\Big) + g_{Na_V}(V,t)\Big(V - E_{\mathrm{K}^+}\Big), \tag{3.30}$$

which they were able to integrate numerically, searching for stable solutions in order to simulate action potentials, in a procedure that resembles a bracketing method to find the conduction velocity.

3.3.4 HH model for an isopotential section of membrane

It is essential to distinguish the cable equation (Equation (3.28)), that approximates the intrinsic biophysics of the axonal membrane, from Equation (3.31). The latter expression is the HH equivalent circuit model (Figure 3.6), which arises from unphysiological (space-clamp) conditions imposed by the voltage-clamp apparatus.

Following a brief supra-threshold current pulse, the space-clamped axon spiked simultaneously at every point along its length—rather than in a travelling wave as is seen during a natural action potential. Hodgkin and Huxley called these space-clamped spikes "membrane action potentials" [21] to distinguish them from physiological APs. In that case there is no axial current, as there is *no longitudinal variability in the membrane potential* that could drive axial currents along the clamped segment of axon (the term on the left-hand-side of Equation (3.28) vanishes).

In the equivalent circuit, the total measured membrane current I_{m} crossing a section of axon that is space-clamped—so that its membrane potential V can be approximated as longitudinally uniform at all times—consists of passive and active components as before:

$$\underbrace{I_{\mathrm{m}}}_{\textbf{electrode}} = \underbrace{C_{\mathrm{m}}\frac{dV}{dt} + \overbrace{g_{\mathrm{leak}}\left(V - E_{\mathrm{leak}}\right) + g_{K_V}(V,t)\left(V - E_{\mathrm{Na}^+}\right) + g_{Na_V}(V,t)\left(V - E_{\mathrm{K}^+}\right)}^{I_{\mathrm{ion}}}}_{\textbf{space-clamped squid axon}}. \tag{3.31}$$

Under the HH voltage-clamp conditions, the ionic current I_{ion} is measured directly because the capacitive term vanishes with $\frac{\partial V}{\partial t} = 0$. With no axial current, the local circuit current can only be what is provided by the command electrode, $I_{\mathrm{m}} = I_{\mathrm{inj}}$, and conservation of charge (current in = current out) requires that I_{ion} must be equal to I_{inj}—the latter of which is known since the voltage-clamp device records it.

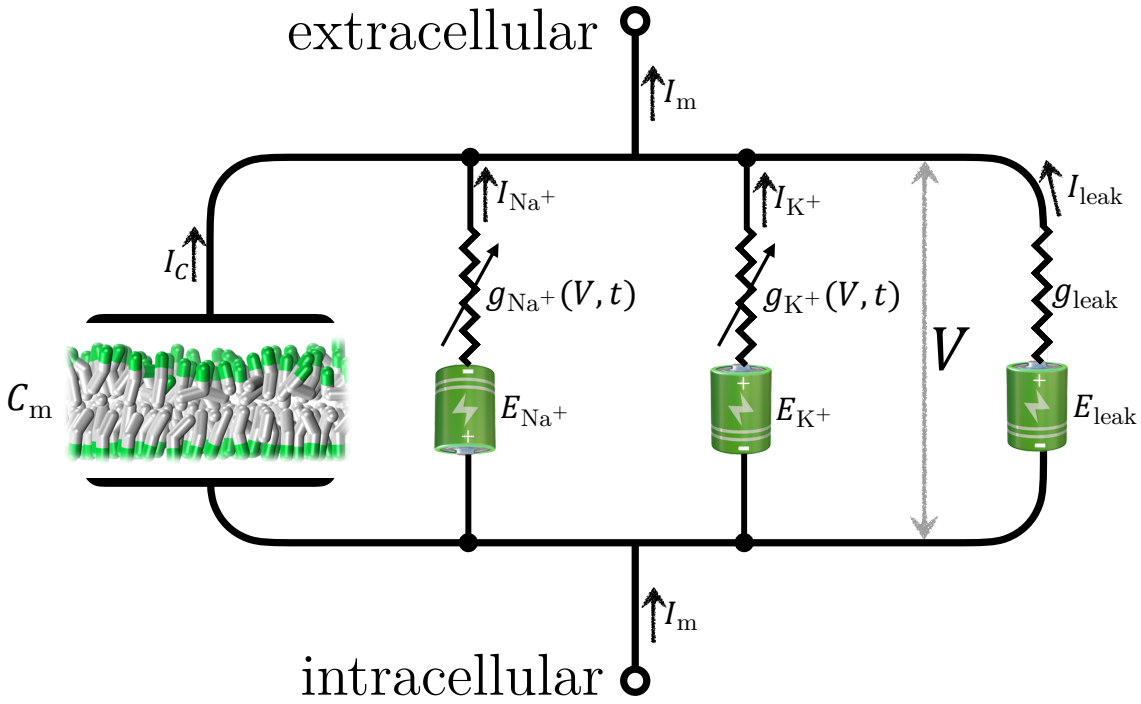

Figure 3.6: **Adaptation of the Hodgkin-Huxley equivalent-circuit model describing the membrane currents in a space-clamped segment of *Loligo* giant axon.** Currents in this diagram correspond to Equation (3.31). The batteries have been drawn explicitly here to highlight a possible sticking point in the mental map from equivalent circuit to anatomy: In a neuron, the electrolytes are on either side of the membrane, which would make for awkward battery casings in this graphic. With the capacitive current, the metamorphosis between equivalent circuit and biological is straightforward: The bilayer is an atoms-thin insulator and, therefore, a self-assembled capacitor (condenser).

The visual analogy in Figure 3.6 between the capacitor symbol and the cell membrane works fairly well; however, *where* is the battery, relative to the membrane? In the latter case, the is inside out, and drawing a battery in the membrane atop a channel does not work even conceptually. For example, where are the positive and negative terminals of the battery? In fact, the positive and negative terminals would be staring at one another from opposite sides of the membrane, and opening an ion channel connects the terminals of the battery representing that specific channel's E_{Nernst}. Where in this picture shall we put the battery casing that contains the electrolyte, which extends to the horizon moving left or right along the axon in this model?

3.3.5 Back to gating

The gating variables $\underbrace{n(V,t)}_{\text{potassium}}$, $\overbrace{h(V,t), m(V,t)}^{\text{sodium}}$ are what make the active conductances in Equations 3.31–3.28 *active*. They model conformational changes in the voltage-sensing ion channel proteins that correspond to the open and closed states of the channels (see Figure 3.4). The active potassium and sodium conductances are then defined in terms of their channels' gating variables:

$$g_{K_V}(V,t) = \bar{g}_{K_V} n^4(V,t), \tag{3.32}$$

$$g_{Na_V}(V,t) = \bar{g}_{Na_V} m^3(V,t) h(V,t), \tag{3.33}$$

see Figure 3.7. The *maximal conductances* are constants denoted $\bar{g}_{K_V}$ and $\bar{g}_{Na_V}$.

To keep our dimensions straight, we remark that **although $\bar{g}_{K_V}$ and $\bar{g}_{Na_V}$ are typically referred to as conductances, they are defined as conductance *densities***—the conductance per unit of membrane area when all ion channels of the

respective type are open and available. In conductance-based models, $\bar{g}_{K_V}$ and $\bar{g}_{Na_V}$ are interpreted as the area densities of Na_V and K_V channels in the membrane.[7] With a single-Na_V conductance of $\approx 25\text{pS}$ [53], the Hodgkin-Huxley model's voltage-gated sodium conductance density $\bar{g}_{Na_V} = 120\frac{\text{mS}}{\text{cm}^2}$ corresponds to roughly 48 Na_V channels per square micrometer.

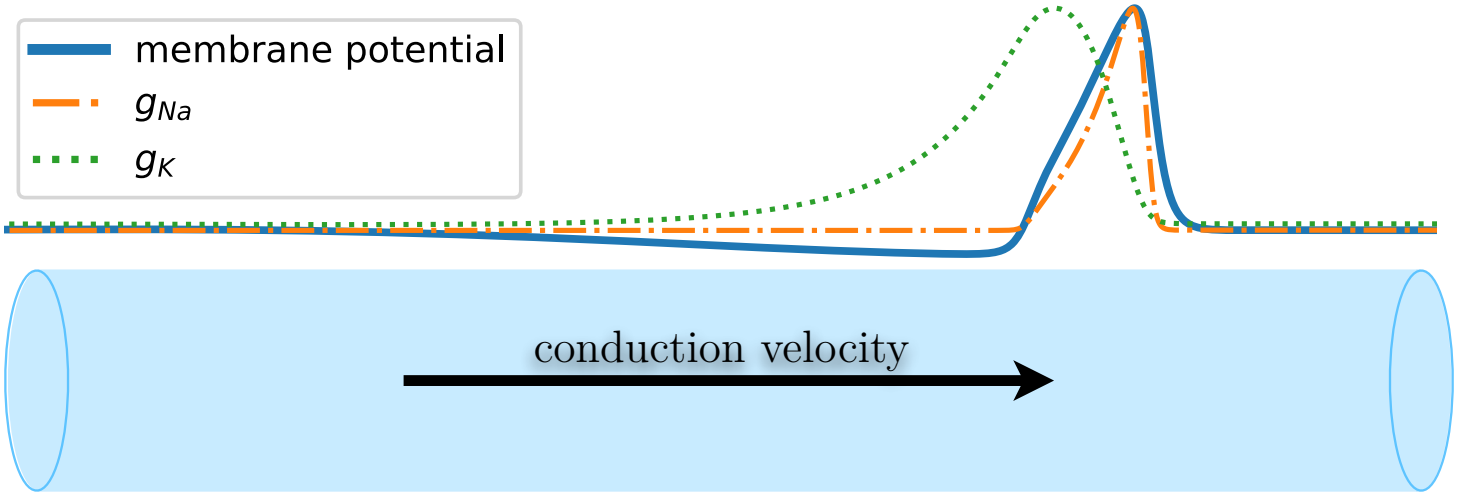

Figure 3.7: **Action potential with accompanying conductance waves.** The membrane potential (solid blue line), sodium conductance (dash-dotted orange line), and potassium conductance (dotted green line) are normalized by their respective peak amplitudes for visual clarity. • At the leading edge of the AP, note that the increase in V_m *precedes* the sharp increase in sodium conductance: *The action potential propagates via electrical self-stimulation*, as the depolarization of the preceding patch of membrane stimulates the opening of Na_V channels ahead of it [20]. See Figure 3.11.

The time-evolution of $n(V,t)$, $m(V,t)$, and $h(V,t)$ is given by the linear differential equations below:

$$\frac{dn}{dt} = \alpha_n(V)\cdot\Big(1-n\Big) - \beta_n(V)\cdot n = \frac{n_\infty(V)-n}{\tau_n(V)}, \tag{3.34}$$

$$\frac{dm}{dt} = \alpha_m(V)\cdot\Big(1-m\Big) - \beta_m(V)\cdot m = \frac{m_\infty(V)-m}{\tau_m(V)}, \tag{3.35}$$

[7] In multicompartmental models, which will be introduced later, these parameters are a function of position—e.g. $\bar{g}_{Na_V} = \bar{g}_{Na_V}(s)$, with s denoting the position in the model neuron.

$$\frac{dh}{dt} = \alpha_h(V) \cdot \Big(1 - h\Big) - \beta_h(V) \cdot h = \frac{h_\infty(V) - h}{\tau_h(V)}, \tag{3.36}$$

where $\alpha_{(\text{gating variable})}(V)$ and $\beta_{(\text{gating variable})}(V)$ are (respectively) the forward and backward rate constants. The voltage-dependent rate constants are instantaneous functions of the membrane potential and have units of probability per unit time

$$\overbrace{\Big(1-u\Big)}^{P(\text{closed})} \underset{\beta_u(V)}{\overset{\alpha_u(V)}{\rightleftharpoons}} \overbrace{u}^{P(\text{open})}. \tag{3.37}$$

Equation (3.37) applies readily to the potassium and sodium *activation* variables ($u = n$ and m, respectively). The sodium *availability* gating variable ($u = h$), which models inactivation, is more subtle and is discussed further in Section 3.3.6. Hodgkin and Huxley fitted the rate constants for each gating variable to action potentials of the squid giant axon (Equations 3.40–3.42 below).

In the rightmost term of Equations 3.34–3.36 (above), the steady state $u_\infty(V)$ and time constant $\tau_u(V)$ of a gating variable $u(V,t)$ are defined as

$$u_\infty(V) = \frac{\alpha_u(V)}{\alpha_u(V) + \beta_u(V)} \quad \Big| \quad \tau_u(V) = \frac{1}{\alpha_u(V) + \beta_u(V)}. \tag{3.38}$$

Under a voltage-step from the initial value $V_\text{m}(t_0) = V_0$ to the new value $V_\text{m}(t_1) = V$, Equations 3.34–3.36 have solutions of the form

$$\boxed{u(V,t) = u_\infty(V) - \Big[u_\infty(V) - u_0\Big]e^{-t/\tau_u(V)}}, \tag{3.39}$$

with $u_0 = u(t = 0)$ being the value of the gating variable just before the voltage step. Hodgkin and Huxley inferred the number of gates involved in the opening and closing of a given channel type from the fitting procedure. For example, when fitting

the potassium current *activation*, they found it was necessary to use $\big(n(V,t)\big)^4$ as their fitting function—with $n(V,t)$ as given in Equation (3.39)—implying *four* gates without ever directly observing channels in the membrane.

Hodgkin and Huxley [21] shifted their equations such that $V_{\text{rest}} = 0\text{mV}$ whereas the HH model in common usage is setup with $V_{\text{rest}} = -65\text{mV}$, approximately the V_{rest} one measures in a squid axon. A disadvantage of notation that sets V_{rest} to 0mV is that it distorts the true value of the Nernst potentials, which are real transmembrane voltages physically determined by the inner and outer ion concentrations and the temperature (Section 2.4.1). The original parameters are seldom used today—it is often preferable that simulators should output realistic voltages—and the following updated rates are much more common (see [14]):

Hodgkin and Huxley [21] shifted their parameters to give an unphysical resting potential of 0mV. Now the convention is to model the unshifted measurements. For the squid axon, V_{rest} was roughly -65mV in the HH experiments.

$$\alpha_n(V) = \frac{1}{100}\frac{V + 55\text{mV}}{1 - e^{-(V+55\text{mV})/10\text{mV}}} \quad \Big| \quad \beta_n(V) = \frac{1}{8}e^{-(V+65\text{mV})/80\text{mV}}, \tag{3.40}$$

$$\alpha_m(V) = \frac{1}{10}\frac{V + 40\text{mV}}{1 - e^{-(V+40\text{mV})/10\text{mV}}} \quad \Big| \quad \beta_m(V) = 4e^{-(V+65\text{mV})/18\text{mV}}, \tag{3.41}$$

$$\alpha_h(V) = \frac{7}{100}e^{-(V+65\text{mV})/20\text{mV}} \quad \Big| \quad \beta_h(V) = \frac{1}{1 + e^{-(V+35\text{mV})/10\text{mV}}}. \tag{3.42}$$

These parameter values give the kinetic curves in Figure 3.8.

3.3.6 Na_V inactivation h, a.k.a. *availability*

In the literature, the gating variable h is frequently called the inactivation. For conceptual clarity, we instead refer to $h(V,t)$, which models the sodium channel inactivation process in HH-style kinetics, as the "*availability*": h actually measures the probability that a channel is *not* inactivated.

That is, h is the **conditional probability** that a given channel in the ensemble will conduct current, provided its *activation* gates are all in the open state. The probability that the channel is inactivated is $(1-h)$, which does not appear in the Hodgkin-Huxley voltage-gated ion currents—see Equations (3.31) and (3.33). We speak of *availability* because that is how the inactivation process shows up in the HH model, e.g. for $Na_V1.2$ channels the time and voltage-dependent sodium conductance is [4]

$$g_{Na_V1.2}(V,t) = \bar{g}_{Na_V1.2} * (m^{Na_V1.2})^3 h^{Na_V1.2}, \tag{3.43}$$

where $\bar{g}_{Na_V1.2}$ is the maximal conductance, $m^{Na_V1.2}$ is the *activation*, and $h^{Na_V1.2}$ is the *availability* of the $Na_V1.2$ channels.

Calling h the inactivation could easily give the false impression that Na^+ conductance *increases* with inactivation, because the conductance *does* increase with h. That is, *none* of the Na_V channels in the HH model are inactivated at the maximal value of $h = 1$. (See Equation (3.43) directly above.) The *availability* nomenclature is designed to make the equations as readily understandable as possible: All Na_V channels are available at $h = 1$ (i.e. *availability* $= 1$), and none are available at $h = 0$ (*availability* $= 0$), regardless of the state of their *activation* gates.

3.3.7 Plotting the HH gating variables

The Hodgkin-Huxley gating variables are plotted in Figure 3.8. The parameters used to generate the curves are those in Equations 3.40, 3.41, and 3.42. Note that sodium

channel *activation* $m(V,t)$ responds much more quickly to changes in the membrane potential than the decrease in sodium channel *availability* $h(V,t)$ or potassium *activation* $n(V,t)$; as reflected in the sodium *activation* time constant—$\tau_m(V)$ in the lower plot—which is much smaller than the other two τ's at all voltages.

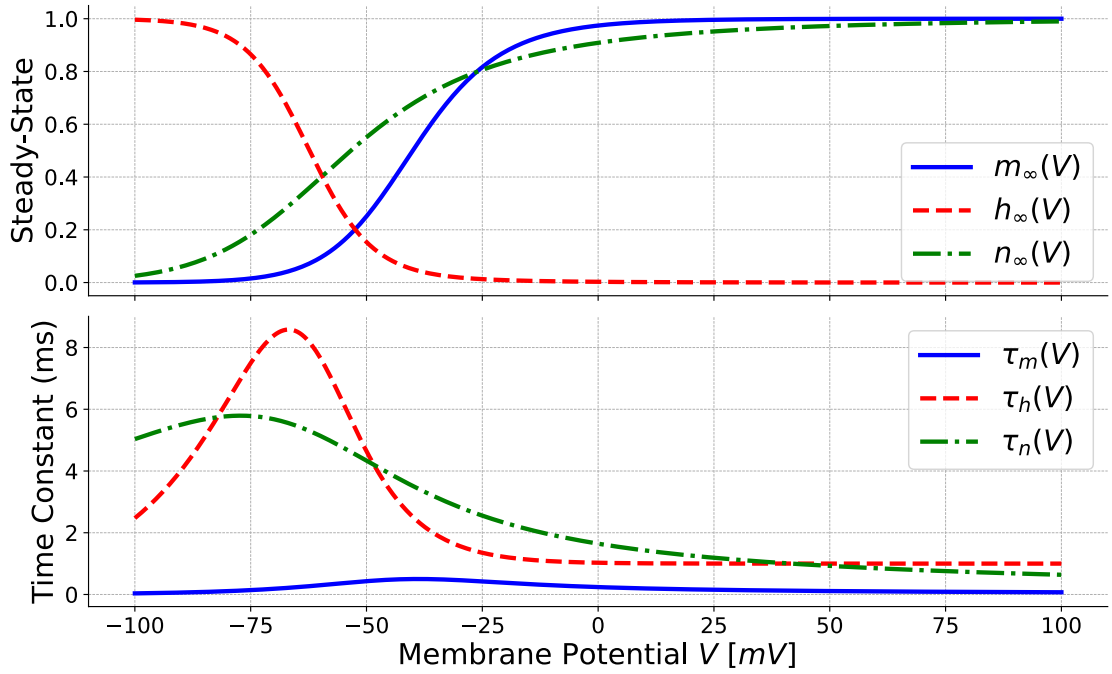

Figure 3.8: **Steady-states and voltage-sensitive time constants of all gating variables in the Hodgkin-Huxley model.** The correspondence between gating variables and ion currents is as follows: m and h describe the *activation* and *availability*[8] gating particles of sodium channels, and n describes the potassium channels' *activation* gating particles.

The fitting of the $\alpha(V)$'s and $\beta(V)$'s depends on the system under consideration (e.g. primate, rodent, or squid axon), the experimental conditions, and the notation used—hence the term Hodgkin-Huxley-*style* kinetics. Their gating variable approach has been adapted to model a large and ever-growing number and variety of neurons in various species [41].

[8](which models the inactivation—or self-blocking—of sodium channels)

3.3.8 Loligo in the lab

With the HH model now written out (above), we ought to visit the physical world. Here, we will put those equations into context by describing their origin in the squid called *Loligo*.

A moment is well-spent to reunite the equations of the Hodgkin-Huxley model with the interesting creature whose axons they describe.

Figure 3.9: **Loligo have giant axons (Figure 3.10) that enable rapid uniform contraction of the muscles of the mantle which forces a propulsive jet of water through the syphon.** Because cephalopods lack myelin, increasing the axon diameter is their evolved way of sending action potentials at higher velocities. When startled, the squid rockets away and ejects ink. In the next figure is the axon of a squid that did not escape... Credit: Wikipedia, © Hans Hillewaert / CC BY-SA 4.0.

The **squid giant axon** from *Loligo*—not to be confused with axons of the giant squid[9] which likely are huge as well albeit impractical to the electrophysiologist tasked with obtaining and dissecting the live creatures—is one of the largest single-cell structures observed in any animal (Figure 3.10). Here, **"largest" refers to the ratio of the**

[9] (Architeuthis dux)

giant axon's volume to the surface area of its plasma membrane—its length is unremarkable compared to other peripheral axons.

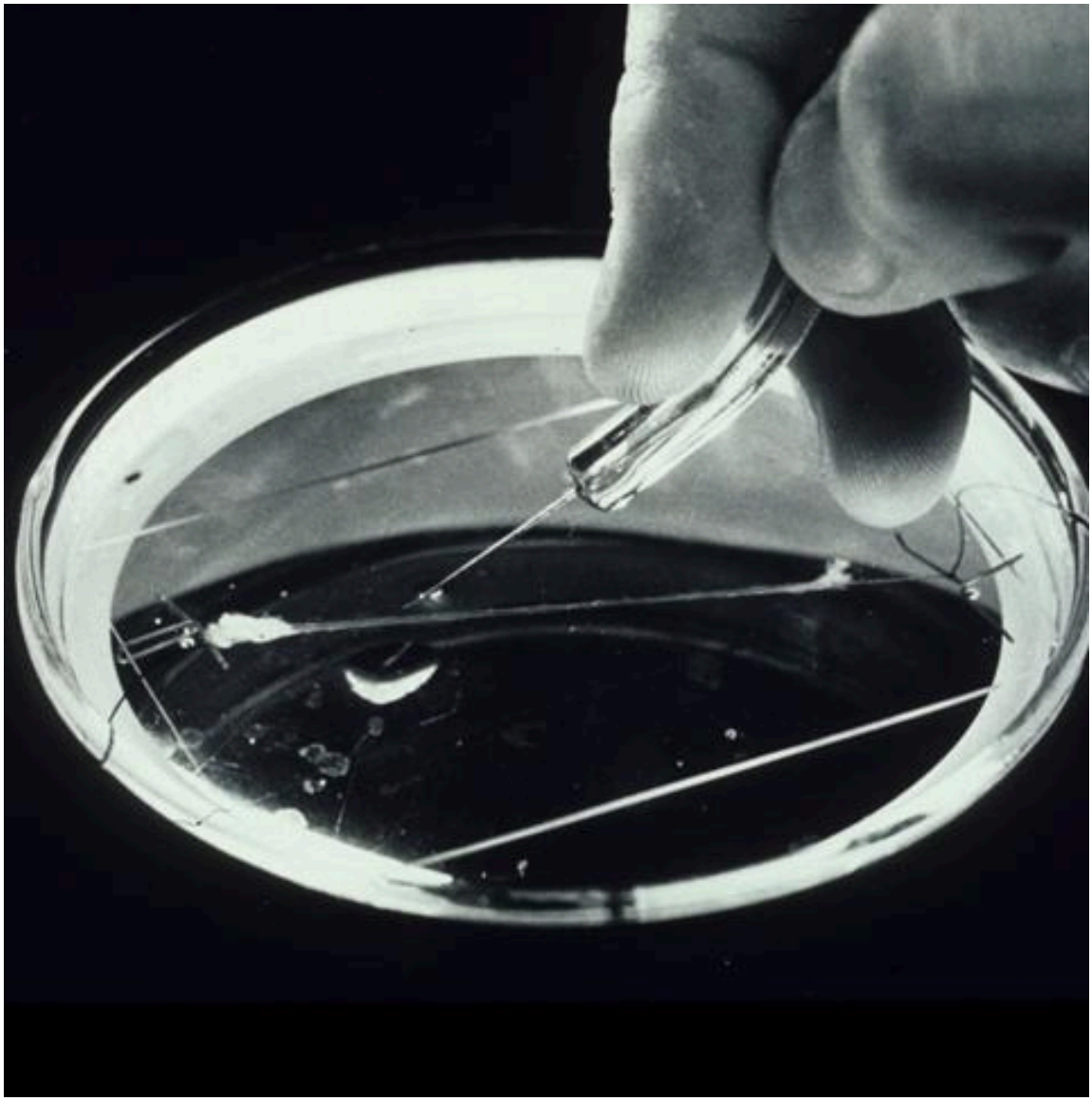

Figure 3.10: **A squid giant axon, isolated in the lab.** Its large diameter $\sim 1.0\text{mm}$ makes this axon visible to the unaided human eye. [Public domain image from the N.I.H. History office on Wikipedia[10].]

With a diameter $\sim 1\text{mm}$, the *width* of this axon is comparable to the *height* of the entire dendritic tree of a mammalian cortical neuron. (For comparison, the axon of a pyramidal neuron is $\sim 1\mu\text{m}$ in diameter—one-thousandth that size.)

[10] https://commons.wikimedia.org/wiki/File:Giant_Axon_of_Squid_(14356033761).jpg

The squid's giant axons allow it to rapidly contract all of the muscles in its mantle Figure 3.9. The contraction forces a jet of water aft, propelling *Loligo* to safety when threatened.[11] This jet propulsion works similarly to a submerged water balloon: Tension in the rubber skin increases the internal pressure, forcing the water out of the balloon, whereas the muscles in the mantle squeeze water out of the squid.

To do this, the mantle needs to contract its muscles in unison, which requires action potentials to arrive synchronously at varying distances from the squid's central nervous system—where the decision to flee presumably originates. The speed of the squid's reaction is, therefore, limited by the slowest parts of the mantle, i.e. where signals must travel the farthest, and the giant axon is an anatomical bottleneck that limits the swiftness of the escape response.

Action potentials travel faster down wider axons—conduction velocity increases as the root of the diameter (Equation (3.13))—and the extraordinary dimensions of the squid giant axon evolved to open that bottleneck.

[11] It is said that the jet is useful for hunting as well. For leisurely swimming, the squid propels itself with its rhomboidal fins, also called "wings".

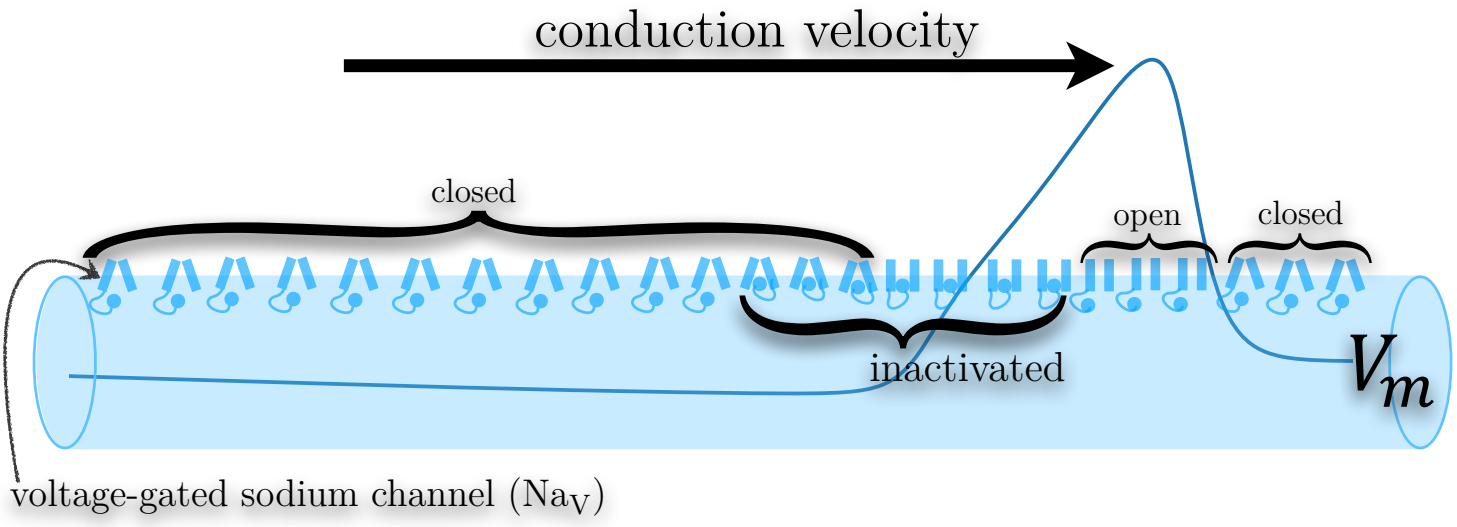

Figure 3.11: **Depiction of Na_V channel states propagating the action potential along an unmyelinated axon (K_V channels not shown).** Action potentials are the amplification and regenerative propagation of a focal depolarization via the tipping of voltage-sensing ion channels in neighbouring patches of membrane into their open state. As one Na^+ channel opens, the resulting transmembrane current depolarizes the membrane neighbouring it, causing the channels therein to open, and therefore let in their own current, continuing the release of free energy—stored in the transmembrane ion concentration gradients—that sustains the travelling wave of depolarization along the axon (see Figures 3.7 and 3.11). This phenomenon is modelled by the cable equation (Equation (3.28)).

Ignoring ion pumping, the resting potential is approximated by the chord equation:

$$V_{\text{rest}} \approx \frac{g_{\text{Na}^+}E_{\text{Na}^+} + g_{\text{K}^+}E_{\text{K}^+} + g_{\text{leak}}E_{\text{leak}}}{g_{\text{Na}^+} + g_{\text{K}^+} + g_{\text{leak}}}. \tag{3.44}$$

The meaning of the above equation is that the conductance of each ion pulls the membrane potential towards its reversal potential E_{Nernst}. For example, if the sodium conductivity suddenly increased, what would happen to V_{rest}?

The Equation (3.44) holds in the ohmic approximation that is assumed in Hodgkin-Huxley style conductance-based models. In permeability-based models, the resting potential takes a different form (see Equation (3.68)).

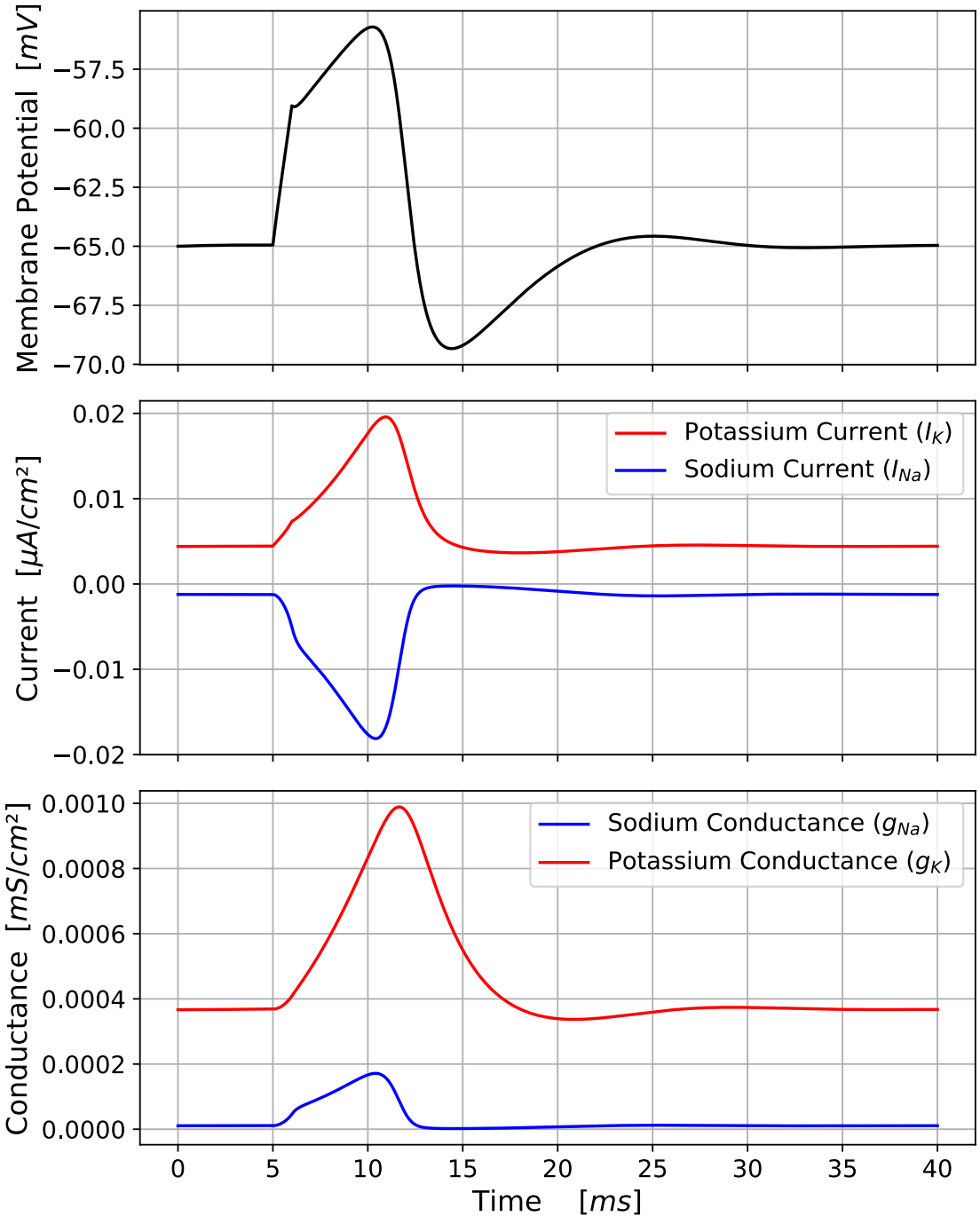

Figure 3.12: **Subthreshold behaviour of the Hodgkin-Huxley model.** Passive response to `1ms` pulse. Note that, below the AP threshold, the sodium conductance is always less than the potassium conductance. Compare with Figure 3.13, wherein the sodium conductance significantly exceeds the potassium conductance at the onset of the action potential.

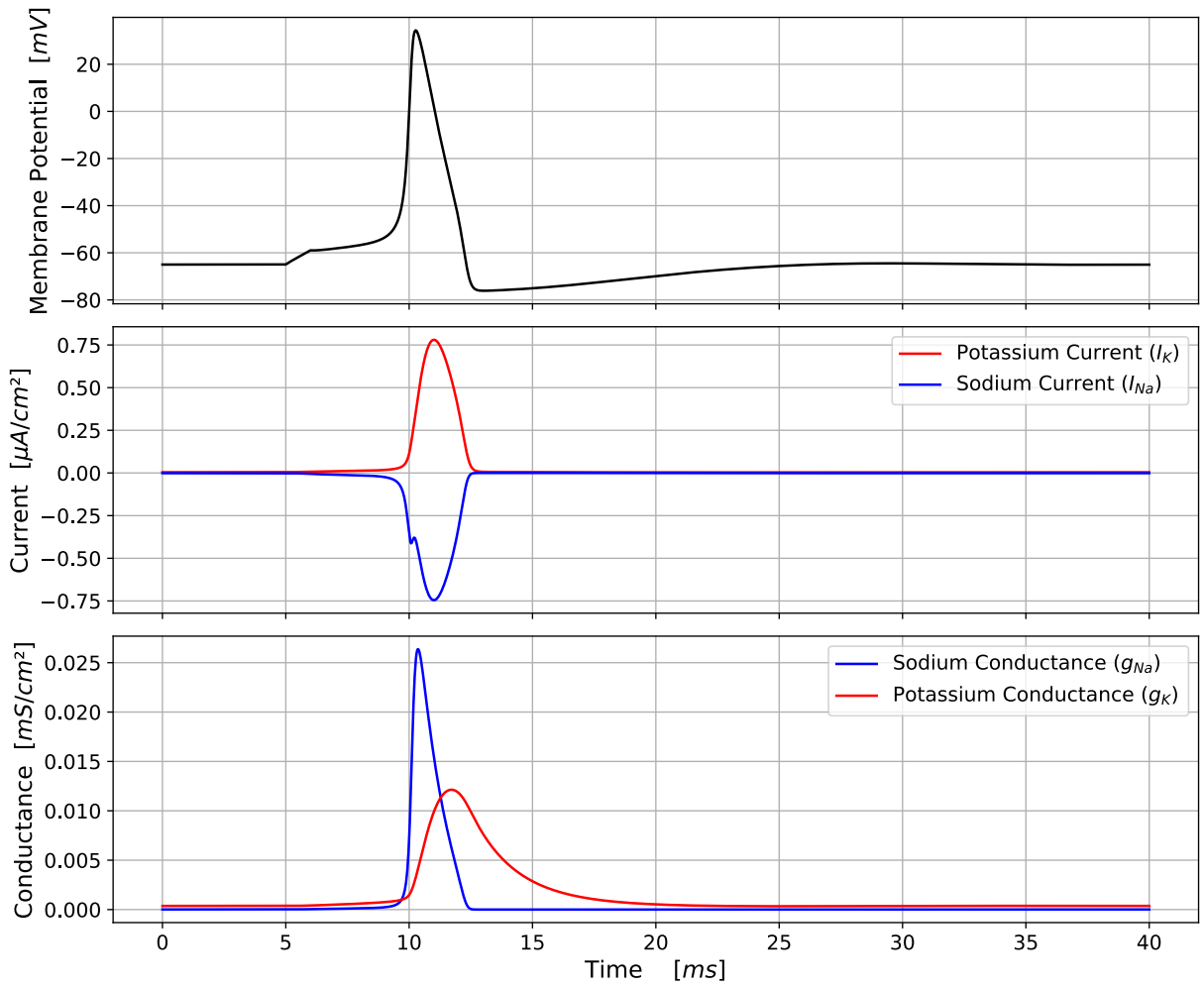

Figure 3.13: **Suprathreshold behaviour of the HH model: Action Potential.** AP elicited by `1ms` pulse. When the threshold is exceeded, voltage-gated sodium channels make themselves known: Suddenly, the sodium conductance reveals itself to be a function of the membrane potential[12]. The effect of g_{Na^+} suddenly increasing is to *move* the "resting potential"[13] upward by shifting the balance of conductances in Equation (3.21) toward E_{Na^+}. Effectively, the neuron has a new (temporary) target potential, toward which it will passively relax. As V_{m} relaxes toward the new target, the target voltage continues to accelerate upward. The active sodium conductance from Na_V channels in the membrane provides positive feedback, triggering a wave of depolarization called an action potential (AP). In the middle plot, notice the notch in the Na_V current as the Na^+ driving force hits a minimum when the membrane potential peaks near E_{Na^+}.

[12] voltage-gated conductances also depend on the recent history of the membrane potential, but that will be discussed later.

[13] The quotation marks are meant to indicate that this is not the true resting potential but a transient change.

3.4 Pumps – Na^+/K^+ adenosine triphosphatase

Ion pumps charge the neuron's batteries, and ion channels drain them.[14]

Ion channel proteins in the cell membrane have regions with high affinity for, e.g. sodium over potassium, in the portion of the protein called the *selectivity filter* [20]. The electrogenic Na^+/K^+ pump protein, too, has regions of high affinity, called *binding sites*, some of which select for sodium ions and others that bind potassium ions. There are three Na^+ binding sites and two K^+ binding sites in each pump macromolecule.[15]

Unlike voltage-gated ion *channels*—which actively modify their permeability in response to changes in the membrane potential, thereby controlling the rate at which permeant ions flow *down* their concentration gradients—the Na^+/K^+ pump burns fuel (adenosine triphosphate, ATP) to ship the Na^+ and K^+ ions back across the membrane *against* their Nernst potentials.

In that sense, the Na^+/K^+ pumps are the counterpart to the voltage-gated Na_V and K_V channels: The latter *consume* energy stored in the non-equilibrium inner and outer ion concentrations via their excitable conductances, and the former *maintain* the concentration gradients, and in-so-doing perpetually charge the neuron's batteries [43].

Na^+/K^+ pumps are present in virtually all animal cells. Ion pumping is energetically costly, which is why brumating turtles (see Figure 3.14) reduce Na^+/K^+ pump activity during their long breathless winter trapped beneath the ice [27].

[14] Paraphrasing [43].
[15] There are multiple Na^+/K^+ pump isoforms.

(Note: This turtle was promptly and gently returned to the location and direction it was originally heading when it approached the photographer. It may have been on the move due to nearby tree removal by Hydro One, who were restoring power following a recent microburst.)

Figure 3.14: **A Blanding's turtle (*Emydoidea blandingii*) – another ectothermic brumator.** Like the painted turtle, Blanding's turtles hibernate—technically, brumate—underwater *without breathing air for months at a time* during the harsh winter [27]. While holding their breath under the ice, they dramatically reduce Na^+/K^+ pump current to conserve fuel (ATP) and to limit the accumulation of toxic metabolites. (Aside: Blanding's turtles live at least as long as humans do and can *reproduce throughout their entire lives, including the females*—which has attracted attention from researchers in the field of human aging, longevity, and robust rejuvenation [10].)

The Na^+/K^+ pump can be thought of as a hybrid of a molecular motor and a set of selectivity filters like those seen in ion channels. Its ion-shuttling motion can be described as an enzymatic reaction with Michaelis-Menten kinetics, in which the inner and outer concentrations of a given $\underbrace{\text{ion species}}_{S}$—$[S]_{\text{in}}$ and $[S]_{\text{out}}$—are treated as if they were distinct reactants and products in a chemical reaction (Equation (3.45)). A chemical reaction does still occur, as the pumps catalyze the hydrolysis of ATP, which makes sodium–potassium adenosine triphosphatase (the pump) a genuine enzyme.

Although in such processes there is always some variability, a typical pump cycle consists of shuttling three Na^+ ions out of the cell and two K^+ ions inside. The ***net*** current emitted by the pump protein is, therefore, *outward*—the ejection of one elementary charge (e) out of the neuron per revolution. Its energy efficiency, when comparing the free energy imparted to the neuron by moving the ions against their potentials versus the chemical energy of the ATP molecule consumed in each cycle, is roughly 75% [43].

Being a major source of energy consumption for the cell, the pump rate is limited by the intracellular sodium and extracellular potassium concentrations. In other words, the pumps are stimulated to run by $[Na^+]_{\text{in}}$ and $[K^+]_{\text{out}}$, and will slow down as the neuron approaches its homeostatic transmembrane concentrations of said ions. To model the hyperpolarizing action of Na^+/K^+ ATPase, we implemented the pump current following Kager et al. [30]

$$I^{\text{pump}} = I_{\text{Max}}\left(1 + \frac{K_{M_{\text{Na}^+}}}{[\text{Na}^+]_{\text{in}}}\right)^{-3}\left(1 + \frac{K_{M_{\text{K}^+}}}{[\text{K}^+]_{\text{out}}}\right)^{-2}, \tag{3.45}$$

The exponent "-3" on the sodium term, and -2 on the potassium term, are for the 3 Na^+ ions shuttled out and the 2 K^+ ions shuttled into the cell, respectively. The coefficients $K_{M_{\text{Na}^+}} = 10\,\text{mM}$ and $K_{M_{\text{K}^+}} = 3.5\,\text{mM}$ are the Michaelis-Menten constants

for aqueous sodium and potassium ions' interaction with the Na^+/K^+ ATPase ([8], [35]). They are defined via the Michaelis-Menten rule for the velocity of enzymatic reactions

$$v([S]) = v_{\max} \overbrace{\left(\frac{[S]}{K_{M_S} + [S]}\right)}^{P_{ES}} = v_{\max} \overbrace{\left(1 + \frac{K_{M_S}}{[S]}\right)^{-1}}^{P_{ES}}, \tag{3.46}$$

in which K_{M_S} is the substrate concentration ($[S]$) at which the reaction rate $v([S])$ is half of its maximum $v_{\max}$ (see Nelson et al. [43, Section 10.4.1]). The dimensionless term in round brackets denoted P_{ES} in Equation (3.46) is the steady-state probability of a single enzyme, chosen at random from a thermodynamic ensemble, of being in its bound state with a single substrate molecule S.

In the context of the Na^+/K^+ pump current's kinetics, there are two substrates: $[Na^+]_{\text{in}}$ and $[K^+]_{\text{out}}$. Further, the pump requires that three Na^+ ions and two K^+ ions bind to it. Equation (3.45) treats the probability of each of these five required ions binding to the pump as independent. Hence, the pump current is governed by their concentration-dependent compound "P_{ES}"-type probabilities.

For our purposes, the most readily useful fact about Na^+/K^+-ATPase is the $3:2$ ratio of its sodium and potassium currents (respectively):

$$I^{\text{pump}} = \left(I^{\text{pump}}_{Na^+} + I^{\text{pump}}_{K^+}\right) \leftarrow \begin{cases} I^{\text{pump}}_{Na^+} = 3I^{\text{pump}} \\ I^{\text{pump}}_{K^+} = -2I^{\text{pump}}. \end{cases} \tag{3.47}$$

Using this ratio, Nelson et al. [43] demonstrates a simple method of estimating V_{rest} of real neurons through a model with passive chloride leak current and the resting ohmic Na^+ and K^+ currents constrained to match their respective pump currents.

Because of the $3:2$ ratio, when adding Na^+/K^+ pumps to the standard HH model—as is done in the *CLS* [28] and *T-CLS* [2] models (Sections 4 and 5, respectively)—one must also include *passive* Na^+ and K^+ conductances ensuring the leak currents at

V_{rest} are in approximately the same ratio. The pumps are always running (Equation (3.46)), even at V_{rest}, and without specific ion leaks to cancel the pump currents, the model does not achieve homeostasis.

3.5 Goldman-Hodgkin-Katz (GHK)

The maximal conductance densities in the HH model (see Section 3.3.5) approximate the phenomenon of ions permeating the membrane through open channels as if the current depended *linearly* on the voltage at *steady state*—it does not. That assumption is acknowledged as the *ohmic approximation*, which arose from empirical measurements of the voltage-dependence of the Na^+ and K^+ currents [21].

Isolating the electrical currents due to the flow of sodium and potassium ions, a *positive (outflowing) current* was measured when $V > \overset{E_{\text{Nernst}}}{\widetilde{E_{\text{S}}}}$, and the *current was negative (inflowing)* when $V < E_{\text{S}}$—with zero current at the ion's respective Nernst potential E_S. These observations led to an $\overrightarrow{\text{ohmic driving force}} \propto (V - E_S)$—see page 66. Noting that, although the driving forces of the ionic currents in the HH-model are linear with respect to V, the *conductances* multiplying them are *nonlinear* thanks to the gating variables. In this way, gating variables in the HH model can compensate for the ohmic approximation so long as the *concentration gradients* remain fixed.

Let the subscript "$_S$" be a placeholder for the specific ion species, so that we can efficiently write equations that apply to all relevant ions.

The transmembrane ionic currents are more accurately described by the GHK current equation (3.58), which is a *permeability*-based description derived from first-principles. Permeability is a property of the membrane: Whereas the measured maximal conductance per unit membrane area depends strongly on inner and outer ion concentrations—which can change significantly when multiple action potentials penetrate smaller ($\sim 0.1\mu m$) neurites[16] such as thin axons and dendrites—permeability remains consistent when gating is taken into account.

The ohmic approximation is phenomenological, whereas GHK derives from the microscopic physics governing membrane currents. Although the latter contains some false assumptions, it is a robust physical model [20].

The GHK equations are introduced here following Hille [20]. Pores are not mentioned in the model: it treats the membrane as a uniform, hydrophobic layer (thickness l),

[16] "A neurite or neuronal process refers to any projection from the cell body of a neuron."—https://en.wikipedia.org/wiki/Neurite

with aqueous solutions of ions on either side. Ions are assumed not to interact with one another as they traverse the membrane.

3.5.1 Permeability without electrodiffusion - define P_S

Before considering electrical effects, we can define the permeability coefficient via solubility-diffusion theory by considering a non-electrolyte molecule S. Permeability of the membrane to a molecule S is defined by the measured relation between the molar flux M_s across the membrane and difference of the concentrations $\Delta c_S \stackrel{\text{def}}{=} [S]_{\text{out}} - [S]_{\text{in}}$ on each side of it:

The molar flux M_S has units $\frac{\text{mol}}{\text{cm}^2 \cdot \text{s}}$. It is simply a rescaled number flux $M_S = J_S / \text{N}_\text{A}$, where $\text{N}_\text{A} = 6.0221 \times 10^{23}$ molecules-per-mole is Avogadro's number.

$$\boxed{M_s = -P_S \Delta c_S}. \tag{3.48}$$

The role of P_S in Equation (3.48) is reminiscent of the diffusion coefficient seen in Equation (2.19): Both coefficients yield a flux of molecules in response to a non-uniformity of the concentration. We can relate permeability to diffusion by introducing an $\widetilde{\text{effective}}$ concentration gradient inside the idealized homogenous membrane [20, page 444]:

$$\widetilde{\nabla c_S} \stackrel{\text{def}}{=} \Delta c_S \beta_S^\star. \tag{3.49}$$

Plugging the above expression into Fick's first law (page 33) gives the molar flux as

$$M_S = -\frac{\Delta c_S D_S^\star \beta_S^\star}{l}, \tag{3.50}$$

and hence the permeability as

$$\boxed{P_S = \frac{D_S^\star \beta_S^\star}{l}}. \tag{3.51}$$

The superscript "$\star$" indicates that the diffusion coefficient $D_S^\star$ and the water-membrane partition coefficient $\beta_S^\star$ in the preceding equations are material properties within the

membrane. The partition coefficient is defined as the ratio of concentrations of S in the membrane versus the interfacing aqueous solution at equilibrium,

$$\beta_S^\star = \frac{[S]_{\text{membrane}}}{[S]_{\text{water}}}. \tag{3.52}$$

Diffusion is introduced in Section 2.3.4.

3.5.2 GHK - permeability of the membrane to electrolytes

The apparent permeability of the membrane to ions comes from ion channels—the phospholipid bilayer is effectively impermeable to ions—but the presence of these channels and their gating properties are ignored for the moment. (When in doubt, assume the channels are open.)

The Goldman-Hodgkin-Katz equations [22] include electrodiffusion effects to allow them to model transmembrane ion currents in terms of permeability. The explicit solution for the current is obtained by integrating the Nernst-Planck equation

$$I_S = -z_S F D_S^\star \left(\frac{d[S]}{dx} + \frac{z_S F}{RT}[S](x)\frac{\overset{\mathbb{E}}{\widetilde{dV}}}{dx} \right), \tag{3.53}$$

As before, $D_S^\star$ is the diffusion coefficient within the membrane. The molar gas constant is $R \overset{\text{def}}{=} \mathsf{N_A}\not{k}_{\mathsf{B}}$, and the Faraday constant is $F \overset{\text{def}}{=} \mathsf{e}\mathsf{N_A}$. The valence of the ion, denoted z_S, is an integer, and T is the absolute temperature.

across the membrane, assuming constant $D_S^\star$ and that $V(x)$ decreases linearly (i.e. $V(x) = x\mathbb{E}$) inside the membrane. Equation (3.53) is written as an electric current density due to the flux of ions rather than a generic number flux of molecules $\mathbb{J}$ (cf. Equation (2.46)). As before, the current results from a diffusion term driven by an imbalance in the intracellular and extracellular concentrations of a permeant ion species S, and a drift term driven by the membrane potential acting on said ions.

Noting that

$$\left[e^{\frac{z_S F}{RT}V}\right]\left(\frac{d[S]}{dx} + \frac{z_S F}{RT}[S](x)\frac{dV}{dx}\right) = \frac{d}{dx}\left[[S](x)e^{\frac{z_S F}{RT}V}\right], \tag{3.54}$$

we can solve the differential equation 3.53 using the integrating factor $\xi = e^{\frac{z_S F}{RT}V}$. With I_S being constant at every point as we cross the membrane, the integral of Equation (3.53) becomes

$$\int_0^l dx\, I_S e^{\frac{z_S F}{RT}V(x)} = I_S \int_0^l dx\, e^{\frac{z_S F}{RT}V(x)} = -z_S F D_S^\star \int_0^l dx \left(\frac{d}{dx}\left[[S](x)e^{\frac{z_S F}{RT}V(x)}\right]\right). \tag{3.55}$$

The resulting closed-form solution for $I_S(V)$ is provided in Equation (3.58) below. (Though I do not repeat the steps here, the reader may wish to consult e.g. Hille [20, Chapter 14] or Ermentrout and Terman [15, Chapter 1] for the full derivations.)

While ion channels were unknown at the time the GHK model was derived, we speak of Na_V and K_V channels as displaying a property called *ion selectivity* since sodium channels are much more permeable to Na^+ ions than K^+ ions (and all other ion species) and vice-versa. Said channels are named to reflect their selectivity—the property that allows them to generate action potentials.

3.5.3 GHK current equation

The GHK equation for the current I_S of ion species S (Equation (3.58)) has two components: one for ions exiting the cell ($I_{S,\,\text{efflux}}$), and another for ions entering the cell ($I_{S,\,\text{influx}}$).

$$I_{S,\,\text{efflux}} = V_m P_S \left(\frac{z_S^2 F^2}{RT}\right)\left(\frac{[S]_{\text{in}}}{1 - e^{-z_S F V_m/RT}}\right), \tag{3.56}$$

As with the HH model, one must ***intercept zero-division errors*** *when programming a GHK-based simulation, due to the* $(1 - e^{\pm V})$*-style term in the denominator.*

$$I_{S,\text{ influx}} = -V_m P_S \left(\frac{z_S^2 F^2}{RT}\right)\left(\frac{[S]_{out} e^{-z_S F V_m/RT}}{1 - e^{-z_S F V_m/RT}}\right). \tag{3.57}$$

When the influx and efflux components are combined, we obtain the net current in the form of the complete **GHK current equation** [20]

$$\boxed{I_S = \underbrace{V_m P_S \left(\frac{z_S^2 F^2}{RT}\right)\left(\frac{[S]_{in} - [S]_{out} e^{-z_S F V_m/RT}}{1 - e^{-z_S F V_m/RT}}\right)}_{I_{S,\text{ efflux}} + I_{S,\text{ influx}}}}. \tag{3.58}$$

The GHK current equation (above) gives nonlinear current-voltage curves when transmembrane concentration gradients are present, with the curvature disappearing—i.e. truly ohmic currents—only when the inner and outer ion concentrations are equal [15]. The latter statement can be easily checked by setting $[S]_{in} = [S]_{out}$ in Equation (3.58).

Hodgkin-Huxley-style Na_V and K_V channel gating dynamics can be included in the GHK model by replacing the permeability coefficient P_S in Equation (3.58) with the product of a *maximal permeability* $\bar{P}_S$ and appropriate gating variables:

$$\left\{P_{Na^+},\, P_{K^+}\right\} \longrightarrow \left\{m^3(V,t)h(V,t)\bar{P}_{Na^+},\, n^4(V,t)\bar{P}_{K^+}\right\}. \tag{3.59}$$

Some properties of GHK currents

A few noteworthy observations regarding $I_S(V)$ (Equation (3.58)) are:

1. At zero membrane potential, the GHK current equation (3.58) reduces to solubility-diffusion theory (Section 3.5.1 above): If we rewrite Equation (3.58)

using the following shorthand

$$I_S = \widetilde{P_S}\widetilde{V_S}\frac{[S]_{\text{in}} - [S]_{\text{out}}e^{-\widetilde{V_S}}}{1 - e^{-\widetilde{V_S}}} \leftarrow \begin{cases} \widetilde{P_S} = z_S F P_S \\ \widetilde{V_S} = \frac{z_S F}{RT} V \end{cases}, \tag{3.60}$$

and take the limit as $\overbrace{\widetilde{V_S} \longrightarrow 0}^{V \longrightarrow 0}$ using l'Hôpital's rule, we recover the electric-current equivalent of Equation (3.48):

$$I_S(V = 0) = \lim_{V \to 0} I_S = \lim_{\widetilde{V_S} \to 0} I_S = \overbrace{\underbrace{z_S F P_S}_{\widetilde{P_S}}\Big([S]_{\text{in}} - [S]_{\text{out}}\Big)}^{\propto -P_S \Delta c_S}. \tag{3.61}$$

In other words, when $V = 0$ the current is purely diffusion-driven.

2. Setting $I_S = 0$ gives the Nernst potential (see Equation (2.53) or Equation (2.61)):
   Starting with Equation (3.60), we write down the condition of zero current at $V = E_S$,

$$\widetilde{P_S}\widetilde{V_S}\left(\frac{[S]_{\text{in}} - [S]_{\text{out}}e^{-\widetilde{V_S}}}{1 - e^{-\widetilde{V_S}}}\right) = 0 \Longrightarrow [S]_{\text{in}} - [S]_{\text{out}}e^{-\widetilde{V_S}} = 0. \tag{3.62}$$

With a bit of rearrangement and expanding $\widetilde{V_S}$ in terms of $V = E_S$, we get

$$[S]_{\text{in}} = [S]_{\text{out}}e^{-\widetilde{V_S}} \Longrightarrow \ln\left(\frac{[S]_{\text{in}}}{[S]_{\text{out}}}\right) = \ln\left(e^{-\frac{z_S F}{RT}E_S}\right), \tag{3.63}$$

which trivially reduces to Equation (2.61) (the Nernst potential), rewritten here for convenience in terms of the molar gas constant R and the Faraday constant F:

$$E_S = -\frac{RT}{z_S F}\ln\left(\frac{[S]_{\text{in}}}{[S]_{\text{out}}}\right). \tag{3.64}$$

3. To make the GHK current equation more intuitive, we can introduce the simplified expression Φ_S, defined here by

$$I_S(V) = P_S\left(\frac{z_S^2F^2}{RT}\right)\Phi_S(V). \tag{3.65}$$

Then, Equation (3.58) gives the simplified "current" Φ_S as

$$\Phi_S(V) = [S]_{\text{in}}V\left(\frac{1-\frac{[S]_{\text{out}}}{[S]_{\text{in}}}e^{-\left(\frac{z_SF}{RT}V\right)}}{1-e^{-\left(\frac{z_SF}{RT}V\right)}}\right). \tag{3.66}$$

Next, using Equation (3.64), we rewrite Φ_S in terms of the reversal potential E_S:

$$\text{Equation (3.66)} \implies \boxed{\Phi_S = [S]_{\text{in}}V\left(\frac{1-e^{-\left(\frac{z_SF}{RT}\right)(V-E_S)}}{1-e^{-\left(\frac{z_SF}{RT}\right)V}}\right)}. \tag{3.67}$$

4. In Figure 3.15 we plot $\Phi_S(V)$—which has the same shape as $I_S(V)$—for a positively charged ion S with valence $z_S = 1$. Some visible features of the GHK current density are:

   - The cation current due to ion species S is positive (outward flowing) when $V > E_S$, and negative (inward flowing) when $V < E_S$, hence the synonym "reversal potential" for the Nernst potential E_S. (**This property is shared with the ohmic approximation used in the original Hodgkin-Huxley model.**) With anions the direction of ion flow is opposite, but the direction of the electrical current flow remains the same.
   - The current is concave-up when $[S]_{\text{in}} > [S]_{\text{out}}$ and concave-down when $[S]_{\text{in}} < [S]_{\text{out}}$—the opposite is true for anions (i.e. $z_S = -1, -2, \ldots$).

- The current becomes asymptotically linear in V when $|V| \gg 0$.

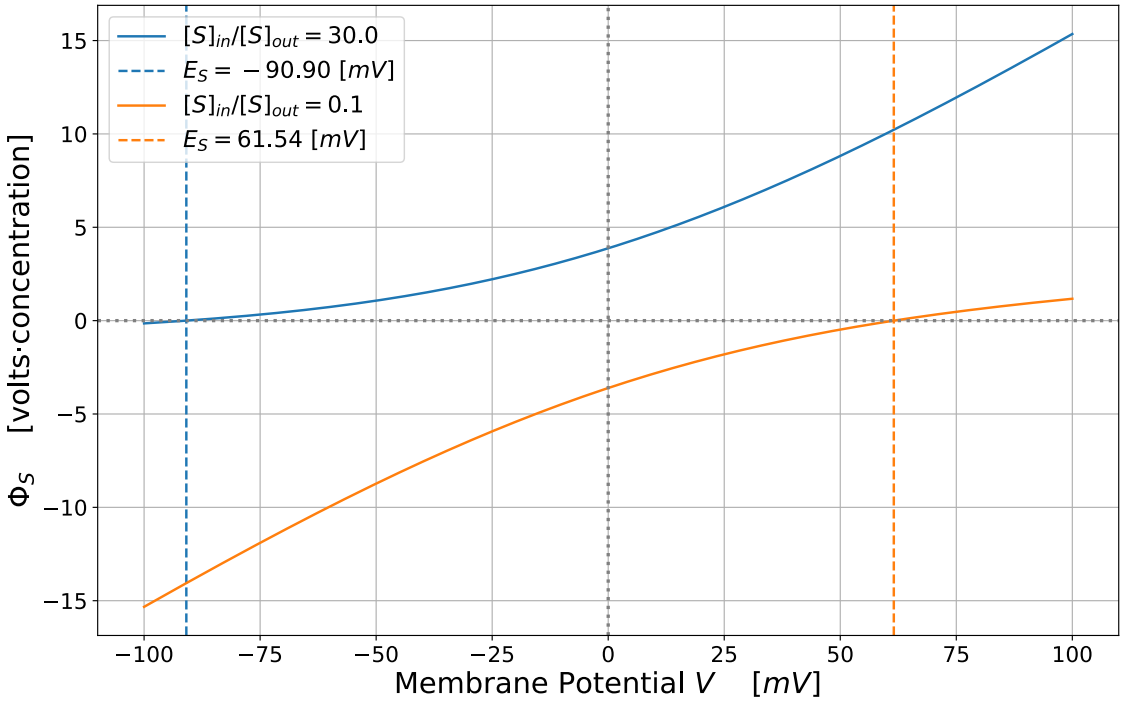

Figure 3.15: **Shape of the GHK current as a function of membrane potential, via the simplified expression $\Phi_S(V)$**—see Equation (3.67). Here we plot the voltage-dependence of the flux of an ion S with valence $z_S = 1$. In the upper curve $[S]_{\text{in}} > [S]_{\text{out}}$, and in the lower curve $[S]_{\text{in}} < [S]_{\text{out}}$. Note: units on the ordinate are somewhat arbitrary since the prefactor $P_S\left(\frac{z_S^2 F^2}{RT}\right)$ is omitted.

Resting potential in the GHK model

The GHK voltage equation gives the resting potential at which the sum of GHK currents for each ion species cancel, resulting in *zero* ***net*** current. In a system wherein only Na^+, K^+ and Cl^- currents are modelled—without Na^+-K^+ pumps—it is

$$V_{\text{rest}} = \frac{RT}{F}\ln\left(\frac{P_{K^+}[K^+]_{\text{out}} + P_{Na^+}[Na^+]_{\text{out}} + P_{Cl^-}[Cl^-]_{\text{in}}}{P_{K^+}[K^+]_{\text{in}} + P_{Na^+}[Na^+]_{\text{in}} + P_{Cl^-}[Cl^-]_{\text{out}}}\right). \tag{3.68}$$

Note that in the above condition, the membrane, cytosol, and extracellular solution are *not* at equilibrium, and the ions' concentration gradients will steadily diminish without active pumping to counteract the steady currents at V_{rest}.

For a single ion species, Equation (3.68) reduces to the Nernst equation (reversal potential) for that ion [53]. The GHK model will be revisited in *Chapter7 - Conversion of ohmic pyramidal cell model to GHK current*.

Part III

Published Research and Additional Results

Chapter 4

Calculating the Consequences of Left-Shifted Na_V Channel Activity in Sick Excitable Cells

4.1 Statement of originality and contributions

My contribution to this paper, which covers various aspects of coupled *left-shift* (*CLS*) damage, is Section 10 of Joós, Barlow, and Morris [28], including the regime diagram in Fig. 8 (page#301). In that figure, I analyzed the output of the single-compartment *CLS* model (with Na^+/K^+-pumps) across a broad range of damage conditions and mapped the excitability and spiking patterns exhibited by the model. Here we provide examples of those firing patterns from simulations run solely for this chapter, which are not in [28], in Figures 4.2, 4.3, 4.8, 4.9, 4.10 and 4.11.

I wrote the simulation code that generated the regime diagram (Figure 4.4), analyzed the scores of simulations needed to create it, and programmed the *CLS* model as a density mechanism (CLS.mod) in NEURON[1] (see ModelDB entries – Section 0.3). The full paper is included as (Appendix B | Joós, Barlow, and Morris (2017) on

[1] https://www.neuron.yale.edu/neuron/

page#282. Before my contributions, CLS simulations were run using FORTRAN code authored by Pierre-Alexandre Boucher [8].

Some preliminary work on identifying CLS regimes was done in [8]—see **Fig. 5(B)**, 'Regimes'—but the data was sparse, especially when Na^+/K^+-pumps were included. I mapped the *boundaries* separating quiescent and spontaneously firing excitotoxic regimes (and the boundaries between various pathological cell states), which is necessary to explore mechanisms for staying on the healthy side of those lines—information that may eventually contribute to improved recovery from stroke, head trauma, treatment of neuropathic pain, and other forms of pathological ectopic signalling [2].

I have relied on Boucher, Joós, and Morris [8] and Yu, Morris, Joós, and Longtin [58], as well as the co-authored paper Joós, Barlow, and Morris [28] as guides while writing the sections introducing the CLS model below. As usual, I created all of the plots with my own simulations and model code.

4.2 Introduction: CLS model

The coupled *left-shift* (CLS) model introduces two cellular-damage parameters (denoted LS and AC) to capture changes in the sodium channel gating properties of injured neurons [8]. LS models the hyperpolarizing shift in a damaged sodium channel's steady-state *activation* and *availability*—denoted $m_\infty(V)$ and $h_\infty(V)$—in Hodgkin-Huxley-style Na_V kinetics, see Figure 4.1. AC stands for "Affected Channels", which is a parameter ranging from 0 to 1 that sets the density of damaged Na_V channels as a fraction of the total density of Na_Vs in the membrane. It is a single-compartment neuron model: At each moment in time, it computes a single value for the membrane potential, ion concentrations, transmembrane currents, and other variables describing its Hodgkin-Huxley style kinetics. In this study, the neuron's surface

area, internal and external volumes, Na_V and K_V channel densities, etc., were adjusted to simulate a node of Ranvier. We can treat the node as a single compartment since, being $\approx$ 1–2µm in length, its membrane potential $V_{\mathrm{m}}(t)$ is approximately uniform.

The *CLS* model resembles Hodgkin and Huxley's space-clamped squid axon—Equation (3.31) in Section 3.3.4: *HH model for an isopotential section of membrane* (page#68)—with Michaelis-Menten style $\mathrm{Na}^+/\mathrm{K}^+$-pumps (Equation (3.45)) replacing the electrode:

$$C_{\mathrm{m}}\frac{dV}{dt} = -\left(I_{Na_V} + I_{\mathrm{Na}_{\mathrm{leak}}}\right) - \left(I_{K_V} + I_{\mathrm{K}_{\mathrm{leak}}}\right) - I_{\mathrm{leak}} - I^{\mathrm{pump}}. \tag{4.1}$$

The pumps continue to run as long as there is ATP to burn and ions to bind, so $I_{\mathrm{Na}_{\mathrm{leak}}}$ and $I_{\mathrm{K}_{\mathrm{leak}}}$ are added to saturate the pumps at homeostatic $[\mathrm{Na}^+]_{\mathrm{in}}$ and $[\mathrm{K}^+]_{\mathrm{out}}$ concentrations. Parameters for the voltage-gated channels are as given in Equations (3.40), (3.41) and (3.42). For the full set of equations, see Section 5 of Joós, Barlow, and Morris [28] on page#294 and *Pumps* in Background II: Action potentials and ion channels (page#83).

Single-compartment models are sometimes called point neurons because their idealized cylindrical or spherical shape and uniform properties make them mathematically equivalent to a point in space with a membrane potential $V_{\mathrm{m}}(t)$, currents, and other parameters associated with it. For example, the differential equations that describe a cylindrical compartment with membrane area A, through which a *uniform* sodium current density $J(t) = \frac{I(t)}{A}$ flows, also describe the point-current $I(t) = J(t)A$. In single-compartment models, the membrane is just a parameter.

(This is not to say that point-neuron models are simple. They are capable of reproducing complex firing patterns, including bifurcations to bursting and chaotic spiking, and can describe the time evolution of various ion currents and concentrations, calcium buffering, temperature effects, and other interesting phenomena.)

A long section of axon that is space-clamped can also be modelled as a single compartment. Hodgkin and Huxley [21] refer to "membrane action potentials" in their space-clamped squid axon experiments, wherein the entire membrane would spike as one. At that time, nonlinear differential equations were solved by mechanical computers, and they gained precious speed integrating the non-propagating (space-clamped) APs by hand.

4.2.1 *CLS*: Malfunctioning ion channels in a damaged membrane

Coupled *Left-shift* (*CLS*, see Figure 4.1) refers to an experimentally observed phenomenon wherein chemical or mechanical injury to a neuron alters the kinetics of some fraction (*AC*) of its voltage-gated sodium channels (Wang et al. [56], Boucher et al. [8], Joós et al. [28]). Both the destructive effects of calpain on the cytoskeleton following ischemia (e.g., stroke) and direct mechanical injury to axons following blunt-force trauma cause blebbing of the cell membrane. The bilayer detaches from the cytoskeleton and bulges outward under osmotic pressure.

$AC \stackrel{\text{def}}{=}$ ***A**ffected* ***C**hannels*,

i.e., the fraction of left-shifted Na_V channels relative to all Na_V channels in the neuronal membrane.

The blebbed, fluidized membrane alters the function of ion channels within it since the channels' kinetics are influenced by interactions with cytoskeletal proteins as well as by the surface tension and deformation imparted to them by the stretched bilayer. For example, sodium channels such as $Na_V1.6$ are integral membrane proteins; they are embedded in the bilayer, passing through it several times along their length as if threaded by a needle (Figure 3.4).

This structural damage shifts the "w" term in Equation (3.20) such that more channels are in the open state at the neuron's homeostatic resting potential, leading to an increased "window conductance" to sodium ions at V_{rest} [8]. Consequently, a persistent depolarizing "window current" enters the cell through its *left-shift*ed Na_V channels—see caption of Figure 4.1, below.

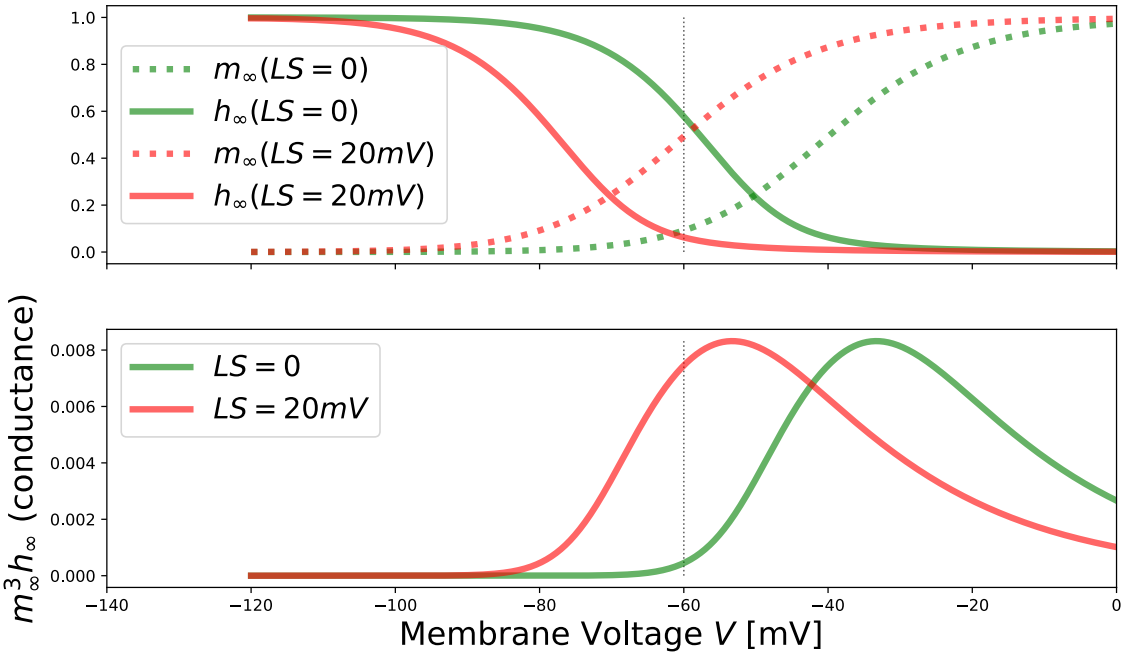

Figure 4.1: **Coupled Left-Shift (CLS) model of neuronal injury.** The dashed vertical line indicates the neuron's resting potential (V_{rest}). The *activation* m and inactivation (or, *availability*) h of voltage-gated sodium channels are functions of the membrane voltage V, but *when damaged they do not see the true* V. Healthy (or, *intact*) channel kinetics are plotted in green. Damaged channels (plotted in red) react to V as healthy channels would to $\widetilde{V} = V + LS$. In other words, the gating properties of the channels affected by CLS are *left-shift*ed by LS millivolts: $m = m(V + LS, t)$, $h = h(V + LS, t)$. **Note:** The markedly increased Na_V conductance at V_{rest} in the lower plot—due to *left-shift*—creates a self-generated depolarizing window current in the neuron.

The CLS model gets its name from the fact that, in the scenario described above, experiments [56] show that the *activation* and *availability* of the injured sodium channels—denoted $m(V, t)$ and $h(V, t)$, respectively—are "coupled" in their response to cellular damage. They exhibit roughly the same hyperpolarizing shift (*left-shift*, denoted 'LS') in their voltage-dependent kinetics (illustrated in Figure 4.1).

m and h move to the left together along the voltage axis; hence the term Coupled Left-Shift (CLS). See Figure 4.1.

4.2.2 CLS renders neurons hypersensitive and hyperexcitable

CLS-induced window current (introduced above) can render the neuron **hypersensitive** (i.e. decreased threshold or exaggerated response to ordinary stimuli) and **hyperexcitable** (i.e. spontaneous, unstimulated action potentials and ectopic discharge). Both phenomena can include excitotoxic high-frequency spiking, which is potentially lethal to the cell.

*In neuroscience, **Hypersensitivity** and **hyperexcitability** are not entirely distinct concepts. There is significant overlap in their usage, and the definitions provided in the paragraph to the left are not universal.*

Under mild CLS damage, the model node of Ranvier can remain quiescent and simultaneously become hypersensitive to external stimuli. In that regime, where AC multiplies LS to produce only a subthreshold window current, no appreciable change occurs in the membrane potential (aside from transient spiking if LS and AC are increased abruptly).

The neuron thus *appears* unaffected by the *left-shift*ed Na_V channels in its membrane —until it is stimulated (see Figure 4.2). Then we observe that much less injected current is needed to initiate firing, and the neuron—though it was quiescent—exhibits a hypersensitive response (a burst of high-frequency action potentials).

The damage to *individual* channels need not be mild for the (AC, LS) combination to constitute mild CLS: Even if the *affected channels* themselves are severely *left-shift*ed (e.g. $LS \gtrsim 15\text{mV}$) and produce significant *per-channel* window currents, there may still be too few of them ($AC \ll 1$) to allow for spontaneous action potentials (see Figure 4.4).

To summarize the preceding description of hypersensitivity, compare:

(I) Figure 4.3, which shows the subthreshold response of a *healthy* cell ($AC = 0$) to a $1.0\mu\text{A/cm}^2$ current pulse (no action potentials), and

(II) Figure 4.2, which shows the *hypersensitive* response—tonic firing—of the same cell to a twenty-times *weaker* pulse ($I_{\text{stim}} = 0.05\mu\text{A} / \text{cm}^2$) when all its Na_V channels are affected by relatively mild *left-shift*: $(AC = 1, LS = 1.75\text{mV})$.

Hyperexcitability in the CLS model—e.g. the ectopic regimes with spontaneous (unstimulated) action potentials in Figure 4.4—is demonstrated in Figure 4.8 (bursting, page#117) and Figure 4.9 (tonic firing, page#118).

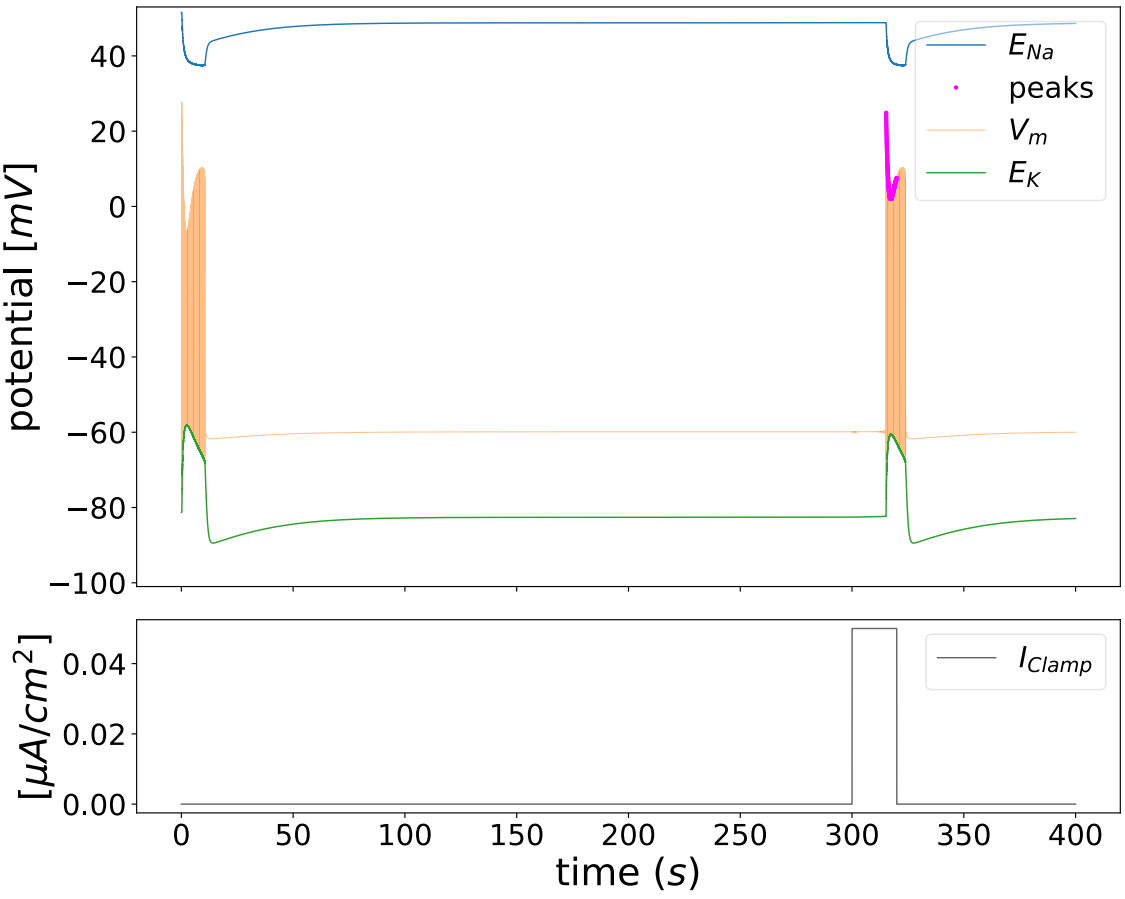

Figure 4.2: **Quiescent, injured neuron: $(AC = 1, LS = 1.75\text{mV})$. Hypersensitive response to stimulation when the neuron's voltage-gated sodium channels have sustained relatively mild CLS damage.** The stimulating current density (lower plot) is $I_{\text{stim}} = 0.05\mu\text{A} / \text{cm}^2$, *one-twentieth the amplitude* of the subthreshold pulse in Figure 4.2. This configuration of the model maps to the purple region—labelled "Quiescent (Hypersensitive)" on the right-hand side of Figure 4.4—just below the blue (spontaneous periodic bursting) regime. Note: The initial burst at $t = 0$ is a *transient* response to the suddenly applied *left-shift* (LS), after which the neuron was able to restore equilibrium. The second burst was caused by the square current pulse shown in the lower plot.

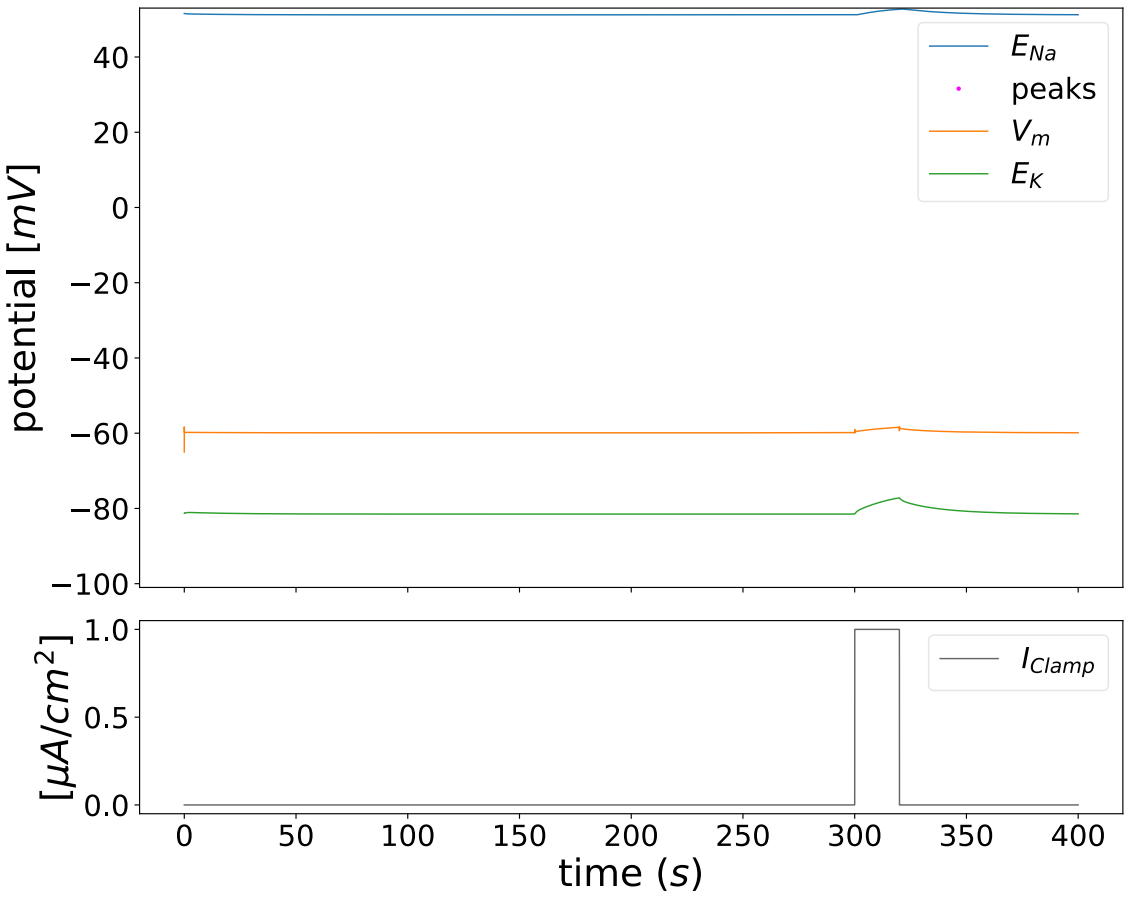

Figure 4.3: **Quiescent, healthy neuron ($AC = 0$): The model system's response to subthreshold stimulus in the absence of any CLS damage.** Since the fraction of *A*ffected *C*hannels (AC) is zero, LS has no effect. In the regime diagram of the CLS model (Figure 4.4), this damage-free condition maps to the origin. The stimulating current density (amplitude of the square pulse in the lower plot) is $I_{\text{stim}} = 1.0\mu\text{A} / \text{cm}^2$. **Compare with Figure 4.2**—in which the injected current pulse is **twenty times *weaker*** than it is here—where due to CLS damage, a hypersensitive response (tonic spiking) is observed.

Miniature copy of Figure 4.2:

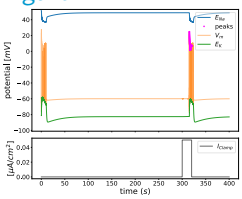

Full-size figure on page# 104.

4.3 Ectopic regimes – Section 10: Joós, Barlow, and Morris (2017)

Depending on the severity of CLS, neurons may become *hypersensitive* (Figure 4.2) or *hyperexcitable*—emitting spontaneous bursts (Figure 4.8, Figure 4.11) or firing tonically (Figure 4.9, Figure 4.14) *without* any external stimulation. The severity and character of the ectopic spiking patterns resulting from CLS depend on the degree of *left-shift* (LS, more millivolts being worse) and the fraction of Na_V channels that are affected (Affected Channels, AC). The variables LS and AC produce a *regime diagram* (Figure 4.4) of altered neuronal activity, excitability, and shifted steady-states [8], which we have mapped out in detail [28].

Figure 4.4 delineates the boundaries between quiescent and spontaneously spiking regimes in the CLS model. The key boundaries for this thesis are those marking the transitions from the regime labelled 'Quiescent (Hypersensitive)' to the 'Spontaneous Periodic Bursting' regime, and then from the latter regime into 'Spontaneous Tonic Firing'.

Ectopic spiking may persist even after injured neurons have had time to repair their blebbed membranes, since experiments show that CLS does not reverse after transient membrane stretching [56]. The resulting pathological depolarizing inward sodium current continually stresses the neuron's ability to maintain healthy ion concentrations via its Na^+/K^+ pumps. This CLS-induced window current is also metabolically stressful to the damaged neuron since ion pumping is a major source of its adenosine triphosphate (ATP) consumption. A factor which may mitigate cell loss from excitotoxic firing (modelled by CLS) is the turnover of sodium channels: Membrane proteins tend to turn over on a timescale of days [13], however, ectopically spiking neurons may perish in the hours following a stroke.

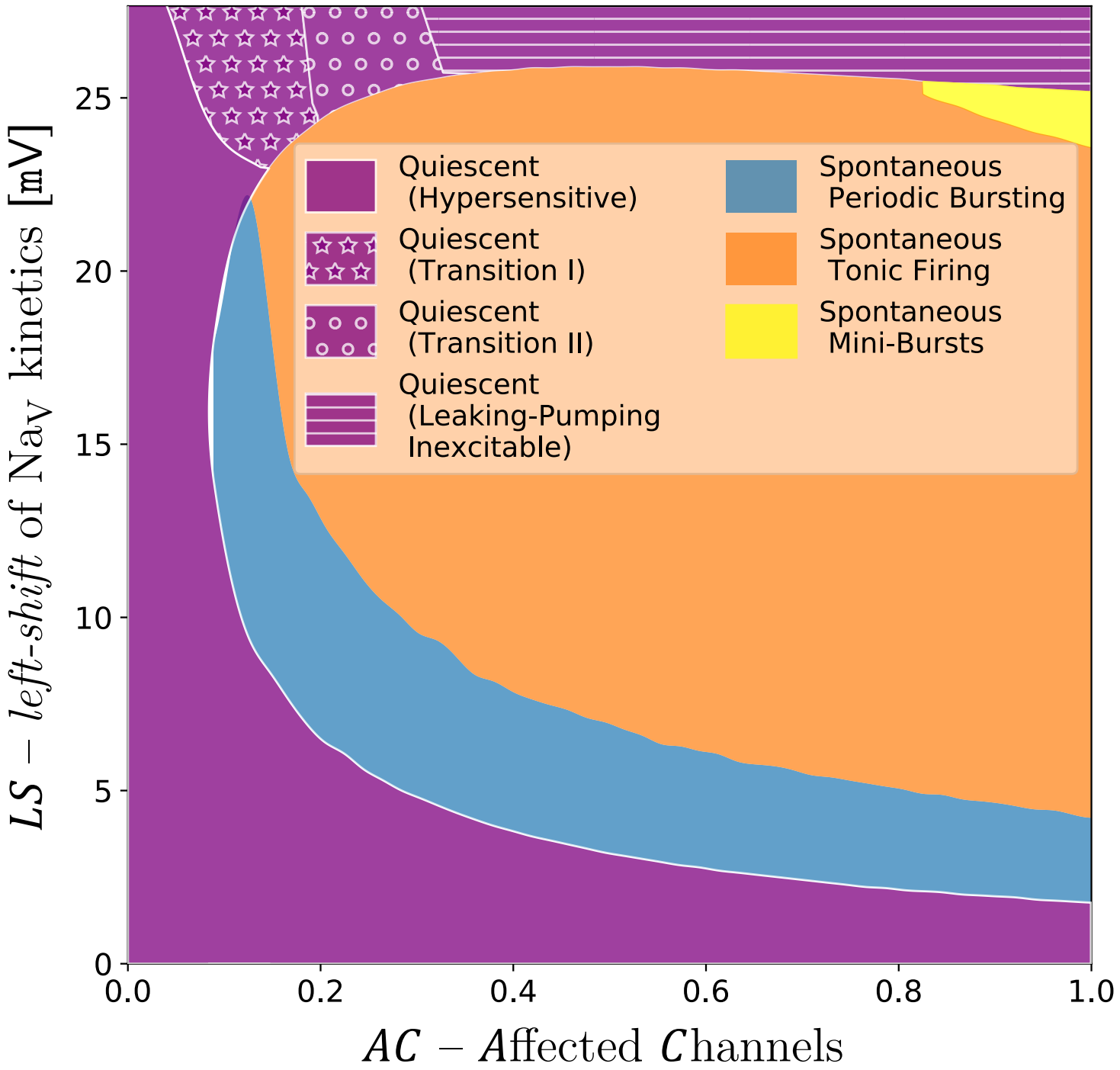

Figure 4.4: **Regime diagram of the *CLS* model of neuronal damage—a single-compartment model exhibiting multiple excitotoxic spiking behaviours.** This diagram is published as Fig. 8 in Joós, Barlow, and Morris [28], which is included as an appendix (page#282). AC denotes the *fraction* of the total number of Na_V channels in the membrane that are *left-shift*ed (*A*ffected *C*hannels, $AC \in [0, 1]$), and LS is the per-channel severity of the *left-shift* (see Figure 4.1). Illustrative voltage traces of ectopic bursting, tonic firing, and mini-bursts are provided in Figures 4.8, 4.9 and 4.11.

The regime diagram of *CLS* (Figure 4.4, above) is altered significantly by temperature effects, and our modelling has shown that modest cooling may be neuroprotective since a few ℃ may suppress pathological spiking long enough to allow the cells to heal. Temperature effects are modelled in ***Barlow, Joós, Trinh, and Longtin (2018)*** [2] (see Section 5.3).

Dynamical analysis performed by Yu, Morris, Joós, and Longtin [58] revealed that these transitions are instances of subcritical and supercritical Hopf bifurcations (see Fig. 7 of Joós, Barlow, and Morris [28] on page #298).

4.3.1 Dynamical systems theory

> (A note to readers wishing to skip this mini-introduction to dynamical systems theory: The discussion of ectopic regimes resumes in Section 4.3.7: *Bifurcations observed in the CLS model* on page#116.)

To understand the spontaneous ectopic firing patterns in the *CLS* model, which are mapped in Figure 4.4, we must think in terms of bifurcation diagrams. Yu, Morris, Joós, and Longtin [58] performed a dynamical analysis of the standard node of Ranvier *CLS* model from [8], including the effects of malfunctioning electrogenic pumps. Before discussing the results of that analysis we will introduce the necessary elements of dynamical systems theory (DST).

4.3.2 Attractors, repellers, fixed points, and limit cycles

The following section is based on Izhikevich [26], Ermentrout and Terman [15] and Strogatz [54].

The full repertoire of electrical activity that, e.g., a pyramidal neuron is capable of, with its active dendrites, adaptive morphology, and tens of thousands of synapses, is simply unknown. Complicated as pyramidal neurons (and other neurons) may

be, their axons are comparatively simple. Ultimately, the orchestra of somatodendritic currents produces one-dimensional output—in the form of action potentials (spikes)—which the axon conveys to other neurons.

Axonal spiking patterns are much easier to understand since, unlike the activity in the dendrites, APs can be observed at a single point, distal to the soma. Patterns of action potentials can be classified without understanding the biological events that give rise to them [26].

Although neurons send action potentials down their axons, there is no claim here that axonal action potentials are the sole form of output neurons generate. For example, grey matter in the cerebral cortex includes dendro-dendritic synapses, which may allow an entirely separate level of computation that is independent of the axon.

The spiking patterns that we will seek to describe in this section correspond to action potentials rather than the spatiotemporal patterns of dendritic computation. In the CLS model, we observe quiescence, spontaneous bursting, and spontaneous tonic spiking. Dynamical systems theory can describe these patterns and classify the transitions (bifurcations) that occur as the model switches from one spiking pattern to another.

It is necessary to introduce some notation—in particular, the meaning of filled (•) and open (○) circles, which indicate stable and unstable equilibria (respectively) in phase space. Consider a one-dimensional dynamical system:

$$\dot{V} = F(V), \tag{4.2}$$

A fixed point in a one-dimensional system is any point where $F(V) = 0$.

where $\dot{V}$ denotes the derivative of V with respect to time, and $F(V)$ is sketched in Figure 4.5. At both fixed points (equilibria) in that figure $F(V) = 0$, by definition.

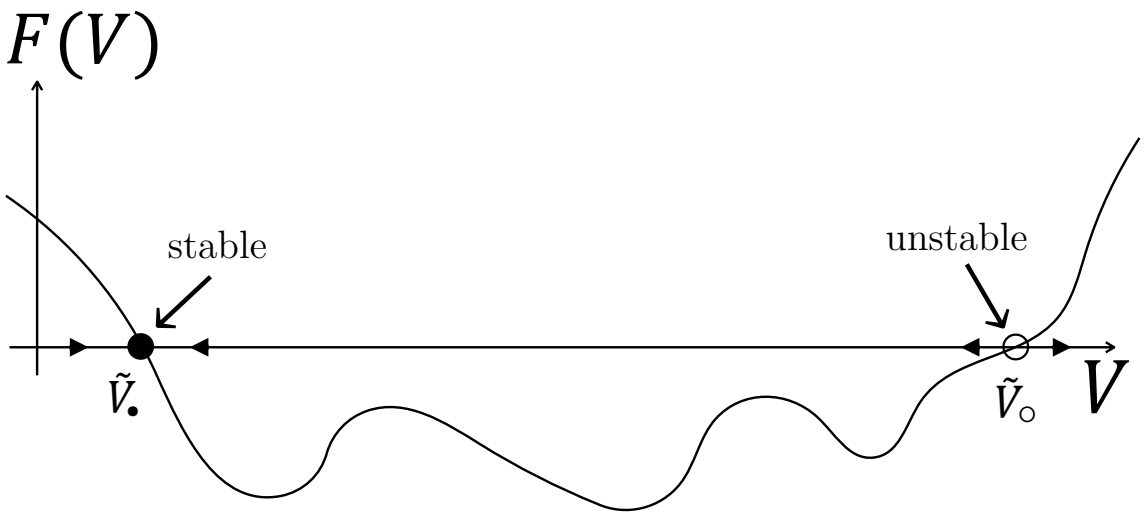

Figure 4.5: **Phase portrait of a one-dimensional dynamical system with one stable (•) and one unstable (○) fixed point.**

The fixed point (•) on the left in Figure 4.5 is a *stable equilibrium* since, nearby that point, when $V < \tilde{V}_\bullet$, $\overset{\dot{V}}{\widehat{F(V)}}$ is positive (V is increasing toward the fixed point), and likewise, when $V > \tilde{V}_\bullet$, $F(V)$ is negative (V is decreasing and moves toward the fixed point).

Conversely, the only way for the system to stay at the fixed point (○) on the right is to begin exactly at $V = \tilde{V}_\circ$. This fixed point is an *unstable equilibrium* since, in the vicinity of the point, $F(V)$ is negative when $V < \tilde{V}_\circ$ and positive when $V > \tilde{V}_\circ$ (V is moving away from ○ whenever $V \neq \tilde{V}_\circ$).

The above can be summarized as follows: In a one-dimensional dynamical system, a fixed point $\tilde{V}$ is stable if $\frac{d}{dV}F(V)\Big|_{V=\tilde{V}} < 0$. At this point, Izhikevich [26] introduces eigenvalues, not because it is necessary for the one-dimensional case, but because eigenvalues will be used to evaluate the stability of equilibria in two-dimensional (and higher) dynamical systems. In one-dimensional systems, we can write the eigenvalue λ at a fixed point as the slope

$$\lambda = \frac{d}{dV}F(V)\Big|_{V=\tilde{V}}. \tag{4.3}$$

If λ is negative, the fixed point is stable (see Figure 4.5).

Ectopic spiking such as tonic firing manifests in the phase plane as a *limit cycle*. One-dimensional systems on the real axis ($V \in \mathbb{R}$) cannot produce limit cycles (spiking), so we will need to look at two-dimensional dynamical systems and their equilibria.

A limit cycle is an isolated closed periodic orbit in the phase plane.

A two-dimensional dynamical system can be written as

$$\begin{cases} \dot{x} = f(x, y) \\ \dot{y} = g(x, y), \end{cases} \tag{4.4}$$

For example, in the Morris-Lecar model, the phase plane (phase space) is the (V, n)–plane, and we would write:
$\begin{cases} \dot{V} = f(V, n) \\ \dot{n} = g(V, n). \end{cases}$

where $\dot{x}$ is the time-derivative of x. The phase space is the xy–plane, trajectories are solutions $\big(x(t), y(t)\big)$ and the velocity vector at a given point $(x_1, y_1) = \big(x(t_1), y(t_1)\big)$ along a trajectory is $\big(f(x_1, y_1), g(x_1, y_1)\big)$.

That last point deserves some emphasis: at every point in the phase plane, the velocity (and therefore the direction) of the time-evolution of the model is uniquely determined by the coordinates (x, y) via the functions $f(x, y)$ and $g(x, y)$. The functions f and g describe a vector field $\vec{F}(x, y) = f(x, y)\hat{x} + g(x, y)\hat{y}$ in the phase plane, and trajectories that are solutions of the system (Equation (4.4)) are tangent to $\vec{F}$.

Equilibria (fixed points) are found by computing the nullclines of the system—i.e. the two curves defined by $\underbrace{\dot{x} = 0}_{f=0}$ and $\underbrace{\dot{y} = 0}_{g=0}$—and finding points where they intersect ($\dot{x} = \dot{y} = 0$). The equilibria can be classified, and their stability determined, via the eigenvalues (λ_1, λ_2) of the *Jacobian* matrix M, which must be computed at each fixed point $(\tilde{x}, \tilde{y})$:

$$M(\tilde{x},\tilde{y}) = \left.\begin{pmatrix} \frac{\partial f}{\partial x} & \frac{\partial f}{\partial y} \\ \frac{\partial g}{\partial x} & \frac{\partial g}{\partial y} \end{pmatrix}\right|_{\substack{x=\tilde{x} \\ y=\tilde{y}}} \begin{cases} \lambda_{1,2} = \frac{1}{2}\left(\tau \pm \sqrt{\tau^2 - 4\Delta}\right) \\ \underbrace{\tau = (\lambda_1 + \lambda_2)}_{\text{trace of } M}, \quad \underbrace{\Delta = \lambda_1\lambda_2}_{\text{determinant of } M} \end{cases}. \tag{4.5}$$

$$\begin{cases} \lambda_1, \lambda_2 \in \mathbb{R} \text{ and } \lambda_1 \times \lambda_2 < 0 & \longleftarrow \text{saddle} \\ \lambda_1, \lambda_2 \in \mathbb{R} \text{ and } \lambda_1 \times \lambda_2 > 0 & \longleftarrow \text{node} \\ \lambda_2 = \lambda_1^* & \longleftarrow \text{focus (spiral).} \end{cases} \tag{4.6}$$

In 2-D systems, equilibria can exhibit a rotational component, which occurs when the eigenvalues of the Jacobian have a nonzero imaginary part: $\Im(\lambda) \neq 0$. The equilibria listed in Equation (4.6) are stable if $\Re(\lambda_1), \Re(\lambda_2) < 0$. A detailed introduction to dynamical systems theory can be found in Izhikevich [26, Chapters 3 and 4] and Strogatz [54].

4.3.3 Bifurcations of nodes and limit cycles

In dynamical systems theory, a bifurcation occurs when the variation of some parameter produces a qualitative change in the system's phase portrait. A parameter that can effect such a change is called a *bifurcation parameter*. In the CLS model, the *left-shift* (LS) of the voltage-gated sodium channel (Na_V) activation and availability kinetics can serve as a bifurcation parameter with AC—the proportion of **a**ffected **c**hannels—held constant (see Fig. 2(J-K-L) in [58]).

Limit cycles are (isolated) periodic solutions to Equation (4.4), such that $\big(x(t + T_{lc}), y(t+T_{lc})\big) = \big(x(t), y(t)\big)$, where T_{lc} is the period of the oscillation. They appear as a result of bifurcations wherein a stable equilibrium point becomes unstable in response to the variation of one or more parameters in the dynamical system. The

tonic spiking exhibited by the CLS model above a certain value of I_{MaxPump} is an example of a limit cycle (see Fig. 3(D) [58]).

4.3.4 Hopf bifurcation

Hopf bifurcations—which describe the onset of tonic firing and bursts in the CLS model—are characterized by the emergence or vanishing of a limit cycle. In a Hopf bifurcation, the system begins with a pair of complex-conjugate eigenvalues,

$$\lambda_2 = \lambda_1^*, \tag{4.7}$$

that is,

$$\begin{cases} \Re(\lambda_1) = \Re(\lambda_2) = \mu, \\ \Im(\lambda_2) = -\Im(\lambda_1) = \pm i\omega. \end{cases} \tag{4.8}$$

The λ's are computed from the local Jacobian (Equation (4.5)) near the bifurcation, which occurs at $\mu = 0$. When crossing this bifurcation, the real parts of the Jacobian's complex-conjugate eigenvalues vanish—that is, the eigenvalues become purely imaginary $(\lambda_1, \lambda_2) \longrightarrow \big(\Im(\lambda_1), \Im(\lambda_2)\big)$—and then the real parts change sign (see Equation (4.6)).

Having introduced stable and unstable fixed points in one-dimensional systems (see Figure 4.5), the same notation is extended below in Figure 4.6 and Figure 4.7 to depict (respectively) a *supercritical* and a *subcritical* Hopf bifurcation in a two-dimensional dynamical system: Filled circles (•) and open circles (○) indicate (respectively) stable and unstable equilibria. The closed-loop trajectories drawn with a solid line are stable limit cycles (attractors), and the loops drawn with a dashed line are unstable limit cycles (repellers).

4.3.5 Supercritical Hopf bifurcation

A supercritical Hopf bifurcation is a soft transition where the amplitude of the new limit cycle can be arbitrarily small, growing (when near the bifurcation) as the square root of the system's distance from the bifurcation point (HB) when the bifurcation parameter is just above HB.

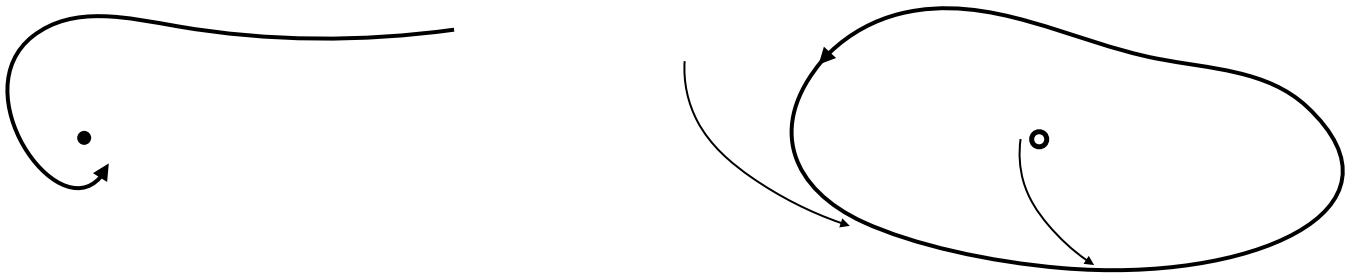

Figure 4.6: **Phase portrait of a supercritical Andronov-Hopf bifurcation.** This is the bifurcation that occurs at the point marked "HB" on the right in Fig. 2(L) of Yu, Morris, Joós, and Longtin [58], wherein *LS* is the bifurcation parameter, and in Fig. 3(D) of the same paper, which uses I_{MaxPump} as a bifurcation parameter. (Graphic inspired by Figure 1.12 of Izhikevich [26].)

4.3.6 Subcritical Hopf bifurcation

The subcritical Hopf bifurcation is an **abrupt transition**, where a finite-amplitude limit cycle appears suddenly rather than the amplitude increasing smoothly from zero, as in the supercritical case.

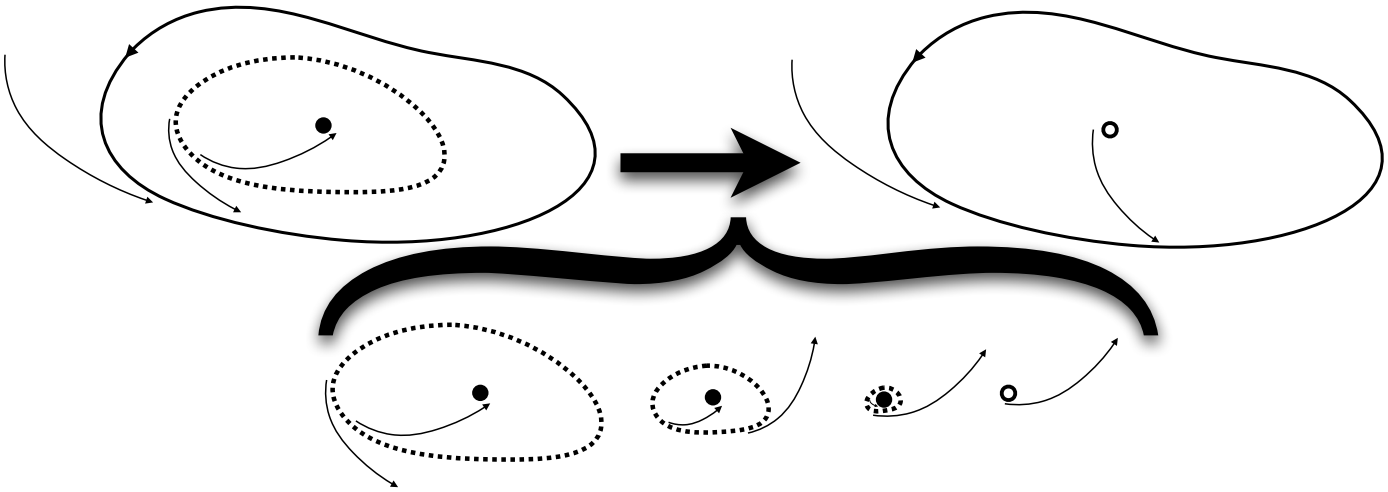

Figure 4.7: **Phase portrait of a subcritical Andronov-Hopf bifurcation.** This is the bifurcation that occurs at the points marked "HB" in the *CLS* model with Na^+/K^+–pumps, shown in Fig. 7 of [28] (included on page #298). This phase portrait sketch would be perpendicular to the screen in those bifurcation diagrams. Moving left to right in the sketch above, one can see why a subcritical Hopf bifurcation is abrupt: Once the formerly stable node becomes a repeller due to the unstable limit cycle collapsing onto it, the system must "'jump" to the stable limit cycle.

In the **upper-left** of Figure 4.7, the system is *bistable*, having a stable fixed point (•) encircled by a stable limit cycle (attractor) at the outside with an unstable limit cycle (repeller) sandwiched between the two. On the other side of the bifurcation (**upper-right**), the system has left the bistability regime and now has only a stable (spiking) limit cycle. **Below the overbrace**, the shrinking amplitude of the inner unstable limit cycle is depicted as it collapses onto the stable fixed point during the bifurcation, leaving behind an unstable fixed point. (Graphic inspired by Figure 1.12 of Izhikevich [26].)

4.3.7 Bifurcations observed in the *CLS* model

In the bifurcation diagrams of the *CLS* (Coupled Left-Shift) model with pumps—Fig. 7 of Joós, Barlow, and Morris [28] on page #298 in Appendices, originally Fig. 5 of Yu, Morris, Joós, and Longtin [58]—the three-dimensional burst trajectory (Fig. 7A) is mapped onto a two-dimensional cross-section with E_{Na^+} as the control parameter. Filled circles indicate where the stable limit cycle pierces the cross section (Figs. 7B and 7C) and open circles correspond to unstable limit cycles in the same manner.

At the onset of bursting, the bifurcation diagram includes a textbook example of a subcritical Hopf bifurcation and fold of limit cycles[2] (Fig. 7B). By the end of the burst ("bursting offset", Fig. 7C), the Nernst potentials (E_{Na^+}, E_{K^+}) have diminished, and the phase portrait has changed considerably.

Through their bifurcation analysis, Yu et al. [58] demonstrated that the maximal pump current induces a supercritical Hopf bifurcation in the *CLS* model. If concentrations, and therefore Nernst potentials, are held fixed—meaning no slowly oscillating state due to the homeostatic electrogenic pump current interacting with the membrane current—tonic spiking also results from a subcritical Hopf bifurcation when *LS* is the control parameter.

They found that bursting (Figure 4.8, below) results from slow oscillations in the sodium and potassium Nernst potentials—limited by the intracellular sodium and extracellular potassium concentrations' response to the pump and voltage-gated ion currents—which create a dynamic threshold, driving the model back and forth across a subcritical Hopf bifurcation. The bursting begins with a Hopf bifurcation into tonic spiking, and the homeostatic response drives the system back down into a resting state.

[2] also called a saddle-node of limit cycles

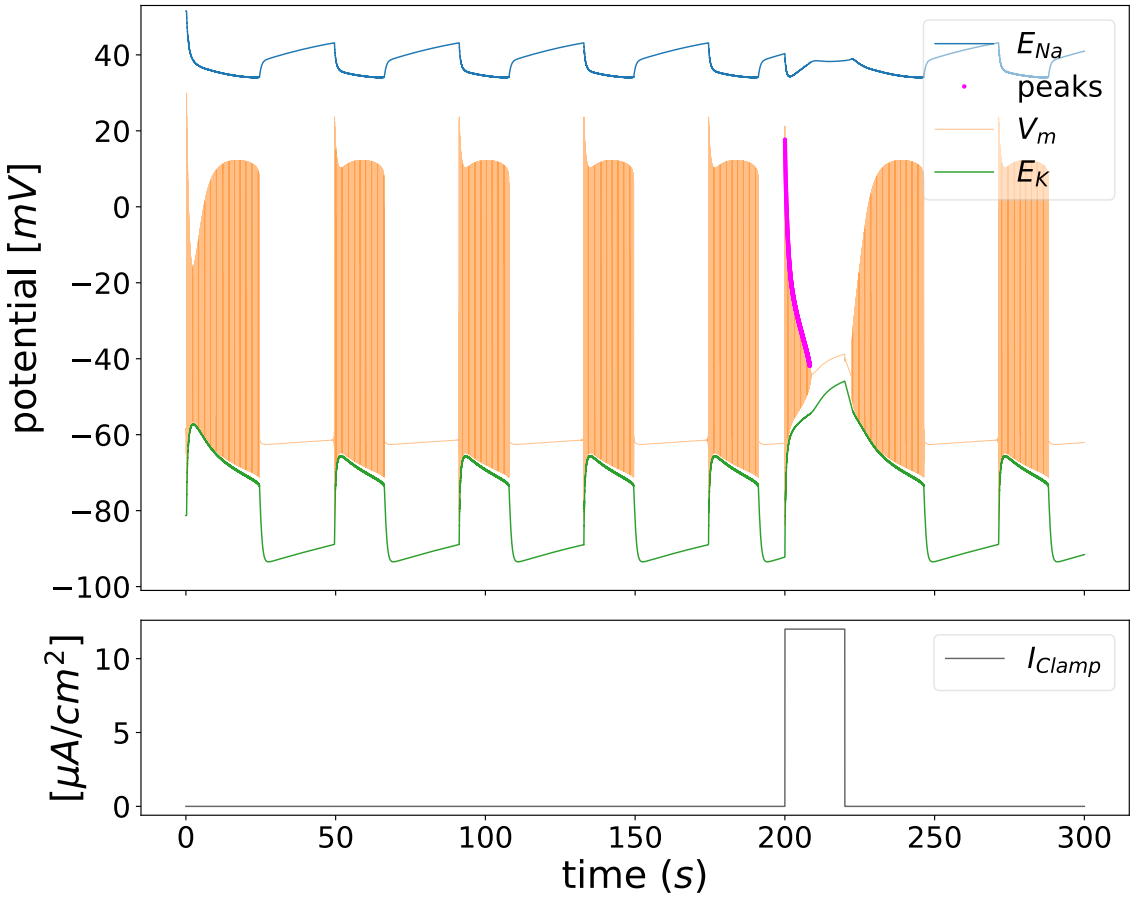

Figure 4.8: — **Hyperexcitable: $LS = 3.0\text{mV}$, $AC = 1$ – spontaneous bursting in the CLS model.** The damage parameters—or CLS coordinates in Figure 4.4—are $(AC, LS) = (1, 3.0\text{mV})$. The burst cycle is robust to perturbations by injected current, resuming shortly after the end of the pulse. (See the blue regime in Figure 4.4 legended "Spontaneous Periodic Bursting".)

While the onset of bursting was characterized as a subcritical Hopf bifurcation, by the time of burst offset, the depletion of E_{Na^+} and E_{K^+}, along with concomitant changes to $[Na^+]_{in}$ and $[K^+]_{out}$, which govern I^{pump}, cause the burst-offset bifurcation to be much more complex. The precise dynamics of burst termination were not fully characterized, though there was evidence of period-doubling cascades leading to chaos.

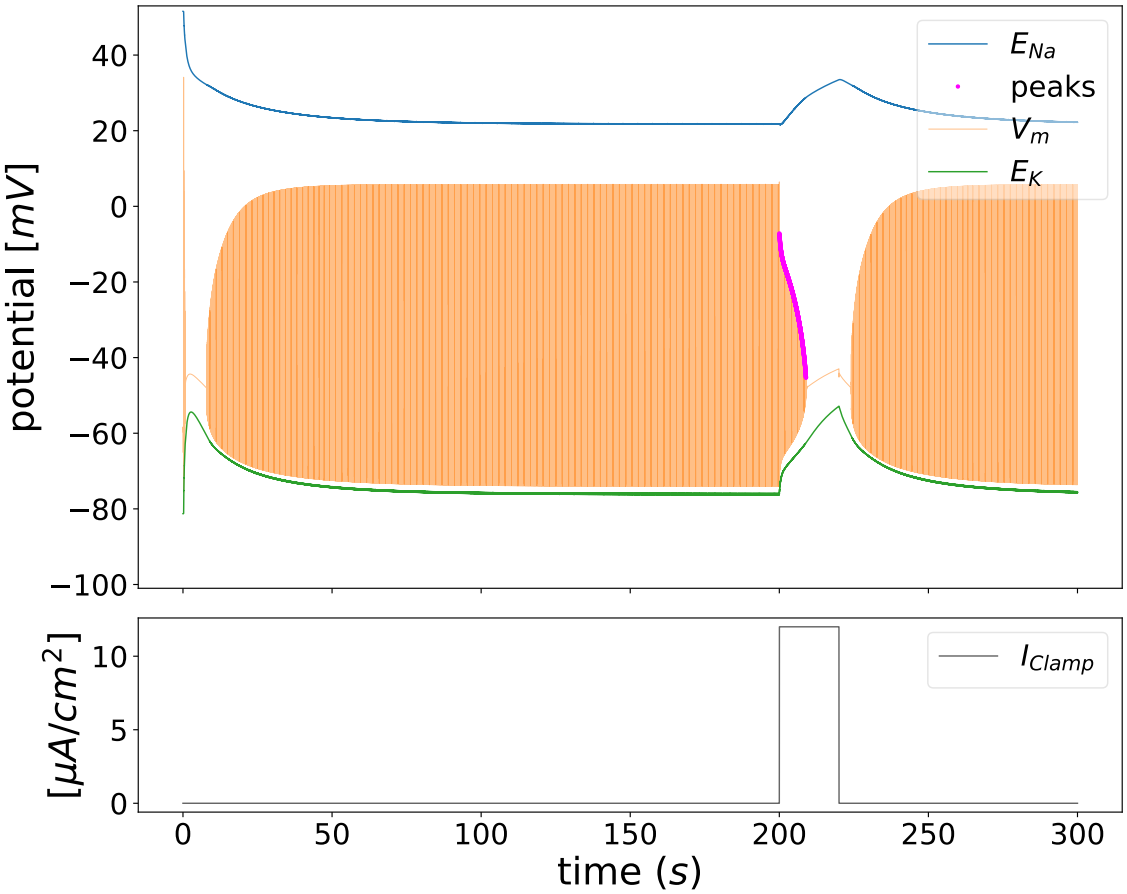

Figure 4.9: **Hyperexcitable: Spontaneous tonic firing in the *CLS* model at $LS = 10.0\text{mV}$, $AC = 1$ (see the orange regime in Figure 4.4 legended "Spontaneous Tonic Firing").** The constant ectopic spiking is interrupted by the square pulse of electrode current at $t = 200\text{ms}$ (lower plot).

During tonic firing (Figure 4.9) and in quiescent states, a balance is achieved between the electrodiffusion-driven transmembrane currents—Na^+ and K^+ ions traversing the membrane through open voltage-gated channels and leaks—and the Na^+/K^+ pump

current (active transport). During bursting, no such cycle-to-cycle balance between the two ion flows occurs. Instead, the system oscillates back and forth across a subcritical Hopf bifurcation (defined in Section 4.3.6). With bursting, balance is achieved on the timescale of the burst frequency, which is much slower than the spiking frequency in tonic firing or inside a burst.

As demonstrated below in Figure 4.12 (Section 4.3.8), the oscillation of the sodium concentrations (and therefore E_{Na^+}) is sufficient to achieve bursting. The dynamics in that figure are similar to the bifurcation diagram with fixed E_{K^+} in Fig. 7B of Joós et al. [28] (originally in [58]), which closely resembles a "sub-Hopf/fold cycle" bifurcation (see [26]). The ***fold*** bifurcation is also known as a ***saddle-node of limit cycles*** [54].

Figure 4.12 is unphysical because the sodium and potassium ions share the same intracellular and extracellular space, and their concentrations are similarly sensitive to their respective transmembrane currents. Fig. 7C [28] on page#298 (originally Fig. 5C in [58]) demonstrates that, as all inner and outer concentrations oscillate during the burst, the variation in E_{K^+} (simultaneous with E_{Na^+}) significantly complicates the phase diagram at the offset of bursting.

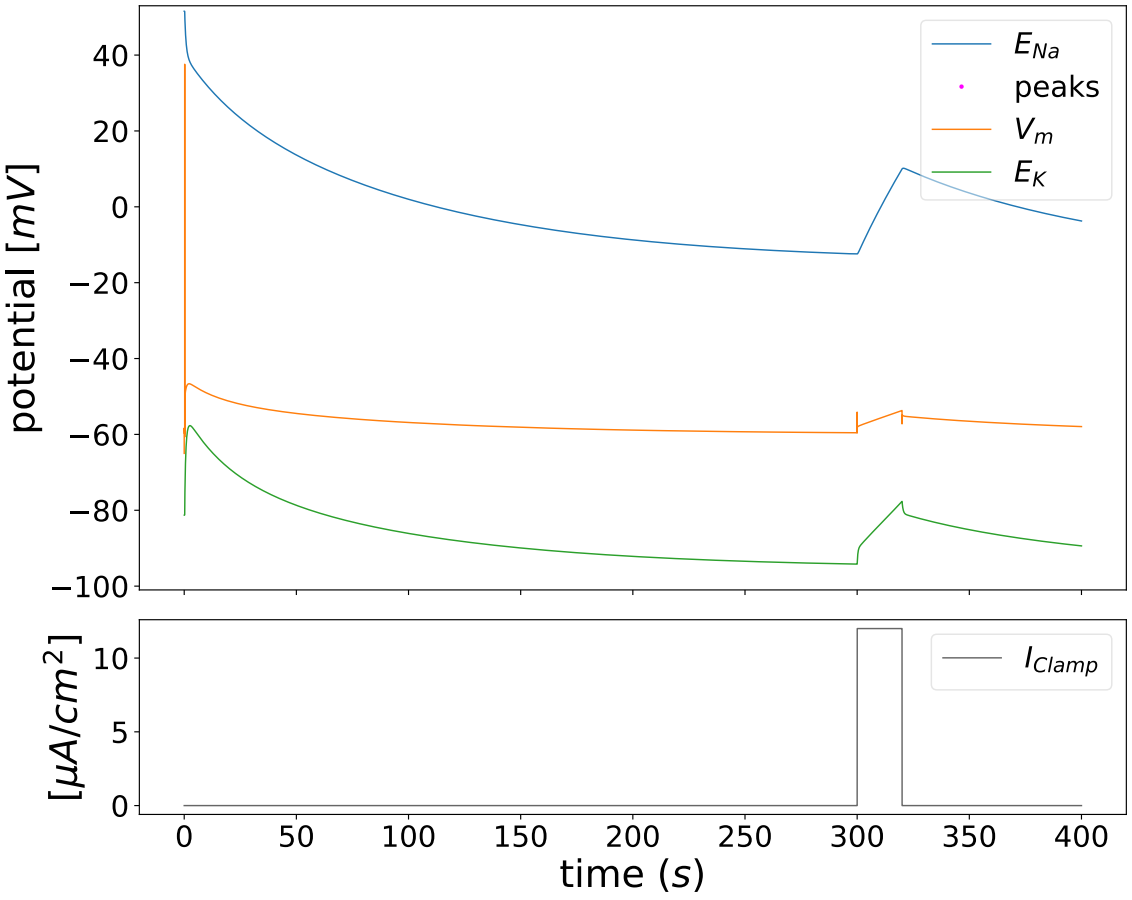

Figure 4.10: **Inexcitable: Response to *intense* stimulation when the neuron has been rendered *inexcitable* by severe CLS damage ($LS = 26$mV, $AC = 1$).** The stimulating current density (lower plot) is $I_{\text{stim}} = 12.0\mu\text{A} / \text{cm}^2$. **Compare with Figure 4.2**, in which a much weaker current pulse ($1.0\mu\text{A} / \text{cm}^2$) was injected, and the CLS damage was comparatively mild. This configuration of the model maps to the purple region just above the yellow (spontaneous mini-bursts) regime on the right-hand side of Figure 4.4.

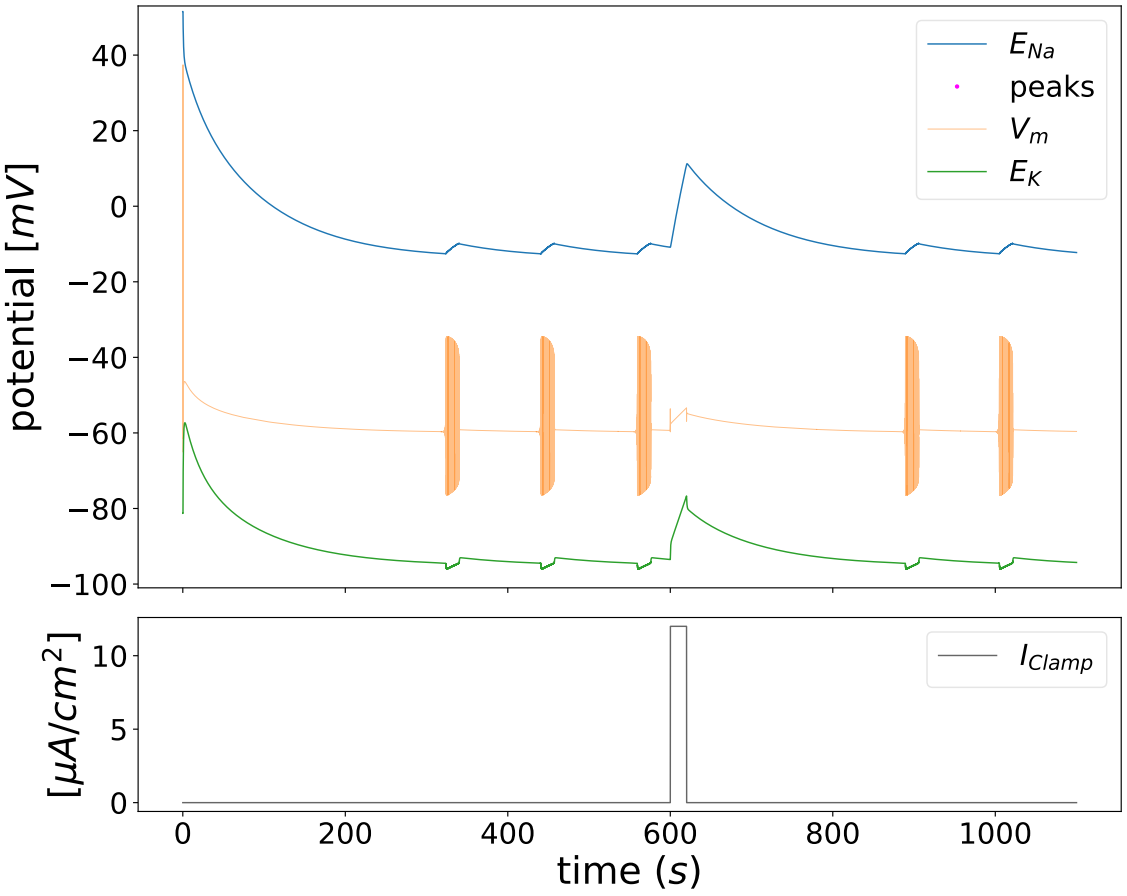

Figure 4.11: **Hyperexcitable: Spontaneous mini-bursts in the CLS model.** The damage parameters—or (AC, LS) coordinates in Figure 4.4—are $(AC = 1, LS = 25.0\text{mV})$. Mini-bursts are robust to perturbations, as demonstrated by the resumption of the pattern following a current pulse at 600s.

4.3.8 Bursting with fixed E_{K^+}

Interestingly, the CLS model is able to burst when the potassium concentrations and E_{K^+} are held fixed, with sodium allowed to fluctuate as before (Figure 4.12). The bifurcation diagram in Fig. 7B of Joós et al. [28] (originally [58]) corresponds to this form of bursting.

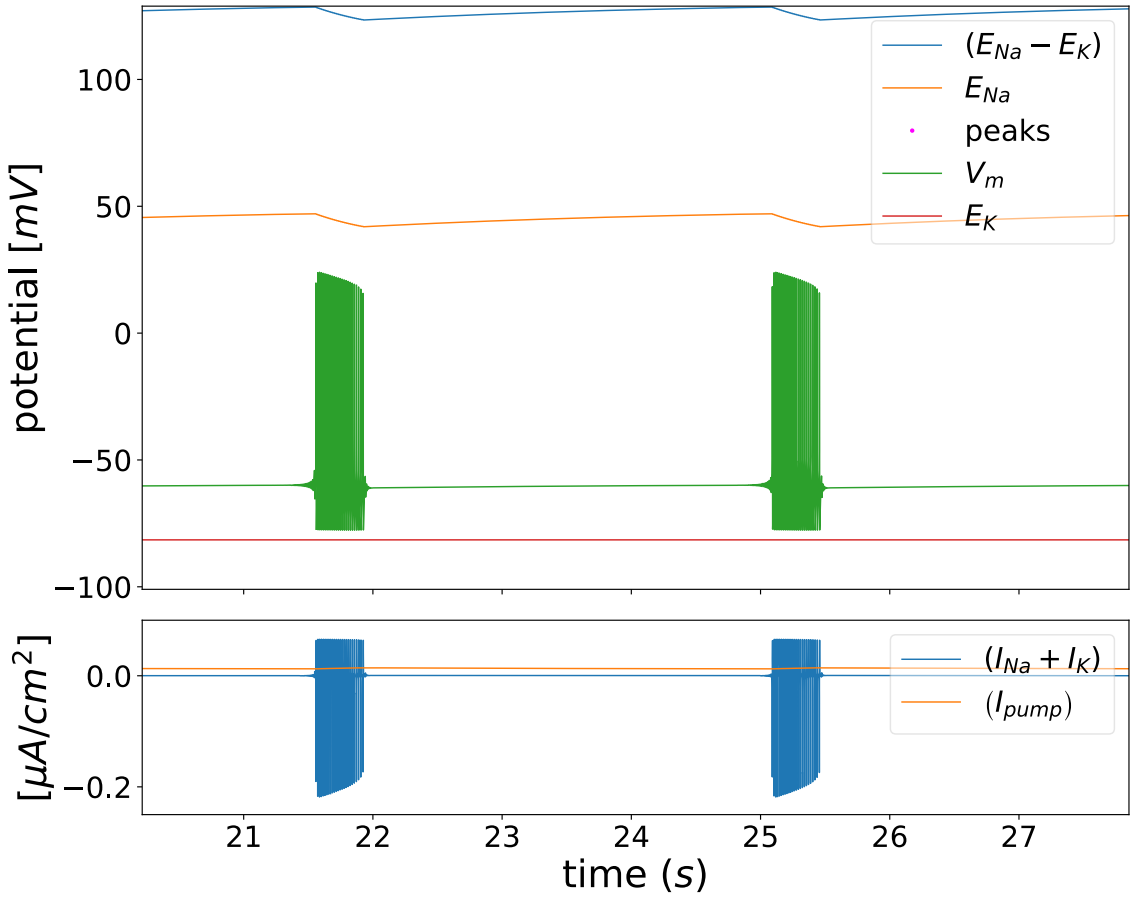

Figure 4.12: **Hyperexcitable: Bursting persists when the potassium concentrations (and therefore E_{K^+}) are held fixed.**

Conversely, when sodium concentrations and E_{Na^+} are held fixed with potassium dynamics unaltered, bursting (and spiking) cease, and *LS* damage merely depletes the potassium concentration gradient and E_{K^+}.

4.3.9 Bursting with simplified pump dynamics

The specific Michaelis-Menten style pump current in the *CLS* model (expressed in Equations 3.45 and 3.46) is *not* required to generate the ectopic bursting and tonic spiking patterns. It captures the rate-limited enzymatic nature of the Na^+/K^+ pump current and its saturation at high ion concentrations, but even with simplified pumps which *fail to saturate*, e.g.

$$I_{\text{crude}}^{\text{pump}} = I_{\text{MM}}^{\text{pump}}\Big|_{V_{\text{rest}}} \times \left(\frac{[\text{Na}^+]_{\text{in}}}{[\text{Na}^+]_{\text{in}}^{\text{rest}}}\right)\left(\frac{[\text{K}^+]_{\text{out}}}{[\text{K}^+]_{\text{out}}^{\text{rest}}}\right), \tag{4.9}$$

The subscript "MM" is added to I_{MM}^{pump} in Equations 4.9 and 4.10 to denote the Michaelis-Menten pump current (Equation (3.45)) at resting ion concentrations with LS = 0 mV.

or

$$I_{\text{linear}}^{\text{pump}} = I_{\text{MM}}^{\text{pump}}\Big|_{V_{\text{rest}}} \times \frac{1}{2}\left(\frac{[\text{Na}^+]_{\text{in}}}{[\text{Na}^+]_{\text{in}}^{\text{rest}}} + \frac{[\text{K}^+]_{\text{out}}}{[\text{K}^+]_{\text{out}}^{\text{rest}}}\right), \tag{4.10}$$

the *CLS* model [28] exhibits the bifurcations from quiescent (hypersensitive) to spontaneous periodic bursting (Figure 4.13), and from bursting to spontaneous tonic spiking (Figure 4.14).

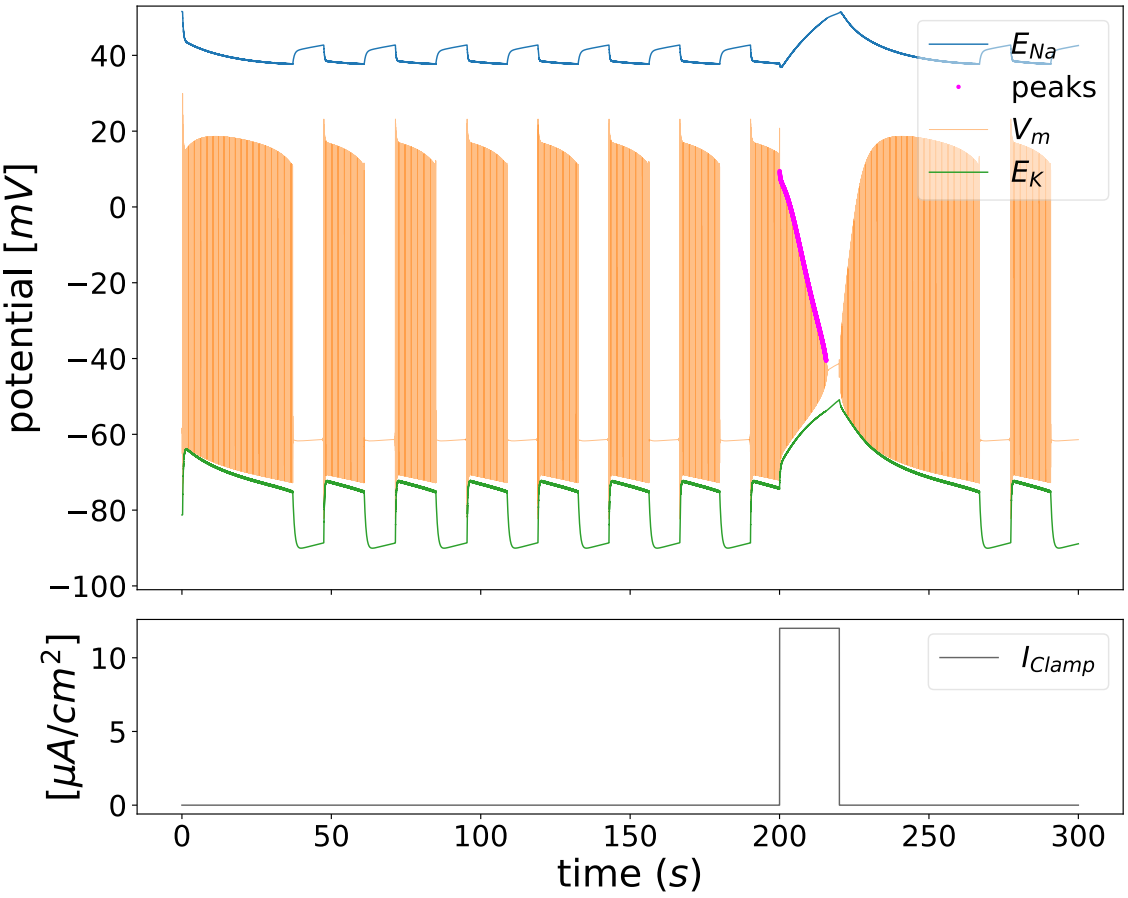

Figure 4.13: **Spontaneous periodic bursting in the CLS model with simplified Na^+/K^+ pump from Equation (4.9).** Compare with Figure 4.8, which uses Michaelis-Menten pump kinetics. The damage parameters—or CLS coordinates in Figure 4.4—are $LS = 3.0\text{mV}$, $AC = 1$. Note that the modified pump will likely distort the boundaries in the regime diagram, however we do not have such a map for this system.

Miniature copy of Figure 4.8:

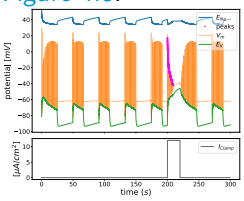

Full-size figure on page# 117.

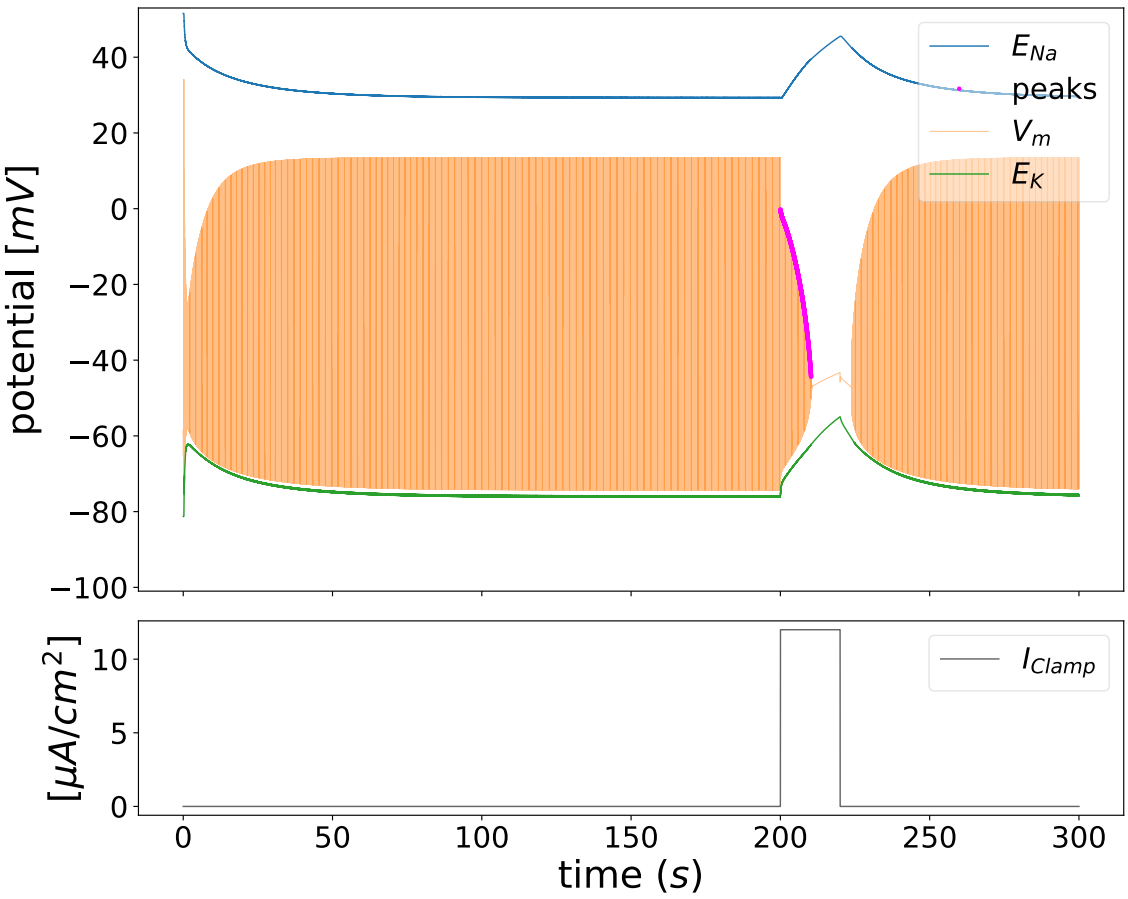

Figure 4.14: **Spontaneous tonic firing in the CLS model with simplified Na^+/K^+ pump from Equation (4.9).** The CLS-damage parameters are $LS = 10.0\text{mV}$ and $AC = 1$. Compare with Figure 4.9, which uses Michaelis-Menten pump kinetics.

Miniature copy of Figure 4.9:

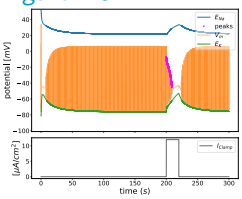

Full-size figure on page# 118.

Chapter 4 Synthesis

The Coupled *Left-shift* (*CLS*) model captures injury-induced hypersensitivity and hyperexcitability via experimentally observed changes in the gating properties of Na_V channels in damaged cell membranes Wang et al. [56], Boucher et al. [8] (see Figure 4.1 and Section 4.2). The parameter *LS* ("*left-shift*" in mV) is the hyperpolarizing shift of injured Na_Vs' *activation* and *availability*, and *AC* corresponds to the fraction of sodium channels that are damaged.

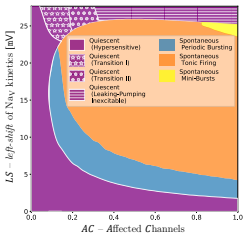

Miniature version of the CLS regime diagram from Figure 4.4 on page# 107.

CLS induces high-frequency ectopic discharge, initially manifesting as periodic bursts of action potentials, followed by tonic firing. In all the *LS*-versus-*AC* plots, the lower ectopic boundary is where a previously quiescent, hypersensitive node abruptly begins emitting repeated trains of self-triggered action potentials, forming characteristic bursting patterns (Figure 4.15).

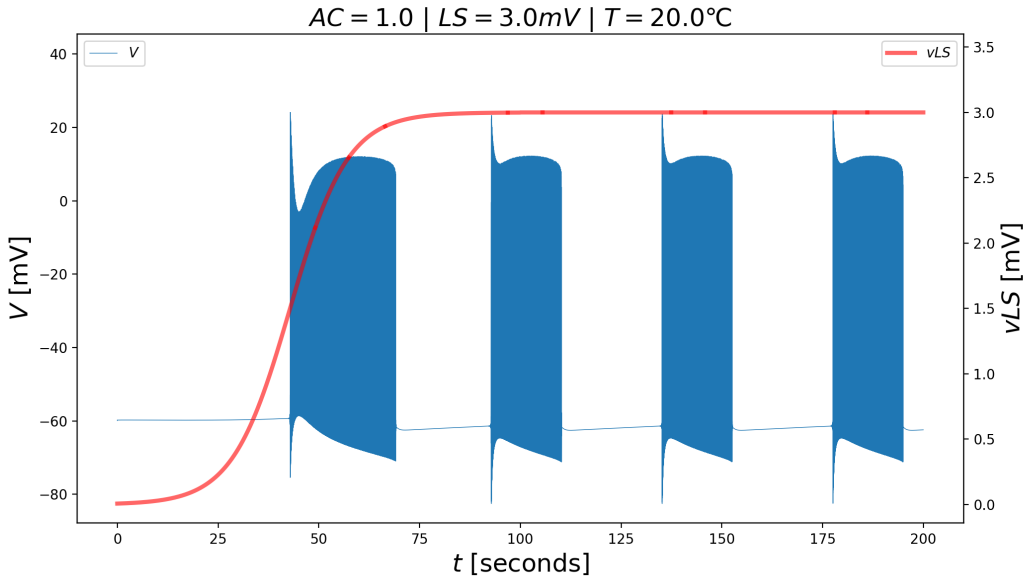

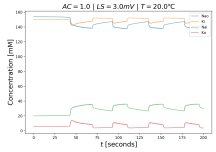

Intracellular and extracellular Na^+ and K^+ concentrations fluctuate in response to the ectopic burst currents, showing the load on the Na^+/K^+ pumps.

Figure 4.15: **Onset of bursting in the *CLS* model with ramped *left-shift*.** In this simulation, all Na_V channels in the node were *left-shift*ed (AC =1.0).

As the system travels upward through the bursting regime in the (LS, AC)–plane, burst duration increases while the inter-burst intervals (IBIs) shorten. Consequently, the neuron spends ever less time in a quiescent or *subthreshold* oscillatory state between high-frequency bursts, culminating in a transition to sustained tonic firing.

As LS increases toward the bursting-to-tonic firing boundary, the bursts continue to lengthen and the IBIs eventually vanish, leaving an unbroken stream of action potentials. The firing frequency during tonic firing at maximum *left-shift* [56] is approximately double the natural frequency of the intact node ($\sim$ 70Hz) near its threshold for bursting Boucher, Joós, and Morris 2012 [8].

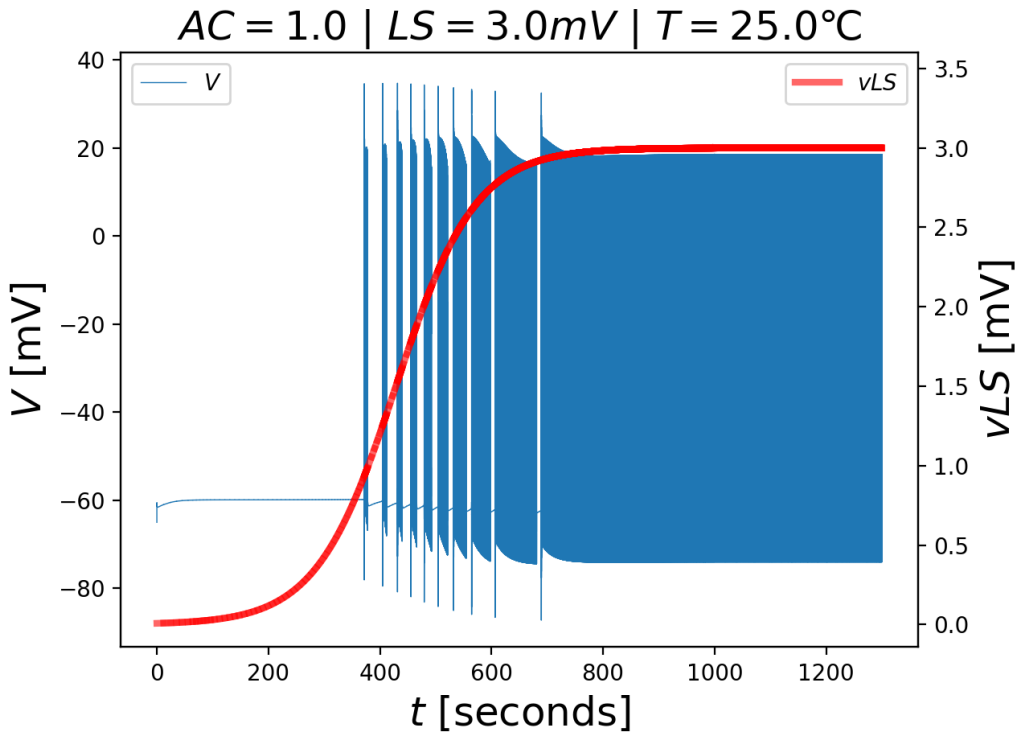

Figure 4.16: **The transition to tonic firing with a slowly ramped *left-shift* LS = 3.0mV.** In this simulation, all Na_V channels in the node were *left-shift*ed (AC =1.0).

Through large batches of simulations like those in Figures 4.15 and 4.16, we traced the LS-voltage threshold of spontaneous pathological bursting and tonic firing as a function of the relative density of damaged channels (AC). The quiescent-to-bursting and bursting-to-tonic thresholds (or, 'ectopic boundaries') are shown below in Figure 4.17.

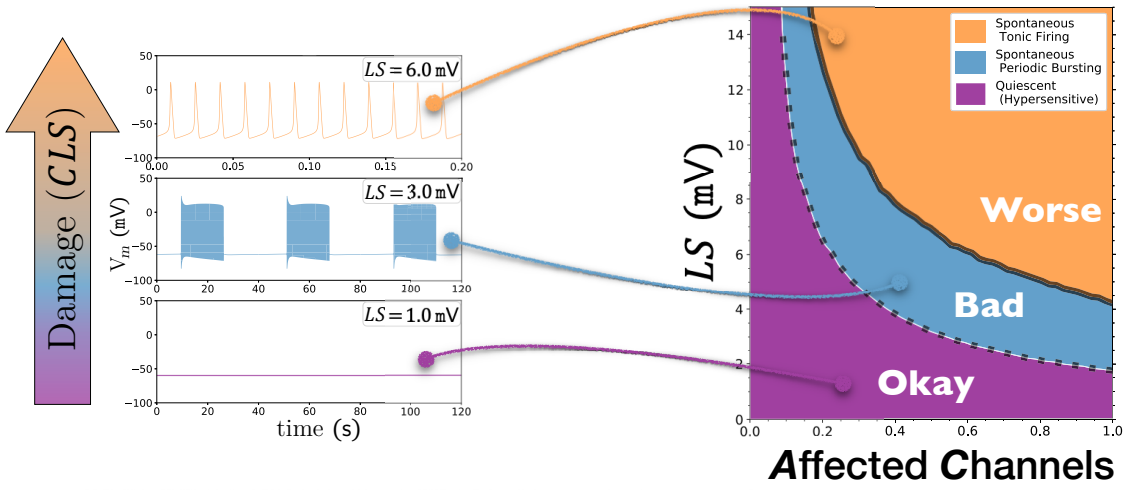

Figure 4.17: Ectopic boundaries in the regime diagram of the *CLS* model with active transport (i.e. Na^+/K pumping and explicit intra- and extracellular ion concentrations[28]). Note the **shorter timescale** on the abscissa) top-left plot. Full diagram in Figure 4.4.

The full regime diagram of the *CLS* model is given in Figure 4.4 (page#107), however, in Figure 4.17 (above) we focus on the bursting and tonic thresholds since they take center stage in Chapter 5. As the reader may have noticed, the simulations in Figures 4.15 and 4.16 had identical *LS* and *AC* yet in the former we see periodic spontaneous bursting, and in the latter, spontaneous tonic firing. The difference between these simulation runs is *temperature*, which is the topic of the next paper Chapter 5.

Chapter 5

Cooling reverses pathological bifurcations to spontaneous firing caused by mild traumatic injury

This paper was featured as an Editor's Pick in *'Chaos: An Interdisciplinary Journal of Nonlinear Science'* (Barlow, Joós, Trinh, and Longtin [2]).

5.1 Statement of originality and contributions

I co-wrote the text of this paper with my supervisors, Professors Joós and Longtin. Prof. Longtin drafted the Introduction, and the three of us spent many hours completing the manuscript in Prof. Joós' office, sometimes running simulations on demand when we hit a snag in our interpretation of the results.

I designed and wrote the model code, performed the simulations, analyzed the data, and created all figures. This project gained inertia when I realized that we could use the CLS model to search for temperature-induced changes in the regime diagram (Figure 4.4). The first question became: Would the lower boundary in Figure 4.4—which separates the quiescent/hypersensitive regime from the spontaneous bursting regime in the (AC, LS) plane—move when the neuron was cooled or heated within physiological limits?

The CLS and Temperature model ("T-CLS" model) is discussed below in the paper (Barlow, Joós, Trinh, and Longtin [2]).

5.2 Introduction: *CLS* and *T*emperature (*T-CLS*)

Whereas the *CLS* model was used to investigate pathological firing patterns (ectopic action potentials) in damaged neurons, in this paper, we approached the matter from a therapeutic perspective: If damage has occurred, what might be the beneficial (or detrimental) effects of temperature changes?

Inflammation often accompanies neurological injury, and with it, temperature tends to increase in the damaged tissue. It is also possible to lower the body temperature of a patient who has suffered a stroke or other CNS trauma. The *CLS* model, being a lucid and empirically justified model of injury, may provide some insight into whether and how cooling can protect neurons from succumbing to excitotoxic processes that exacerbate the initial mechanical trauma and ischemia. Perhaps cooling could give the injured cells time to replace their damaged Na_V channels by temporarily raising their ectopic spiking threshold.

In the *T-CLS* model, temperature sensitivity is added to the *CLS* model via four "Q_{10}" factors (Q_{gate}, Q_{Na^+}, Q_{K^+}, Q_{pump}), see Table 5.1. The subscript "10" refers to a 10℃ temperature change. For example, Q_{Na^+} multiplies the maximal sodium conductance density ($\bar{g}_{Na_V}$) as follows:

$$\bar{g}_{Na_V} \longrightarrow \bar{g}_{Na_V} \times Q_{\text{Na}^+}^{(T-T_{\text{ref}})/10℃}. \tag{5.1}$$

That is, the sodium conductance increases by the factor Q_{Na^+} when the temperature is increased to 10℃ above the 'reference temperature' T_{ref}, and decreases by a factor of $\left(\frac{1}{Q_{\text{Na}^+}}\right)$ when the temperature is decreased to 10℃ below T_{ref}. The Q_{10}'s have no effect when $T = T_{\text{ref}}$.

Parameter	Name	Multiplies
Q_{10} for the kinetic constants	$Q_{\text{gate}} = 3.0$	$\left(\frac{dm}{dt}\right), \left(\frac{dh}{dt}\right), \left(\frac{dn}{dt}\right)$
Q_{10} for the Na_V conductance	$Q_{\text{Na}^+} = 1.4$	$\bar{g}_{Na_V}$
Q_{10} for the K_V conductance	$Q_{\text{K}^+} = 1.1$	$\bar{g}_{K_V}$
Q_{10} for the Na^+/K^+-pump	$Q_{\text{pump}} = 1.9$	I_{maxpump}

Table 5.1: **Q_{10} parameters add temperature sensitivity to the CLS model, and the letter "T" for temperature in "T-CLS".** See TABLE 1 below in Barlow, Joós, Trinh, and Longtin [2].

After including temperature sensitivity in the CLS model code, I ran the necessary batches of simulations and retraced the quiescent-to-bursting curve in (AC, LS) coordinates at two new temperatures. Indeed, the curve moved: When I increased the temperature, spontaneous bursting began at a lower damage threshold, compared to the CLS model without temperature effects. Likewise, the cell was more resilient to damage when cooled (the curve moved upward). Given these results, we went ahead with a systematic study of the quiescent-to-bursting and bursting-to-tonic thresholds' movement with heating and cooling.

I isolated the temperature-driven effects by modifying the CLS model to incorporate them into the channel and pump kinetics one by one—described in FIG. 4. (a) of Barlow, Joós, Trinh, and Longtin [2] below—which can only be done in a simulator. This sensitivity analysis made it possible to understand the biophysical basis for the movement of the ectopic boundaries. Although the temperature is uniform on the scale of a node of Ranvier *in situ*, the beneficial effects of cooling following injury might be reproduced using drugs or other treatments. We sought to determine *which mechanisms*, biophysically, caused cooling to raise the CLS-damage threshold for ectopic bursting (for example).

In 2019, I presented our results at the APS March Meeting (Section 0.5). In addition to the published manuscript, I added simulation code to ModelDB[1], allowing others

[1] https://modeldb.science

to instantiate the effects of *CLS* damage with temperature changes in their own models (listed in Section 0.3).

5.3 Barlow, Joós, Trinh, and Longtin (2018)

In light of recent feedback, the tick labels have been highlighted in two of the plots in Barlow et al. 2018 [2], as included in the main text below. (**Note:** The original as-published figures are included in *Appendix D | Unedited pages #3 & #5 from Barlow, Joós, Trinh, and Longtin (2018)* on page#306.)

- The highlights occur in *FIG. 1.*(a) on page#136 and *FIG. 2.*(a) on page#140—i.e. the third and seventh pages of Barlow et al. 2018, respectively.
- Both figures plot time series of the membrane potential (V_m) in three panels, however, **the timescale on the abscissa varies among the panels**. Specifically, ~ 200ms of tonic firing is shown in the top panel of *FIG. 1.*(a) and the bottom panel of *FIG. 2.*(a), whereas the other two panels in each figure span ~ 120s.
- **To help readers notice the shorter duration plotted with tonic firing, the ms–timescale tick marks have their labels highlighted in colour and use a larger font.**

Chaos

Cooling reverses pathological bifurcations to spontaneous firing caused by mild traumatic injury

Cite as: Chaos **28**, 106328 (2018); https://doi.org/10.1063/1.5040288
Submitted: 16 May 2018 . Accepted: 23 August 2018 . Published Online: 25 October 2018

B. M. Barlow, B. Joos, A. K. Trinh, and A. Longtin

CHAOS **28**, 106328 (2018)

Cooling reverses pathological bifurcations to spontaneous firing caused by mild traumatic injury

B. M. Barlow, B. Joos, A. K. Trinh, and A. Longtin
Department of Physics, Centre for Neural Dynamics, University of Ottawa, 150 Louis Pasteur Priv., Ottawa, Ontario K1N6N5, Canada

(Received 16 May 2018; accepted 23 August 2018; published online 25 October 2018)

Mild traumatic injury can modify the key sodium (Na^+) current underlying the excitability of neurons. It causes the activation and inactivation properties of this current to become shifted to more negative trans-membrane voltages. This so-called coupled left shift (CLS) leads to a chronic influx of Na^+ into the cell that eventually causes spontaneous or "ectopic" firing along the axon, even in the absence of stimuli. The bifurcations underlying this enhanced excitability have been worked out in full ionic models of this effect. Here, we present computational evidence that increased temperature T can exacerbate this pathological state. Conversely, and perhaps of clinical relevance, mild cooling is shown to move the naturally quiescent cell further away from the threshold of ectopic behavior. The origin of this stabilization-by-cooling effect is analyzed by knocking in and knocking out, one at a time, various processes thought to be T-dependent. The T-dependence of the Na^+ current, quantified by its $Q_{10\text{-}Na}$ factor, has the biggest impact on the threshold, followed by $Q_{10\text{-}pump}$ of the sodium-potassium exchanger. Below the ectopic boundary, the steady state for the gating variables and the resting potential are not modified by temperature, since our model separately tallies the Na^+ and K^+ ions including their separate leaks through the pump. When only the gating kinetics are considered, cooling is detrimental, but in the full T-dependent model, it is beneficial because the other processes dominate. Cooling decreases the pump's activity, and since the pump hyperpolarizes, less hyperpolarization should lead to more excitability and ectopic behavior. But actually the opposite happens in the full model because decreased pump activity leads to smaller gradients of Na^+ and K^+, which in turn decreases the driving force of the Na^+ current. *Published by AIP Publishing.*
https://doi.org/10.1063/1.5040288

Experimental studies have revealed that mild trauma in the form of, e.g., physical pressure or chemical stimuli can alter the properties of the main current (sodium) responsible for the voltage swings or "firings" of neurons. This leads to ongoing firings even when the cell should be quiescent. Such pathological firing interferes with the usual input integration properties of the cell, and in particular has been implicated in the genesis of pathological pain, which persists even after the injury-producing stimulus is removed. From a dynamical point of view, this mild trauma lowers the threshold for firing. This paper explores the possibility of using temperature to offset this effect by raising the firing threshold back up. Our modeling study predicts that cooling the neuron by just a few degrees—as is possible, e.g., for peripheral nerve cells—can counteract the pathological state. The sensitivity of the sodium current to temperature is the key determinant of this effect.

I. INTRODUCTION

Temperature is an important determinant of excitable behavior since it has a direct effect on the kinetics of every chemical reaction. This includes the rates of transitions between open and closed states of ionic channel proteins, as well as ionic exchangers and channel conductances. In the central nervous system (CNS), the temperature is tightly controlled to enable normal cellular function. In the peripheral nervous system, and especially in nerves near the skin surface, the temperature can vary over a greater range, according to the external temperature, and the excitability is adapted to accommodate a range of functions. In fact, specialized neurons known as thermoreceptors in the skin and elsewhere continually report a wide range of local temperatures to the CNS.

Injury in the form of a mild stretching of nerve membrane has been shown to cause a concomitant shift in the voltage-dependence of the activation and inactivation gating characteristics of sodium channels.[1] This so-called "coupled left shift" or CLS causes the cell to become more "leaky," which means that the small Na current around the resting potential of the cell is now stronger.[2] When the left shift is sufficiently strong, it can lead to repetitive firing of action potentials (APs or "spikes" or "firings") originating in the damaged section of the axon. This section then produces APs when it normally should not, i.e., it exhibits "ectopic" firing. The job of the axon is to propagate action potentials that arose at the axon initial segment just outside the soma down to target neurons, not to produce its own APs. Target cells are then continually receiving currents at their synapses from such pathologically firing cells. CLS can also affect the soma directly and interfere with its integration properties.

CLS has been modeled mathematically by a simple addition of a left shift (LS) to the voltage of the activation (m) and inactivation (h) gates for the sodium current in the standard Hodgkin-Huxley (HH) formalism.[2,3] Under fairly

generic conditions, as *LS* increases, a bifurcation first occurs from quiescence to a bursting firing pattern in which APs are arranged in clusters separated by quiescent phases. The bursting involves a rapidly firing phase, followed by a quiescent phase, and the whole pattern repeats. As *LS* increases even more, another bifurcation occurs, this time from bursting to tonic firing. At this transition, the quiescent interval between the clusters of spikes has shrunk such that only the rapidly firing "tonic" phase remains. These bifurcations are summarized in Fig. 1 for the more detailed HH model we present below. It is in fact a phase diagram illustrating the position of the tonic and bursting solutions in the two-dimensional subspace spanned by the *LS* parameter and the *AC* parameter that quantifies the fraction of channels affected by CLS.

A dynamical analysis of these solutions and their bifurcations at a single node of Ranvier was reported in Ref. 4. There, a numerical bifurcation tool was used as well as a slow-fast analysis: the fast sub-system generates the rapid limit cycle associated with the spikes during the active phase of the burst, while the dynamics of the Nernst potentials form the slow one (see Sec. II). In the context of transmission down an axon, CLS has negative consequences on information transmission, especially at low frequencies.[5] Bursting is also associated with the presence of subthreshold oscillations, which have been implicated in neuropathic pain, i.e., pain signals that outlast the injury.[6–8] In fact, it appears that the joint effect of such oscillations and noise, associated with channel conductance fluctuations and other sources of cellular stochasticity, produces firing patterns that highly resemble those seen in the context of neuropathic pain.

These "injured" ectopic dynamics set the stage for investigating the role played by temperature in injured cells. Temperature (T) is part of the original HH formalism,[3] which includes a temperature factor in the equations for the three gating variables: m and h for the voltage-gated Na^+ channel (or Nav), and n for the voltage-gated K^+ channel (or Kv) (see below). But the effect of temperature extends beyond simply speeding up kinetics. It is generally assumed that increases in temperature also lead to higher conductances and to stronger ionic pump activity.[9]

If T is too high, the standard HH axon loses its ability to generate APs altogether, i.e., it undergoes conduction block (see Ref. 10 for a more recent survey). In therapeutic applications, it is also known that the ability of a neuron to respond to high frequency biphasic stimulation is temperature dependent.[11] Beyond a certain threshold frequency, the nerve conduction is blocked, but this threshold increases with temperature. At some point, the smaller refractory period at higher T loses to inactivation and repolarizing forces. But before this point is reached, T changes can significantly alter firing patterns. In the majority of cells in the CNS, this is bad news, but for non-noxious thermoreceptors in the periphery as well as in specialized areas of the CNS (hypothalamus), the variation in firing pattern encodes the information about T changes, and the body can adapt by, e.g., sweating to remove heat or shivering to generate heat.

It has been shown that, upon cooling a nerve, its axons conduct more slowly. Given that there is already a distribution of propagation velocities due to heterogeneity in axon diameters, the cooling will cause a bigger "dispersion" in time delays of propagation down the nerve, as predicted in model studies.[12] One consequence of this enhanced temporal dispersion is thought to be the loss of synchrony of activation of postsynaptic targets, with possible clinical manifestations.

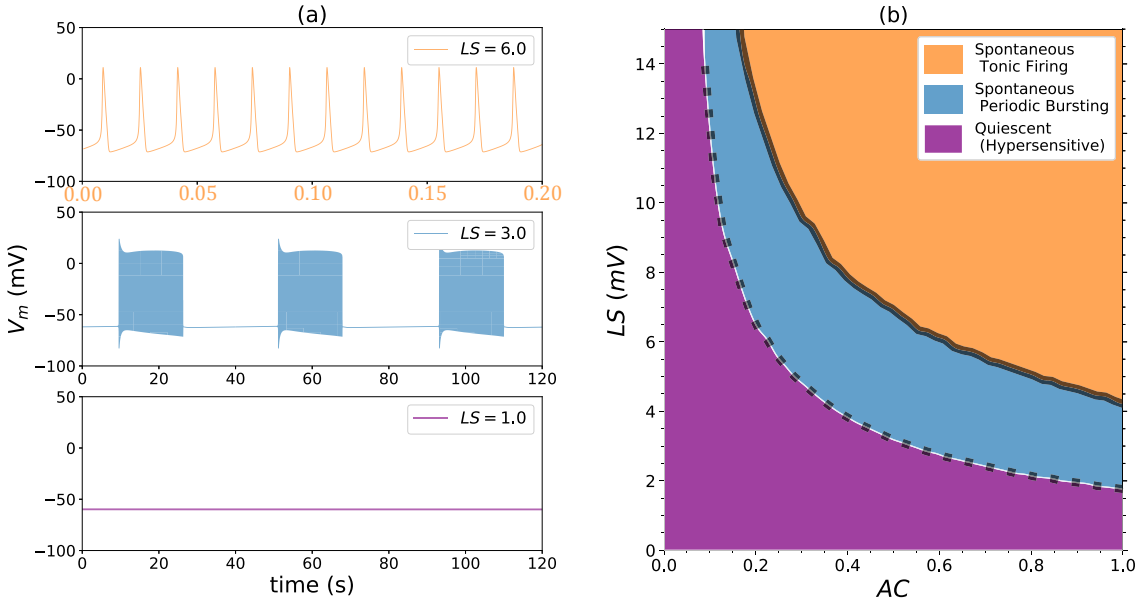

FIG. 1. As the left-shift (*LS*) voltage increases, the system becomes ectopic. In (a), time series of the membrane potential are shown with all channels left-shifted by the amount indicated; in other words, the fraction of affected channels (*AC*) equals 1. Damage increases from the bottom plot upward. The regime diagram (b) features two boundaries. The lower boundary (dashed black line) is the bursting threshold. Below it, the node remains stable (quiescent regime). Above this threshold, the node becomes ectopic: at first bursting spontaneously and then firing tonically above the upper boundary.

Increased T is known to favor conduction block in central demyelinated axons,[13] which is one of the explanations for the worsening of symptoms of multiple sclerosis upon warming (and improvement upon cooling—see Ref. 14 for a review of the early literature on this topic). Actually, nerve conduction studies use temperature as a parameter to help disambiguate problems relating to conduction block from those related to changes in dispersion.[10] Mild cooling of the brain, e.g., by 3° to 4°, is also used as a neuroprotective measure following, e.g., stroke and traumatic brain injury as it reduces metabolism, fever, excitotoxicity (overactivation of glutamate receptors), and intracranial pressure.[15] Another recent study[16] of the effect of temperature on excitability parameters in human motor axons reveals predictable effects such as increased refractory period upon cooling. But other effects, especially on sensory axons, were more ambiguous, and complicated by the transient nature of certain currents such as the transient hyperpolarization induced by warming; the latter increases the activity of the Na^+/K^+ electrogenic pump, the net effect of which is one positive charge pushed out of the cell on each cycle (included in our model below).

In this paper, we address the following question: given that mild injury can cause a transition from quiescence to pathological firing and that temperature modulates excitability, is there a way for changes in temperature to reverse the negative effects of CLS, at least in a qualitative sense? Our model below lays the groundwork to formulate this question biophysically, computationally, and from a nonlinear dynamics perspective and provides some answers. Our model of T- and CLS-dependent ectopy, or T-CLS for short, is inspired by cold receptor models. Such neurons are tasked with reporting the static and time-dependent changes in ambient temperature at various places on the body, mainly on the skin including the eyes and tongue. They are free nerve endings that branch out from a myelinated axon whose soma lies in the dorsal root ganglion in the spinal cord. Cold receptors increase their firing rate upon cooling; warm receptors do the opposite, and although they are well-documented, their dynamics have not yet been modeled. Cold thermoreceptors actually work using a noisy subthreshold oscillation, the amplitude and frequency of which are T-dependent. This has been described experimentally[17–19] as well as in computational models.[20,21] The patterns of activity of cold receptors range from bursting to tonic (i.e., periodic without spike clustering), and then to a form of tonic firing where spikes appear randomly deleted from a periodic sequence. These were documented early on by Braun, Hensel, and Schäfer and their colleagues in Marburg.[18,19]

Our model formulation thus takes advantage of the knowledge gained from decades of study of temperature-induced firing pattern changes in thermoreceptors. The paper is organized as follows. In Sec. II, we recall the CLS model and discuss how to implement temperature-sensitivity. Results that address the question raised above are then presented, first on CLS and then on T-CLS, culminating in a phase diagram that involves only T and LS. We go on to dissect the various components of this temperature correction to the CLS effects. The paper ends with a Discussion and outlook onto future questions.

II. MODEL

A. The Coupled Left Shift (CLS) model of nodal damage

The model presented here has been used previously to describe the dynamics of the trans-membrane voltage at a single node of Ranvier in a myelinated axon.[2,4] Such nodes, about a micron in length, are about a millimeter apart along the length of the axon. We focus strictly on the behavior of one node; CLS-induced disruptions to propagating action potentials and information processing have been recently discussed,[5] and the T-dependent properties of these effects are beyond the scope of our study. Axonal voltage excursions were modeled at an individual node of Ranvier with the Hodgkin-Huxley (HH) model using the values in Ref. 2 (and similar to those in Refs. 4, 5, and 22). The parameter values and meaning are listed in Table I. We start with the basic equation for the membrane potential (V_m written as V for simplicity),

$$C\frac{dV}{dt} = -I_{Na} - I_K - I_{pump} - I_{Naleak} - I_{Kleak} - I_{leak}, \quad (1)$$

where C is the specific nodal membrane capacitance. The total current density I_{Na} through the Nav channels is $I_{Na} = g_{Na}(V - E_{Na})$, where $g_{Na} = \bar{g}_{Na}m^3h$ (m and h are gating variables, the former measuring the activation and the latter the inactivation, but is also known as the availability). Likewise, the total current density I_K through Kv channels is $I_K = g_K(V - E_K)$, with $g_K = \bar{g}_K n^4$. Here, $\bar{g}_{Na}$ and $\bar{g}_K$ are the maximal conductances of the Nav and Kv channels, respectively; E_{Na} and E_K are the sodium and potassium Nernst

TABLE I. Parameters for the node of Ranvier model with temperature dependence

Membrane capacitance	$C = 1\ \mu F/cm^2$
Maximal Nav conductance	$\bar{g}_{Na} = 120\ mS/cm^2$
Maximal Kv conductance	$\bar{g}_K = 36\ mS/cm^2$
Faraday constant	$F = 96\,485.3399$ C/mol
Constant	$R = 8.314\,459\,8$ CV/(mol K)
Temperature	$T_0 = 293.15$ K
Volume of inside compartment	$Vol_i = 3\ \mu m^3$
Volume of outside compartment	$Vol_o = 3\ \mu m^3$
Surface area of node	$A = 6 \times 10^{-8} cm^2$
Initial inside Na^+ concentration	$[Na^+]_i = 20$ mM
Initial outside Na^+ concentration	$[Na^+]_o = 154$ mM
Initial inside K^+ concentration	$[K^+]_i = 150$ mM
Initial outside K^+ concentration	$[K^+]_o = 6$ mM
Initial Na^+ Nernst potential	$E_{Na} = 51.5$ mV
Initial K^+ Nernst potential	$E_K = -81.3$ mV
Pump K^+ leak conductance	$g_{Kleak} = 0.1\ mS/cm^2$
Pump Na^+ leak conductance	$g_{Naleak} = 0.25\ mS/cm^2$
Leak conductance	$g_{leak} = 0.5\ mS/cm^2$
Leak reversal potential	$E_{leak} = -59.9$ mV
Maximum pump current	$I_{maxpump} = 90.9\ \mu A/cm^2$
Pump K^+-dissociation constant	$K_{M_K} = 3.5$ mM
Pump Na^+-dissociation constant	$K_{M_{Na}} = 10$ mM
Q_{10} for the kinetic constants	$Q_{gate} = 3.0$
Q_{10} for the Nav conductance	$Q_{Na} = 1.4$
Q_{10} for the Kv conductance	$Q_K = 1.1$
Q_{10} for the Na^+/K^+ pump	$Q_{pump} = 1.9$

reversal potentials, respectively; and n^4 gives the open probability of potassium channels. In the HH formulation, gating variables m, h, and n evolve according to

$$\frac{dm}{dt} = \alpha_m(1-m) - \beta_m m, \tag{2}$$

$$\frac{dh}{dt} = \alpha_h(1-h) - \beta_h h, \tag{3}$$

$$\frac{dn}{dt} = \alpha_n(1-n) - \beta_n n. \tag{4}$$

The forward (α_m and α_h) and backward rate functions (β_m and β_h) describe the first-order transitions between activation (m) and inactivation (h) processes in Eqs. (4) and (5), and are functions of the membrane voltage V:

$$\alpha_m = 0.1\frac{(V+40)}{1-\exp[-(V+40)/10]}, \tag{5}$$

$$\beta_m = 4\exp[-(V+65)/18], \tag{6}$$

$$\alpha_h = 0.07\exp[-(V+65)/20], \tag{7}$$

$$\beta_h = \frac{1}{1+\exp[-(V+35)/10]}. \tag{8}$$

The rate functions α_n and β_n for the potassium gating variable n in Eq. (4) also depend on V as

$$\alpha_n = 0.01\frac{(V+55)}{1-\exp\left(-\frac{V+55}{10}\right)}, \tag{9}$$

$$\beta_n = 0.125\ \exp\left(-\frac{V+65}{80}\right). \tag{10}$$

Experimental findings for recombinant I_{Na} from nodal type Nav1.6 channels[1] show that mechanical injury causes an irreversible hyperpolarizing ("left")-shift to the sodium activation and inactivation variables. The steady-state product of activation and inactivation, $m^3h(V)_{t\to\infty}$, i.e., the window conductance, also left-shifts. This CLS can be modeled[2,4] by replacing in the dynamics of m and h the membrane voltage V by $(V+LS)$.

However, axon injury is spatially non-homogeneous[23] and is therefore likely to result in spatially inhomogeneous CLS. We do not consider this situation here: when an LS is applied, it is done so to all Nav channels homogeneously.

To discuss issues related to ectopic firing, we have to keep track of the movements of the two ions involved in excitability and introduce Na^+/K^+ ATPase pumps. It is a reasonable assumption that the net flows of Na^+ and K^+ are zero when averaged over time and the cell is in its "healthy" excitable state. There are many cellular components that take part in maintaining homeostasis, and the precise way in which all these components interact is complex and not fully understood. Our model cannot take into account all these factors. Thus, we only add the Na^+/K^+ pump and the Na^+ and K^+-specific leak currents. Note that the resulting formalism goes beyond the standard Goldman-Hodgkin-Katz (GHK) equations by explicitly including the main putative processes that sustain the ionic gradients.

Our strategy has been to set up the system in a homeostatic state for the healthy node to better address the consequences of the additional demand on the availability of ionic resources, especially with respect to the maintenance of the gradients, which determine the Nernst potentials. This required keeping track of the movement of the Na^+ and K^+ ions. This setup was used in our previous work[2,4,5] on which this current study is based. CLS is such an increased demand. When the CLS is small, the system equilibrates to a new quiescent state with reduced gradients, reflected in a shift in the Nernst potentials. As you increase CLS beyond a certain point, there is a transition in which the steady-state Na^+ current, known as "window current," is sufficient to trigger action potentials. In this case, there is a new steady state in which the Nernst potentials are time-varying.

The sodium-potassium exchanger or Na^+/K^+ pump produces a current

$$I_{pump} = I_{maxpump}\left(1+\frac{K_{M_K}}{[K^+]_o}\right)^{-2}\times\left(1+\frac{K_{M_{Na}}}{[Na^+]_i}\right)^{-3}, \tag{11}$$

where $I_{maxpump}$ is the maximal current generated by the pump, K_{M_K} and $K_{M_{Na}}$ are Michaelis-Menten kinetic constants, and the Na^+ and K^+ currents flowing through the pump are $I_{Napump} = 3I_{pump}$ and $I_{Kpump} = -2I_{pump}$ since the pump moves out 3 Na^+ ions while bringing in 2 K^+ ions every cycle (its net effect is thus to hyperpolarize the inside of the cell).

The pump continually works. Its rate is determined by the inner and outer ion concentrations $[Na^+]_i$ and $[K^+]_o$, and the Michaelis-Menten constants which give the values of those concentrations at which the capture rate of the pump for a given ion is at half maximum. However, these constants do not determine the equilibrium concentrations of the Na^+ and K^+ ions, rather these are determined by balancing the total charge [Eq. (1)] and the currents associated with the ionic species Na^+ and K^+.

Finally the model includes the following leak currents which are as usual given by

$$I_{Naleak} = g_{Naleak}(V-E_{Na}); \quad I_{Kleak} = g_{Kleak}(V-E_K);$$
$$I_{leak} = g_{leak}(V-E_{leak}). \tag{12}$$

The concentrations of Na^+ and K^+ inside and outside the cell are then governed by

$$\frac{d[Na^+]_i}{dt} = -\frac{(I_{Na}+I_{Napump}+I_{Naleak})A}{FVol_i}, \tag{13}$$

$$\frac{d[Na^+]_o}{dt} = \frac{(I_{Na}+I_{Napump}+I_{Naleak})A}{FVol_o}, \tag{14}$$

$$\frac{d[K^+]_i}{dt} = -\frac{(I_K+I_{Kpump}+I_{Kleak})A}{FVol_i}, \tag{15}$$

$$\frac{d[K^+]_o}{dt} = \frac{(I_K+I_{Kpump}+I_{Kleak})A}{FVol_o}, \tag{16}$$

where F is the Faraday constant, A is the area of the node, and Vol_i and Vol_o the inner and outer volumes of the node. We made the extracellular volume equal to the intracellular volume for simplicity. There is no qualitative change in behavior when the exterior volume is varied relative to the interior volume (see Fig. 11 in Ref. 2). Just as a note, the intracellular

volume was chosen as fairly small to observe phenomena over relatively short time scales.

Finally, the Nernst potentials for the Nav and Kv currents are given by

$$E_{Na} = -\frac{RT}{F} \ln \frac{[Na^+]_i}{[Na^+]_o}, \tag{17}$$

$$E_K = -\frac{RT}{F} ln \frac{[K^+]_i}{[K^+]_o}, \tag{18}$$

and they will vary if T changes, or following anything that changes the concentration ratios of each ion type. We recall that neuron excitability is based on low $[Na^+]_i$ and high $[Na^+]_o$ (or positive E_{Na}) working together with a high $[K^+]_i$ and low $[K^+]_o$ (or negative E_K).

A phase diagram for this model is shown in Fig. 1, along with examples of quiescent, bursting, and tonic firing patterns. Bursting does not occur in the standard four-dimensional HH system. Rather, an additional slow subsystem is required, which increases the dimensionality of the system. In our system, bursting arises due to the slow changes in ionic concentrations in Na^+ and K^+ ions, which in turn affect the Nernst potentials; these provide the battery power to generate action potentials in the first place.[2,4] Bursting is then a consequence of the fact that, during the active firing phase of the burst, the ionic gradients become depleted, and the Nernst potentials move toward zero (from above in the case of E_{Na} and from below in the case of E_K). Once they are too depleted, firing ceases, and homeostatic forces, namely the Na^+/K^+ pump, recharge the batteries until firing starts up again. In the healthy case, this depletion is kept in check by the pump; however, the increased leakiness caused by CLS is an extra load on the pump, and eventually it cannot keep up, and ectopic bursting ensues. At high *LS* values, a bifurcation from quiescence directly to tonic firing can occur.[24]

The bursting is organized around a subcritical Hopf bifurcation in the quiescent state. The slow dynamics move the state point past this bifurcation, and the solution is drawn to a stable fast spiking limit cycle. The Nernst potentials begin to deplete, and at some point, the solution falls off the fast limit cycle onto the lower fixed point branch of the subcritical Hopf point. The precise mechanism by which this drop to the quiescent phase occurs has not been worked out in full detail due to its complexity, as it occurs in the vicinity of a period-doubling cascade. In some cases, the last spikes in the burst reflect the presence of that cascade, and the bursting solutions appear to be chaotic rather than strictly periodic.[4] In any case, the presence of the Hopf produces decaying oscillations in voltage at the end of the burst phase, as well as at the end of the quiescent phase. This explains the relevance of this form of bursting with subthreshold oscillations to observations in the context of neuropathic pain.[2,4,6–8] Temperature effects reported below preserve these subthreshold oscillations, although a thorough bifurcation analysis is beyond the scope of our paper.

B. Incorporating temperature dependence

We wish to study the effect of temperature on the pathological behavior of the CLS model. Ideally, we would like to see how temperature plays off against, or along with, the *LS* factor. A lot of our knowledge about the effect of temperature on neurons comes from studies of cellular pacemakers. Willis *et al.*[25] as well as Wiederhold and Carpenter[26] have in fact advocated using pacemakers as model systems for thermoreceptors. Until recently, thermoreceptors were thought to do their work by virtue of the temperature-dependence of the basic processes underlying their excitability. In other words, there did not seem to be any "specialized" temperature receptor. The situation has changed for more than a decade now since TRP receptors were discovered. They are thought to underlie part of the cold and warm sensitivity, and especially the extreme warm sensitivities seen, e.g., in snakes and vampire bats. The TRP channel variety present in many cold receptors, TRPM8, has in fact been incorporated in a recent model for cold thermoreception.[27] This is a fascinating and rapidly moving field, which we will stay away from because we are considering the effect of temperature on generic nerve cells, not thermoreceptors with their specific complement of TRP channels.

Temperature is known to affect the ratio of the maximal sodium to potassium conductance, with the numerator increasing faster than the denominator.[9,28,29] As mentioned above, T increases the kinetics of the activation and inactivation gates by a substantial factor. The standard way to quantify temperature dependence is through a Q_{10} factor which quantifies how much a kinetic rate changes upon a 10 °C increase in temperature. For example, the gating kinetics in HH speed up by a factor $\Phi = 3.0^{(T-T_0)/10}$, where T_0 is the reference temperature where the factors are measured. This factor Φ multiples the right hand side of all the gating variable derivatives, thereby increasing their rate of change upon warming, in the same way other chemical reactions are sped up by warming. The Q_{10} factor for the kinetic constants is 3.0 in this example, and in our paper as well. The Q_{10} for the maximal Nav conductance is 1.4,[28,29] while that for Kv is 1.1[28] (see also Table I). These Q_{10}'s are within the physiological range for these respective processes.[20,28–31]

Note that, with respect to the Q_{10} for the pump, we are using the generally accepted model that the rate of an enzymatic reaction varies exponentially with small changes in temperature. In practice, we chose a value of 1.9 for the Q_{10} of the pump that lies between the Q_{10} values for the conductances and the gate kinetics—although we will investigate the effect of this latter value. Our goal was to obtain a generic picture for the effect of T variations on the basic bifurcation diagram of the CLS model. Furthermore, as we will show below, upon sweeping the Q_{pump} at fixed T, there are no surprises: there is a transition from quiescent to bursting. Different values for Q_{pump} will simply shift the bifurcation picture quantitatively.

Note that the precise values for these Q_{10}'s is not so important as dissecting out their individual effects, and more generally, as offering a framework in which to understand the dynamical interactions of T and other parameters. In fact, the results reported below for each T-dependent process can simply be graded along with the magnitude of their associated Q_{10}. We chose 20 °C as the reference temperature to be consistent with previous simulations in Refs. 2, 4, 5, and 24. There is nothing special about this reference temperature. Others could

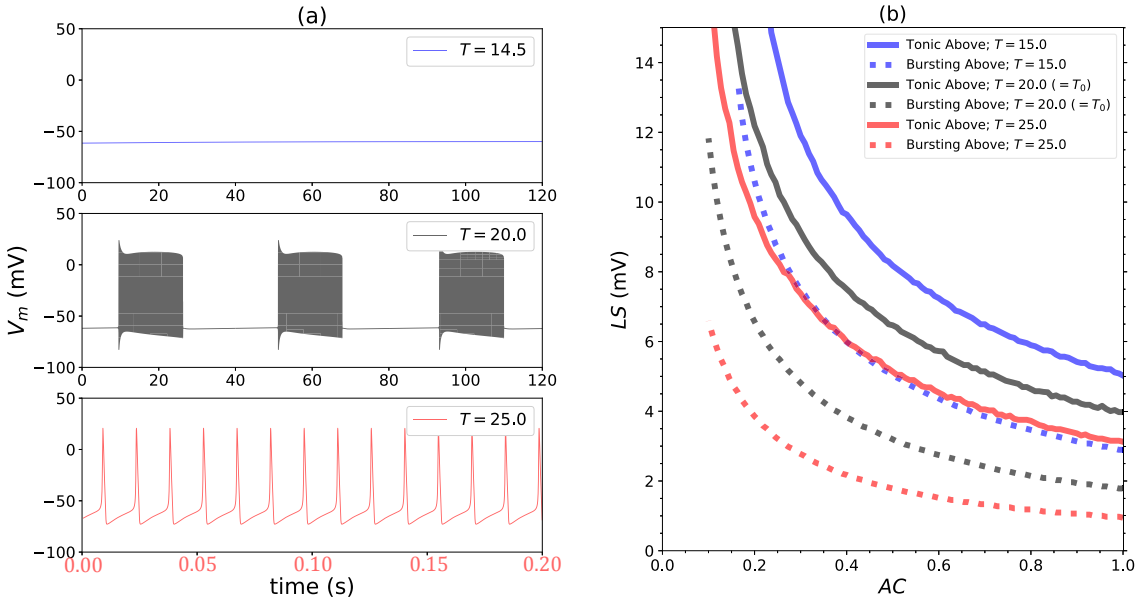

FIG. 2. T-CLS: (a) As *temperature* is varied, the system moves from quiescent, to bursting, to tonic firing; at fixed left-shift (here $LS = 3.0$ mV, $AC = 1$). This effect can be understood in terms of the regime diagram: Temperature moves the ectopic boundary. (b) The dashed and solid lines have the same meaning as in Fig. 1(b). Temperature increases from the top downward.

have been chosen. For example, we could have decided to calibrate our model at 37 °C. Given the dependence of the Nernst potentials on absolute temperature, this simply implies that we would have been working with slightly different ratios of internal to external concentrations. We would expect qualitatively similar results to Fig. 2(b) by increasing/decreasing the temperature by 5 °C.

The Nernst potentials are directly proportional to T as we can see in their definitions above. Their increase with T expresses the fact that the strength of the diffusion of the ions to dissipate their gradients also increases with T. However, for simplicity, the Nernst potential for the weaker leak current, made up mostly of chloride, is given a T-independent value. The same goes for the (weak) maximal leak conductance g_{leak}. The consequences of these choices are highlighted in the Discussion section. Note that the magnitude of the Nernst potentials is directly proportional to temperature, although with temperature being in Kelvins, this is a limited effect for 5°-10° changes. However, their dependence on the effect of T on ionic concentration ratios, due to the pump, is more significant as we will see below.

As mentioned above, there is a more intimate link between our CLS model and cold receptor models on which our temperature analysis is built: both involve bursting oscillations, and their associated subthreshold oscillations (see, e.g., Refs. 20, 21, 26, and 29). However, there are some important dynamical differences. Models of cold receptors burst for a different reason than the CLS model above. They typically possess an endogenous slow-wave oscillation that causes parabolic bursting. The slow wave goes on even if spikes are not present, a clear slow-fast decomposition of the full dynamics. The cold receptor models burst due to a slow subsystem that involves an inward current (such as persistent Na^+) and a slow subthreshold outward current. The latter, although generally thought to involve K^+, has been assigned a more generic mechanism for its activation (see Ref. 26 and references therein), or been given a specific calcium dependence and accompanying calcium buffering dynamics.[20,32] In contrast, leaking Nav channels initiate ectopic firing in the CLS model. This can lead to bursts because the slow dynamics of the Na^+/K^+ pump struggle to restore ion gradients during the active firing phase of ectopic firing. Thus, during the active phase, the Nernst potentials become depleted, and firing stops at some point; the gradients are restored by the pump during this quiescent phase. This CLS burst oscillation does not persist in the absence of firing.

All numerical integrations were carried out using the NEURON simulation environment (www.neuron.yale.edu) running on an Apple laptop computer. The code is based on a Python script stored on ModelDB (http://modeldb.yale.edu/234111).[24] This code allows users to explore the phase diagram in Fig. 1(b) by selecting (AC, LS) coordinates and running simulations. NEURON's built in adaptive time step method (CVode) was used.

III. RESULTS

We will discuss the effect of temperature in terms of the phase diagram of the original coupled left shift (CLS) model. Figure 1(a) shows the behavior observed as the damage is increased at a node with all Nav's left-shifted. The node stays quiescent for small damage up to a critical value, then as LS is increased further the Na^+ current flowing in triggers a burst of APs which lasts for a finite time. In that phase, APs are produced spontaneously until the ion gradients are too depleted to maintain firing with the stimulating I_{Na} current. As LS is

increased further, the interburst time diminishes until comparable to the period of the bursting APs. The system then fires continuously or tonically. The boundaries of the different regions are given in Fig. 1(b). This variant of the Hodgkin-Huxley model (HH) is insensitive to temperature except for small changes to excitability due to the absolute temperature prefactor in the Nernst potentials E_K and E_{Na}.

To study the effect of temperature on CLS-induced spontaneous firing, a set of temperature factors Q_{10}'s are added to the model: Q_{pump}, Q_{Na}, Q_K, and Q_{gate} (values listed in Table I). Figure 2 summarizes the changes to the system's behavior with temperature when these Q_{10}'s are included. In Fig. 2(a), we fix $LS = 3.0\,\text{mV}$ and use temperature to move the system from quiescent, to bursting, to tonic firing. Temperature pushes the system in and out of ectopicity. In Fig. 2(b), we reproduce the ectopic boundaries shown in Fig. 1(b) at three temperatures. At the reference temperature ($T = T_0 = 20.0\,°\text{C}$), the boundaries are unchanged—this is equivalent to the original CLS model. Heating to $T = 25.0\,°\text{C}$ lowers the ectopic boundaries (i.e., spontaneous firing begins with less damage than at the reference temperature). Cooling to $T = 15.0\,°\text{C}$ raises the boundaries—points near the boundary which were ectopic at the reference temperature can be rendered quiescent with moderate cooling. Temperature thus alters the phase diagram by shifting the ectopic boundaries, but qualitatively the story is unchanged.

Heating reinforces left shift, cooling counteracts it. An injured neuron is more sensitive to temperature, and a chilled neuron can remain quiescent at greater left shift. Figure 3 summarizes the combined effect of left-shift and temperature in the form of a new phase diagram, analogous to Fig. 1(b) but in the *T-LS* space. We focused on the first transition (quiescence to bursting) because our objective is to discuss remedial strategies to return an ectopically firing node to quiescence.

Our extended HH model has plenty of moving parts before temperature sensitivity is introduced. To understand the effect of the various Q_{10}'s, we run "knock-in" simulations, wherein a single Q_{10} (e.g., Q_{Na}) is active and the rest are set to unity. These simulations are plotted together in

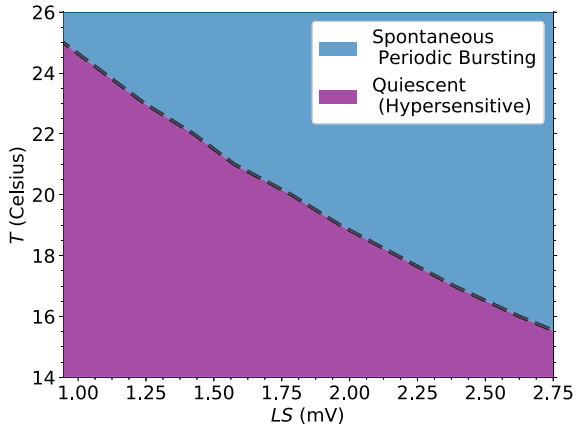

FIG. 3. Another regime diagram: Temperature versus left-shift at $AC = 1$. Temperature and CLS work together—decreasing one allows for an increase in the other. An injured neuron is more sensitive to temperature, and a chilled neuron is more robust to CLS injury [cf. Figs. 1(b) and 2(b)].

Fig. 4, in which we see that Q_{Na} moves the ectopic boundary significantly more than any of the others. The dominance of Q_{Na} is not surprising: sodium currents determine excitability, and hence ectopicity. Temperature affects every cellular mechanism but its effect on voltage-gated sodium channels dominates here, followed by electrogenic pumps (via Q_{Na} and Q_{pump}, respectively). In Fig. 4(b), we sum the four knock-in simulations' deviations from the reference curve and observe that the result (roughly) reproduces the complete temperature sensitive model.

To explain the effects of temperature and left shift, we inspect the absolute value of the voltage gated sodium current I_{Na} at V_{rest}. (Taking the absolute value simplifies the discussion. For example, since V_{rest} is negative and E_{Na} is positive, the driving force $(V_{rest} - E_{Na})$ is larger when E_{Na} is strengthened). Writing $\Delta T = T - T_0$, the magnitude of the Nav current is

$$|I_{Na}(V_{rest})| = \overline{g_{Na}} m_\infty^3 h_\infty Q_{Na}^{\Delta T/10}(|V_{rest}| + E_{Na}). \tag{19}$$

Unpacking Eq. (19), from left to right: The activation m and inactivation (availability) h variables are functions of the membrane voltage, but when damaged they respond to V as a healthy one does at $\tilde{V} = V + LS$. In other words, $m = m(V + LS)$ and $h = h(V + LS)$. This means that LS leads to a larger steady state Nav current. The temperature parameter Q_{Na} serves to multiply the entire voltage gated sodium conductance by a factor $Q_{Na}^{\Delta T/10}$, producing a larger current at any given V. T shows up twice in the driving force $|(V - E_{Na})|$. First, the *absolute* temperature multiplies the Nernst potential E_{Na} [see Eq. (17)]. Second, Q_{pump} drives the concentrations $[Na^+]_i$ and $[Na^+]_o$ whose ratio forms the argument of the logarithm in E_{Na}.

The resting potential is not affected by left shift or temperature: Where quiescent solutions exist, the conservation of Na^+ and K^+ ions in our model causes $V_{rest} = E_{leak}$. That is, the resting potential is determined by E_{leak} and therefore is independent of LS and T, as we now show. At $V = V_{rest}$, the current balance equation becomes

$$0 = C\frac{dV}{dt} = -\sum I = -\{I_{Na,total} + I_{K,total} + I_{leak}\}, \tag{20}$$

where each total current includes voltage gated channels, pumps, and leak. The model's explicit ion conservation (via the electrogenic Na^+/K^+ pump) is a helpful constraint. Since at equilibrium each ion's total current is individually zero, Eq. (20) becomes three separate equations:

$$\begin{cases} 0 = I_{Na,total} = [g_{Na} + g_{Na,leak}](V - E_{Na}) + 3I_{pump}, \\ 0 = I_{K,total} = [g_K + g_{K,leak}](V - E_K) - 2I_{pump}, \\ 0 = I_{leak} = g_{leak}(V - E_{leak}). \end{cases} \tag{21}$$

Equation (21) says that to reach equilibrium, the model must tune the sodium and potassium concentrations—using the pump and voltage gated channels—such that $V = E_{leak}$.

The main role of I_{pump} is to restore the Na^+ and K^+ ion gradients. As seen in Eq. (21), equilibrium occurs when the outward (Na^+) and inward (K^+) pump currents are respectively balanced by the conductance and leak currents associated with these ions. The role of the pumps is to maintain ion

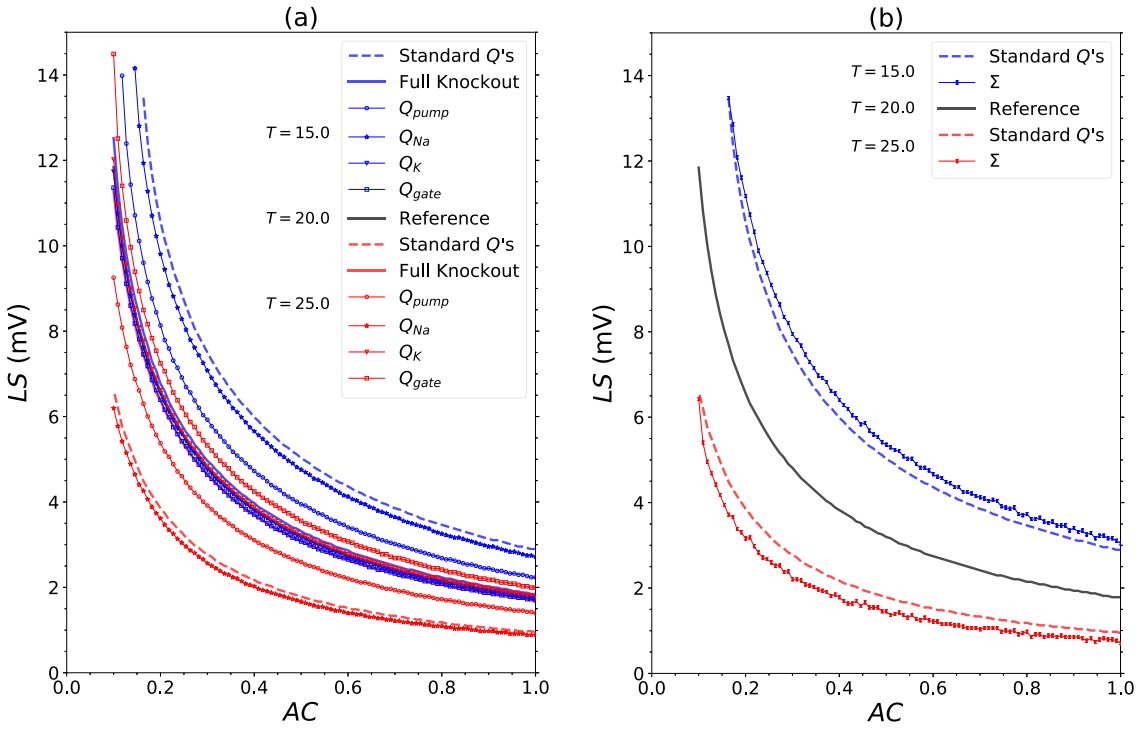

FIG. 4. (a) To isolate the effects of the four Q_{10}'s, Q_{pump}, Q_{Na}, Q_K, and Q_{gate} (listed in Table I), we plot the altered ectopic boundary "one Q_{10} at a time," along with the full knock-out and the reference case of full knock-in. That is, a single Q_{10} is switched on while the rest are set to unity. From this plot, it is clear that Q_{Na} and Q_{pump} dominate temperature's mediation of ectopicity. In (b), the combined effect of the Q_{10}'*s* is roughly recovered by summing the effect of each Q_{10} on its own.

gradients or restore them when depleted by firing. Increased pump currents—following, e.g., an increased Q_{pump} (see Fig. 5 below)—have to be balanced by increased steady-state Na^+ and K^+ currents. Since in our model V_{rest} is set by E_{leak}, which therefore can only change if E_{leak} changes (it is fixed throughout this study), such increased currents can only be achieved with a larger driving force (V-E_X) (where X is either Na^+ or K^+), i.e., an upper shift in the positive E_{Na} and a lowering of the negative E_K. And this is in fact what the pumps accomplish. By pumping out Na^+ and pumping in K^+, the pumps increase the Na^+ and K^+ gradients, leading to larger positive values of E_{Na} and more negative values of E_K. The increase in E_{Na}, notably, increases I_{Na} through the driving force $|(V - E_{Na})|$ [see Eq. (21)]. This has the consequence of lowering the ectopic threshold as T increases even if I_{pump} was the only T-dependent process. In the model with full T-dependence, the increase in the g_{Na} conductance further lowers the ectopic threshold.

The purpose of Fig. 5 is precisely to show this surprising effect of the pumps. In that figure, we show how the different currents behave as the size of the pump current is slowly increased while keeping the operating temperature at $T = 25$ °C and all other Q_{10}'s equal to one for a slightly damaged node ($LS = 1.5$ mV; $AC = 1.0$); this can be interpreted as a ramp in the Q_{pump} value. One sees that the Nernst potentials become bigger in absolute value. Furthermore, at some point, the subthreshold oscillations appear, and eventually a bursting solution occurs, with a very long time interval between active phases, since we are near the bursting/tonic boundary. The presence of the subthreshold oscillations is a consequence that the ramp keeps the transient response alive. In fact, since the linearization of the dynamics around the equilibrium has complex eigenvalues with negative real part prior to burst onset, the ramp expresses the oscillation at a frequency equal to the imaginary component of the eigenvalue. As a whole, the paradox of how a pump that produces a net outflux of positive charge can make the system more excitable is resolved by noting that the concentration ratio $[Na^+]_i/[Na^+]_o$ determines the driving force for the sodium current.

We chose a ramp of Q_{pump} that drives the system across a bifurcation from quiescence to bursting, because the effect of increasing Q_{pump} may be counterintuitive. A hyperbolic tangent ramp was imposed whose asymptotic value is just above the onset of bursting. The bifurcation will occur at different values of Q_{pump} depending on the chosen temperature. In Fig. 5, the temperature is 25 °C.

An analytical demonstration of how cooling moves the quiescent-to-bursting bifurcation boundary to higher values of LS is beyond the scope of our work, but we make a few comments in this direction. Our eight-dimensional dynamical model has a fixed point when the system is quiescent. Effectively, it is only six-dimensional since the total number of Na^+ and K^+ ions is conserved. The voltage component of this fixed point corresponds to the resting potential. Previous bifurcation analyses (see Fig. 2 in Ref. 4) reveal that the fixed point progressively loses stability as LS increases and

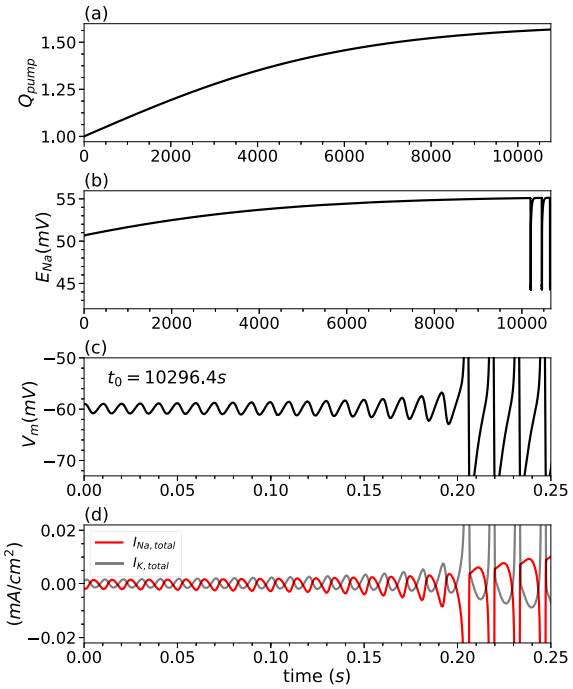

FIG. 5. Response of the system to ramped Q_{pump}, at fixed temperature, and on two time scales. (a) Here Q_{pump} alone is activated (knock in). The initial state is $LS = 1.5$ mV, $AC = 1.0$, and $T = 25$C. Q_{pump} is slowly ramped from a value of 1.0 following a shifted tan$h$ whose $t \to +\infty$ asymptote is slightly above 1.5. (b) Response of E_{Na} during the ramp. The bifurcation to bursting is crossed around 10 000 s when Q_{pump} is about 1.5 [see (a)]. Due to the long timescale, a single spike in E_{Na} here corresponds to an entire burst that lasts about 6 s, and the time duration between bursts is 140 s. The rate during bursting is about 54 Hz. Short timescale: (c) Membrane voltage near the onset of bursting; (d) Total sodium and potassium currents near the onset of bursting.

becomes unstable beyond the quiescent-to-bursting threshold. This results from the increase in the sodium window current at rest. The approach of a bifurcation to sustained firing is a general consequence of increasing the net inward current to an excitable system. Warming also increases the sodium window current through its increase of the pump activity and the conductances, as well as of the Nernst potentials, both directly and via the higher concentration gradients caused by a stronger pump [see Fig. 5(b)]. This increased sodium ion current overrides the opposing effect of the increased kinetic rates [Fig. 4(a)], and further destabilizes the fixed point for a given *LS*; cooling stabilizes this point and can thus undo some of the effect of *LS*.

Finally to test the robustness of the effects of cooling, additive (current) noise on the current balance equation was included and integrated using the Euler-Maruyama algorithm (not shown). The cooled node which was shown in Fig. 2(a) remains quiescent with subthreshold oscillations driven by the noise, and very rare spiking. When the system is brought closer to threshold, the noise induces bursts of varying duration, as in Yu *et al.*[4] Thus, a preliminary analysis of the effect of current noise on T-CLS suggests that it modifies the dynamics as in the CLS case.

IV. DISCUSSION

We have considered the dynamics of the standard HH equations with two concomitant parameter changes: (1) the midpoint voltage for Nav activation and inactivation, duly shifted to a lower (more negative) value due to a CLS phenomenon; and (2) temperature changes. Of the two, the former is clearly the more delicate one from a dynamical point of view, as it enables the cell to start firing in the absence of any input. Specifically, the pumps cannot keep up their ionic balancing act in the presence of enhanced Na^+ leakiness, and the Nernst potentials start to collapse during sustained firing, such that the behavior that appears after quiescence in a mildly injured cell is bursting. The bifurcations underlying the successive transition between quiescence, bursting, and tonic as the left shift increases have been worked out in much detail.[4]

Interestingly, temperature does not change this state of affairs qualitatively, but rather only quantitatively for the range of parameters we have explored. In other words, changing the maximal conductances and the kinetic rates for the gates and the pumps still leads to a picture where quiescence goes to bursting and then tonic, albeit at higher *LS* values when T is lowered. In some as of yet unexplored part of parameter space, temperature changes may have a more drastic effect on the bifurcations leading to bursting and tonic limit cycle solutions. Regardless, the fact that the thresholds are simply moved around by temperature is potentially attractive from an intervention point of view: one can expect a fairly straightforward effect of cooling on a traumatized nerve.

In the absence of any Q_{10}'s, the sole temperature dependence of our model stems from the direct proportionality of the Nernst potentials to absolute temperature. As we saw in Fig. 4, this modifies the boundary for ectopic behavior only very slightly, but in the same direction: cooling raises the threshold, while warming lowers it. By allowing only one temperature dependency to take effect at once, we found [Fig. 4(a)] that the sodium current I_{Na} is the main player in moving the boundary; the Na^+/K^+ pump comes in second, contributing a threshold shift of about a third of that of Q_{Na}. In contrast, the effect of K^+ is rather minimal, although in the opposite direction; this is not surprising since it has the smallest Q_{10}. Interestingly, only the gating kinetics have a significant effect that is opposite to that of all the other factors considered here [Fig. 4(a)].

Our knock-in simulations also reveal that, to a good approximation, the total effect of temperature on the quiescent-bursting boundary is given by the algebraic sum of these effects [Fig. 4(b)]. We have also done single knock-out simulations, where only one Q_{10} at a time (for the pump, Nav, Kv, or the gates) is set equal to 1. Those results support the conclusions from the knock-in and summing simulations, and for that reason are not shown.

The effect of T lies in the fact that the total Nav current is made up of an *LS*-dependent but T-independent gating factor (m^3h), multiplied by a *LS*-independent but T-dependent battery term. It is also interesting that the resting potential is insensitive to the value of *LS* or of T. In fact, by construction, V_{rest} is always equal to E_{leak} in our model. Here is the result

of our more detailed formulation of HH dynamics that tallies every Na^+ or K^+ ion going across the membrane and that includes the Na^+/K^+ exchanger by necessity. In fact, the ionic species' currents are individually balanced and sum to zero in the resting state, i.e., the quiescent state where no firings occur. This is necessary to avoid continual accumulation of an ionic species on one side of the membrane or the other. Hence in the resting state, the total Na^+ and K^+ currents are individually zero; from the current balance equation, this implies that $V_{rest} = E_{leak}$.

This value contrasts with the well-known standard HH system, which has four state variables (voltage, Nav activation and inactivation gates, and Kv activation date). In that system, V_{rest} is not necessarily E_{leak}, but rather the root of a more complex set of nonlinear equations involving all the conductances and the Nernst potentials. In the standard HH, V_{rest} depends on T and LS, even though experimentally the resting potential in squid axon does not depend significantly on T.

Relatedly, we have assumed that the mechanisms meant to keep the chloride gradient across the membrane constant are affected minimally by the mild injury. This means that the Nernst potential for chloride is unaffected by the mild injury. However, like all Nernst potentials, the magnitude of E_{leak} will be proportional to absolute T. Furthermore, it is reasonable to assume that the maximal leak conductance g_{leak}, as well as the smaller Na^+ and K^+ leakages through the pump, will have a Q_{10}. For the pump leakage, this effect is likely quite small. As for g_{leak}, it may have a Q_{10} on the order of the ones given the Na^+ and K^+ conductances. But the leak conductance is often an order of magnitude less than those of the fast spiking Nav and Kv conductances, and the battery term is small near resting potential. Incorporating these extra T-dependencies may amount to an increased stabilization of the quiescent state as T increases, since V_{rest} should decrease slightly following the increase with T due to both factors entering I_{leak} (i.e., the conductance and the battery term). It is to be seen how this plays out in a given experimental system, with its own complement of ions making up the leakage currents and their associated temperature dependencies. But at the very least, it would seem that making the leak terms thermosensitive could "offset the offset" a bit, i.e., offset the potential benefit of cooling for reversing mild traumatic injury.

Our work has focused on a single node of Ranvier and found that the ectopy brought upon by CLS can be counteracted by cooling. While the results were obtained in the specific context of a node, the fact that the model revolves around an expanded HH system with plausible Q_{10} values suggests that it is generically applicable to any system where this model provides a good description of the un-traumatized dynamics at ordinary temperatures.

While our study suggests that cooling can alleviate the symptoms of CLS and its associated neuropathic pain, it also predicts that warming will exacerbate the injury by lowering the threshold for ectopic activity. In the pain literature, allodynia describes the situation where a normally non-painful mild stimulus (mechanical, temperature, etc.) becomes painful. In this sense, the heightened ectopic activity in our model brought on by warming could partly underlie "hot allodynia" seen clinically. It is not clear how large temperature changes can be in the context of our CLS model, the experimental basis for which was determined at a fixed reference temperature. This argues for a better calibration of the temperature between model and CLS experiments to begin making quantitative predictions, and also for doing CLS experiments at different temperatures to see if the coupled-left shift is always the right picture, at least for sodium.

One has to recognize that this is a simplified yet necessary preliminary step toward understanding the effects of temperature on normal and injured or diseased states. There are many factors at play, and our model captures a small number of them. For example, a recent study[33] reported that cooling induced undesirable changes in motor axons that were consistent with depolarization; yet, the effect on sensory axons was comparatively deemed "more complicated" as it may involve different expression levels of hyperpolarization-activated channels. And, there are many different parameter changes that can be investigated in detailed model systems such as Aplysia, beyond the simple generic ones considered here.[34] A further consideration is the modeling of the electrogenic pump. Classic work has shown that the membrane potential in squid axon is T-independent; our model reproduces that finding. However, this property varies across neurons; for example, membrane potential increases with warming in mammalian optic nerve,[35] a property ascribed to a combination of the electrogenic pump modeled here as well as other electrically neutral mechanisms of sodium entry. Clearly, a specific model system in which many effects can be studied is a valuable tool, and generalizations must be done with caution.

We note that current state-of-the-art models of thermoreception actually avoid the question of the Q_{10} for the pump by omitting the pump altogether.[27,31] Willis *et al.*[25] and Wiederhold and Carpenter[26] have paid special attention to the Na^+/K^+ electrogenic pump, stating that its activity increases with temperature, and since its net effect is hyperpolarizing, temperature increases should hyperpolarize the membrane potential. This effect is incorporated in our model, given that every cycle of the pump produces a net outflux of positive charge. Curiously, increasing temperature when only the Na^+/K^+ pump is assumed to be T-dependent [i.e., knocked-in: see Fig. 4(a)] leads to a lowering of the threshold, meaning that effectively the system is depolarized. The reason why this occurs is due to an indirect effect on the Nernst potential for Na^+: increased pump activity makes E_{Na} more positive, due to the increased disparity between inner and outer Na^+ concentrations. Given that the battery term (V-E_{Na}) is a main component of I_{Na}, the net effect of increased pump activity is a depolarization. The magnitude of this effect will of course depend on the precise value of Q_{pump}, which in our study was intermediate between that of the maximal conductances (1.1 and 1.4) and of the gate kinetics (3).

Future work will consider the propagation aspects of the proposal put forth here, as was done for the CLS effect.[5] In particular, while CLS may be confined to a certain area of the nerve, it may be challenging to alter the temperature only at these areas. One may then contend with the desired effect in the traumatized area, along with potentially undesirable effects nearby where a healthy nerve is cooled,

which would impede its normal excitability. Ultimately, the precise beneficial effects of temperature, if any, will depend on how well the CLS model captures the mild traumatic injury in the first place, and whether the injury is indeed mild or not. Other temperature-dependent processes may also be at play. And there are specific forms of neuropathic pain that involve temperature sensation, such as cold allodynia. It remains to be seen whether the model described here is relevant to that specific condition. Another factor is that transients may play a role, since it is known that the effect of CLS can become "expressed" only once a neuron tries to propagate action potentials.[5] Thus, there may be interesting neural use-dependent effects that one could try to mitigate with temperature. The results presented here suggest that cooling should also mitigate this kind of stimulus-induced ectopicity.

ACKNOWLEDGMENTS

This work was supported by the Natural Sciences and Engineering Research Council (Canada).

[1]J. A. Wang, W. Lin, T. Morris, U. Banderali, P. F. Juranka, and C. E. Morris, "Membrane trauma and Na+ leak from Nav1.6 channels," Am. J. Physiol. **297**, C823–C834 (2009).
[2]P. A. Boucher, B. Joós, and C. E. Morris, "Coupled left-shift of Nav channels: Modeling Na^+ loading and dysfunctional excitability of damaged axons," J. Comput. Neurosci. **33**, 301–319 (2012).
[3]A. L. Hodgkin and A. F. Huxley, "A quantitative description of membrane current and its application to conduction and excitation in nerve," J. Physiol. **117**, 500–544 (1952).
[4]N. Yu, C. E. Morris, B. Joos, and A. Longtin, "Spontaneous excitation patterns computed for myelinated axons with injury-like impairments of nodal Na/K pumps and sodium channels," PLoS Comput. Biol. **8**(9), e1002664 (2012).
[5]M. Lachance, A. Longtin, C. E. Morris, N. Yu, and B. Joos, "Leak/pump dynamics in a model of mild axonal injury yield neuropathic input/output abnormalities in saltatory propagation," J. Comput. Neurosci. **37**, 523–531 (2014).
[6]R. Amir, M. Michaelis, and M. Devor, "Membrane potential oscillations in dorsal root ganglion neurons: Role in normal electrogenesis and neuropathic pain," J. Neurosci. **19**, 8589 (1999).
[7]Y. Kovalsky, R. Amir, and M. Devor, "Simulation in sensory neurons reveals a key role for delayed Na current in subthreshold oscillations and ectopic discharge: Implications for neuropathic pain," J. Neurophysiol. **102**, 1430–1442 (2009).
[8]J. S. Choi and S. G. Waxman, "Physiological interactions between Na(v)1.7 and Na(v)1.8 sodium channels: A computer simulation study," J. Neurophysiol. **106**, 3173–3184 (2011).
[9]D. O. Carpenter, "Ionic and metabolic bases of neuronal thermosensitivity," Fed. Proc. **40**, 2808–2813 (1981).
[10]H. Franssen, G. H. Wieneke, and J. H. J. Wokke, "The influence of temperature on conduction block," Muscle Nerve **22**, 166–173 (1999).
[11]C. Tai, J. Wang, J. R. Roppolo, and W. C. de Groat, "Relationship between temperature and stimulation frequency in conduction block of amphibian myelinated axon," J. Comput. Neurosci. **26**, 331–338 (2009).
[12]G. J. M. Rutten, R. D. A. Gaasbeek, and H. Franssen, "Decrease in nerve temperature: A model for increased temporal dispersion," Electroencephalogr. Clin. Neurophysiol. **109**, 15–23 (1998).
[13]M. Rasminsky, "The effects of temperature on conduction in demyelinated single nerve fibers," Arch. Neurol. **28**, 287–292 (1973).
[14]K. J. Smith, "Conduction properties of central demyelinated and remyelinated axons, and their relation to symptom production in demyelinating disorders," Eye **8**, 224–237 (1994).
[15]H. A. Choi, N. Badjatia, and S. A. Mayer, "Hypothermia for acute brain injury—Mechanisms and practical aspects," Nat. Rev. Neurol. **8**, 214–222 (2012).
[16]M. C. Kiernan, K. Cikurel, and H. Bostock, "Effects of temperature on the excitability properties of human motor axons," Brain **124**(Pt 4), 816–825 (2001).
[17]H. Bade, H. A. Braun, and H. Hensel, "Parameters of the static burst discharge of lingual cold receptors in the cat," Pfluegers Arch. **382**, 1–5 (1979).
[18]H. A. Braun, H. Bade, and H. Hensel, "Static and dynamic discharge patterns of bursting cold fibers related to hypothetical receptor mechanisms," Pfluegers Arch. **386**, 1–9 (1980).
[19]H. A. Braun, K. Schäfer, H. Wissing, and H. Hensel, "Periodic transduction processes in thermosensitive receptors," in *Sensory Receptor Mechanisms*, edited by W. Hamann and A. Iggo (World Scientific, Singapore, 1984), pp. 147–156.
[20]A. Longtin and K. Hinzer, "Encoding with bursting, subthreshold oscillations and noise in mammalian cold receptors," Neural Comput. **8**, 215–255 (1996).
[21]H. A. Braun, M. T. Huber, M. Dewald, K. Schäfer, and K. Voigt, "Computer simulations of neuronal signal transduction: The role of nonlinear dynamics and noise," Int. J. Bifurc. Chaos **8**, 881–889 (1998).
[22]W. L. Maxwell, "Histopathological changes at central nodes of Ranvier after stretch injury," Microsc. Res. Tech. **34**, 522–535 (1996).
[23]A. Ochab-Marcinek, G. Schmid, I. Goychuk, and P. Hänggi, "Noise-assisted spike propagation in myelinated neurons," Phys. Rev. E **79**, 011904 (2009).
[24]B. Joos, B. M. Barlow, and C. E. Morris, "Calculating the consequences of left-shifted Nav channel activity in sick excitable cells," in *Voltage-Gated Sodium Channels: Structure, Function and Channelopathies. Handbook of Experimental Pharmacology*, edited by M. Chahine (Springer, Cham), Vol. 246.
[25]J. A. Willis, G. L. Gaubatz, and D. O. Carpenter, "The role of the electrogenic sodium pump in modulation of pacemaker discharge of Aplysia neurons," J. Cell. Physiol. **84**, 463–471 (1974).
[26]M. L. Wiederhold and D. O. Carpenter, in *Cellular Pacemakers, Vol. 2: Function in Normal and Diseased States*, edited by D. O. Carpenter (Wiley-Interscience, New York, 1982), pp. 27–58.
[27]E. Olivares, S. Salgado, J. P. Maidana, G. Herrera, M. Campos, R. Madrid, and P. Orio, "TRPM8-dependent dynamic response in a mathematical model of cold thermoreceptor," PLoS One **10**(10), e0139314 (2015).
[28]A. L. Hodgkin and R. D. Keynes, "Active transport of cations in giant axons from Sepia and Loligo," J. Physiol. **128**, 2840 (1955).
[29]J. R. Schwarz, "The effect of temperature on Na currents in rat myelinated nerve fibres," Pflugers Arch. **406**, 397 (1986).
[30]B. Hille, *Ionic Channels of Excitable Membranes*, 2nd ed. (Sinauer, Sunderland, MA, 1992); 3rd ed. (2001); for Q10 values, see p. 51.
[31]M. T. Huber and H. A. Braun, "Stimulus-response curves of a neuronal model for noisy subthreshold oscillations and related spike generation," Phys. Rev. E **73**, 041929 (2006).
[32]K. Schäfer, H. A. Braun, and H. Hensel, "Static and dynamic activity of cold receptors at various calcium levels," J. Neurophysiol. **47**, 1017–1028 (1982).
[33]M. O. Kovalchuk, H. Franssen, L. J. Van Schelven, and B. T. H. M. Sleutjes, "Comparing excitability at 37°C versus at 20°C differences between motor and sensory axons," Muscle Nerve **57**, 574–580 (2018).
[34]N. G. Hyun, K. H. Hyun, K. Lee, and B. K. Kaang, "Temperature dependence of action potential parameters in Aplysia neurons," Neurosignals **20**, 252–264 (2012).
[35]T. A. Coates, O. Woolnough, J. M. Masters, G. Asadova, C. Chandrakumar, and M. D. Baker, "Acute temperature sensitivity in optic nerve axons explained by an electrogenic membrane potential," Pflugers Arch. **467**, 2337–2349 (2015).

Chapter 5 Synthesis

Previously, in Chapter 4, we mapped the *left-shift* voltage thresholds of pathological spontaneous firing patterns in the CLS model of a node of Ranvier with active Na^+/K^+ pumps (Figure 4.4). Given that excitotoxic spiking can be fatal to damaged neurons in the hours and days following injury, we adapted the CLS model to investigate whether *physiological* temperature perturbations could prevent cell loss by stabilizing hyperexcitable CLS-regimes.

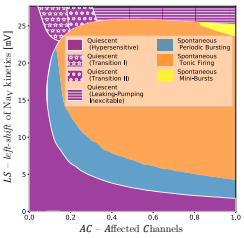

$\Delta T = 0$: *Miniature version of the single temperature* CLS *regime diagram from Figure 4.4 on page#107.*

With temperature modulation, the two-dimensional regime diagram from Chapter 4 becomes a *three-dimensional* 'T-CLS regime *cube*' in (AC, LS, T) coordinates. In FIG. 2(b) of [2] (Section 5.3) we slice that cube perpendicular to its Temperature axis (pointing out of the page) at $\Delta T = -5℃$, $0.0℃$, and $+5℃$. Each slice reveals a cross-section of the parameter space with two ectopic boundaries—one separating the quiescent and bursting regimes, the other marking the transition from bursting to tonic firing—at a specific ΔT. Superimposing these ΔT-slices in FIG. 2(b) shows that the thresholds for bursting and tonic firing both *decrease* with heating ($\Delta T > 0$) and *increase* with cooling ($\Delta T < 0$).

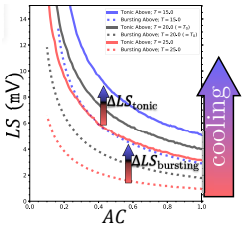

FIG. 2(b) on page#140 superimposes regime diagrams at three temperatures ($\Delta T = -5℃$, $0.0℃$, *and* $+5℃$) *to show the effect of temperature on hyperexcitability . Compare with Figure 4.4.*

As described in Table 5.1 and Section 5.2, the T-CLS model adds temperature sensitivity to the simulated Na_V and K_V channels' gating variables and maximal conductances, and to the electrogenic Na^+/K^+ pumps' maximum velocity, through a set of scaling parameters called "Q-tens" (denoted Q_{10}, see Equation (5.1)).

In prior *CLS* simulations, varying *AC* and *LS* moved the system through different regimes in a *static* excitability map (regime diagram). With the *T-CLS* model, however, temperature moves the *boundaries* between regimes in the (*AC*, *LS*) plane. To the neuron, the regime diagram is a function of ΔT (see FIG. 2(b) above and Appendix C | *T-CLS* model: Graphical summary of Chapter 5 on page#305).

Our *T-CLS* simulations predict that mild cooling can reduce the pathological hyperexcitability observed in neurons following ischemia (stroke), head trauma, and acute inflammation. Likewise, the model predicts that febrile temperatures are especially hazardous to injured neurons, as a few degrees of warming can make a previously quiescent cell with mild *CLS* hyperexcitable.

Therapeutic hypothermia is commonly used to improve neurological outcomes in patients who remain comatose following cardiac arrest, yet similar temperature management protocols are still experimental in stroke and other brain injuries. The *T-CLS* simulations may prove useful in the design of future studies, as the neurological effects of therapeutic hypothermia continue to be investigated.

5.3.1 Varying the sodium channel density

With a bit of interpretation, the *T-CLS* simulations can also reveal the effects of altering the sodium channel density[2] combined with *CLS* damage: In FIG. 4(a) of Barlow et al. [2] (page#142), the curves legended Q_{Na^+} are 'single knock-in simulations' that isolate thermal modulation of $\bar{g}_{Na_V}$ by setting the other Q_{10}'s to unity (i.e. $Q_{\mathrm{K}^+} = Q_{\mathrm{gate}} = Q_{\mathrm{pump}} = 1$).

In those (Q_{Na^+}) curves, raising or lowering the temperature corresponds (respectively) to increasing or decreasing the *effective* Na_V channel density—since $Q_{\mathrm{Na}^+}^{\Delta T/10^{\circ}\mathrm{C}}$ multiplies $\bar{g}_{Na_V}$—albeit with a small offset due to the temperature term in the Nernst

[2]The maximal Na_V conductance density ($\bar{g}_{Na_V}$) can be interpreted as a measure of the density of voltage-gated sodium channels in the membrane.

potential (see the *full* knock-out curves in the same figure). Using this special case to approximate the effects of Na_V density modulation, we see that reducing the Na_V density has a protective effect that is similar to cooling the neuron.

The analysis above reinterprets temperature effects in the Q_{Na^+} single knock-in simulations as modulations of Na_V channel density *at a fixed temperature*, accompanied by *left-shift* as seen in Chapter 4. These existing simulations do *not* simultaneously capture $\boldsymbol{CLS}$ *with* temperature modulation *and* variable Na_V density. Future studies could generate $\boldsymbol{T\text{-}CLS}$ regime diagrams at various temperatures, as we have done in FIG. 2.(b) of Barlow et al. [2] (page#140), but with multiple fixed $\bar{g}_{Na_V}$ (Na_V density) values.

In such cases, reducing Na_V density (which raises thresholds, similar to cooling) could interact with the heating effects from the full set of Q_{10} factors, i.e.

$$Q_{\mathrm{Na}^+}, Q_{\mathrm{K}^+}, Q_{\mathrm{gate}}, Q_{\mathrm{pump}} \neq 1.$$

Modulating Na_V density and temperature could be especially relevant to medical interventions such as the administration of Na_V channel blockers in hypothermic or febrile neurons following trauma.

Chapter 6

The pattern of ion channels in the axon initial segment affects feedback sent to dendrites

The title above is accurate, but the official title of the paper that this section is about—Barlow, Longtin, and Joós [4]—is '*Impact on backpropagation of the spatial heterogeneity of sodium channel kinetics in the axon initial segment*'. It was the best title we could think of, *prior* to finalizing the publication.

The simulations in this chapter analyze the effects of different spatial distributions of voltage-gated ion channels[1] in the proximal axon of pyramidal neurons on excitability, and the impact on electrical feedback—called backpropagation—that is sent to dendrites[2] when the pattern of those ion channels is modified (see **Fig.1** of Barlow, Longtin, and Joós [4], on page#158). The models in previous chapters have featured a single Na_V channel protein—albeit with `CLS` damage creating a subpopulation of *left-shift*ed channels—but Na_Vs come in several varieties. As described below and in the paper (Section 6.3), this study includes two Na_V subtypes: $Na_V1.6$, which is found in axons, and $Na_V1.2$, which is found in the soma and dendrites and the proximal axon at certain developmental stages. We began by building upon the model

[1] introduced in Section 3.2.
[2] see Figure 2.8 for dendritic morphology.

of Hu et al. [23], focusing on the cell morphology and channel kinetics which they fitted to their electrophysiological measurements.

6.1 Statement of originality and contributions

I designed, programmed, and conducted the simulations, performed all data analysis and visualization, and wrote the original draft of this paper. The full list of contributions is itemized below and in the paper (Section 6.3 | Barlow, Longtin, and Joós [4], on page#153):

- **Conceptualization**: Benjamin S. M. Barlow, André Longtin, Béla Joós.
- **Formal analysis**: Benjamin S. M. Barlow, André Longtin, Béla Joós.
- **Funding acquisition**: André Longtin, Béla Joós.
- **Investigation**: Benjamin S. M. Barlow, André Longtin, Béla Joós.
- **Methodology**: Benjamin S. M. Barlow, André Longtin, Béla Joós.
- **Project administration**: André Longtin, Béla Joós.
- **Resources**: André Longtin, Béla Joós.
- **Software**: Benjamin S. M. Barlow.
- **Supervision**: André Longtin, Béla Joós.
- **Validation**: Benjamin S. M. Barlow, André Longtin, Béla Joós.
- **Visualization**: Benjamin S. M. Barlow.
- **Writing – original draft**: Benjamin S. M. Barlow.
- **Writing – review & editing**: Benjamin S. M. Barlow, André Longtin, Béla Joós.

6.2 Introduction

The Axon Initial Segment (AIS)—often called the trigger zone—is the part of the axon where action potentials initiate. It is located near where the axon necks off from the soma (the axon hillock), hence "initial" segment (see Figure 2.10 in Section 2.2, page#21).

In the developing nervous system, pyramidal neurons—the majority of neurons in the cortex—express two different varieties of voltage-gated sodium channels, called $Na_V1.2$ and $Na_V1.6$ [37, 23]. Multiple experimental studies in different neuron types have found that $Na_V1.2$ is *right-shift*ed relative to $Na_V1.6$ [47, 23, 32, 56, 57].[3]

Hu et al. [23] were the first to simulate the effects of separated $Na_V1.2$ and $Na_V1.6$ density profiles, which they treated as static. Their models were based on the reconstructed pyramidal cell modelled by Mainen and Sejnowski [38].

The simulations from [38] showed that changing the shape of a simulated neuron (morphology), when combined with nonlinear HH-style currents, can produce a variety of observed spiking patterns. This is relevant to neuroscience because real neurons exhibit a seemingly endless variety of morphologies, and morphology is plastic at the level of single cells.

When I began this project, the intention was to study the function served by the Na_V channels' interesting pattern of expression (reported in Hu et al. [23] and more recently in Liu et al. [37], among others). I designed simulations that created *hypothetical* sodium channel density profiles in the AIS—inspired loosely by variational calculus—and systematically wiggled them to see whether the neuron's response to

[3] Katz et al. [31] challenged this widely accepted view, but they too found that wild-type neurons expressing $Na_V1.6$ had a lower AP threshold than neurons which were engineered to lack $Na_V1.6$ in the AIS. These latter neurons compensated for the missing $Na_V1.6$ channels by expressing extra $Na_V1.2$ in their place, and the change in threshold was not attributed to a decrease in total Na_V density.

injected current was affected by the new Na_V pattern (see **Fig.1** in Barlow, Longtin, and Joós [4], on page#158).

It turned out that neurons actually *do* wiggle their Na_V expression in the AIS, in a way that is remarkably similar to the "hypothetical" set of density profiles I had been simulating [37]. I modelled backpropagation in the pyramidal neuron morphology from Hu et al. [23] (i.e. from Mainen and Sejnowski [38]). The conclusion from [23], that concentrating $Na_V1.2$ in the proximal AIS—via the separated Na_V distribution that is observed in early development—promotes backpropagation, was derived from modelling results with axonal current injection.

We found that proximal accumulation of $Na_V1.2$ actually increases I_{BP} with orthodromic stimulation, a result that persisted under changes to the somatodendritic excitability balance. Later, I created an independent model from the morphology and biophysics of Hay et al. [19] (Figure 2.8 on page#20), reinforcing the results from my Hu-based simulations.

With somatic current injection, our Hu-based and Hay-based models showed strong qualitative and quantitative agreement: their backpropagation thresholds responded nearly identically to modifications in $Na_V1.2$ and $Na_V1.6$ density profiles (compare **Fig. 2** and **Fig. 7**(A)). Notably, both models agreed in their *departure*, under somatic stimulation, from the earlier finding in [23] that $Na_V1.2$ promotes backpropagation.

With axonal stimulation, we observed a loss of backpropagation in the Hay-based model as $Na_V1.2$ was removed from the proximal AIS (Barlow et al. [4]), consistent with Hu et al. [23]. However, some quantitative differences emerged between the Hu-based and Hay-based models under antidromic stimulation. Initially, with the separated Na_V distribution $(x = 1)$, both models exhibited similar physiological backpropagation thresholds. While the Hay-based model maintained physiological

thresholds across both flat and separated Na_V distributions, I_{BP} increased rapidly in the Hu-based model as the Na_V distribution became more homogeneous ($x \to 0$). Nonetheless, both models displayed the same qualitative trend: axonal I_{BP} decreased as Na_V distributions became more separated (cf. **Fig. 4**, **Fig. 7**(B)).

Despite their numerous significant inherited differences [4], our Hu-based and Hay-based models exhibit qualitative agreement regarding the relationship between AIS sodium channel expression and the backpropagation threshold in both orthodromic and antidromic stimulation (**Fig. 2**, **Fig. 7**(A) and **Fig. 4**, **Fig. 7**(B), respectively). Axonal stimulation itself is unphysiological and was modelled only for comparison with the methodology of [23], whereas the models showed strong agreement under physiological somatic current injection.

Modelling choices and many other details are properly discussed in the paper (Section 6.3) and in the ***Supporting information*** (Section 6.4).

6.3 Barlow, Longtin, and Joós (2024)

PLOS COMPUTATIONAL BIOLOGY

RESEARCH ARTICLE

Impact on backpropagation of the spatial heterogeneity of sodium channel kinetics in the axon initial segment

Benjamin S. M. Barlow[1]*, **André Longtin**[1,2,3], **Béla Joós**[1,2]*

1 Department of Physics, University of Ottawa, STEM Complex, 150 Louis-Pasteur Pvt, Ottawa, Ontario, Canada, **2** Center for Neural Dynamics and AI, University of Ottawa, Ottawa, Ontario, Canada, **3** Department of Cellular and Molecular Medicine, Faculty of Medicine, University of Ottawa, Ottawa, Ontario, Canada

* BBarl039@uOttawa.ca (BSMB); BJoos@uOttawa.ca (BJ)

Citation: Barlow BSM, Longtin A, Joós B (2024) Impact on backpropagation of the spatial heterogeneity of sodium channel kinetics in the axon initial segment. PLoS Comput Biol 20(3): e1011846. https://doi.org/10.1371/journal.pcbi.1011846

Editor: Jonathan Rubin, University of Pittsburgh, UNITED STATES

Received: September 25, 2023

Accepted: January 21, 2024

Published: March 15, 2024

Data Availability Statement: Model code is available on ModelDB at https://modeldb.science/267088.

Funding: We acknowledge the support of the Natural Sciences and Engineering Research Council of Canada (NSERC), to BJ (RGPIN-2018-06835) and AL (RGPIN-2014-06204). The funders had no role in study design, data collection and analysis, decision to publish, or preparation of the manuscript.

Abstract

In a variety of neurons, action potentials (APs) initiate at the proximal axon, within a region called the axon initial segment (AIS), which has a high density of voltage-gated sodium channels (Na_Vs) on its membrane. In pyramidal neurons, the proximal AIS has been reported to exhibit a higher proportion of Na_Vs with gating properties that are "*right-shifted*" to more depolarized voltages, compared to the distal AIS. Further, recent experiments have revealed that as neurons develop, the spatial distribution of Na_V subtypes along the AIS can change substantially, suggesting that neurons tune their excitability by modifying said distribution. When neurons are stimulated axonally, computational modelling has shown that this spatial separation of gating properties in the AIS enhances the backpropagation of APs into the dendrites. In contrast, in the more natural scenario of somatic stimulation, our simulations show that the same distribution can impede backpropagation, suggesting that the choice of orthodromic versus antidromic stimulation can bias or even invert experimental findings regarding the role of Na_V subtypes in the AIS. We implemented a range of hypothetical Na_V distributions in the AIS of three multicompartmental pyramidal cell models and investigated the precise kinetic mechanisms underlying such effects, as the spatial distribution of Na_V subtypes is varied. With axonal stimulation, proximal Na_V *availability* dominates, such that concentrating *right-shifted* Na_Vs in the proximal AIS promotes backpropagation. However, with somatic stimulation, the models are insensitive to *availability* kinetics. Instead, the higher *activation* threshold of *right-shifted* Na_Vs in the AIS impedes backpropagation. Therefore, recently observed developmental changes to the spatial separation and relative proportions of $Na_V1.2$ and $Na_V1.6$ in the AIS differentially impact *activation* and *availability*. The observed effects on backpropagation, and potentially learning via its putative role in synaptic plasticity (e.g. through spike-timing-dependent plasticity), are opposite for orthodromic versus antidromic stimulation, which should inform hypotheses about the impact of the developmentally regulated subcellular localization of these Na_V subtypes.

Competing interests: The authors have declared that no competing interests exist.

Author summary

Neurons use sodium ion currents, controlled by a neuron's voltage, to trigger signals called action potentials (APs). These APs typically result from synaptic input from other neurons onto the dendrites and soma. An AP is generated at the axon initial segment (AIS) just beyond the soma. From there, it travels down the axon to other cells, but can also propagate "backwards" into the soma and dendrites. This "backpropagation" allows the neuron to compare the timing of outgoing and incoming signals at synapses where input was received, a feedback process that modifies its connections to other neurons (spike-timing-dependent synaptic plasticity) which is a mechanism for learning. It is puzzling that in many neurons, sodium ion channels come in two types: high-voltage threshold channels clustered near the soma where the AIS begins, and low-voltage ones further away towards the axon. This separation changes in the early development of the animal, which raises the question of its role in backpropagation. We constructed detailed mathematical models to explore how separation affects backpropagation. Separation either impedes or enhances backpropagation, depending on whether the AP results from input to the soma or dendrites or, less typically, input received in the axon. This is explained by the different effects the separation has on two key kinetic processes that govern sodium currents.

Introduction

In fluorescence microscopy images of neurons, the axon initial segment (AIS) is visible as a patch of axonal membrane near the soma with a high density of voltage-gated ion channels. These channels enable the AIS to initiate and shape action potentials (spikes) and regulate neuronal excitability [1]. The AIS can be thought of as an organelle that lives within the first $\approx 100\mu m$ of axonal membrane and whose function it is to supply the current needed to initiate spikes when the neuron is poised to fire—usually in response to synaptic input. The AIS can move up and down the axon and also change its length on a timescale of hours to days. This phenomenon, called structural AIS plasticity, enables neurons to optimize their sensitivity to specific input frequencies during development and to homeostatically adjust their intrinsic excitability [2–4]. GABAergic input can also impinge on the AIS from axo-axonic synapses, such that the AIS can be modulated directly by interneurons. Synaptic input at the AIS can rapidly and precisely control the excitability of individual neurons for sound localization [5]. Fast AIS plasticity, including receptor-mediated changes to local ion channel properties and endocytosis of voltage-gated channels, occurs on timescales of seconds to minutes [6]. (This is distinct from pathological remodelling induced by ischemia, although in [7], it was recently demonstrated that cortical neurons are more robust to interruptions in blood flow than previously thought.) The outsized electrophysiological influence of the AIS demands robust characterization of this short piece of axon as it interacts with its environment.

Over three-quarters of all neurons in the mammalian cortex are pyramidal cells (see Fig A in S1 Text), which have dendrites spanning the thickness of the cortex (several mm) and AIS lengths on the order of tens of μm [8–11]. The AIS requires a high density of voltage-gated sodium channels (Na_Vs) to prime and initiate action potentials (APs) [12–14]. In pyramidal cells, the AIS features two Na_V subtypes, with an interesting spatial distribution: $Na_V1.2$ channels cluster near the soma (i.e. at the proximal AIS) while $Na_V1.6$ cluster toward the distal AIS [15–17]. However, the purpose of this separated distribution of Na_V subtypes remains unclear [18, 19]. Further, recent experiments have revealed that as neurons develop, the spatial

distribution of Na_Vs in the AIS can change substantially, suggesting that neurons tune their excitability by modifying said distribution [20].

Our modelling study is motivated by the following question: What effect does the separated spatial distribution of $Na_V1.2$ and $Na_V1.6$ in the AIS have on excitability and backpropagation? And does the answer depend on whether stimulation is orthodromic or antidromic? In particular, how does the finding in [15], that the separated distribution of Na_V subtypes favours backpropagation—simulated with axonal (antidromic) current injection—generalize to the more common situation of somatic (orthodromic) stimulation?

It is a prevalent view that the Hodgkin-Huxley style kinetics of $Na_V1.2$ are *right-shifted* relative to those of $Na_V1.6$ by an amount $V_{RS} \sim 10 - 15\text{mV}$ [13–15, 17, 21, 22]. Due to their *right-shifted* gating properties (see Fig P in S1 Text), $Na_V1.2$ channels are often described as "high-threshold" channels, since the *right-shift* increases their half-*activation* voltage, relative to $Na_V1.6$. Because the same *right-shift* also increases $Na_V1.2$ *availability*—i.e. it reduces the proportion of inactivated $Na_V1.2$ channels at a given voltage, compared to $Na_V1.6$—it is an oversimplification for the purposes of this study to call them high- and low-threshold channels, respectively. For this reason we instead say that $Na_V1.2$ channels are *right-shifted*.

Interestingly, $Na_V1.6$ invades the proximal AIS as pyramidal neurons mature [20]. To be meaningful, the statement of Hu et al. that concentrating $Na_V1.2$ in the proximal AIS promotes backpropagation [15], requires that the *right-shifted gating properties* of $Na_V1.2$ do the promoting: Suppose a given stimulus is just barely sufficient to evoke a backpropagating AP (BAP) in the neuron with $Na_V1.2$ concentrated in the proximal AIS and $Na_V1.6$ in the distal AIS. If the function of said channel distribution is to ensure backpropagation of the AP to the soma and dendrites (as stated in [15]), then backpropagation should fail with the same stimulus if the proximal AIS were instead populated with $Na_V1.6$.

In [15], the rôle of $Na_V1.2$ in promoting backpropagation is contingent upon simulations wherein the density of $Na_V1.2$ was incrementally lowered in the AIS. However, at the proximal AIS, the active Na^+ conductance was almost entirely composed of $Na_V1.2$ channels. It does not follow then, that concentrating $Na_V1.2$ in the proximal AIS promotes backpropagation, from the fact that removing *the only* Na_V channels in that area (which happen to be $Na_V1.2$ at that developmental stage [20]) stopped backpropagation.

A more recent experimental paper which is the most directly relevant to [15] is Katz et al. (2018) [18], which compared AP thresholds in engineered mouse pyramidal neurons lacking $Na_V1.6$ to wild-type neurons with $Na_V1.2$ and $Na_V1.6$ in the AIS. In [18], they downplay the importance of Na_V subtypes in determining the excitability differences seen in the proximal versus distal AIS. Whereas antidromic stimulation was used in [15], orthodromic stimulation (somatic current injection) was used in [18]. There were no data available that isolated the effect of orthodromic versus antidromic stimulation w.r.t. the role of Na_V subtypes in the AIS in setting the backpropagation threshold. Here our modelling shows that the stimulation site matters, and can invert the experimental conclusions, which should motivate a comparative experimental study.

The separated Na_V distribution is reported to promote backpropagation—which is important for learning—following axonal stimulation [15]. There is also evidence that mutations which alter the gating properties of $Na_V1.2$ are involved in epilepsy and autism [23]. Backpropagated spikes drive learning by depolarizing the postsynaptic membrane, which triggers metabolic events that give rise to synaptic plasticity, including spike-timing-dependent plasticity [24]. There is experimental evidence that postsynaptic backpropagation can release retrograde messengers into the synapse, and influence the future release of neurotransmitters from the presynaptic neuron [25]. A backpropagating action potential can also underlie bursting in cortical neurons as it can return to the cell body from the dendrites as a depolarizing after-potential,

which in turn can initiate another somatic AP [26, 27]. Bursting can also occur in layer 5 pyramidal cells following the generation of a dendritic BAP-activated Ca^{2+} spike (BAC spike), e.g. in the presence of synaptic input. The associated BAPs can further influence the dendritic dynamics [28–31].

Not all layer 5 pyramidal cells can generate dendritic spikes as the size of the apical dendritic tree varies [32]. Dendritic spikes have also been reported to vary across species, and are not common in human layer 5 pyramidal cells [33], owing partly to their enhanced dendritic compartmentalization [34]. Thus, to further understand the original reports that Na_V segregation promotes BAPs, we investigate how Na_V segregation in the AIS can decrease the BAP threshold (described below) using the model of [15] (itself based on [26]). This provides the backbone to study the basic effects on BAPs of the AIS excitability profile, under both somatic and axonal stimulation. For the sake of generality, we complement these results by considering a state-of-the-art model of layer 5 pyramidal cells with perisomatic BAPs and dendritic BAC firing [29], adapted to include a more realistic AIS and axon.

Other computational powers are attributed to the AIS. Moving the initiation site away from the soma (i.e. toward the distal AIS) beyond a critical distance enables high-frequency spiking in cortical neurons, increasing the maximum spike frequency by an order of magnitude [14]. Separating $Na_V1.6$ into the distal AIS is said to push the initiation site toward that location, owing to those channels' lower voltage threshold [15, 21]. However, in [35], simulations having only one Na_V type demonstrated that passive cable properties are sufficient to locate AP initiation at the distal AIS.

In our simulations, we alter the composition of the AIS and look for changes in the backpropagation threshold. We distribute *right-shifted* Na_V gating properties along the AIS by differentially distributing two functionally distinct classes of sodium channels, referred to here as $Na_V1.2$ and $Na_V1.6$ following [15, 21] and [20]. We systematically alter the Na_V distribution, by varying the extent to which Na_V subtypes are spatially segregated in the AIS without affecting the total Na_V density.

We compute the threshold for backpropagation as the amplitude of a brief current pulse that causes an AP to propagate back into the dendrites and cause a sufficient depolarization (Sections B and C in S1 Text). This is done in three biophysically detailed and independently tuned multicompartmental pyramidal cell models ([15, 29]), two of which are based on the Hu et al. (2009) model and involve the same morphology but with differing soma-dendrite excitability balance (cell geometries are provided in Figs A and B in S1 Text). This threshold is computed as a function of the spatial segregation of the Na_V subtypes in the AIS by continuously varying their density profiles from fully overlapping to strongly separated (Fig 1).

We show that Na_V separation reduces the backpropagation threshold with axonal stimulation but can impede backpropagation with somatic stimulation. This asymmetrical result was not expected. To explain our results, we independently modify the *right-shift* (V_{RS}) of selected $Na_V1.2$ gating variables and their respective time constants by an amount ΔV_{RS} (i.e. $V_{RS} \rightarrow V_{RS} + \Delta V_{RS}$). These modifications to $Na_V1.2$ gating are applied only in the AIS.

Sweeping ΔV_{RS} (while clamping other gating variables to nominal V_{RS} values) reveals that (I) $Na_V1.2$ *availability* and its time constant explain how proximal $Na_V1.2$ promotes backpropagation with axonal stimulation, and (II) the threshold of steady-state *activation* explains how $Na_V1.2$ suppresses backpropagation and reduces excitability with somatic stimulation.

Being a feature of pyramidal cells, the plastic distribution of AIS Na_V subtypes that we model applies to something like eight out of ten cortical neurons [8]. Various experimental and computational techniques used to study the biophysical determinants of AIS excitability across the lifespan have involved different stimulation sites [36, 37]. Here we demonstrate

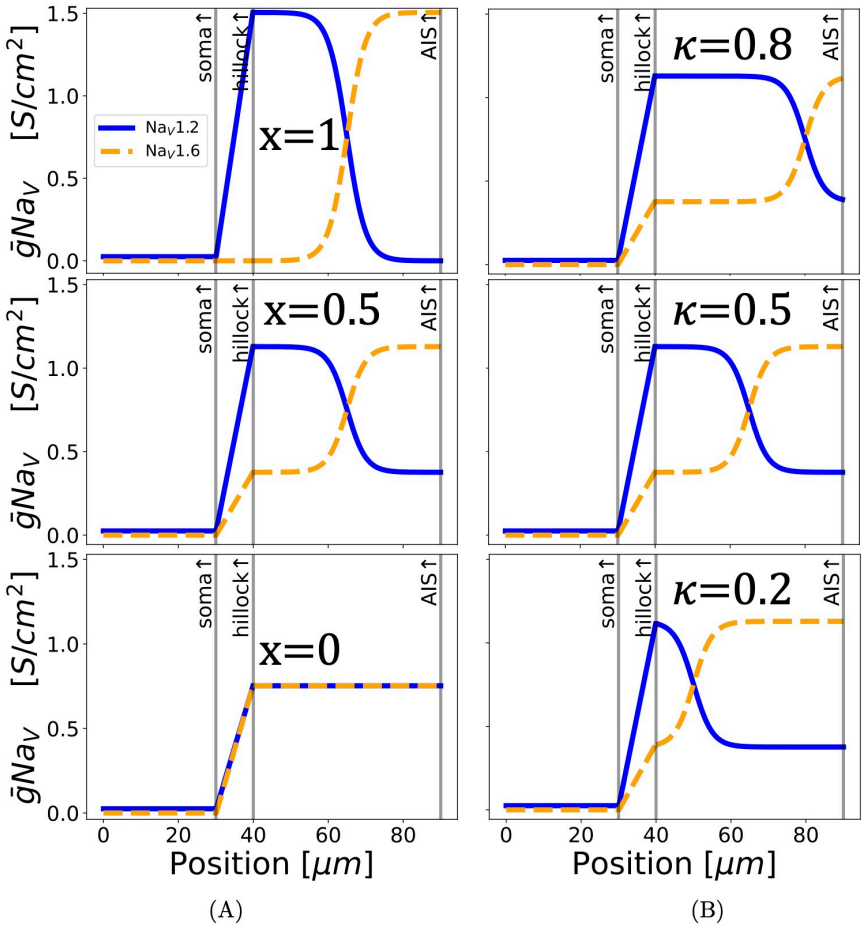

Fig 1. Modifying the spatial distribution of Na_V subtypes in the AIS while keeping the total conductance constant. (**A**) The spatial separation of Na_V subtypes in the AIS is varied using the parameter "x" with $\kappa = 0.5$. The top plot is a model setup with a separated distribution [15, 20] of Na_Vs in the AIS. The high threshold $Na_V1.2$ (indicated in blue) are concentrated close to the soma, and the low threshold $Na_V1.6$ (indicated in orange) are kept distal to the soma. Moving from top to bottom, both Na_V subtypes are distributed ever more evenly along the AIS. We chose the parameter name "x" to vary the spatial separation of the AIS Na_V distributions, because the separated distribution is x-shaped. Setting $x = 1$ in our simulations gives the separated distribution, and $x = 0$ gives the "flat" distribution wherein both Na_V subtypes are uniformly mixed. (**B**) Variation of the crossover location (κ) of Na_Vs in the AIS with $x = 0.5$. We have lengthened the AIS to 50μm in this graphic for visual clarity.

https://doi.org/10.1371/journal.pcbi.1011846.g001

opposing effects on backpropagation with orthodromic versus antidromic stimulation by altering the separated Na_V distribution. Both stimulation modes are used by experimentalists [11, 15, 18, 38], and certain pyramidal neurons are also known to receive axo-axonic input at the AIS as well as somatodendritic input [6]. It is thus important to know whether and how the spatial profile of Na_V channel subtypes really enhances backpropagation in vivo, and whether moving the stimulating electrode can bias or even invert experimental findings, as our work demonstrates. Apart from explaining the dynamical mechanism behind the dependence of AP generation on AIS Na_V distribution, we clearly show that the site of stimulation matters, a finding that is present robustly in different models and which merits experimental

confirmation. Changes to AIS properties and the follow-on effects on backpropagation must affect the entire cortex.

Results

Hypothetical Na_V distributions in the AIS

We begin with our implementation of the model from Hu et al. (2009) [15] (Hu-based model), using their morphology, K_V and Na_V kinetics (for details, see Materials and methods). The standard AIS length in our model is 25 μm, based on measurements from [10]. A key feature of the Na_V distribution that changes during development, is the extent to which the voltage-gated sodium channel subtypes $Na_V1.2$ and $Na_V1.6$ are localized in the proximal and distal AIS, respectively [20]. In our simulations, the relative proportion of $Na_V1.2$ versus $Na_V1.6$ at a given position along the AIS can be changed without affecting the total Na_V density at any point (Eq 6).

Fig 1 shows how the parameters x and κ control the way Na_V subtypes are spread out along the AIS. When x is at its highest value of 1, the subtypes $Na_V1.2$ and $Na_V1.6$ are spaced apart from each other, with $Na_V1.2$ concentrated in the proximal AIS and $Na_V1.6$ in the distal AIS, approximating the distribution observed in developing pyramidal neurons (see [20]). Decreasing x transforms this separated distribution into a uniform mix ($x \to 0$) where $Na_V1.2$ and $Na_V1.6$ are distributed homogeneously. This can be seen in Fig 1A.

Every distribution except the uniform Na_V mix has a location along the AIS at which the density of $Na_V1.6$ overtakes the $Na_V1.2$ density. That location, which we call the Na_V crossover and denote κ, is also varied in our simulations (see Fig 1A; κ is a dimensionless length normalized by the AIS length).

To cement our results, we will further apply identical transformations to the Na_V distribution in a cell having a 'backward' AIS, that is, with *distal* $Na_V1.2$ and *proximal* $Na_V1.6$. The results from the backward AIS model are nearly a mirror image of our findings.

For each hypothetical Na_V distribution, a short current pulse (1ms) is injected at a specific site, and the minimum (i.e. threshold) pulse amplitude I (in nA) required to elicit a spike is determined. Brief pulse durations separate the stimulation waveform from the intrinsic response of the cell. We define excitability in terms of two thresholds: backpropagation threshold I_{BP} (AP leading to a spike in the distal dendrites) and forward-propagation threshold I_{FP} (axonal AP threshold, recorded without regard to the amplitude of the somatodendritic depolarization).

Current is injected either in the middle of the soma (somatic stimulation) or the axon just distal to the AIS (axonal stimulation). In both cases, forward propagation refers to an AP travelling down the axon, and backpropagation always refers to an AP visible as a spike in the dendrites. Backpropagation was deemed to have occurred if all apical dendritic tips exceeded -63.0mV (i.e. a depolarization of 7.0mV above V_{rest}) following stimulation (see Fig C in S1 Text).

In the following sections, we implement the above Na_V distributions in the Hu-based model [15] (Fig A in S1 Text), which we chose as a starting point because of its seminal role in the study of how Na_V subtypes in the AIS affect backpropagation. At V_{rest}, the *activation* of $Na_V1.2$ and $Na_V1.6$ is negligible, so the total conductance at rest is not affected by x or κ (see Fig Pi in S1 Text).

Due to the "curse of dimensionality" and limitations in the spatial resolution of experimental measurements, many parameters in multicompartmental models—such as the density of ion channels at every point on the cell membrane—must be estimated and require tuning, introducing subjective judgement on the part of the modeller (reviewed in [39]). Hu et al. [15]

based their simulations on a hand-tuned model from [26]. The adjustment and re-adjustment of hand-tuned models is a potentially endless cycle [39]. It is desirable to have a model which is tuned automatically via an objective procedure, to break the loop of hand-tuning. To this end, in Generalization to Hay-based model and modified Hu-based model, we repeat the procedure described above—i.e. varying the Na_V distributions in the AIS as in Fig 1—in the model of Hay et al. (2011) [29] (Fig B in S1 Text). Hay et al. used an evolutionary algorithm to optimize the densities of nine simulated ion channels in each compartment of reconstructed layer-5b pyramidal neurons. The ground truth in that fitting consisted of somatodendritic spiking patterns recorded in a variety of such neurons from adult rats.

The third model, a modification of our Hu-based model with significant qualitative differences in its backpropagating action potential, is included in Section D in S1 Text. In the latter model, the dendritic excitability is much higher, with negligible attenuation of the backpropagating action potential. The dendritic Na_V density is increased 10-fold relative to the Hu-based model in the main text, and the somatic Na_V density is decreased 3-fold. Multiple models with differing conductances, biophysics, and morphology demonstrate the robustness of our results, as we can modify the density profiles of $Na_V1.2$ and $Na_V1.6$ in the AIS without affecting any other compartments. For further details, see Materials and methods and S1 Text.

Somatic stimulation

In Fig 2, both negatively and positively sloped backpropagation threshold curves with respect to x are present, indicating that Na_V separation can promote or impede backpropagation (respectively). Changes in threshold can be as large as 30%. Moving the Na_V crossover (κ) toward the distal AIS shifts the backpropagation threshold curves upward. A qualitative change, namely the sign of the slope, occurs around $\kappa = 0.4$.

An intuitive explanation for this latter effect is that moving the crossover location away from the soma causes the AIS to be dominated by $Na_V1.2$ channels (see Fig 1B, $\kappa = 0.8$), which have a higher *activation* voltage threshold than $Na_V1.6$. APs still initiate in the distal AIS, but the dominant $Na_V1.2$ renders the cell less excitable. Further, for $\kappa \gtrsim 0.4$, the backpropagation threshold increases as we tend toward the separated, x-shaped distribution of Na_Vs. This behaviour is the opposite of what is observed for axonal stimulation below and in [15]. We repeated these simulations with AIS length up to 100μm (Fig L in S1 Text) and also with stimulation at the main apical dendrite (Fig N in S1 Text) instead of the soma, and obtained the same qualitative results as Fig 2 (see Section D.1 in S1 Text).

The negatively sloped curves do not necessarily imply that proximal $Na_V1.2$ promotes backpropagation in the case of somatic stimulation. In those curves ($\kappa \lesssim 0.4$), the AIS is mainly populated with $Na_V1.6$ when $x > 0$. Also note that decreasing κ places more $Na_V1.6$ channels nearer to the soma (see Fig 1B, $\kappa = 0.2$). In that case, the threshold-lowering effect of Na_V separation could come from the increased total $Na_V1.6$ density that results from increasing x when κ is relatively small, rather than from the proximal accumulation of $Na_V1.2$ with increasing x. Further, increasing κ (which increases the ratio of $Na_V1.2$ to $Na_V1.6$ in the AIS) raises the threshold for all curves in Fig 2 (see also Fig M in S1 Text). It is then consistent to postulate that for somatic stimulation, the backpropagation threshold is increased by AIS $Na_V1.2$ at all values of x and κ, and Fig 2 is consistent with AIS $Na_V1.6$ enhancing excitability and backpropagation. In other words, for **somatic stimulation**:

- when $\kappa < 0.5$ and $x > 0$, the AIS is dominated by $Na_V1.6$: increasing x decreases the proportion of total AIS Na_V conductance due to $Na_V1.2$ (negative slope: separated distribution yields the lowest backpropagation threshold).

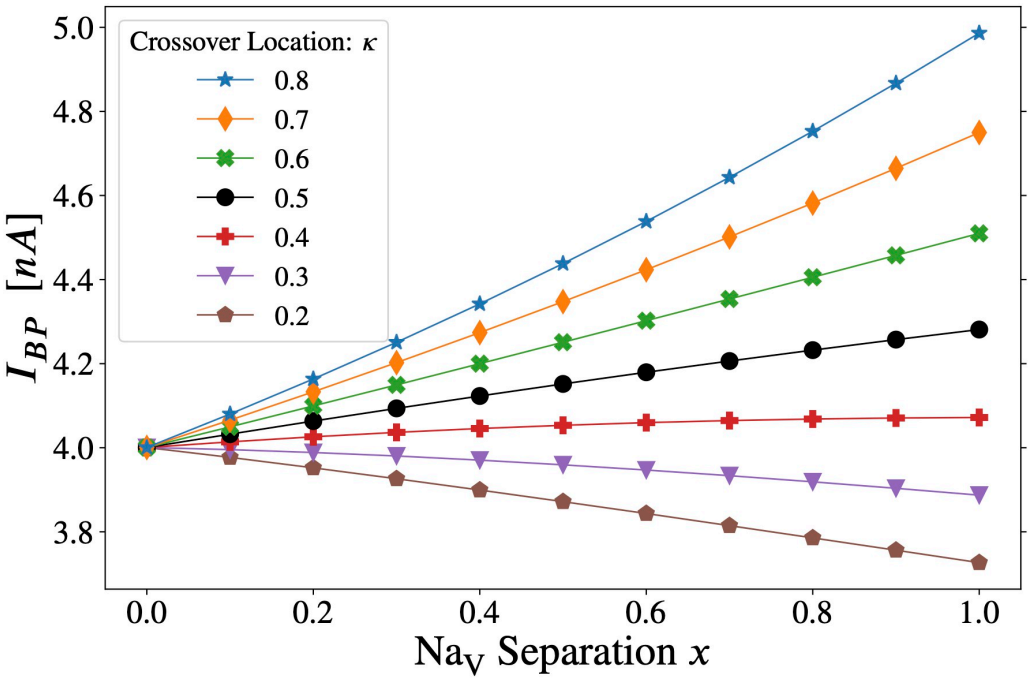

Fig 2. Somatic stimulation: Combined effect of varying crossover location (κ) and Na_V separation (x) in the axon initial segment. The threshold for forward AP propagation is the same as for backpropagation. Varying the separation parameter "x" from $x = 0$ to $x = 1$, the distribution of Na_V channels goes from flat (homogeneous) to separated, the latter approximating the distribution observed in developing pyramidal neurons (see Fig 1A). Note that curves for all values of κ converge to a single point at $x = 0$, since κ can have no effect when the two Na_V subtypes are uniformly distributed along the AIS. The lines have been drawn to guide the eye.

https://doi.org/10.1371/journal.pcbi.1011846.g002

- when $\kappa > 0.5$ and $x > 0$, the AIS is dominated by $Na_V1.2$: increasing x increases the proportion of total AIS Na_V conductance due to $Na_V1.2$ (positive slope: separated distribution yields the highest backpropagation threshold).

This effect is shown in Fig R in S1 Text. Although the above description is an appealing simplification, the impact of the spatial separation of Na_V subtypes (x) remains important, even when the AIS has equal amounts of $Na_V1.2$ and $Na_V1.6$. In other words, the combined effect of x and κ cannot be reduced to the resulting ratio of total $Na_V1.2$ versus $Na_V1.6$.

Lengthening the hillock with κ fixed also moves the crossover away from the soma. Curves with negative slope in Fig 2 became positively sloped when the hillock was lengthened from 10μm to 30μm (Fig O in S1 Text). The forward propagation threshold for somatic stimulation with a single 1ms current pulse is not included in a separate figure since it is identical to the backpropagation threshold in this model. This does not depend on the somatic injection site. The effect of Na_V gating properties in the AIS on backpropagation threshold is examined systematically in Modifying the *right-shift* of $Na_V1.2$ gating properties in the AIS.

An informative variation on Fig 2 is shown in Fig 3C in which the AIS is "put on backward", such that $Na_V1.2$ is concentrated in the distal AIS and $Na_V1.6$ is proximal to the soma. As one might expect, the effect of varying x and κ in Fig 3 is opposite to what is seen in Fig 2, albeit with some new curvature at low κ. This reinforces the observation that proximal $Na_V1.6$ facilitates backpropagation with somatic stimulation.

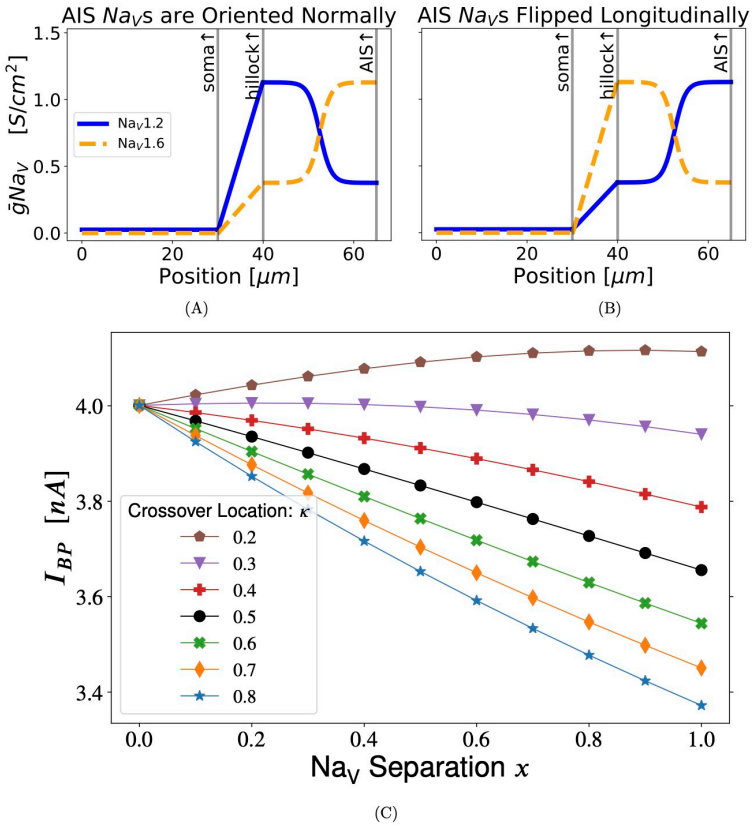

Fig 3. Somatic stimulation with a flipped Na_V distribution: Backward AIS. When the AIS Na_V distribution is flipped proximal-to-distal, setting $x = 1$ concentrates $Na_V1.6$ at the proximal AIS and $Na_V1.2$ at the distal AIS—the opposite of what is observed in many pyramidal cells [15–17]. **(A)** AIS with proper longitudinal placement of Na_Vs. **(B)** AIS with a longitudinally flipped Na_V distribution. In both plots, $x = 0.5$ and $\kappa = 0.5$. **(C)** Somatic stimulation with AIS Na_Vs flipped as in **(B)**: This result is close to a mirror image of Fig 2. The lines have been drawn to guide the eye.

https://doi.org/10.1371/journal.pcbi.1011846.g003

Axonal stimulation

With axonal stimulation (current injection just distal to the AIS), Na_V separation consistently lowers the backpropagation threshold (Fig 4). Contrary to somatic stimulation (Fig 2), moving the Na_V crossover (κ) toward the distal AIS shifts the backpropagation threshold curves downward.

The decreasing threshold with respect to x in Fig 4 is consistent with the conclusion from [15], which used axonal stimulation, that proximal $Na_V1.2$ in the AIS promotes backpropagation. Our results for κ, with axonal stimulation, provide new support for their findings.

This agreement is interesting because our method of modifying the AIS Na_V distribution (described above in Fig 1) is quite different from their simulations. Our transformations deliberately preserve the total Na_V density at every AIS segment—if $Na_V1.2$ is removed, $Na_V1.6$ must take its place. Conversely, in [15], the density profile of $Na_V1.2$ is scaled by a constant factor everywhere in the AIS, leaving the $Na_V1.6$ profile intact. We denote the scaling factor

$$\alpha_{Na_V1.2} \geqslant 0. \quad (1)$$

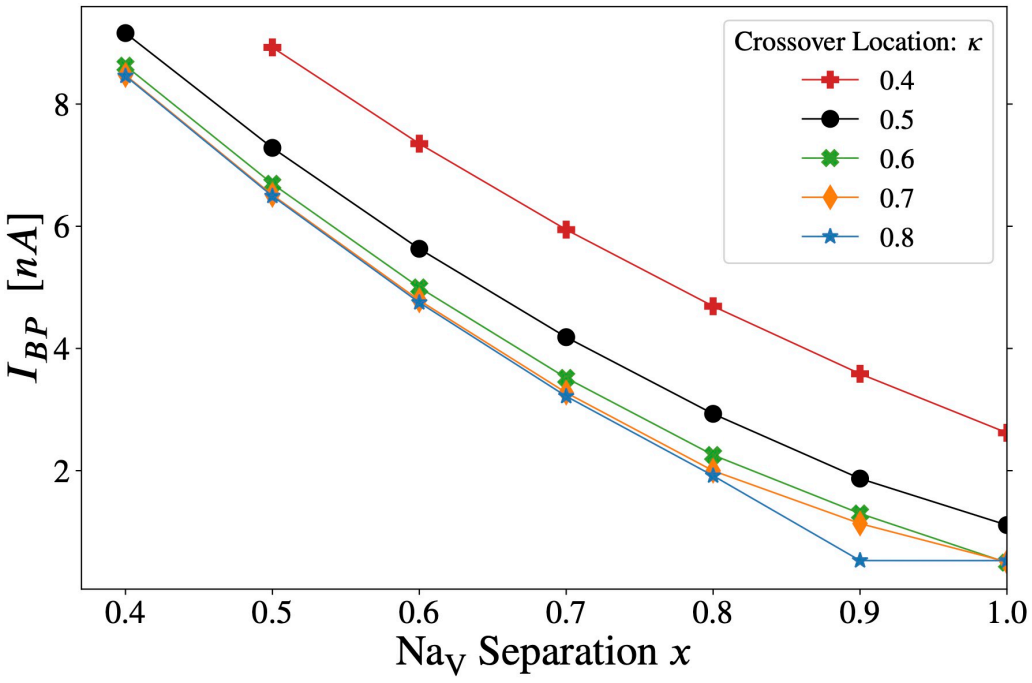

Fig 4. Axonal stimulation: Effect of varying crossover location (κ) and Na_V separation (x) in the AIS on the backpropagation threshold (see Fig 1). When computing the threshold, the stimulating current was limited to a maximum of 10nA, to prevent unphysiological local depolarization at the stimulation site. Due to the smaller diameter of the axon (relative to the soma), 10nA is sufficient to depolarize the membrane potential to $\approx +80$mV at the stimulation site, whereas the resting potential is $V_{rest} = -70$mV. To achieve backpropagation within that constraint (following axonal stimulation), our model required some amount of proximal $Na_V1.2$, delivered through the combined effects of Na_V separation ($x \gtrsim 0.5$) and a sufficiently distal crossover position $\kappa \gtrsim 0.4$. Separating the two Na_V subtypes ($x \to 1$) lowers the threshold, in agreement with the finding in [15] that proximal accumulation of $Na_V1.2$ promotes backpropagation, albeit due to different gating properties (Fig 6B). Increasing κ raises the proportion of $Na_V1.2$ (relative to $Na_V1.6$) in the AIS and lowers the backpropagation threshold as well. Threshold changes here are larger than for somatic stimulation (Fig 2). The lines have been drawn to guide the eye.

https://doi.org/10.1371/journal.pcbi.1011846.g004

That is, if the $Na_V1.2$ density profile is scaled down in [15], nothing is added to compensate for the missing channels. Under the latter transformation, we expect that $\alpha_{Na_V1.2} > 1$ would lower I_{BP} and $\alpha_{Na_V1.2} < 1$ would raise I_{BP} in our models as well, since scaling the density profile of $Na_V1.2$ in a separated distribution with a specified κ and $x > 0$ would scale the total AIS Na_V conductance, especially at the proximal AIS. We have reproduced this procedure in the Hay model, see Rescaling the $Na_V1.2$ density profile by a uniform factor in the AIS.

It is one thing to say that reducing (increasing) the total density of voltage-gated sodium channels in the proximal AIS, which happen to be $Na_V1.2$ channels, will raise (lower) the back-propagation threshold (respectively). But since we preserved the local Na_V density in our results (above), the changes to I_{BP} can only be a manifestation of the spatial heterogeneity of sodium channel *gating properties*. Since *right-shift* is the most important feature distinguishing $Na_V1.2$ from $Na_V1.6$ in this model, we included a sensitivity analysis, see Modifying the *right-shift* of $Na_V1.2$ gating properties in the AIS. The analysis in that section explains how the proximal accumulation of $Na_V1.2$ is able to simultaneously lower I_{BP} with axonal stimulation (Fig 4) and raise I_{BP} with somatic stimulation (Fig 2).

Forward propagation threshold

The forward-propagation threshold I_{FP}, also referred to as the AP threshold, is shown in Fig 5 for the Hu-based model. With axonal stimulation only, it is possible to elicit an action potential without creating sufficient depolarization in the apical dendrites to meet our strict criterion for backpropagation (see Figs D and C in S1 Text). Note, however, that the most distal dendrites depolarize to several mV above their local resting potential (see Fig Dii in S1 Text). Stimulation amplitude is an order of magnitude lower than in the case of I_{BP}. This is expected with axonal stimulation due to the high Na_V density of the distal AIS, its electrical isolation from the soma, its proximity to the stimulus, and our stringent definition of I_{BP} (Section B in S1 Text). (Antidromically stimulated axonal APs that do not trigger a somatodendritic BAP have been observed in several neuron types [36, 37].) Further, as discussed in [39], Hu et al. [15] built their model on [26], in which somatic invasion of the axonal action potential is reduced.

As with I_{BP}, increasing x lowers I_{FP}. Na_V separation concentrates $Na_V1.6$ in the distal AIS, making it more excitable in the portion nearer to the stimulation site. This finding is consistent with [15], who found that distal $Na_V1.6$ density places the lowest initiation threshold (and therefore the AP trigger zone) at the distal AIS. However, [35] has shown that cable properties are sufficient to explain why the trigger zone is located at the distal AIS (see Discussion). Moving the crossover distally ($\kappa \to 1$) increases the total proportion of $Na_V1.2$ in the AIS and thereby raises the I_{FP} threshold due to *activation right-shift*.

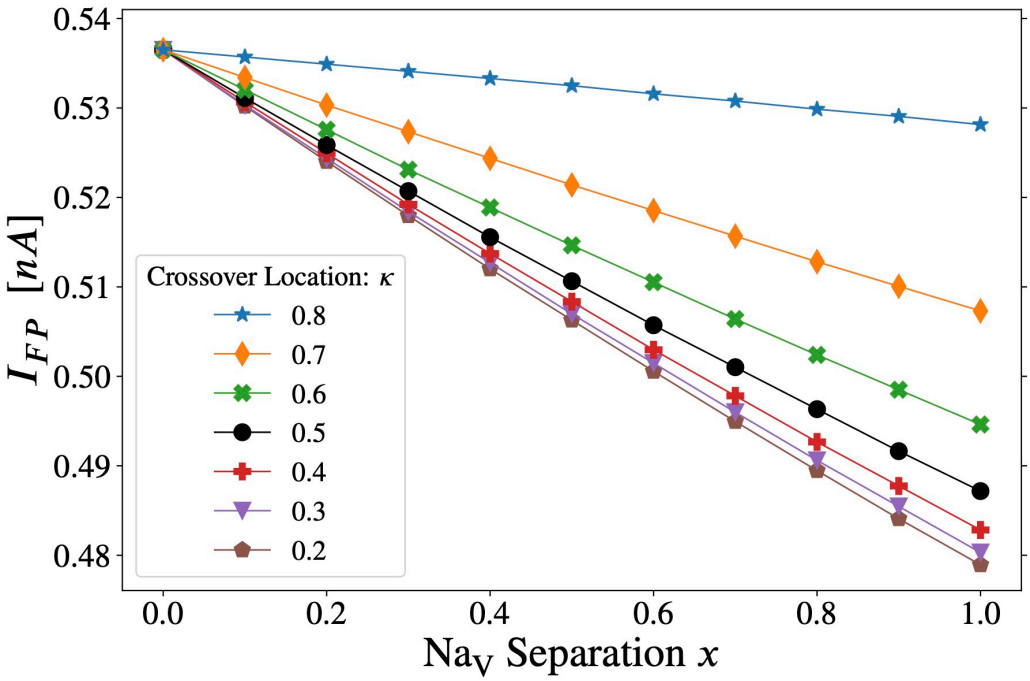

Fig 5. Axonal stimulation: Effect of x and κ on forward propagation threshold. The trend for all constant κ curves is that raising the proportion of total AIS $Na_V1.6$ (by reducing κ) or concentrating $Na_V1.6$ in the distal AIS (by increasing x) lowers the threshold to initiate forward propagating action potentials (see Fig 1). Note that although this threshold current pulse is not sufficient to satisfy our strict backpropagation criterion (see Section B in S1 Text), the most distal apical dendrites will be depolarized by several mV relative to their local resting potential (see Fig Dii in S1 Text). The lines have been drawn to guide the eye.

https://doi.org/10.1371/journal.pcbi.1011846.g005

Modifying the *right-shift* of $Na_V1.2$ gating properties in the AIS

Our results from varying the Na_V distribution may be counterintuitive. With axonal stimulation, concentrating low-threshold (i.e. *left-shifted*) $Na_V1.6$ channels at the distal AIS ought to promote forward propagation (and it does, see Fig 5), but why would concentrating the high-threshold (i.e. *right-shifted*) $Na_V1.2$ channels at the proximal AIS promote [15] backpropagation (see Fig 4)? And how does the asymmetry come about, such that separating Na_V subtypes can raise the backpropagation threshold with somatic stimulation, but always lowers it with axonal stimulation?

In this section, we perform a type of sensitivity analysis with respect to the effects of the *right-shifted* $Na_V1.2$ subtype. Fig 6 allows us to isolate the effects of *activation right-shift* versus *availability right-shift* on the backpropagation threshold.

Na_V subtypes are defined by their gating properties. Each Na_V distribution (Fig 1) produces a corresponding spatial profile of gating properties, including a profile of *right-shift*. (Gating properties are detailed in Section F in S1 Text, see Fig P in S1 Text.) In Fig 6, the AIS Na_Vs' separation is fixed at $x = 1$. This spatial separation of Na_Vs concentrates *right-shift* in the proximal AIS, by concentrating $Na_V1.2$ in that region (see Fig 1).

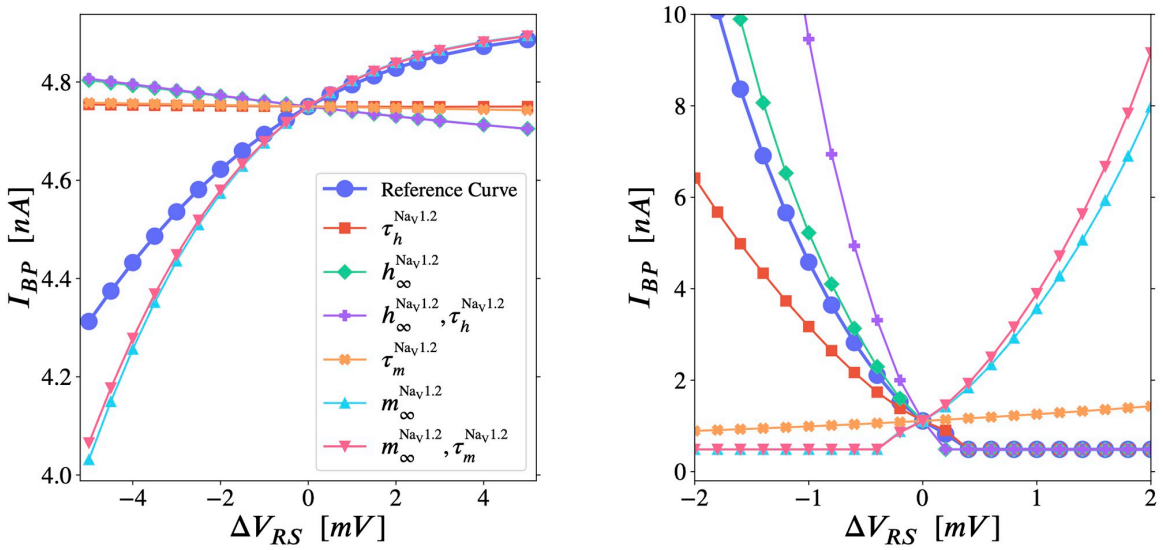

(A) Somatic stimulation (B) Axonal stimulation

Fig 6. Sensitivity analysis of the backpropagation threshold to the *right-shift* of $Na_V1.2$ gating properties. Along each curve, the gating properties named in the legend have their *right-shift* changed from V_{RS} to $(V_{RS} + \Delta V_{RS})$, and all the others are left unchanged (full definition and notation in Section F.2 in S1 Text). When $\Delta V_{RS} = 0$, the *right-shift* is the reference value (or 'nominal value') of 13.0mV used for $Na_V1.2$ in our simulations—see Section F.2 in S1 Text, V_{RS} indicated by small "→" in Fig P in S1 Text—around which we are performing this sensitivity analysis. The reference curve (legended ●) shows the net effect of *right-shifting* all $Na_V1.2$ properties on I_{BP}, via its slope. (It may be useful to imagine points on the reference curve as being pulled toward all the other curves that only change one property. The reference curve would then be the result of the combined pulls of those curves.) For each mode of stimulation, we identify the key gating properties through which *right-shift* controls backpropagation, by comparing the single property curves (▲$m_\infty^{Na_V1.2}$, ✕$\tau_m^{Na_V1.2}$, etc.) to the reference curve (●). **(A) Somatic stimulation**: The reference curve has a positive slope (*right-shift* raises I_{BP}), and it follows curves legended with $m_\infty^{Na_V1.2}$ near the nominal point (i.e. near $\Delta V_{RS} = 0$). Hence, I_{BP} is governed by Na_V steady-state *activation* and is insensitive to the *right-shift* of all Na_V time constants. **(B) Axonal stimulation**: The reference curve has a negative slope (*right-shift* lowers I_{BP}, i.e. promotes backpropagation), and it follows curves legended with $h_\infty^{Na_V1.2}$ or $\tau_h^{Na_V1.2}$. I_{BP} is then governed by proximal Na_V *availability*, owing to the *right-shift* of $Na_V1.2$. Notably, with axonal stimulation, I_{BP} is also sensitive to the *right-shift* of $\tau_h^{Na_V1.2}(V)$, the—voltage-sensitive—*availability* time constant. Results are summarized in Table 1. The lines have been drawn to guide the eye. In both plots, $x = 1.0$. On the left $\kappa = 0.7$(to increase the slope, see Fig 2), and on the right, $\kappa = 0.5$.

https://doi.org/10.1371/journal.pcbi.1011846.g006

Modifying the *right-shift* of all gating properties of $Na_V1.2$ in the AIS. Our model sets the nominal *right-shift* of $Na_V1.2$ at $V_{RS} = 13.0\text{mV}$ for compatibility with [15]. We use the parameter ΔV_{RS} to alter, in the AIS only, the *right-shift* of specific $Na_V1.2$ gating properties. (For additional details, see Sections F.2 and F.3 in S1 Text.)

When a gating property (e.g. $m_\infty^{Na_V1.2}$) appears next to a curve in the legend of Fig 6, the voltage-dependence of said property is displaced by ΔV_{RS} (see, e.g., Eq 3). Likewise, if a gating property is *not* displayed in the legend, its voltage-dependence *isn't* affected by ΔV_{RS}.

For conceptual clarity, we call the variable h—which models the process by which Na_V channels are inactivated (or blocked) in Hodgkin-Huxley style kinetics [40]—the *availability*. For example, since the $Na_V1.2$ conductance is given by $g_{Na_V1.2}(V,t) = \bar{g}_{Na_V1.2} * (m^{Na_V1.2})^3 h^{Na_V1.2}$—where $\bar{g}_{Na_V1.2}$ is the maximal conductance and $m^{Na_V1.2}$ is the *activation*—$h^{Na_V1.2}$ is the proportion of those channels which are *not* inactivated. That is, $h^{Na_V1.2}(V,t)$ is the probability that a $Na_V1.2$ channel selected at random is *available* to conduct sodium current. The inactivation is actually given by $(1 - h)$ since, in such models, all channels are inactivated when $h = 0$ and all are available when $h = 1$.

Note that the *activation* $m^{Na_V1.2}(V,t)$ and *availability* $h^{Na_V1.2}(V,t)$ of real $Na_V1.2$ channels are *right-shifted* by similar amounts when compared to the corresponding gating properties of $Na_V1.6$ [13, 15, 17, 21, 22]. (Although certain receptors can temporarily *right-shift activation* without shifting steady-state *availability* [41].) In our simulations, we can simultaneously decrease (or increase) the *right-shift* of $m^{Na_V1.2}$ and $h^{Na_V1.2}$ together, making the $Na_V1.2$ channels more (or less) similar to the $Na_V1.6$ channels in the AIS (respectively). This produces the 'reference curves' legended '●' in Fig 6A and 6B. In those curves, ΔV_{RS} shifts the voltage-dependence of every $Na_V1.2$ gating property.

That is, as functions of membrane potential, the steady states and time constants in the curves marked '●' are defined

$$\bullet \leftarrow \begin{cases} m_\infty^{Na_V1.2} = m_\infty^{Na_V1.2}(V - \Delta V_{RS}), \\ \tau_m^{Na_V1.2} = \tau_m^{Na_V1.2}(V - \Delta V_{RS}), \\ h_\infty^{Na_V1.2} = h_\infty^{Na_V1.2}(V - \Delta V_{RS}), \\ \tau_h^{Na_V1.2} = \tau_h^{Na_V1.2}(V - \Delta V_{RS}), \end{cases} \tag{2}$$

in the AIS.

Fig 6 connects local gating properties in the AIS, and their influence on the backpropagation threshold under somatic and axonal stimulation, to the effects of altering the Na_V distribution (seen above in Figs 2 and 4, respectively). For example, making ΔV_{RS} negative will *left-shift* the voltage-gated sodium current in the proximal AIS, which is analogous to adding more proximal $Na_V1.6$. However, this is merely an analogy: With $x = 1$ and $\kappa \gtrsim 0.8$, the proximal AIS has only $Na_V1.2$ channels, and positive values of ΔV_{RS} will *right-shift* the sodium current in that area beyond what is attainable by changing the local mix of Na_V subtypes.

The reference curve (●) in Fig 6A shows that *right-shifting* Na_Vs in the AIS *increases* I_{BP} for somatic stimulation. And the reference curve in Fig 6B confirms that proximal *right-shift* from $Na_V1.2$ *lowers* I_{BP} for axonal stimulation.

Modifying the *right-shift* of selected gating properties of $Na_V1.2$ in the AIS. Since ΔV_{RS} only affects $Na_V1.2$ channels *within the AIS* (example provided in Fig Qii in S1 Text), we can determine which *right-shifted* gating properties drive the changes to I_{BP} that occur when the Na_V distribution is altered. To make said observation, in Fig 6 we also "shift-clamp" selected gating properties: We ignore the experimental fact that Na_V *activation* and *availability* tend to *right-shift* in unison [17, 21, 22, 42, 43], and that the steady-state of a gating variable and its

voltage-sensitive time constant *right-shift* together as well [40]. Rather, we isolate the effects of individual $Na_V1.2$ gating properties in our simulations by shifting some of them while leaving others alone.

We can apply ΔV_{RS} to $Na_V1.2$ *availability* $h^{Na_V1.2}(V,t)$ without affecting the voltage dependence of the same channels' *activation* $m^{Na_V1.2}(V,t)$ in our model. This is done via the steady-state *availability* $h_\infty^{Na_V1.2}(V-\Delta V_{RS})$ and its voltage-dependent time constant $\tau_h^{Na_V1.2}(V-\Delta V_{RS})$, while leaving the corresponding *activation* variables—$m_\infty^{Na_V1.2}(V)$ and $\tau_m^{Na_V1.2}(V)$—unchanged. The curve legended "✚$h_\infty^{Na_V1.2}$, $\tau_h^{Na_V1.2}$" does just that, and likewise, in the "▼$m_\infty^{Na_V1.2}$, $\tau_m^{Na_V1.2}$" curve, the $Na_V1.2$ *activation* is shifted by ΔV_{RS} without affecting *availability*.

Further, we apply ΔV_{RS} to $\tau_h^{Na_V1.2}(V)$ without modifying any other gating properties—including $h_\infty^{Na_V1.2}(V)$—in the curve legended "■$\tau_h^{Na_V1.2}$". We do the same for $h_\infty^{Na_V1.2}(V)$, $\tau_m^{Na_V1.2}(V)$ and $m_\infty^{Na_V1.2}(V)$, in the curves legended "◆$h_\infty^{Na_V1.2}$", "✕$\tau_m^{Na_V1.2}$", and "▲$m_\infty^{Na_V1.2}$" respectively. Fig 6 computes the new backpropagation threshold $I_{BP}(\Delta V_{RS})$ under the aforementioned transformations. (For mathematical details, see Shift-Clamping and the Hodgkin-Huxley model in Materials and methods, and Section F.2 in S1 Text.)

An example transformation is given below by Eq 3, in which only $\tau_h^{Na_V1.2}(V)$ has its *right-shift* modified by ΔV_{RS} (see Fig Qii in S1 Text). The other three $Na_V1.2$ variables have the nominal *right-shift* of 13mV. The $I_{BP}(\Delta V_{RS})$ curves in Fig 6 that correspond to Eq 3 are legended ■$\tau_h^{Na_V1.2}$:

$$\blacksquare\,\tau_h^{Na_V1.2} \leftarrow \begin{cases} \tau_h^{Na_V1.2} = \tau_h^{Na_V1.2}(V-\Delta V_{RS}) \\ h_\infty^{Na_V1.2} = h_\infty^{Na_V1.2}(V) \\ \tau_m^{Na_V1.2} = \tau_m^{Na_V1.2}(V) \\ m_\infty^{Na_V1.2} = m_\infty^{Na_V1.2}(V). \end{cases} \tag{3}$$

(Fig Q in S1 Text visualizes the impact of Eq 3 on gating properties as a function of position at V_{rest}.)

To unpack these additional curves, we begin at the coordinate we will call 'the nominal point' in each plot of Fig 6, which is the backpropagation threshold at $\Delta V_{RS} = 0$, where all curves must intersect by definition. Starting at the nominal point, as one moves leftward along a given curve ($\Delta V_{RS} < 0$), the gating properties indicated in the legend are *left-shifted* (e.g. Eq 3), and the other gating properties are left alone. Likewise, travelling away from the nominal point to the right ($\Delta V_{RS} > 0$) will *right-shift* the indicated properties, relative to their nominal kinetics (Fig P in S1 Text).

Fig 6B reveals that, with axonal stimulation, the *right-shifted availability* ($h^{Na_V1.2}$) drives I_{BP}. Specifically, the curves legended ◆$h_\infty^{Na_V1.2}$, ■$\tau_h^{Na_V1.2}$, and ✚$h_\infty^{Na_V1.2}$, $\tau_h^{Na_V1.2}$ show how $h_\infty^{Na_V1.2}$ (the *availability* at steady-state, as a function of membrane potential) and $\tau_h^{Na_V1.2}$ (the voltage-dependent time constant of *availability*) work together to promote backpropagation: They drive the reference curve (●) downward as ΔV_{RS} increases, in spite of the higher *activation* threshold. In other words: The threshold-lowering effects that result from *right-shifting* the *availability* overpower the opposing influence of *right-shifted activation*—on its own the latter would raise the threshold (see the curves: ▲$m_\infty^{Na_V1.2}$ and ▼$m_\infty^{Na_V1.2}$, $\tau_m^{Na_V1.2}$ in Fig 6B).

Further, removing the *right-shift* from $\tau_h^{Na_V1.2}$ stops backpropagation: In the ■$\tau_h^{Na_V1.2}$ curve of Fig 6B, all gating properties other than $\tau_h^{Na_V1.2}$, including $h_\infty^{Na_V1.2}$, retain their nominal *right-shift*, yet backpropagation ceases (according to our strict BAP criterion, see Section B in S1 Text) for axonal stimulation when $\Delta V_{RS} \lesssim -2$mV.

Table 1. Summary of sensitivity analysis: Impact of *right-shifted* $Na_V1.2$ gating properties in the AIS on backpropagation threshold (see Fig 6).

Type of Stimulation	● reference curve	Increasing ΔV_{RS} of *availability*			Increasing ΔV_{RS} of *activation*		
		■ $\tau_h^{Na_V1.2}$	◆ $h_\infty^{Na_V1.2}$	+ $h_\infty^{Na_V1.2}$, $\tau_h^{Na_V1.2}$	× $\tau_m^{Na_V1.2}$	▲ $m_\infty^{Na_V1.2}$	▼ $m_\infty^{Na_V1.2}$, $\tau_m^{Na_V1.2}$
Axonal	↓	↓	↓	↓	↑(slight)	↑	↑
Somatic	↑	×	↓(slight)	↓(slight)	×	↑	↑

Arrows (↓,↑) indicate the sign of the **slopes** of backpropagation threshold curves in Fig 6A (somatic stimulation) and Fig 6B (axonal stimulation). A downward arrow (↓) indicates that the backpropagation threshold I_{BP} decreases with increasing *right-shift*, applied to the gating properties specified above it. Likewise, an upward arrow (↑) indicates that the threshold increases when the specified combination of $Na_V1.2$ variables is *right-shifted*. In cells marked "×" the effect of *right-shift* was negligible.

https://doi.org/10.1371/journal.pcbi.1011846.t001

For somatic stimulation, the *right-shifted activation* ($m^{Na_V1.2}$) drives I_{BP}. Travelling from right to left in Fig 6A, the most significant decrease in threshold occurs in the curves legended ▲$m_\infty^{Na_V1.2}$ and ▼$m_\infty^{Na_V1.2}$, $\tau_m^{Na_V1.2}$ as the nominal *right-shift* is removed ($\Delta V_{RS} \to -13.0\text{mV} \Rightarrow V_{RS} + \Delta V_{RS} \to 0$, see Fig P in S1 Text). The ▼$m_\infty^{Na_V1.2}$, $\tau_m^{Na_V1.2}$ curve differs negligibly from the ▲$m_\infty^{Na_V1.2}$ curve, showing that $m_\infty^{Na_V1.2}$ *right-shift* dominates in raising the threshold near the nominal point, and the *right-shift* of $\tau_m^{Na_V1.2}$ matters little.

Our ΔV_{RS} results from Fig 6 are summarized in Table 1.

Generalization to Hay-based model and modified Hu-based model

To demonstrate that our primary result—the separation of $Na_V1.2$ and $Na_V1.6$ into the proximal and distal AIS, respectively, promotes backpropagation with axonal stimulation but can *increase or decrease* I_{BP} with somatic stimulation—is not an artifact of our implementation of the model from Hu et al. (2009) [15] used thus far, we have inserted Na_V distributions analogous to Fig 1 into the model of Hay et al. (2011) [29] below. (Cell morphology in Fig B in S1 Text.)

(Also, in Section D in S1 Text, we include a modified version of the Hu-based model, with increased dendritic excitability and a less excitable soma. It has robust backpropagation in the entire dendritic tree without attenuation. Despite its 10× higher dendritic excitability, 3× lower somatic excitability, and qualitatively different backpropagation pattern, the results reported above are reproduced there as well.)

We replaced the single population of Na_Vs in the Hay model's 60μm AIS with two Na_V subtypes, based on their original Na_V kinetics: One population *left-shifted* by 6mV and the other *right-shifted* by 6mV, relative to the original $V_{1/2}$, to represent $Na_V1.6$ and $Na_V1.2$ respectively. Our manipulations of the Na_V channels' distribution (varying κ and x) did not change the total Na_V density in the AIS, which was kept identical to their model (https://modeldb.science/139653). Further, we attached an additional 400μm-long section of passive cable to the end of the AIS, where their axon originally stopped, to allow the AP to exit the AIS orthodromically as well as antidromically, as is the case in real neurons, in order to make AP generation in the Hay model more realistic. This was necessary to recover our qualitative results.

Our intention was to modify the Hay model as little as was necessary, since its parameters are tailored to a specific neuron and morphology—they will not necessarily transfer well even between specimens of the same cell type (see Hay et al. (2011) [29]). Presumably, the tuning may also be sensitive to the excitability of newly attached compartments.

We note that Hay et al. optimized their models to fit experimentally observed somatic and dendritic spiking patterns, including BAC firing, but their focus was not on action potential initiation. The models that best fit their data had AP initiation in the soma rather than the AIS, but they provide an additional model where APs were constrained to initiate in a 60μm section

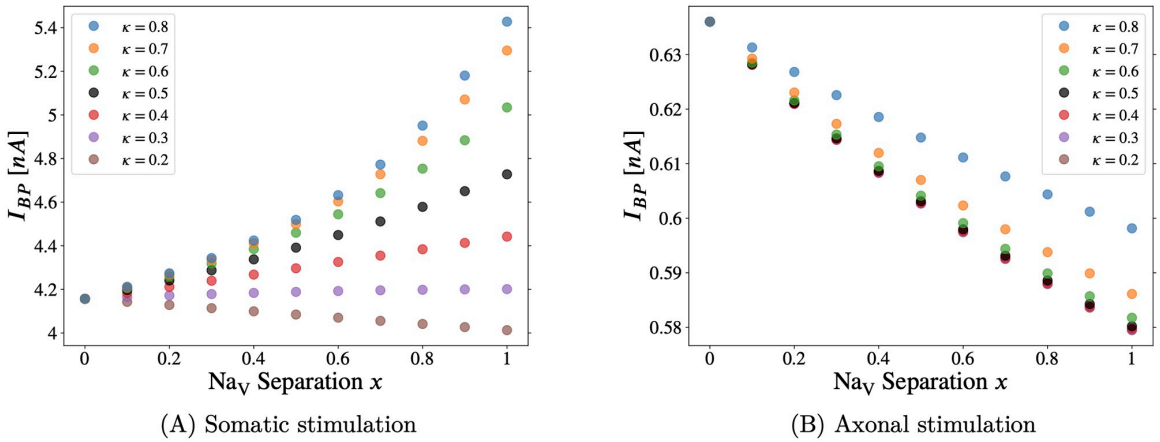

Fig 7. Backpropagation threshold in the Hay model: Combined effect on the backpropagation threshold (I_{BP}, defined below) of varying crossover location (κ) and Na_V separation (x) in the axon initial segment. Varying the separation parameter "x" from $x = 0$ to $x = 1$, the distribution of Na_V channels goes from flat (homogeneous) to separated, the latter approximating the distribution observed in developing pyramidal neurons (see Fig 1A, [20]). Note that curves for all values of κ converge to a single point at $x = 0$, since κ can have no effect when the two Na_V subtypes are uniformly distributed along the AIS. Apical dendrite backpropagation criterion $= -70.0\text{mV}$—see caption of Fig E in S1 Text. In the Hay model, the forward propagation threshold I_{FP} is not defined: There is no nowhere for saltatory conduction to occur, as there is no excitable axon beyond the AIS [29].

https://doi.org/10.1371/journal.pcbi.1011846.g007

named "axon", which had been set aside due to excessive BAP attenuation (see [29]). Since we required a parameter tuning with AP initiation in the AIS, the latter model was the necessary choice, despite its unrealistically strong attenuation of the backpropagated AP.

In Fig 7 we register backpropagation in the Hay model [29] as a depolarization of several mV in the apical dendrites, following current injection. Identical results using a somatic backpropagation measurement criterion are included as Fig F in S1 Text. The threshold was set at -70mV when measuring the depolarization near the bifurcation of the main apical dendrite, where $V_{\text{rest}} \cong -74.1\text{mV}$. See Fig E in S1 Text.

Note the qualitative agreement between the Hay-based model implemented and the Hu-based model above (and the modified Hu-based model in the Supporting Information (Section D in S1 Text)). In Fig 7A, we simulate backpropagation following somatic stimulation. As above in Fig 2 (and Fig H in S1 Text), concentrating $Na_V1.2$ in the proximal AIS tends to raise the backpropagation threshold, and increasing the proportion of total sodium conductance in the AIS allocated to $Na_V1.6$ lowers I_{BP}.

In Fig 7B, we simulate backpropagation following axonal stimulation. As above in Figs 4 and 5 (and Fig J in S1 Text), the separated Na_V distribution ($x \to 1$) lowers the threshold in the Hay model. Quantitatively, Fig 7B is closer to Fig 5, suggesting that the concentration of low-threshold $Na_V1.6$ at the distal AIS, rather than the concentration of $Na_V1.2$ at the proximal AIS, promotes backpropagation. What is important to keep in mind is that, in both models, concentrating $Na_V1.2$ in the proximal AIS only lowered I_{BP} in the case of depolarizing axonal current injection.

Rescaling the $Na_V1.2$ density profile by a uniform factor in the AIS

In this section, we rescale the $Na_V1.2$ density profile in the Hay-based model via the maximal conductance $\bar{g}_{Na_V1.2}$. At each segment of the AIS, $\bar{g}_{Na_V1.2}$ is multiplied by a positive number

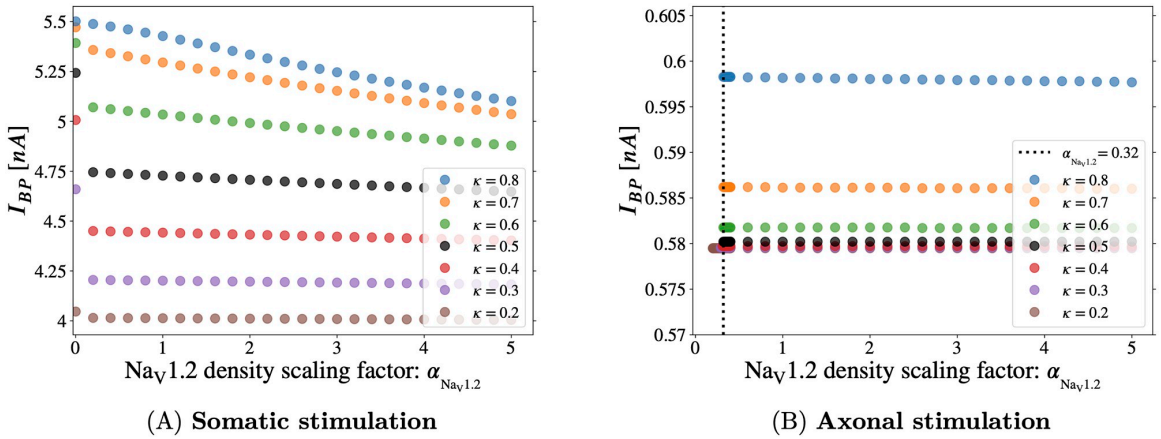

Fig 8. Scaling the $Na_V1.2$ density profile in the AIS of the Hay-based model [29], with somatic vs. axonal stimulation. The backpropagation threshold is computed while the local $Na_V1.2$ density is rescaled by $\alpha_{Na_V1.2}$ at every AIS segment. Here we have set $x = 1$ so that the $Na_V1.2$ and $Na_V1.6$ density profiles are separated, guaranteeing that the proximal AIS is exclusively populated with $Na_V1.2$—see Fig 1. With somatic stimulation **(A)**, backpropagation persists even when $Na_V1.2$ is completely removed from the AIS ($\alpha_{Na_V1.2} = 0$). However, with axonal stimulation **(B)**, backpropagation ends abruptly near $\alpha_{Na_V1.2} \lesssim 0.32$. Yet again, the importance of the proximal $Na_V1.2$ subtype and its qualitative effects on excitability depend heavily on the mode of stimulation. Density of data points is increased near the vertical dashed line to detect backpropagation cutoff.

https://doi.org/10.1371/journal.pcbi.1011846.g008

which we call the $Na_V1.2$ scaling factor, denoted $\alpha_{Na_V1.2}$. That is, at each point s in the AIS,

$$\bar{g}_{Na_V1.2}(s) \to \alpha_{Na_V1.2}\bar{g}_{Na_V1.2}(s), \tag{4}$$

with $\alpha_{Na_V1.2} \geqslant 0$. In Fig 8A the backpropagation threshold is computed with somatic current injection (see Fig E in S1 Text). We observe that reducing the density of $Na_V1.2$, without adding any compensatory $Na_V1.6$ density, increases the threshold as expected—the slope is most visible on the $\kappa = 0.8$ line of Fig 8A, wherein the majority of the AIS (except the most distal region, see Fig 1B) contains $Na_V1.2$ and is therefore affected by $\alpha_{Na_V1.2}$. Even when $Na_V1.2$ is completely removed from the AIS, and consequently the proximal AIS contains no Na_V channels, backpropagation is possible with somatic stimulation.

In Fig 8B it is interesting to see, yet again, the sharp qualitative difference in the role of the $Na_V1.2$ subtype with axonal versus somatic stimulation. As noted above, backpropagation is present in Fig 8A when the AIS $Na_V1.2$ channels are disabled entirely ($\alpha_{Na_V1.2} = 0$). With axonal stimulation however (Fig 8B), the effect of $\alpha_{Na_V1.2}$ was abrupt and binary, akin to a Heaviside function. I_{BP} was nearly flat, except the Hay neuron did not produce a BAP when $\alpha_{Na_V1.2} \lesssim 0.32$—some nonzero Na_V density was required in the proximal AIS for backpropagation.

With somatic stimulation, the neuron is primed for backpropagation by the electrode current, which depolarizes the soma before the AP arrives from the AIS. As $\alpha_{Na_V1.2} \to 0$, increased somatic stimulation can compensate for the resulting loss of depolarizing Na_V current from the proximal AIS.

With axonal stimulation, there is no direct pre-charging of the soma by the injected current pulse. When $\alpha_{Na_V1.2}$ decreases the density of channels at the proximal AIS, the electrode cannot compensate for the lost $Na_V1.2$ current, due to its electrical isolation from the soma. The abrupt BAP cutoff reflects the all-or-none nature of action potentials. The lack of slope in I_{BP}

owes to the fact that the axonal current pulse depolarizes the most distal end of the AIS, which sets the threshold in this case [15] (provided the proximal Na_V density is sufficient, see above). The distal AIS is populated exclusively by $Na_V1.6$ channels, and hence it is unaffected by $\alpha_{Na_V1.2}$.

Discussion

In early development, pyramidal neurons concentrate $Na_V1.2$ in the proximal AIS, and $Na_V1.6$ in the distal AIS. As these cells mature, $Na_V1.6$ invades the proximal AIS, and the two Na_V subtypes lose their separated distribution [20]. We have investigated the effects of Na_V separation in the axon initial segment on the initiation and backpropagation of action potentials in three different pyramidal neuron models. In spite of their different parameters, axonal and dendritic morphology, and biophysics, all three models (see: Somatic stimulation, Axonal stimulation, Modifying the *right-shift* of $Na_V1.2$ gating properties in the AIS, Generalization to Hay-based model and modified Hu-based model, and Section D in S1 Text) indicated that the effects of the separated Na_V distribution depend on whether stimulation is orthodromic (e.g. somatodendritic input) or antidromic (e.g. axonal stimulation).

With somatic stimulation, the greater the proportion of $Na_V1.2$ in the AIS, relative to $Na_V1.6$, the less excitable the cell becomes (increased I_{BP}). Our somatic current injection results are contrary to past modelling which used axonal stimulation [15], although they are consistent with more recent experimental results that used somatic stimulation [18]. The threshold-raising effect of proximal $Na_V1.2$ is confirmed by repeating the simulations with a model cell in which the AIS has been flipped longitudinally (Fig 3), placing $Na_V1.6$ proximally and $Na_V1.2$ distally in the AIS.

Our results using axonal stimulation agree qualitatively with and expand upon past modelling efforts [15]: In all three models, with axonal current injection, excitability is greatest (lowest I_{BP}) when Na_V subtypes are separated in the AIS ('*x*-shaped distribution'). Further, in the Hu-based models (Fig 4, Fig J in S1 Text), increasing the total proportion of $Na_V1.2$ in the AIS —by moving the Na_V crossover κ distally—promotes backpropagation as well. In the Hay-based model, removing Na_Vs from the proximal AIS halted backpropagation. We also find that increased distal $Na_V1.6$ concentration (which results from the separated distribution) lowers the AP threshold (Fig 5).

Testing both modes of stimulation can contribute to resolving inconsistencies between experiments such as [18] and [15], where stimulation was orthodromic in the former and antidromic in the latter. In [18], AP initiation was observed in pyramidal neurons which were engineered to be $Na_V1.6$-deficient. In those neurons, the AIS was populated entirely with $Na_V1.2$, however they still found that the AIS Na_V current was *left-shifted* relative to the somatic current. From this and other observations, the authors in [18] suggest that the distribution of Na_V subtypes is not so important in shifting the local voltage-gated Na^+ current.

We note that, compared to control neurons, the $Na_V1.6$-deficient neurons' AIS Na_V current was *right-shifted*, and the orthodromic AP threshold (amplitude of a 2ms current pulse [18]) was nearly doubled. This is consistent with our results and the modelling assumption that *right-shift* is associated with $Na_V1.2$ in the AIS—the model is agnostic about the molecular details. The decrease in excitability reported in [18] may have been even larger had they used more mature neurons. Their neurons were obtained from 4–5 week old mice, at which point the AIS will still be largely populated with $Na_V1.2$, whereas in wild type mice $Na_V1.6$ replaces much of the $Na_V1.2$ by 90 days [20, 30]. Our results indicate that with axonal stimulation, $Na_V1.6$-deficient cells may have a lower backpropagation threshold than the wild type.

The loss of the separated Na_V distribution in the AIS at later developmental stages, accompanied by the proximal localization of $Na_V1.6$, may enhance excitability to healthy orthodromic stimulation while protecting against the backpropagation of ectopic activity from damaged axons into the soma and dendrites. Further, research into the genetic causes of autism spectrum disorder has revealed that $Na_V1.2$ knockout can enhance pyramidal cells' tendency to send action potentials and simultaneously reduce backpropagation (somatodendritic hypoexcitability) [19]. Whereas [19] reported an interplay between $Na_V1.2$ and K_V, in contrast, our results are explained by the spatial distribution of Na_V *right-shift* within the AIS (Table 1, Fig 6A). Indeed, the reduced excitability resulting from AIS $Na_V1.2$ owes to the asymmetric impact of *availability* on backpropagation in axonal versus somatic stimulation (Fig 6).

Although *right-shifting* $Na_V1.2$ steady-state *availability*, $h_\infty^{Na_V1.2}(V)$, in the AIS is necessary to promote backpropagation (i.e. decrease I_{BP}) when stimulation is axonal, it is not sufficient on its own. Our modelling shows that the voltage-sensitive time constant of *availability*, $\tau_h^{Na_V1.2}(V)$, must be *right-shifted* as well (Fig 6B, ■$\tau_h^{Na_V1.2}$ curve).

It is straightforward to explain why increasing ΔV_{RS} lowers I_{BP} in the ◆$h_\infty^{Na_V1.2}$ curves of Fig 6A and 6B: *Right-shifting* steady-state $Na_V1.2$ *availability* increases Na^+ conductance at all voltages because $h_\infty^{Na_V1.2}(V)$ is monotonically decreasing (Fig Pi in S1 Text). However, without sensitivity analysis, it was *not* obvious that removing the nominal *right-shift* from the voltage-sensitive time constant $\tau_h^{Na_V1.2}$—without modifying steady-state *activation* ($m_\infty^{Na_V1.2}$) or *availability* ($h_\infty^{Na_V1.2}$)—would on its own be sufficient to eliminate the I_{BP}-lowering effects of $Na_V1.2$ for axonal stimulation. This effect is demonstrated in the curve legended ■$\tau_h^{Na_V1.2}$ of Fig 6B. It follows that the *x*-distribution's tendency to promote backpropagation is not merely a result of increased steady-state *availability* of proximal AIS Na_Vs, but is a dynamic effect—dependent on the *right-shift* of $\tau_h^{Na_V1.2}(V)$ as well.

From Fig Pii in S1 Text, we can see that *right-shifting* $Na_V1.2$ slows down the *inactivation* process via its time constant—which is the voltage-sensitive time constant of *availability*. The membrane potential traverses the $\tau_h^{Na_V1.2}(V)$ curve during an AP. *Right-shifting* $\tau_h^{Na_V1.2}(V)$ moves the maximum value of the time constant to depolarized voltages, and slows down *inactivation* so that more channels are *available* to assist with backpropagation.

There is an interplay between cable properties and the distribution of Na_Vs in determining the site of AP initiation [44]. Electrical isolation of the initiation site may amplify the effect of concentrating $Na_V1.6$ in the distal AIS. Via fluorescence imaging of intracellular Na^+ concentration following single action potentials, [35] located the greatest Na^+ influx at the middle of the AIS, whereas the distal AIS (initiation site) had only 1/4 of this maximum. They inferred that the density of Na_V channels decreases toward the initiation site, and thus Na_V density does not determine the precise location where APs begin.

Although [35] did not require $Na_V1.6$ accumulation at the distal AIS to explain the distal location of the initiation site, the authors suggest that local Na_V density can have a large effect on neuronal excitability. Temperature may also play a role in local AIS Na^+ influx measurements due to the spatial separation of Na_V subtypes. The pyramidal neurons in [35] and [18] were cooled to $\cong 21^\circ$, and $Na_V1.2$ and $Na_V1.6$ differ in their responses to temperature changes [17]. Thus, a deeper exploration of the effects of temperature on AP initiation is warranted.

The temporal resolution of Na^+ influx measurements continues to improve: [45] achieved a resolution of 0.1ms imaging pyramidal cells in mouse brain slices. Another order of magnitude improvement may be sufficient to discern the local contributions of Na_V subtypes to AP initiation. The qualitative dependence of the backpropagation threshold on the somatic-versus-axonal mode of stimulation is compatible with distal AP generation as found in [15, 35] and in our work, but does not seem to rely crucially on the precise determinants of AP onset

position; it relies rather on the *activation* and *availability* properties, and the kinetics of the latter.

The effect of realistic synaptic input is a broad interesting question that is beyond the scope of this study. Furthermore, including it at this point would defeat the purpose of comparing axonal versus somatic stimulation, since antidromic axonal input will be in the form of a brief pulse (no excitatory synaptic input typically occurs onto axons of pyramidal neurons, and when it does it generates an AP). Because our simulations compare orthodromic stimulation to antidromic stimulation, the shape of the injected current must be kept identical in each mode to isolate the effect of the Na_V density profiles on I_{BP}.

We would expect that fast glutamatergic input near the soma, or propagating to the soma from sufficiently synchronized dendritic synaptic inputs, would yield qualitatively similar results as reported here. There may be qualitative changes if the synaptic input has a slower rise time, e.g. for synapses with a large NMDA component.

Since the Na_V distribution changes throughout development, a further investigation—beyond the scope of this paper, as we will explain—would be to understand how accompanying developmental changes in morphological complexity and voltage-gated channel density elsewhere in the neuron [46] interact with developmental plasticity in the AIS. This would require new parameter sets at each iteration of the morphological complexity. Since Hay et al. [29] had to fit each morphology's parameter set to match firing patterns observed in real neurons, that procedure would need to be repeated. If sufficient experimental data are not available to perform the fitting at each iteration, new electrophysiological experiments would be necessary at the corresponding developmental stages. That endeavour is beyond the scope of the present study. Also, there is experimental evidence that AIS plasticity is not limited to development [6]. Our strategy was to restrict our investigation to the effects of varying the heterogeneous distribution of Na_V subtypes in the AIS on backpropagation threshold, with different modes of stimulation. Note, that the changing Na_V distributions we simulate are not strictly intended to replicate observed plasticity. Even if the Na_V distribution in the AIS of real neurons were static, modelling the hypothetical distributions would nonetheless assist in understanding its function via the resulting changes to cellular excitability.

Our model neurons were kept identical in all results presented above; only the AIS was altered. Our results therefore can only be explained by the distribution of Na_V subtypes (or, the distribution of *right-shifted* Na_V gating properties) within the AIS. Given the τ_h-dependence of the antidromic backpropagation threshold in Modifying the *right-shift* of $Na_V1.2$ gating properties in the AIS, and the differential temperature sensitivity of $Na_V1.2$ versus $Na_V1.6$ [17], there is good reason to expect that the effects of Na_V separation predicted here will be temperature-dependent.

In summary, we have simulated a range of hypothetical Na_V distributions in the axon initial segment of three 3D-reconstructed biophysical pyramidal cell models, including two distinct morphologies and three different parameter tunings. Our modelling shows that the spatial profile of $Na_V1.2$ and $Na_V1.6$ in the AIS and the kinetics of their *availability* and *activation* are important determinants of excitability and the backpropagation threshold. We predict that the separation of Na_V subtypes observed in early development has an asymmetrical effect on excitability which depends on whether the neuron is stimulated orthodromically or antidromically. With orthodromic stimulation, Na_V separation impedes backpropagation and reduces excitability unless the crossover is brought close to the soma. Backpropagation and excitability are both enhanced by Na_V separation when stimulation is antidromic. Maintaining a static Na_V distribution, we altered the *right-shift* of selected $Na_V1.2$ gating properties. This revealed that steady-state *activation right-shift* controls the orthodromic backpropagation threshold, and dynamic *availability right-shift* is necessary to explain the antidromic threshold. Furthermore,

given that learning is linked to backpropagation, the evolving separation of the Na_V subtypes may impact synaptic weight modification across developmental stages.

Materials and methods

The pyramidal cell models (Figs A and B in S1 Text) were implemented in NEURON 8.0 [47] via Python. For cell geometry, local membrane properties, additional simulations, and a variety of calculations, clarifications, and definitions, see S1 Text, which has its own table of contents.

Our Hay-based model is biophysically and morphologically identical to the original [29], aside from the modified *right-shift* in axonal Na_V channels that we introduced to create $Na_V1.2$ and $Na_V1.6$ variants in the AIS, and an additional passive section attached to the end of the axon. Our implementation of the Hay model (https://modeldb.science/139653) is detailed in Generalization to Hay-based model and modified Hu-based model.

Our Hu-based model [15] uses the same reconstructed morphology as the original model (https://modeldb.science/123897), which is a Layer 5 pyramidal neuron from cat visual cortex, modified from [26] (see SI, Section A in S1 Text). We added explicit intracellular and extracellular concentrations of sodium, potassium, and chloride ions. Because of this change, the Nernst potentials E_{Na^+}, E_{K^+}, E_{Cl^-} are calculated locally from each compartment's specific ionic concentrations, which respond to transmembrane currents. The $Na_V1.2$, $Na_V1.6$, and K_V kinetics from [15] are included as well.

We also included active transport via a Na^+/K^+-pump current, to maintain the transmembrane concentration gradients of Na^+ and K^+. In our Hu-based model, all ions are subject to longitudinal diffusion, both intra- and extracellular, implemented using NEURON's RxD facility [48, 49]. The cell maintains a resting potential $V_{rest} \cong -70\text{mV}$ at steady-state, and restores this state following stimulation. The biophysics that governs local ion concentrations (and Nernst potentials) in the Hu-based model is summarized in Biophysics, Hu-based model.

AIS—Na_V density profiles

In all of the models presented in this study, the density profiles of $Na_V1.2$ and $Na_V1.6$ are left- and right-handed sigmoidal functions (respectively) of normalized length s along the AIS. The proximal end of the AIS is located at $s = 0$, and the distal end is located at $s = 1$. The channel densities are expressed as maximal conductances $\bar{g}_{Na_V1.6}$ (s) and $\bar{g}_{Na_V1.2}$ (s), where the total maximal Na_V conductance $\bar{g}_{Na_V}$ is constant along the AIS:

$$\bar{g}_{Na_V} = \bar{g}_{Na_V1.2}(s) + \bar{g}_{Na_V1.6}(s) = \text{const.} \tag{5}$$

The density profiles are given by

$$\begin{cases} \bar{g}_{Na_V1.2}(s) & = \dfrac{\bar{g}_{Na_V}}{2}\Big(1 - x \cdot \tanh(\sigma(s-\kappa))\Big), \\ \bar{g}_{Na_V1.6}(s) & = \bar{g}_{Na_V} - \bar{g}_{Na_V1.2}(s) \\ & = \dfrac{\bar{g}_{Na_V}}{2}\Big(1 + x \cdot \tanh(\sigma(s-\kappa))\Big). \end{cases} \tag{6}$$

We chose the hyperbolic tangent function $\tanh(s)$, but other sigmoidal functions would do just as well. The parameter x controls the separation of the Na_V distribution, that is, how separated the two Na_V subtypes are. When $x = 0$, the distribution becomes flat—$Na_V1.2$ and $Na_V1.6$ are mixed uniformly along the AIS. When $x = 1$, the proximal end of the AIS contains only $Na_V1.2$, and the distal end of the AIS contains only $Na_V1.6$. The parameter σ is the reciprocal

of the 'transition width' of the AIS Na_V distributions normalized by the AIS length. In all simulations shown here, $\sigma = 10.0$. Additional details are provided in Section E in S1 Text.

Shift-Clamping and the Hodgkin-Huxley model

Here we provide additional details of the sensitivity analysis performed in Fig 6. In the Hodgkin-Huxley model [40] a gating variable u evolves according to its voltage-dependent forward and backward transition rates $\alpha_u(V)$ and $\beta_u(V)$ as

$$\frac{du}{dt} = \alpha_u(V)[1-u] - \beta_u(V)u, \tag{7}$$

where u could be Na_V *activation m* or *availability h*, or K_V *activation n*, etc. This can be rewritten using the steady-state $u_\infty(V)$ and voltage-dependent time constant $\tau_u(V)$ of the gating variable

$$\frac{du}{dt} = \frac{u_\infty(V) - u}{\tau_u(V)}, \tag{8}$$

where u_∞ and τ_u are computed from α_u and β_u via

$$u_\infty(V) = \frac{\alpha_u(V)}{\alpha_u(V)+\beta_u(V)} \quad \text{and} \quad \tau_u(V) = \frac{1}{\alpha_u(V)+\beta_u(V)} \quad . \tag{9}$$

When shifting the voltage-dependence of u_∞ by ΔV_{RS} (see Modifying the *right-shift* of $Na_V1.2$ gating properties in the AIS), it is natural to assume that one should apply the same shift to τ_u given Eq 9, since u_∞ and τ_u are both functions of $\alpha_u(V)$ and $\beta_u(V)$ in such models. However, our simulations can shift $u_\infty(V)$ or $\tau_u(V)$ independently of one another: e.g. $\tau'_u(V) = \tau_u(V - \Delta V_{RS})$, $u'_\infty(V) = u_\infty(V)$. The forward and backward rates become

$$\alpha'_u = \frac{u'_\infty(V)}{\tau'_u(V)} \quad \text{and} \quad \beta'_u = \frac{1-u'_\infty(V)}{\tau'_u(V)}. \tag{10}$$

Putting this to use, one can modify the *right-shift* of combinations of

$$\left\{\tau_h^{Na_V1.2}(V),\ h_\infty^{Na_V1.2}(V),\ \tau_m^{Na_V1.2}(V),\ m_\infty^{Na_V1.2}(V)\right\}, \tag{11}$$

by adding "$-\Delta V_{RS}$" to the argument of the selected variables' $u_\infty(V)$s or $\tau_u(V)$s.

Biophysics, Hu-based model

Action potentials propagate via the cable equation

$$C\frac{\partial V}{\partial t} = \frac{d}{4R_a}\frac{\partial^2 V}{\partial s^2} - I_{\text{membrane}}, \tag{12}$$

where V is the membrane potential, C is the specific membrane capacitance, d is the neurite diameter, R_a is the axial resistance, s is the position along the axis of the cable, and I_{membrane} is the total transmembrane current density of all ion species in the model.

Here we describe the currents in our Hu-based model. (The changes we made to the Hay model are described in Generalization to Hay-based model and modified Hu-based model.) In the Hu-based model, we added explicit intracellular and extracellular concentrations of sodium, potassium, and chloride ions at each compartment. We denote the intracellular/extracellular concentration of a given ionic species "Z" as $[Z]_{in}$, $[Z]_{out}$ respectively. These

concentrations depend on the spatial coordinate—i.e. $[Z]_{in} = [Z]_{in}(s)$—but that is not written explicitly, to simplify the notation. The Nernst potentials (reversal potentials) E_{Na^+}, E_{K^+}, E_{Cl^-} of Na^+, K^+, and Cl^- are not fixed parameters but are instead determined by the intracellular and extracellular concentrations of those ions:

$$E_Z(s) = -\frac{kT}{q_z}\ln\left(\frac{[Z]_{in}}{[Z]_{out}}\right). \tag{13}$$

Transmembrane concentration gradients of Na^+ and K^+ are governed by active transport (Na^+/K^+-pump) and longitudinal diffusion. At each time step, ionic concentrations all over the cell are updated using transmembrane currents (Eq 16) and Fick's law. At the j^{th} compartment this gives:

$$\begin{cases} \frac{\partial}{\partial t}[Z]^j_{in} = -\left(\frac{A^j}{FVol^j_{in}}\right) I^j_Z + D_Z \nabla^2 [Z]^j_{in} \\ \\ \frac{\partial}{\partial t}[Z]^j_{out} = \left(\frac{A^j}{FVol^j_{out}}\right) I^j_Z + D_Z \nabla^2 [Z]^j_{out}, \end{cases} \tag{14}$$

where I^j_Z is the transmembrane current density of ion species Z at compartment j, with $Z = Cl^-$, K^+, Na^+. D_Z denotes the diffusion coefficient of ion Z. A^j and $Vol^j_{in(out)}$ are (respectively) the membrane area and intracellular/extracellular volume at the j^{th} compartment. F is the Faraday constant. The total transmembrane current density at the j^{th} compartment is

$$I^j_{membrane} = I^j_{Cl^-} + I^j_{K^+} + I^j_{Na^+}. \tag{15}$$

Omitting the compartment index j, the specific transmembrane currents are

$$I_{membrane} \leftarrow \begin{cases} I_{Cl^-} = g_{Cl^-}(V - E_{Cl^-}) \\ I_{K^+} = (g_{K_V} + g_{K,leak})(V - E_{K^+}) - 2I_{pump} \\ I_{Na^+} = (g_{Na_V} + g_{Na,leak})(V - E_{Na^+}) + 3I_{pump}. \end{cases} \tag{16}$$

g_{Cl^-}, $g_{K,leak}$, and $g_{Na,leak}$ are passive leak conductances whereas g_{K_V} and g_{Na_V} have voltage-gated Hodgkin-Huxley (HH)-style kinetics (Eq S6 in S1 Text). Since channels are nonuniformly distributed along the cell membrane, conductances vary with location. I_{pump} is the net current produced by the Na^+/K^+-pump as a function of $[K^+]_{out}$ and $[Na^+]_{in}$,

$$I_{pump} = I_{maxpump}\left(1 + \frac{K_{M_{K^+}}}{[K^+]_{out}}\right)^{-2}\left(1 + \frac{K_{M_{Na^+}}}{[Na^+]_{in}}\right)^{-3}, \tag{17}$$

where $I_{maxpump}$ controls the maximal pump current, $K_{M_{K^+}}$ and $K_{M_{Na^+}}$ are Michaelis-Menten kinetic constants, and the Na^+ and K^+ currents flowing through the pump are $I_{Na^+,pump} = 3I_{pump}$ and $I_{K^+,pump} = -2I_{pump}$. (Calcium dynamics are omitted in this section since Hu et al. [15] did not include the dendritic calcium spike initiation zone—see [39]. In Generalization to Hay-based model and modified Hu-based model, we include the Hay model, which features state-of-the-art calcium dynamics.).

Supporting information

S1 Text. For cell geometry, local membrane properties, additional simulations, and a variety of calculations, clarifications, and definitions, see this file.
(PDF)

Acknowledgments

We wish to thank: Catherine E. Morris, for directing our attention to the AIS. Nicholas T. Carnevale and Robert A. McDougal, for generously helping us to solve a number of model implementation challenges using NEURON. We also thank Louis Jacques for helpful discussion.

Author Contributions

Conceptualization: Benjamin S. M. Barlow, André Longtin, Béla Joós.

Formal analysis: Benjamin S. M. Barlow, André Longtin, Béla Joós.

Funding acquisition: André Longtin, Béla Joós.

Investigation: Benjamin S. M. Barlow, André Longtin, Béla Joós.

Methodology: Benjamin S. M. Barlow, André Longtin, Béla Joós.

Project administration: André Longtin, Béla Joós.

Resources: André Longtin, Béla Joós.

Software: Benjamin S. M. Barlow.

Supervision: André Longtin, Béla Joós.

Validation: Benjamin S. M. Barlow, André Longtin, Béla Joós.

Visualization: Benjamin S. M. Barlow.

Writing – original draft: Benjamin S. M. Barlow.

Writing – review & editing: Benjamin S. M. Barlow, André Longtin, Béla Joós.

References

1. Debanne D, Campanac E, Bialowas A, Carlier E, Alcaraz G. Axon Physiology. Physiological Reviews. 2011; 91(2):555–602. https://doi.org/10.1152/physrev.00048.2009 PMID: 21527732
2. Adachi R, Yamada R, Kuba H. Plasticity of the Axonal Trigger Zone. Neuroscientist. 2015; 21(3):255–265. https://doi.org/10.1177/1073858414535986 PMID: 24847046
3. Gulledge AT, Bravo JJ. Neuron Morphology Influences Axon Initial Segment Plasticity. eNeuro. 2016; 3 (1). https://doi.org/10.1523/ENEURO.0085-15.2016 PMID: 27022619
4. Verbist C, Müller MG, Mansvelder HD, Legenstein R, Giugliano M. The location of the axon initial segment affects the bandwidth of spike initiation dynamics. PLOS Computational Biology. 2020; 16(7): e1008087. https://doi.org/10.1371/journal.pcbi.1008087 PMID: 32701953
5. Franken TP, Bondy BJ, Haimes DB, Goldwyn JH, Golding NL, Smith PH, et al. Glycinergic axonal inhibition subserves acute spatial sensitivity to sudden increases in sound intensity. eLife. 2021; 10:e62183. https://doi.org/10.7554/eLife.62183 PMID: 34121662
6. Petersen AV, Cotel F, Perrier JF. Plasticity of the Axon Initial Segment: Fast and Slow Processes with Multiple Functional Roles. Neuroscientist. 2017; 23(4):364–373. https://doi.org/10.1177/1073858416648311 PMID: 27143656
7. Vrselja Z, Daniele SG, Silbereis J, Talpo F, Morozov YM, Sousa AMM, et al. Restoration of brain circulation and cellular functions hours post-mortem. Nature. 2019; 568(7752):336–343. https://doi.org/10.1038/s41586-019-1099-1 PMID: 30996318

8. Shepherd GM, Marenco L, Hines ML, Migliore M, McDougal RA, Carnevale NT, et al. Neuron Names: A Gene- and Property-Based Name Format, With Special Reference to Cortical Neurons. Frontiers in Neuroanatomy. 2019; 13. https://doi.org/10.3389/fnana.2019.00025 PMID: 30949034
9. Kole MHP, Stuart GJ. Signal Processing in the Axon Initial Segment. Neuron. 2012; 73(2):235–247. https://doi.org/10.1016/j.neuron.2012.01.007 PMID: 22284179
10. Höfflin F, Jack A, Riedel C, Mack-Bucher J, Roos J, Corcelli C, et al. Heterogeneity of the Axon Initial Segment in Interneurons and Pyramidal Cells of Rodent Visual Cortex. Frontiers in Cellular Neuroscience. 2017; 11:332. https://doi.org/10.3389/fncel.2017.00332
11. Shu Y, Duque A, Yu Y, Haider B, McCormick DA. Properties of Action-Potential Initiation in Neocortical Pyramidal Cells: Evidence From Whole Cell Axon Recordings. Journal of Neurophysiology. 2007; 97 (1):746–760. https://doi.org/10.1152/jn.00922.2006 PMID: 17093120
12. Mainen ZF, Joerges J, Huguenard JR, Sejnowski TJ. A model of spike initiation in neocortical pyramidal neurons. Neuron. 1995; 15(6):1427–1439. https://doi.org/10.1016/0896-6273(95)90020-9 PMID: 8845165
13. Kole MHP, Ilschner SU, Kampa BM, Williams SR, Ruben PC, Stuart GJ. Action potential generation requires a high sodium channel density in the axon initial segment. Nat Neurosci. 2008; 11(2):178–186. https://doi.org/10.1038/nn2040 PMID: 18204443
14. Brette R. Sharpness of Spike Initiation in Neurons Explained by Compartmentalization. PLOS Computational Biology. 2013; 9(12):e1003338. https://doi.org/10.1371/journal.pcbi.1003338 PMID: 24339755
15. Hu W, Tian C, Li T, Yang M, Hou H, Shu Y. Distinct contributions of Nav1.6 and Nav1.2 in action potential initiation and backpropagation. Nat Neurosci. 2009; 12(8):996–1002. https://doi.org/10.1038/nn.2359 PMID: 19633666
16. Tian C, Wang K, Ke W, Guo H, Shu Y. Molecular identity of axonal sodium channels in human cortical pyramidal cells. Front Cell Neurosci. 2014; 8. https://doi.org/10.3389/fncel.2014.00297 PMID: 25294986
17. Ye M, Yang J, Tian C, Zhu Q, Yin L, Jiang S, et al. Differential roles of NaV1.2 and NaV1.6 in regulating neuronal excitability at febrile temperature and distinct contributions to febrile seizures. Sci Rep. 2018; 8(1):753. https://doi.org/10.1038/s41598-017-17344-8 PMID: 29335582
18. Katz E, Stoler O, Scheller A, Khrapunsky Y, Goebbels S, Kirchhoff F, et al. Role of sodium channel subtype in action potential generation by neocortical pyramidal neurons. PNAS. 2018; 115(30):E7184–E7192. https://doi.org/10.1073/pnas.1720493115 PMID: 29991598
19. Spratt PWE, Alexander RPD, Ben-Shalom R, Sahagun A, Kyoung H, Keeshen CM, et al. Paradoxical hyperexcitability from NaV1.2 sodium channel loss in neocortical pyramidal cells. Cell Reports. 2021; 36(5). https://doi.org/10.1016/j.celrep.2021.109483 PMID: 34348157
20. Liu H, Wang HG, Pitt G, Liu Z. Direct Observation of Compartment-Specific Localization and Dynamics of Voltage-Gated Sodium Channels. J Neurosci. 2022; 42(28):5482–5498. https://doi.org/10.1523/JNEUROSCI.0086-22.2022 PMID: 35672149
21. Rush AM, Dib-Hajj SD, Waxman SG. Electrophysiological properties of two axonal sodium channels, $Na_v1.2$ and $Na_v1.6$, expressed in mouse spinal sensory neurones: Sodium channels in sensory neurones. The Journal of Physiology. 2005; 564(3):803–815. https://doi.org/10.1113/jphysiol.2005.083089 PMID: 15760941
22. Wang JA, Lin W, Morris T, Banderali U, Juranka PF, Morris CE. Membrane trauma and Na+ leak from Nav1.6 channels. American Journal of Physiology-Cell Physiology. 2009; 297(4):C823–C834. https://doi.org/10.1152/ajpcell.00505.2008 PMID: 19657055
23. Ben-Shalom R, Keeshen CM, Berrios KN, An JY, Sanders SJ, Bender KJ. Opposing Effects on Na V 1.2 Function Underlie Differences Between SCN2A Variants Observed in Individuals With Autism Spectrum Disorder or Infantile Seizures. Biological Psychiatry. 2017; 82(3):224–232. https://doi.org/10.1016/j.biopsych.2017.01.009 PMID: 28256214
24. Feldman D. The Spike-Timing Dependence of Plasticity. Neuron. 2012; 75(4):556–571. https://doi.org/10.1016/j.neuron.2012.08.001 PMID: 22920249
25. Regehr WG, Carey MR, Best AR. Activity-Dependent Regulation of Synapses by Retrograde Messengers. Neuron. 2009; 63(2):154–170. https://doi.org/10.1016/j.neuron.2009.06.021 PMID: 19640475
26. Mainen ZF, Sejnowski TJ. Influence of dendritic structure on firing pattern in model neocortical neurons. Nature. 1996; 382(6589):363–366. https://doi.org/10.1038/382363a0 PMID: 8684467
27. Doiron B, Longtin A, Turner RW, Maler L. Model of Gamma Frequency Burst Discharge Generated by Conditional Backpropagation. Journal of Neurophysiology. 2001; 86(4):1523–1545. https://doi.org/10.1152/jn.2001.86.4.1523 PMID: 11600618
28. Larkum ME, Kaiser KMM, Sakmann B. Calcium electrogenesis in distal apical dendrites of layer 5 pyramidal cells at a critical frequency of back-propagating action potentials. Proc Natl Acad Sci USA. 1999; 96(25):14600–14604. https://doi.org/10.1073/pnas.96.25.14600 PMID: 10588751

29. Hay E, Hill S, Schürmann F, Markram H, Segev I. Models of Neocortical Layer 5b Pyramidal Cells Capturing a Wide Range of Dendritic and Perisomatic Active Properties. PLoS Comput Biol. 2011; 7(7): e1002107. https://doi.org/10.1371/journal.pcbi.1002107 PMID: 21829333

30. Spratt PWE, Ben-Shalom R, Keeshen CM, Burke KJ, Clarkson RL, Sanders SJ, et al. The Autism-Associated Gene Scn2a Contributes to Dendritic Excitability and Synaptic Function in the Prefrontal Cortex. Neuron. 2019; 103(4):673–685.e5. https://doi.org/10.1016/j.neuron.2019.05.037 PMID: 31230762

31. Payeur A, Guerguiev J, Zenke F, Richards BA, Naud R. Burst-dependent synaptic plasticity can coordinate learning in hierarchical circuits. Nat Neurosci. 2021; 24(7):1010–1019. https://doi.org/10.1038/s41593-021-00857-x PMID: 33986551

32. Fletcher LN, Williams SR. Neocortical Topology Governs the Dendritic Integrative Capacity of Layer 5 Pyramidal Neurons. Neuron. 2019; 101(1):76–90.e4. https://doi.org/10.1016/j.neuron.2018.10.048 PMID: 30472076

33. Beaulieu-Laroche L, Brown NJ, Hansen M, Toloza EHS, Sharma J, Williams ZM, et al. Allometric rules for mammalian cortical layer 5 neuron biophysics. Nature. 2021; 600(7888):274–278. https://doi.org/10.1038/s41586-021-04072-3 PMID: 34759318

34. Beaulieu-Laroche L, Toloza EHS, Van Der Goes MS, Lafourcade M, Barnagian D, Williams ZM, et al. Enhanced Dendritic Compartmentalization in Human Cortical Neurons. Cell. 2018; 175(3):643–651. e14. https://doi.org/10.1016/j.cell.2018.08.045 PMID: 30340039

35. Baranauskas G, David Y, Fleidervish IA. Spatial mismatch between the Na+ flux and spike initiation in axon initial segment. PNAS. 2013. https://doi.org/10.1073/pnas.1215125110 PMID: 23341597

36. Michalikova M, Remme MWH, Kempter R. Spikelets in Pyramidal Neurons: Action Potentials Initiated in the Axon Initial Segment That Do Not Activate the Soma. PLOS Computational Biology. 2017; 13(1): e1005237. https://doi.org/10.1371/journal.pcbi.1005237 PMID: 28068338

37. Michalikova M, Remme MWH, Schmitz D, Schreiber S, Kempter R. Spikelets in pyramidal neurons: generating mechanisms, distinguishing properties, and functional implications. Reviews in the Neurosciences. 2020; 31(1):101–119. https://doi.org/10.1515/revneuro-2019-0044

38. Hu W, Shu Y. Axonal bleb recording. Neurosci Bull. 2012; 28(4):342–350. https://doi.org/10.1007/s12264-012-1247-1 PMID: 22833034

39. Almog M, Korngreen A. Is realistic neuronal modeling realistic? Journal of Neurophysiology. 2016; 116 (5):2180–2209. https://doi.org/10.1152/jn.00360.2016 PMID: 27535372

40. Hodgkin AL, Huxley AF. A quantitative description of membrane current and its application to conduction and excitation in nerve. The Journal of Physiology. 1952; 117(4):500–544. https://doi.org/10.1113/jphysiol.1952.sp004764 PMID: 12991237

41. Yin L, Rasch MJ, He Q, Wu S, Dou F, Shu Y. Selective Modulation of Axonal Sodium Channel Subtypes by 5-HT $_{1A}$ Receptor in Cortical Pyramidal Neuron. Cereb Cortex. 2015; p. bhv245. https://doi.org/10.1093/cercor/bhv245

42. Boucher PA, Joós B, Morris CE. Coupled left-shift of Nav channels: modeling the Na+-loading and dysfunctional excitability of damaged axons. J Comput Neurosci. 2012; 33(2):301–319. https://doi.org/10.1007/s10827-012-0415-7 PMID: 22476614

43. Joos B, Barlow BM, Morris CE. Calculating the Consequences of Left-Shifted Nav Channel Activity in Sick Excitable Cells. In: Chahine M, editor. Voltage-gated Sodium Channels: Structure, Function and Channelopathies. vol. 246. Cham: Springer International Publishing; 2017. p. 401–422. https://doi.org/10.1007/164_2017_63

44. Ma Y, Huguenard JR. Reemerging role of cable properties in action potential initiation. PNAS. 2013; 110(10):3715–3716. https://doi.org/10.1073/pnas.1300520110 PMID: 23440200

45. Filipis L, Canepari M. Optical measurement of physiological sodium currents in the axon initial segment. J Physiol. 2021; 599(1):49–66. https://doi.org/10.1113/JP280554 PMID: 33094478

46. Zhu JJ. Maturation of layer 5 neocortical pyramidal neurons: amplifying salient layer 1 and layer 4 inputs by Ca2+ action potentials in adult rat tuft dendrites. The Journal of Physiology. 2000; 526(3):571–587. https://doi.org/10.1111/j.1469-7793.2000.00571.x PMID: 10922009

47. Carnevale NT, Hines ML. The NEURON book. Cambridge, UK; New York: Cambridge University Press; 2006.

48. McDougal RA, Hines ML, Lytton WW. Reaction-diffusion in the NEURON simulator. Front Neuroinform. 2013; 7. https://doi.org/10.3389/fninf.2013.00028 PMID: 24298253

49. Samson E, Marchand J, Snyder KA. Calculation of ionic diffusion coefficients on the basis of migration test results. Mat Struct. 2003; 36(3):156–165. https://doi.org/10.1617/14002

6.4 Supporting information

S1 Text: Supporting Information

Contents

A Model: pyramidal cell geometry

Fig A displays the first of the two neurons used in this paper. The dendritic morphology is a digital reconstruction of a Layer 5 pyramidal neuron from cat visual cortex, modified from [26]. These neurons have dendrites roughly as tall as the thickness of the cortex (several mm) and axon initial segment length similar to the width of a human hair (tens of µm [9]).

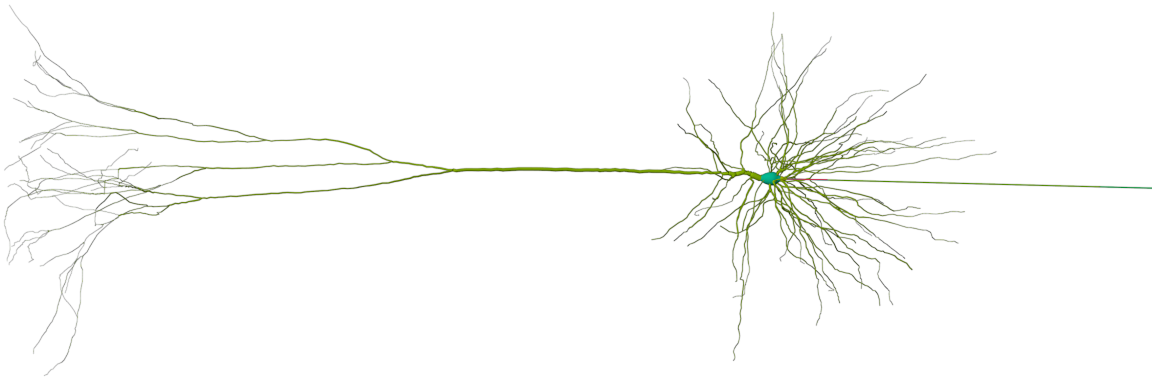

Fig A: **Geometry from the Hu model [15] (https://modeldb.science/123897): Layer 5 pyramidal neuron from cat visual cortex.** Somatodendritic morphology is digitally reconstructed from a real cell; hillock, AIS, and axon are added. Image created using blenderNEURON: blenderNEURON.org, blender.org.

The same reconstructed cell geometry was used in [15]. A cylindrical axon similar to that used in [15] was attached to the reconstructed soma by a 10µm long tapered hillock. The axon proper includes fifteen nodes of Ranvier (gray dots on the axon in Fig C) separated by myelinated 100µm internodes. The axon initial segment length was set to $\ell = 25.0\mu m$, consistent with [10]. Voltage-gated channels are present all over the cell. Channel densities and passive leaks are given as conductances. The local conductances vary with position —representative values have been tabulated in Section I.

In past modelling, there is sometimes a long section of bare axon following the AIS, or myelination may begin immediately at the end of the AIS. To ensure our results did not depend on this morphological feature, we ran simulations (axonal and somatic stimulation) with and without a 400µm section of bare axon separating the AIS from the first internode. The effects of Na_V distribution, summarized in Figures Fig H and Fig J, were qualitatively similar and similar in magnitude with and without the bare axon.

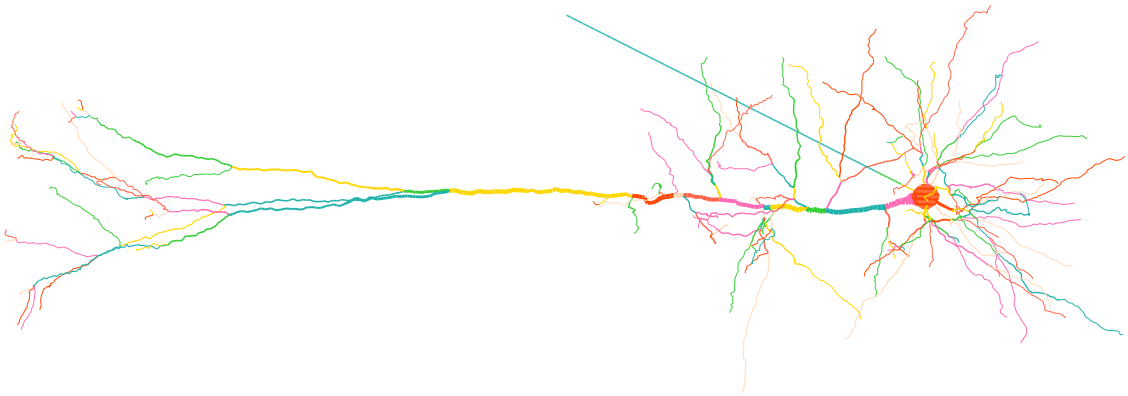

Fig B: **Morphology of the rat layer-5b neocortical pyramidal neuron in Hay et al. [29].** In the Hay model (https://modeldb.science/139653), the AIS consists of two straight NEURON Sections called "axon[0]" and "axon[1]", each 30μm in length, making the AIS 60μm long. The diagonal segment leading directly to the soma on the right is a 400μm long passive cable attached to the end of the AIS.

B Spikes and backpropagation in the Hu-based model

When pyramidal cells spike, the action potential can travel backward into the dendrites. This phenomenon is called backpropagation. For example, Fig C shows the response of the neuron following a somatic current pulse just above (left) and just below (right) the backpropagation threshold I_{BP}. Peak voltage is recorded across the entire cell model. The peak voltage at the tips of the dendrites is indicated in orange stars ★ and has a higher amplitude, consistent with the sealed-end effect. Backpropagation was deemed to have occurred if all apical dendritic tips exceeded -63.0mV (i.e. a depolarization of 7.0mV above V_{rest}) following stimulation.

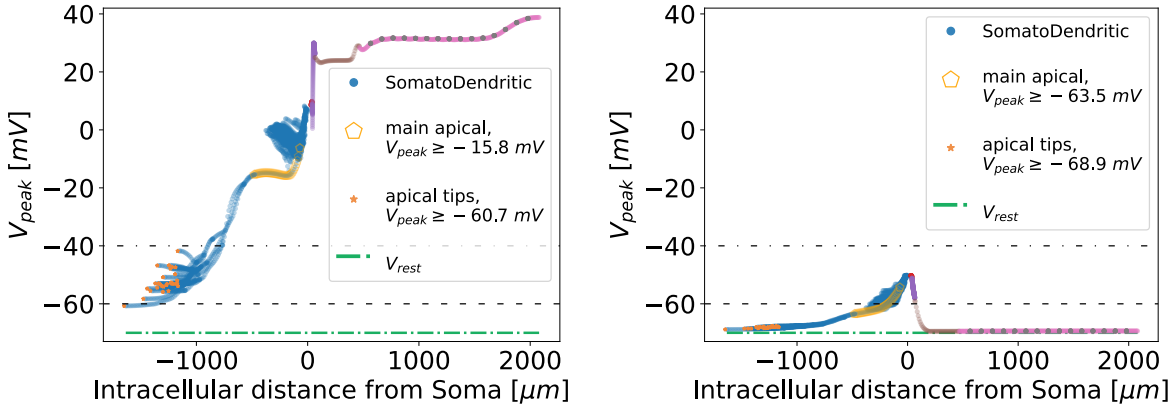

(i) Somatic stimulation, $I \gtrsim I_{BP} = I_{FP}$

(ii) Somatic stimulation, $I < I_{BP} = I_{FP}$

Fig C: **Backpropagation with somatic stimulation.** Each data point maps to a location in the reconstructed pyramidal neuron. On the abscissa, negative values indicate that a datapoint is located in the soma or dendrites, and positive values correspond to the hillock, AIS, and axon. (The correspondence between the abscissa and cell morphology is illustrated in Fig G.) ($x = 1, \kappa = 0.7$) This and similar figures are inspired by "Figure 4" of [12].

Note the qualitative change that occurs in the peak dendritic voltages of Fig Ci and Fig Di, when the cell is above threshold. A minuscule increase in the injected current amplitude has caused the entire main apical dendrite to depolarize well above -40mV, despite being mostly below -60mV when the current was slightly below this threshold. Note the attenuation in the peak voltage when comparing the basal dendrites to the apical tips. Also note the variety of different peak voltages in the dendrites, compared to the subthreshold condition. Our backpropagation criteria for the Hu-based model required this qualitative change since it was a robust feature of those simulations. Recall also that the purpose of the dendrites in

our modelling is to define a backpropagation threshold, not necessarily to mimic the detailed features of backpropagation. For our purposes, it is enough that the dendrites exhibit a threshold, and that threshold changes as a result of altering the distributions of Na_Vs in the AIS.

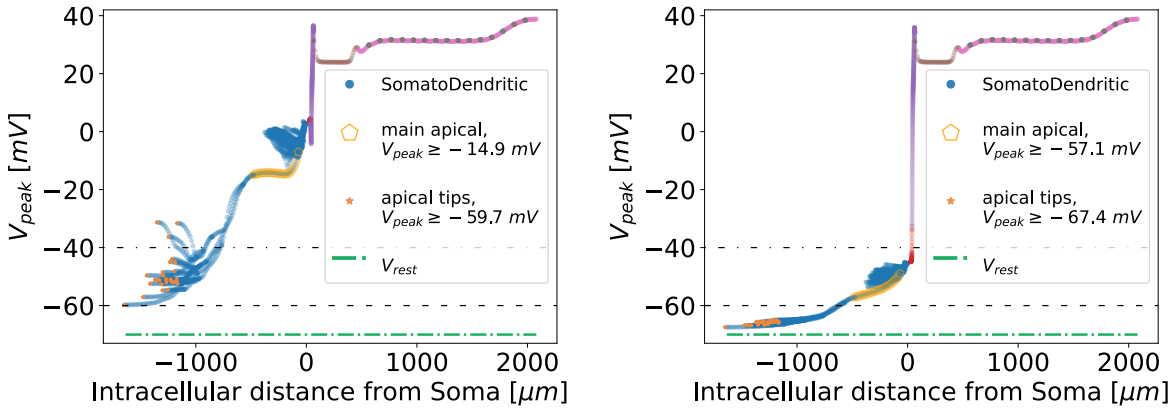

(i) Axonal stimulation, $I \gtrsim I_{BP} > I_{FP}$

(ii) Axonal stimulation, $I_{BP} > I > I_{FP}$

Fig D: **Axonal stimulation in the Hu-based model: spikes with and without backpropagation —by our stringent criterion.** Current is injected just distal to the AIS. Each data point maps to a location in the reconstructed pyramidal neuron. (The correspondence between the abscissa and cell morphology is illustrated in Fig G.) In (i), an action potential (AP) has backpropagated. Note the variability of V_{peak} in the somatodendritic region of the neuron, and the significant attenuation as the wave travels into the distal dendrites. In (ii), an AP has occurred but the pattern of depolarization in the dendrites does not satisfy the backpropagation criterion we have used for this model. Note that the peak voltage in the soma and dendrites remains nearer to the resting potential $\approx -70\text{mV}$, never exceeding -40mV. Also note the lack of variability in the somatodendritic V_{peak}. The qualitative change in these two plots occurs sharply, just above $I_{BP} \approx 2.7\text{nA}$ ($x = 1, \kappa = 0.4$). By some definitions, both of these scenarios would be considered backpropagation, since there is always a few mV of depolarization in the most distal dendrites. As this qualitative change is a robust feature of the Hu-based model, we have defined backpropagation in those simulations to require it. In defining a forward propagation threshold (I_{FP}), we call the scenario on the right, where an AP has been sent down the axon orthodromically from the stimulation site (i.e. to the right in this panel) "forward propagation" or "forwardprop" regardless of the amplitude of the somatodendritic depolarization. Antidromically stimulated APs that do not backpropagate have been observed in several neuron types [36, 37]. This and similar figures are inspired by "Figure 4" of [12].

C Spikes and backpropagation in the Hay-based model

The backpropagation criteria we used with the Hay model[29] are given in the caption of Fig E.

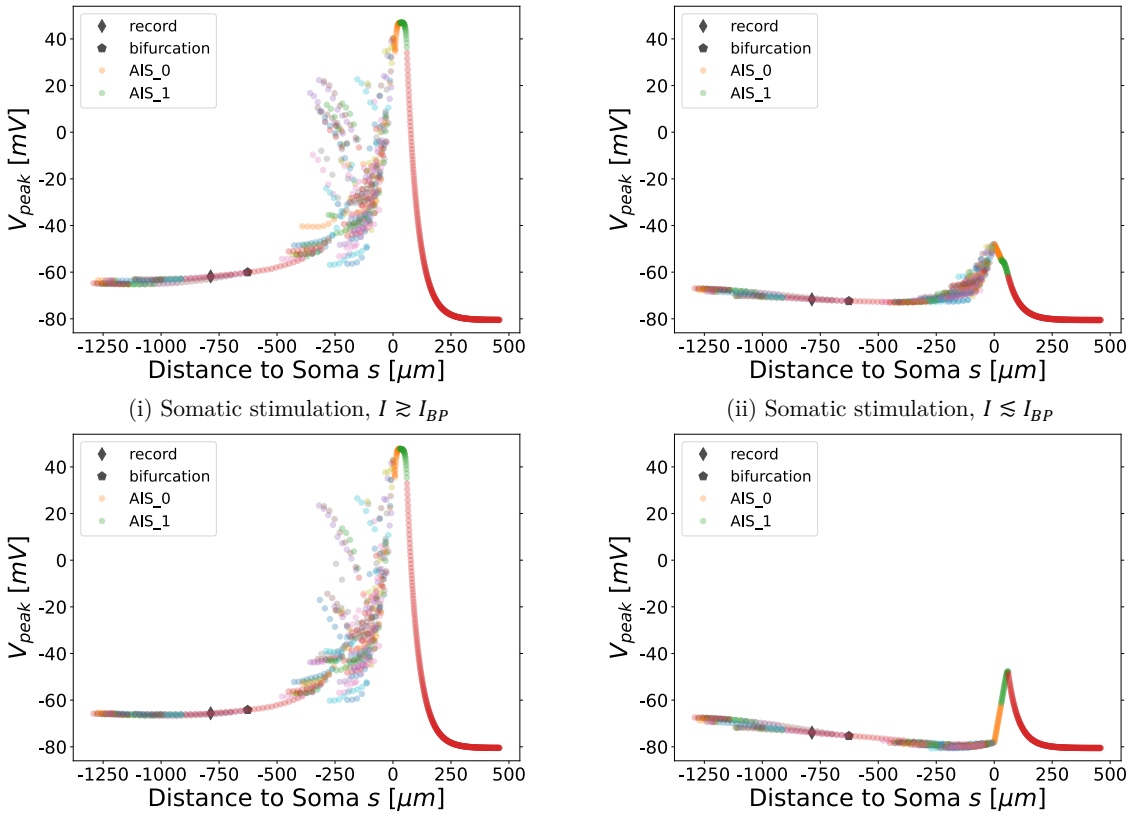

(i) Somatic stimulation, $I \gtrsim I_{BP}$

(ii) Somatic stimulation, $I \lesssim I_{BP}$

(iii) Axonal stimulation, $I \gtrsim I_{BP}$

(iv) Axonal stimulation, $I \lesssim I_{BP}$

Fig E: **Backpropagation criteria in the Hay-based model.** Each data point maps to a location in the reconstructed pyramidal neuron. On the abscissa, negative values indicate that a data point is located in the soma or dendrites, and positive values correspond to the AIS and passive cable. (The correspondence between the abscissa and cell morphology is illustrated in Fig G.) In (**i**) and (**iii**) backpropagation has occurred, whereas in (**ii**) and (**iv**), the stimulation is (just) below the BAP threshold. In the model, backpropagation was recorded either at the soma (neighbouring the left end of the section labelled "AIS_0", membrane potential exceeding 10mV), or in the apical dendrites (just distal to the main bifurcation of the main apical dendrite, membrane potential exceeding -70mV). The resting potential was $\cong -80.5\text{mV}$ at the soma, and $\cong -74.1\text{mV}$ at the apical recording site (see legend).

In Fig E, compare the depolarization of the distal AIS ('AIS_1' in the legend) in the Hay model [29] when current is injected somatically versus axonally, with the neuron just below I_{BP}: In the somatic case (Fig Eii) the distal AIS never reaches -60mV, while in the axonal case (Fig Eiv) it exceeds -50mV. Hay

et al. did not include an axon[29], and here the AIS is followed by a passive cable, rather than an excitable axon composed of myelinated internodes segmented by nodes of Ranvier. Hence a forward-propagation threshold I_{FP} is ill-defined in this model. Were the Hay model to include such an axon, the increased depolarization of the distal AIS in (Fig Eiv) compared to (Fig Eii) would be sufficient to cause an axonal AP in the former without doing so in the latter. Thus we argue, that the ability of the Hu-based model —with its excitable axon— to generate APs without meeting our criterion for backpropagation (Fig Dii), is an artifact of axonal stimulation under the conditions simulated here. Antidromically stimulated APs that do not backpropagate have been observed in several neuron types [36, 37].

C.1 Identical results with somatic criterion

In the main text (Fig 7) the dendritic backpropagation criterion was used, however, the somatic criterion produces the same result, as shown below. In Fig Fi and Fig Fii, backpropagation is registered if the somatic membrane potential exceeds $\mathsf{10.0mV}$. The threshold need not be this high, but it does not affect the results since the somatic depolarization is large.

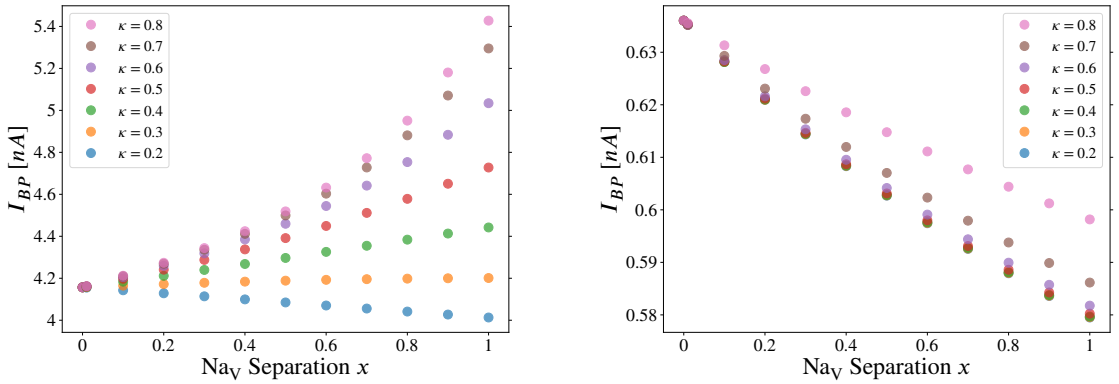

(i) Somatic stimulation (ii) Axonal stimulation

Fig F: **Backpropagation in the Hay model: Somatic backpropagation criterion.** To see the equivalency of the somatic criterion used here, with the apical dendritic backpropagation criterion used in the main text, compare with Fig 7. Here we plot the combined effect on the backpropagation threshold (I_{BP}, defined below) of varying crossover location (κ) and Na_V separation (x) in the axon initial segment. Varying the separation parameter "x" from $x = 0$ to $x = 1$, the distribution of Na_V channels goes from flat (homogeneous) to separated, the latter approximating the distribution observed in developing pyramidal neurons (see Fig 1A). Note that curves for all values of κ converge to a single point at $x = 0$, since κ can have no effect when the two Na_V subtypes are uniformly distributed along the AIS. Somatic backpropagation criterion $= \mathsf{10.0mV}$ —see caption of Fig E.

D Modified version of Hu-based model

In the version of our Hu-based model from the main text, the Na_V density in the dendrites was decreased by a factor of 10 from the original Hu model, to produce attenuation in the backpropagated action potential. Likewise, the somatic Na_V density was increased by a factor of 3. In the tuning presented here, the original somatic and dendritic Na_V densities of Hu et al. [15] are kept, and backpropagation is robust, without attenuation. A high amplitude, regenerative BAP infiltrates the entire dendritic tree.

We redefined the threshold criterion, such that backpropagation was deemed to have occurred if all apical dendritic tips exceeded -10.0mV following stimulation. The higher threshold value was appropriate to record backpropagation due to the robust BAP, which did not show attenuation (see Fig G). Although this tuning diverges from the qualitative features of BAPs in real pyramidal cells, at least for single action potentials [28, 29], the relationship between the backpropagation threshold and the Na_V distribution presented in Results was preserved again (see the figures below).

That is, despite the significant qualitative differences between the tuning of the Hu et al. [15] based model below (Fig G) which lacks BAP attenuation, the other Hu et al. based model above in the main text (Somatic stimulation, Axonal stimulation) which we modified for BAP attenuation, and the Hay et al. [29] based model above in Generalization to Hay-based model and modified Hu-based model, qualitative effects of modifying the Na_V distribution in the AIS are identical, and for somatic stimulation they are quantitatively similar as well. This can be clearly concluded by comparing Fig H, Fig 2, and Fig F.

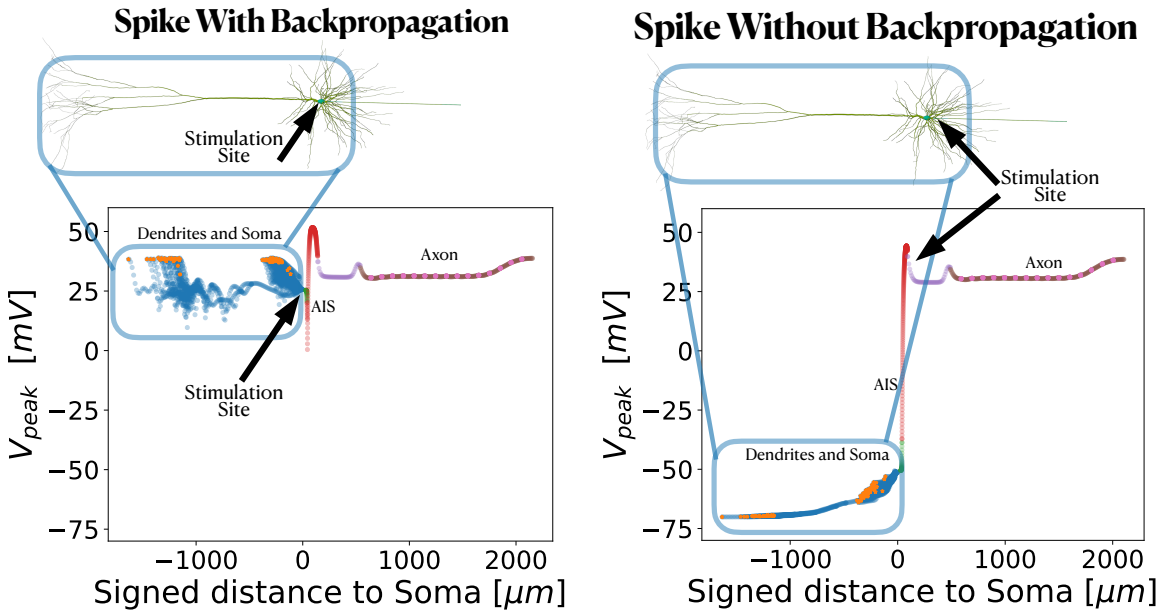

Fig G: Spikes with and without backpropagation: Each data point maps to a location in the reconstructed pyramidal neuron (compare with the cell morphology above the plot). On the abscissa, negative values indicate that a datapoint is located in the soma or dendrites, and positive values correspond to the hillock, AIS, and axon. Beginning on the right-hand side: an action potential (AP) has occurred following axonal stimulation (current injected just distal to the AIS). Note that the peak voltage in the soma and dendrites remains near the resting potential $\approx -70\text{mV}$, indicating that backpropagation did not occur. We call this scenario where an AP has been sent down the axon orthodromically from the stimulation site (i.e. to the right in this panel) "forward propagation" or "forwardprop" regardless of the amplitude of the somatodendritic depolarization. To the left is an AP that backpropagated: the entire cell spiked, in this case following somatic stimulation; backpropagation can also occur following axonal stimulation. The somatodendritic peak voltages are indicated by a blue box in each case. This and similar figures are inspired by "Figure 4" of [12].

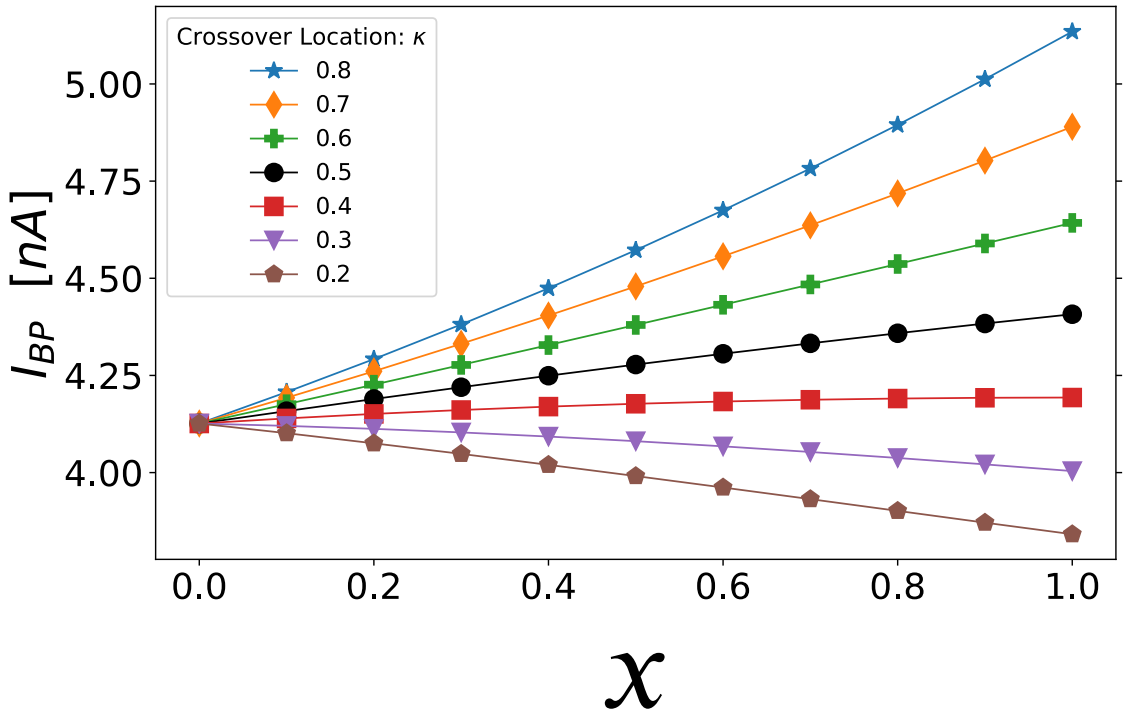

Fig H: Somatic Stimulation: Combined effect of varying crossover location (κ) and Na_V separation (x) in the axon initial segment. The threshold for forward AP propagation is the same as for backpropagation. Varying the separation parameter "x" from $x = 0$ to $x = 1$, the distribution of Na_V channels goes from flat (homogeneous) to separated, the latter approximating the distribution observed in developing pyramidal neurons (see Fig 1A). Note that curves for all values of κ converge to a single point at $x = 0$, since κ can have no effect when the two Na_V subtypes are uniformly distributed along the AIS. The lines have been drawn to guide the eye.

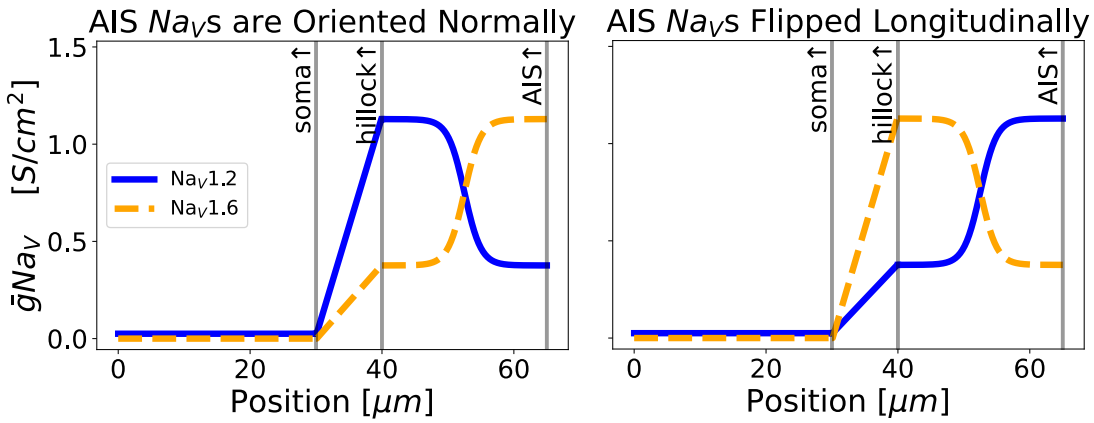

(i) (ii)

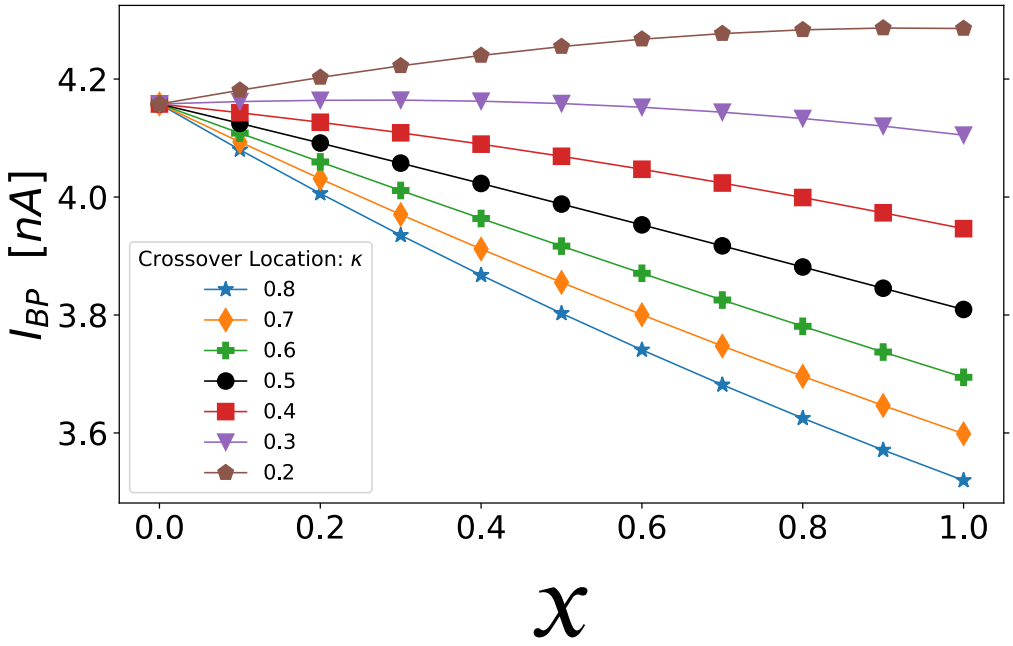

(iii)

Fig I: When the AIS Na_V distribution is flipped, setting $x = 1$ concentrates $Na_V1.6$ at the proximal AIS and $Na_V1.2$ at the distal AIS —the opposite of what is observed in many pyramidal cells [15, 16, 17]. (i) AIS with proper longitudinal placement of Na_Vs. (ii) AIS with a longitudinally flipped Na_V distribution. In both plots, $x = 0.5$ and $\kappa = 0.5$. (iii) Somatic stimulation with AIS Na_Vs flipped as in (ii): This result is close to a mirror image of Fig H. The lines have been drawn to guide the eye.

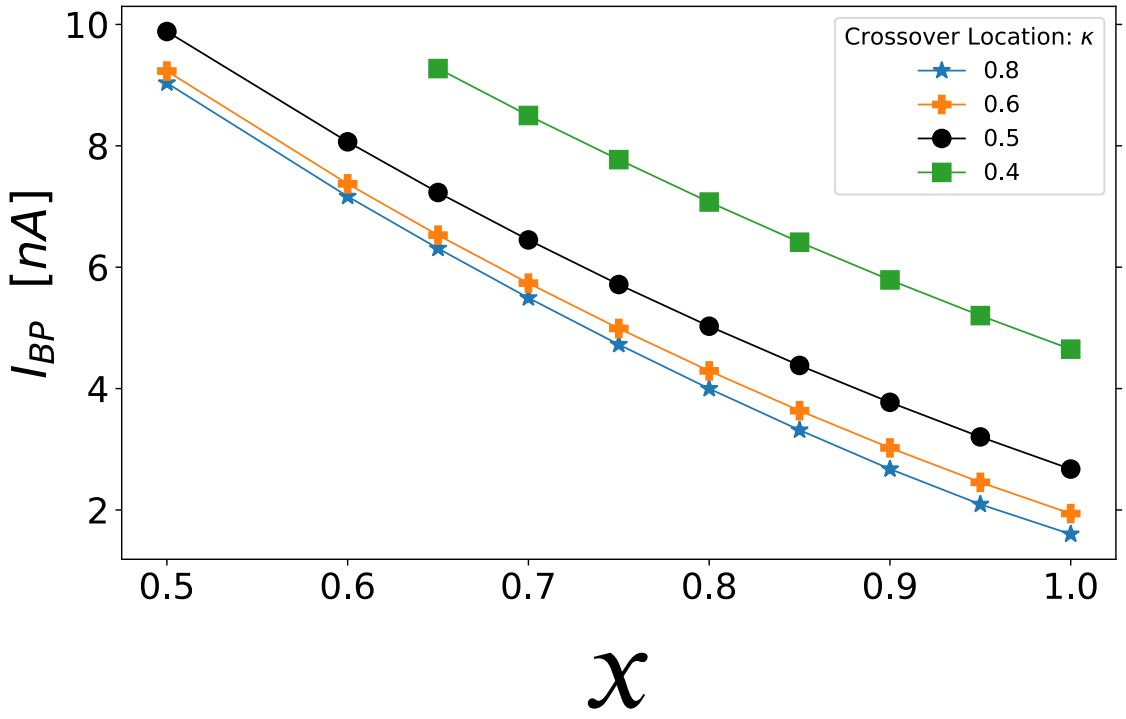

Fig J: Axonal Stimulation: Effect of varying crossover location (κ) and Na_V separation (x) in the AIS on the backpropagation threshold (see Fig 1). When computing the threshold, the stimulating current was limited to a maximum of $10nA$, to prevent unphysiological local depolarization at the stimulation site. Due to the smaller diameter of the axon (relative to the soma), $10nA$ is sufficient to depolarize the membrane potential to $\approx +80mV$ at the stimulation site, whereas the resting potential is $V_{rest} = -70mV$. To achieve backpropagation within that constraint (following axonal stimulation), our model required some amount of proximal $Na_V1.2$, delivered through the combined effects of Na_V separation ($x \gtrsim 0.5$) and a sufficiently distal crossover position $\kappa \gtrsim 0.4$. Separating the two Na_V subtypes ($x \longrightarrow 1$) lowers the threshold, in agreement with the finding in [15] that proximal accumulation of $Na_V1.2$ promotes backpropagation, albeit due to different gating properties (Fig 6B). Increasing κ raises the proportion of $Na_V1.2$ (relative to $Na_V1.6$) in the AIS and lowers the backpropagation threshold as well. Threshold changes here are larger than for somatic stimulation (Fig H). The lines have been drawn to guide the eye.

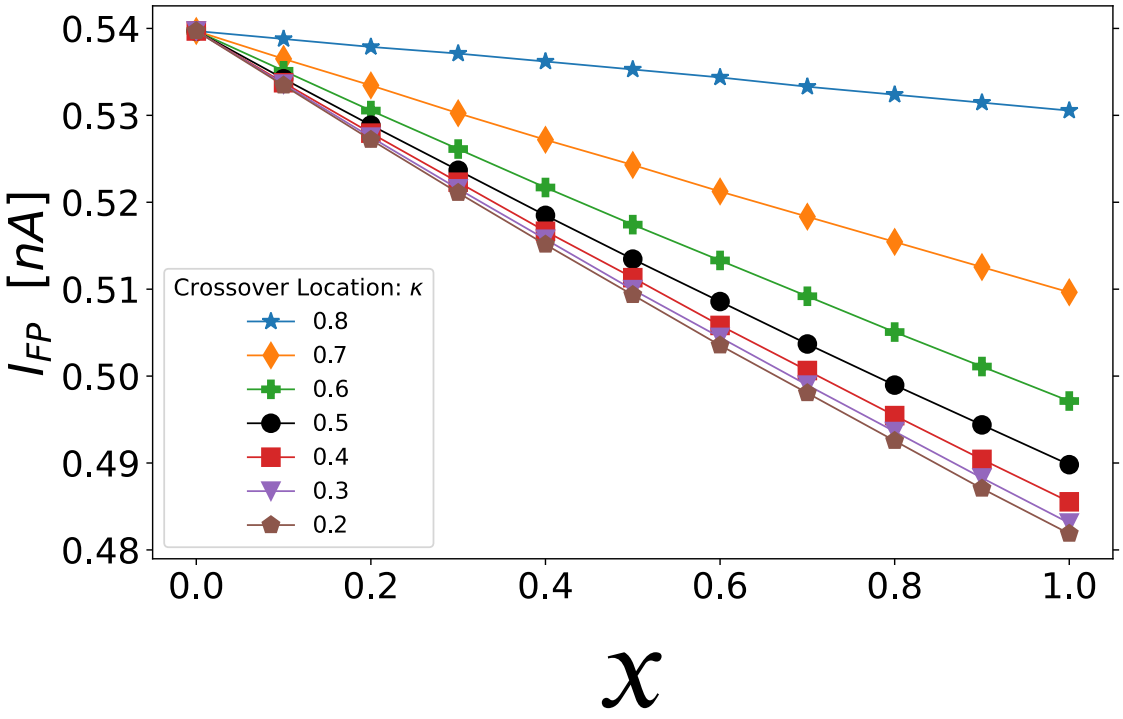

Fig K: Axonal Stimulation: Effect of χ and κ on forward propagation threshold. The trend for all constant κ curves is that raising the proportion of total AIS $Na_V1.6$ (by reducing κ) or concentrating $Na_V1.6$ in the distal AIS (by increasing χ) lowers the threshold to initiate forward propagating action potentials (see Fig 1). Note that this threshold current pulse is not sufficient to achieve backpropagation. The effect of Na_V separation is much smaller here than for the backpropagation threshold. The lines have been drawn to guide the eye.

D.1 Additional simulations

In the main text, we found that with a 25µm AIS, the slope of I_{BP} versus x for somatic stimulation became flat around $\kappa \approx 0.4$, which is 20µm away from the soma since $L_{\text{hillock}} = 10\mu\text{m}$ (Fig 2). In Fig L, with a 100µm AIS, the I_{BP} slope flattens around $\kappa \approx 0.1$, which again corresponds to a distance of roughly 20µm from the soma since the distance in µm to the crossover position is $\kappa \times \ell_{\text{AIS}}$. This suggests that the threshold-lowering effect of Na_V separation for small κ (Fig 2) results from the increased proximal density of $Na_V1.6$ when the crossover is brought near to the soma —and is not due to the proximal density of $Na_V1.2$, consistent with Fig M.

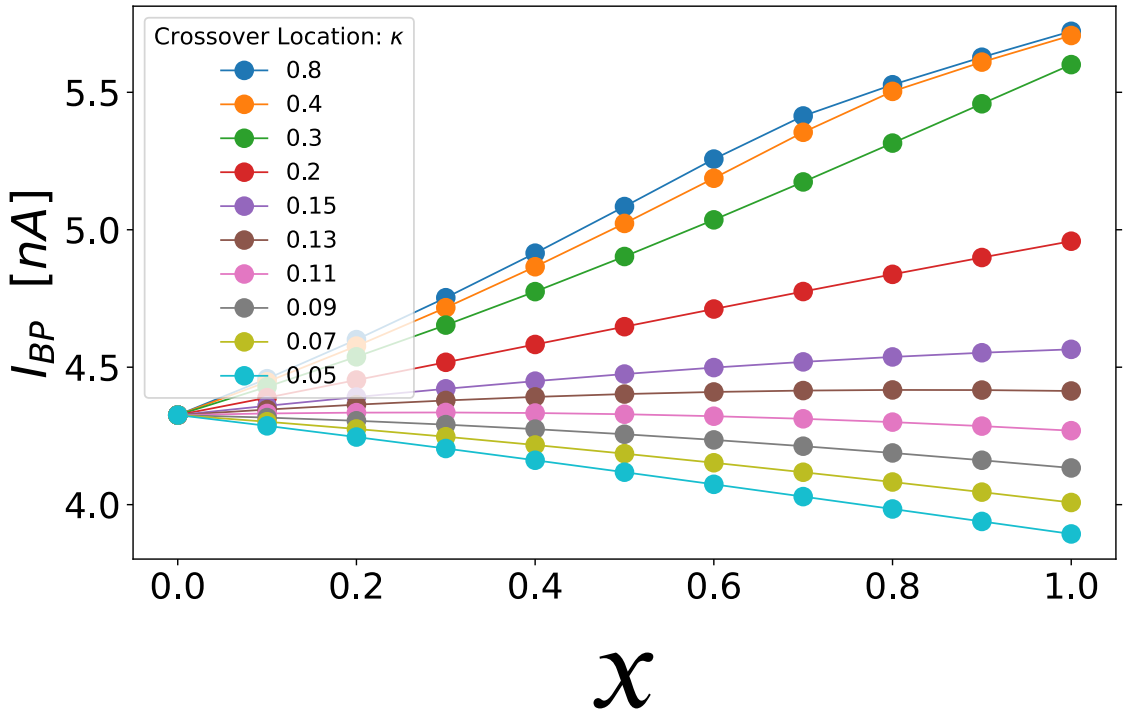

Fig L: Somatic Stimulation with AIS lengthened to 100µm (compare with Fig 2 in the main text where the AIS length was 25µm): Combined effect of varying crossover location (κ) and Na_V separation (x) in the axon initial segment. The distance in µm to the crossover position is $\kappa \times \ell_{\text{AIS}}$. The lines have been drawn to guide the eye.

Fig M demonstrates that increasing κ raises the backpropagation threshold when current is injected somatodendritically (orthodromic stimulation), even when the slopes in Fig 2 are negative. Increasing κ

means moving the Na_V crossover location away from the soma, which increases the proportion of $Na_V1.2$ (versus $Na_V1.6$) in the AIS; see Fig 1B.

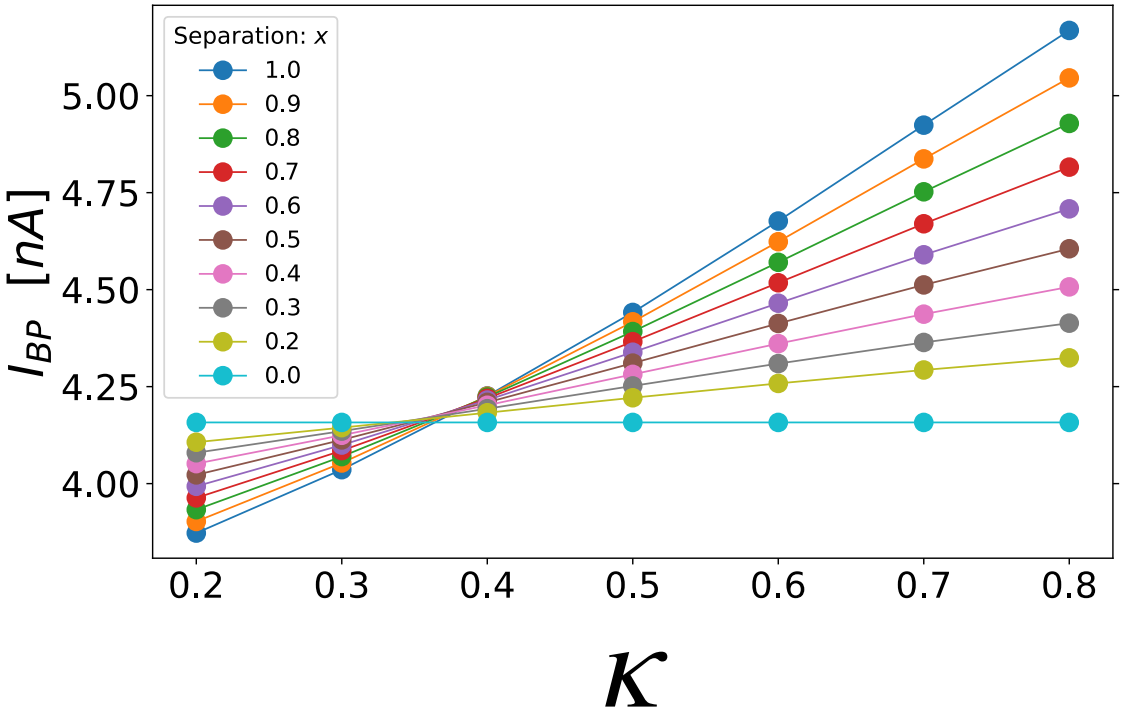

Fig M: Somatic Stimulation with nominal AIS length ($\ell_{\text{AIS}} = 25.0\mu\text{m}$). The combined effect of varying crossover location (κ) and Na_V separation (x) in the axon initial segment. Increasing κ raises the backpropagation threshold. Here the abscissa is the normalized crossover position κ, instead of Na_V separation (compare with Fig 2). In Fig 2, all curves converge at $x = 0$. Here, that intersection point is replaced by the $x = 0$ *line*. Notice that every $x > 0$ curve has a positive slope: the backpropagation threshold I_{BP} *increases* with κ. Increasing κ when $x > 0$ necessarily increases the ratio of $Na_V1.2$ conductance to $Na_V1.6$ conductance in the AIS (see Equation S2). It follows that concentrating $Na_V1.2$ in the proximal AIS raises the backpropagation threshold, for somatic stimulation. The lines have been drawn to guide the eye.

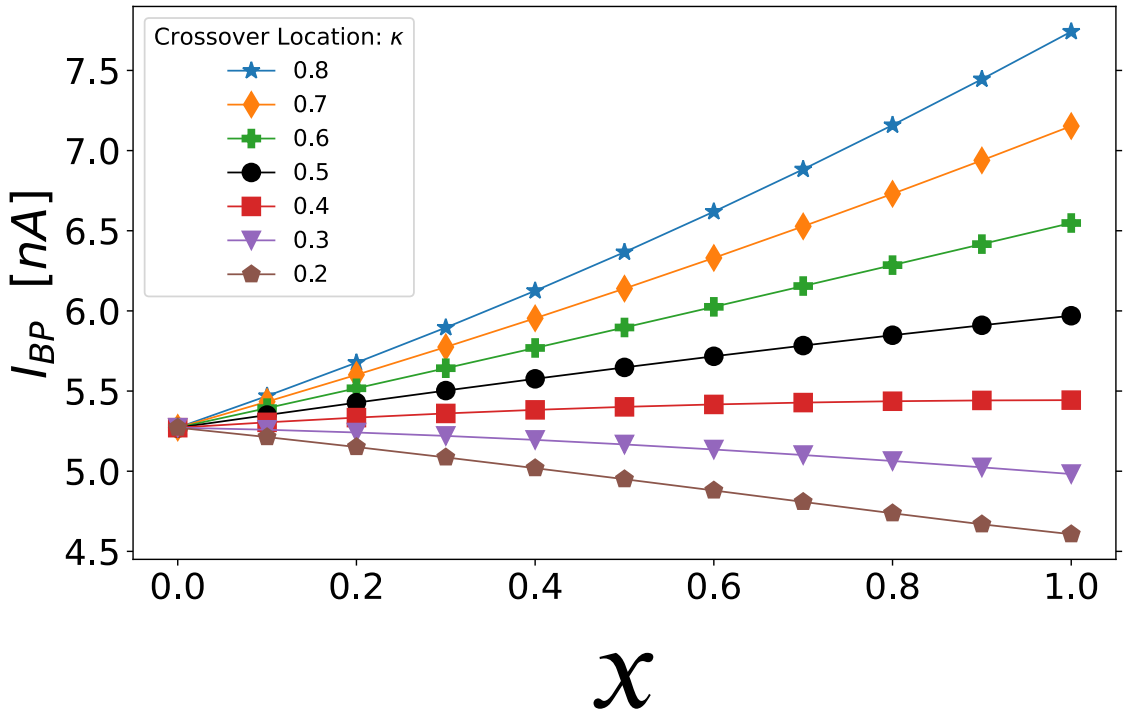

Fig N: Dendritic Stimulation with nominal AIS length ($\ell_{\mathrm{AIS}} = 25.0\mu\mathrm{m}$). Current injection at the main apical dendrite yields the same qualitative behaviour as for somatic stimulation. Compare with (Fig 2). Varying the separation parameter "x" from $x = 0$ to $x = 1$, the distribution of $\mathrm{Na_V}$ channels goes from flat (homogeneous) to separated, the latter approximating the distribution observed in developing pyramidal neurons (see Fig 1A). Note that curves for all values of κ converge to a single point at $x = 0$, since κ can have no effect when the two $\mathrm{Na_V}$ subtypes are uniformly distributed along the AIS. The lines have been drawn to guide the eye.

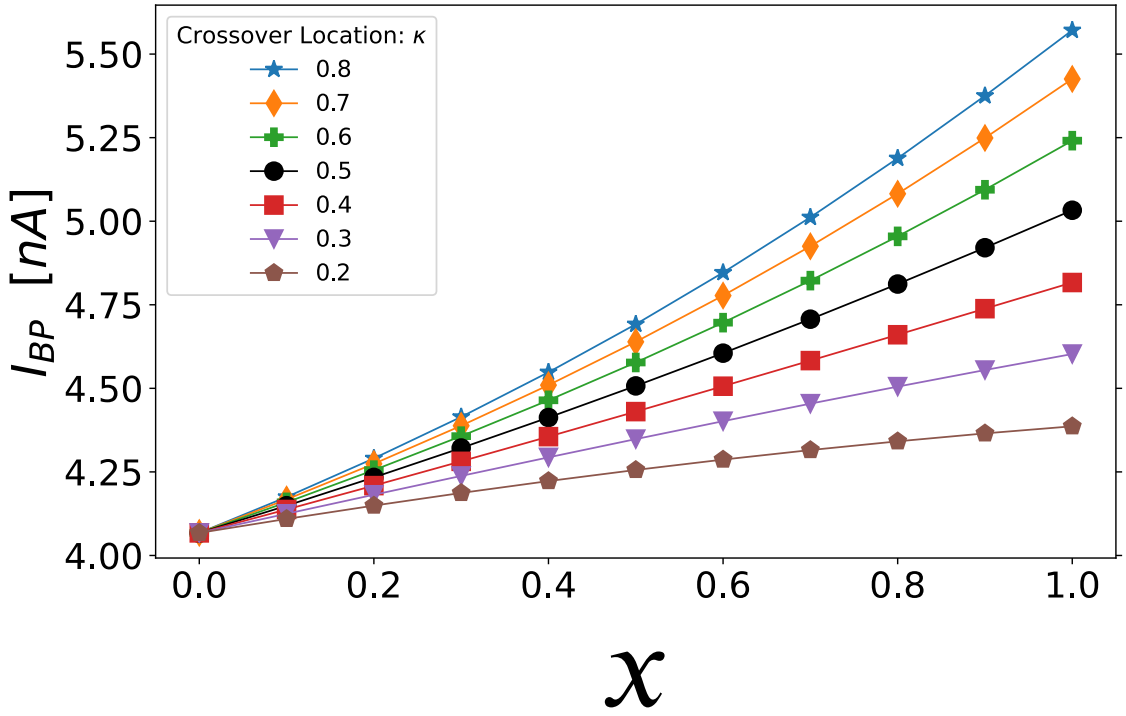

Fig O: Somatic Stimulation: lengthening the hillock to 30µm removes the negative slopes observed in Fig 2 and Fig L. In all other plots, we have used $L_{\text{hillock}} = 10\mu\text{m}$. AIS length is $\ell_{\text{AIS}} = 25.0\mu\text{m}$ as in all other plots unless indicated otherwise. The lines have been drawn to guide the eye.

E AIS - technical details

In all models that were used in this study, the total Na_V conductance of the AIS is proportional to the AIS length ℓ since its diameter is constant:

$$\bar{G}_{Na_V} = \bar{g}_{Na_V} \cdot (\text{Area of AIS}) \propto \bar{g}_{Na_V} \ell_{\text{AIS}}. \tag{S1}$$

As stated in the main text, the density profiles of $Na_V1.2$ and $Na_V1.6$ are left- and right-handed sigmoidal functions (respectively) of normalized length s along the AIS. The proximal end of the AIS is located at $s = 0$, and the distal end is located at $s = 1$. The channel densities are expressed as maximal conductances $\bar{g}_{Na_V1.2}$ (s) and $\bar{g}_{Na_V1.6}$ (s), where the total maximal Na_V conductance $\bar{g}_{Na_V}$ is constant along the AIS:

$$\bar{g}_{Na_V} = \bar{g}_{Na_V1.2}(s) + \bar{g}_{Na_V1.6}(s) = const. \tag{S2}$$

The density profiles are given by

$$\begin{cases} \bar{g}_{Na_V1.2}(s) &= \dfrac{\bar{g}_{Na_V}}{2}\Big(1 - x \cdot \tanh\big(\sigma(s-\kappa)\big)\Big), \\ \bar{g}_{Na_V1.6}(s) &= \bar{g}_{Na_V} - \bar{g}_{Na_V1.2}(s) \\ &= \dfrac{\bar{g}_{Na_V}}{2}\Big(1 + x \cdot \tanh\big(\sigma(s-\kappa)\big)\Big). \end{cases} \tag{S3}$$

We chose the hyperbolic tangent function $\tanh(s)$, but other sigmoidal functions would do just as well. The parameter x controls the separation of the Na_V distribution, that is, how separated the two Na_V subtypes are. When $x = 0$, the distribution becomes flat —$Na_V1.2$ and $Na_V1.6$ are mixed uniformly along the AIS. When $x = 1$, the proximal end of the AIS contains only $Na_V1.2$, and the distal end of the AIS contains only $Na_V1.6$. The parameter σ is the reciprocal of the 'transition width' of the AIS Na_V distributions normalized by the AIS length. In all simulations shown here, $\sigma = 10.0$.

The contribution of $Na_V1.2$ to the total voltage-gated sodium conductance of the AIS (Equation S1) is

$$\bar{G}_{Na_V1.2} \propto \int_0^{\ell_{\text{AIS}}} d\ell' \, \bar{g}_{Na_V1.2}(\ell') = \ell_{\text{AIS}} \int_0^1 ds \, \frac{\bar{g}_{Na_V}}{2}\Big(1 - x \cdot \tanh\big(\sigma(s-\kappa)\big)\Big), \tag{S4}$$

$$\Longrightarrow \bar{G}_{\mathrm{Na_V1.2}} \propto 1 - x \cdot \underbrace{\left(\frac{\ln\big(\cosh(\sigma) - \sinh(\sigma)\tanh(\sigma\kappa)\big)}{\sigma} \right)}_{\text{“}M\text{”}}. \tag{S5}$$

The root of the term labeled “M” in Equation S5 is $\kappa = \frac{1}{2}$, and the slope of M is negative: $M(\kappa < 0.5) > 0$, $M(\kappa > 0.5) < 0$. Since $M(\kappa = 0.5) = 0$, the derivative of $\bar{G}_{\mathrm{Na_V1.2}}$ (and $\bar{G}_{\mathrm{Na_V1.6}}$) with respect to x is zero when the crossover is located in the middle of the AIS, which is the standard configuration for varying $\mathrm{Na_V}$ separation.

We call $\kappa = 0.5$ standard because, in this configuration, the effects on the backpropagation threshold due to varying x can not be due to changes in the total conductance of $\mathrm{Na_V1.6}$ or $\mathrm{Na_V1.2}$ in the AIS. In other words, the results of sweeping x from 0 to 1 with κ fixed at 0.5 in Fig 4, Fig 5, Fig 3, Fig 7, and Fig 2 are purely due to mixing and separating $\mathrm{Na_V1.6}$ from $\mathrm{Na_V1.2}$ in the AIS.

Since by definition $0 \leqslant \kappa \leqslant 1$ and $\sigma > 0$, the partial derivative of M with respect to κ is negative. It follows from Equation S5 that $\bar{G}_{\mathrm{Na_V1.2}}$ increases as the crossover position is moved distally. Likewise $\bar{G}_{\mathrm{Na_V1.6}}$ decreases with increasing κ.

F Voltage-gated channels

The voltage-gated sodium and potassium conductances $g_{\mathrm{Na_V}}(V,t)$ and $g_{\mathrm{K_V}}(V,t)$ in Equation 16 are modeled using HH-style kinetics [40] fitted to mammalian pyramidal cell data by [12], and then further adapted by [15] to include two $\mathrm{Na_V}$ variants (Equation S7). In the Hodgkin-Huxley model, the current density I_{Z} of ion species “Z” through voltage-gated channels of a given type is

$$I_{\mathrm{Z_V}} = \bar{g}_{\mathrm{Z_V}} m^p h^q (V - E_{\mathrm{Z}}), \tag{S6}$$

where $\bar{g}$ is the maximal conductance, $m(V,t)$ is the probability for an *activation* gate to be open, p is the number of *activation* gates per channel, $h(V,t)$ is the *availability* (probability that the channel is *not inactivated*), and q is the number of inactivation gates per channel. $\mathrm{Na_V}$ channels are modeled as having three *activation* gates ($p = 3$) and a single inactivation gate ($q = 1$) so that $g_{\mathrm{Na_V}} \propto m^3 h$. Likewise, $\mathrm{K_V}$ channels have a single *activation* gate and no inactivation ($g_{\mathrm{K_V}} \propto n$).

The gating variables m, h, and n evolve according to Equations 7, 8, and 9. Since the cell features two

Na_V subtypes ($Na_V1.2$ and $Na_V1.6$), the model computes two sets of sodium *activation* and *availability* variables. The current density I_{Na} through the Na_V channels is then

$$I_{Na_V} = \Big(\underbrace{\bar{g}_{Na_V1.2}(m^{Na_V1.2})^3 h^{Na_V1.2}}_{g_{Na_V1.2}} + \underbrace{\bar{g}_{Na_V1.6}(m^{Na_V1.6})^3 h^{Na_V1.6}}_{g_{Na_V1.6}} \Big)(V - E_{Na^+}), \tag{S7}$$

where $g_{Na_V1.2} + g_{Na_V1.6} = g_{Na_V}$ in Equation 16.

Fig P plots the voltage-dependent kinetics of $m^{Na_V1.2}$, $h^{Na_V1.2}$, $m^{Na_V1.6}$ and $h^{Na_V1.6}$. The steady-state *activation* and *availability* functions and their voltage-sensitive time constants were implemented using the parameters provided in [15] and in model code published by [26]. We further modified the channel model code to allow shift-clamping; see Modifying the *right-shift* of $Na_V1.2$ gating properties in the AIS and Shift-Clamping and the Hodgkin-Huxley model.

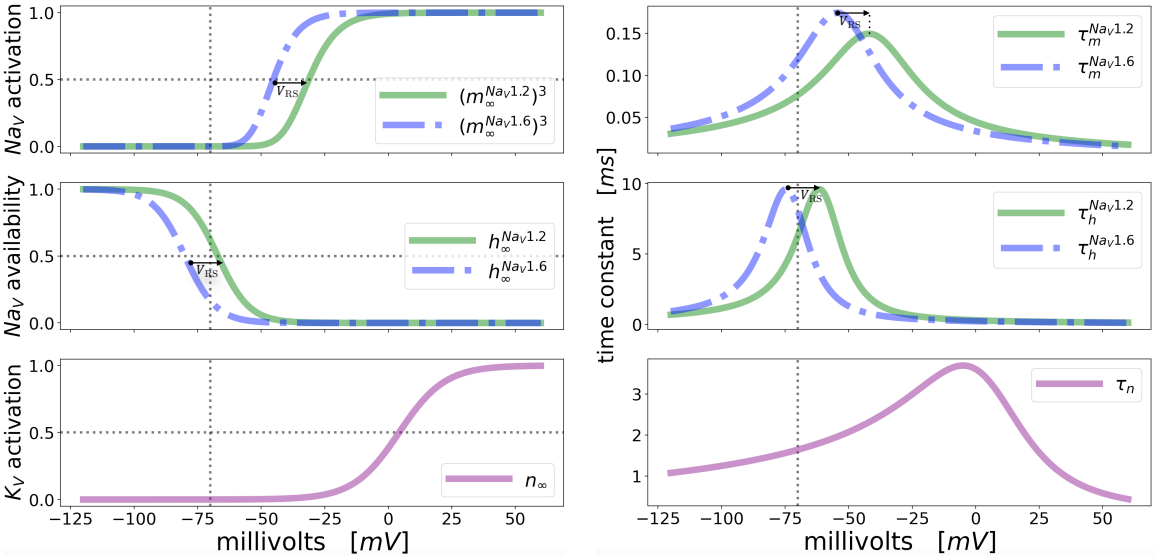

(i) Gating variables' steady-states (ii) And their voltage-sensitive time constants

Fig P: Gating properties of the voltage-gated sodium and potassium channels that are implemented in Hu-based model. Dotted vertical lines indicate the resting potential V_{rest}. **(i)** Steady-state *activation* and *availability* curves for $Na_V1.2$ and $Na_V1.6$, and steady-state K_V *activation*. **(ii)** Voltage-sensitive time constants of $Na_V1.2$, $Na_V1.6$, and K_V. $Na_V1.2$ is *right-shifted* by an amount V_{RS} relative to $Na_V1.6$ (defined in Section F.1). In this model, $V_{RS} = 13.0\text{mV}$; also called the 'nominal *right-shift*' of $Na_V1.2$. V_{RS} is **indicated by arrows** (small •⟶) in the plots of Na_V steady-states **(i)** and time constants **(ii)** above.

V_{RS} is indicated by arrows (small •⟶) in the plots of Na_V steady-states (Fig Pi) and time constants

(Fig Pii).

The *right-shift* of $Na_V1.2$ (defined mathematically in Section F.1) is easiest to observe in the top two plots of Fig Pi. V_{RS} is indicated by arrows (small $\longmapsto$). Steady-state *activation* $\left(m_\infty^{Na_V1.2}(V)\right)^3$ and *availability* $h_\infty^{Na_V1.2}(V)$ curves of $Na_V1.2$ are plotted as solid green lines, and dashed blue lines are the corresponding curves for $Na_V1.6$. The voltage separating the two Na_V subtypes' *activation* curves is approximately the nominal *right-shift*, V_{RS}; however, it varies with position, since the gating variables of Na_V *activation* ($m^{Na_V1.2}$, $m^{Na_V1.6}$) have different slopes [15]. However, the *availability* curves are easier to compare: in this model, $h_\infty^{Na_V1.2}(V)$ is shifted exactly $V_{RS} = 13.0\text{mV}$ to the right of $h_\infty^{Na_V1.6}(V)$. The *right-shift* of $Na_V1.2$ is also visible in the voltage-sensitive time constants (Fig Pii).

F.1 Defining V_{RS}: the *right-shift* of $Na_V1.2$

V_{RS} is a parameter in this model representing the experimentally measured depolarizing shift in the voltage dependence of $Na_V1.2$ *activation* and inactivation kinetics, relative to $Na_V1.6$ kinetics. Because V_{RS} is empirical, it is fixed in this paper.

We define the $Na_V1.6$ half-*activation* voltage $V_{1/2}^{Na_V1.6}$ as the voltage at which a single $Na_V1.6$ *activation* gate (randomly selected from an ensemble of gates held at $V = V_{1/2}^{Na_V1.6}$) has a 50% chance of being in the open state:

$$m_\infty^{Na_V1.6}(V_{1/2}^{Na_V1.6}) \stackrel{\text{def}}{=} \frac{1}{2}.$$

Although the kinetics of $Na_V1.2$ differ from $Na_V1.6$ kinetics in ways *other than right-shift*, we can now use $V_{1/2}^{Na_V1.6}$ to define V_{RS} as the voltage that satisfies

$$\boxed{m_\infty^{Na_V1.2}(V_{1/2}^{Na_V1.6} + V_{RS}) = m_\infty^{Na_V1.6}(V_{1/2}^{Na_V1.6}) = \frac{1}{2}}. \tag{S8}$$

Note that $V_{1/2}^{Na_V1.6}$ and V_{RS} are unique since m_∞ is monotonically increasing. Equation S8 also contains the half-*activation* voltage for $Na_V1.2$,

$$\left(V_{1/2}^{Na_V1.6} + V_{RS}\right) = V_{1/2}^{Na_V1.2}, \tag{S9}$$

which is depolarized or "*right-shifted*" by an amount V_{RS} relative to $Na_V1.6$ (see Fig P).

To simulate alterations to $Na_V1.2$ *right-shift* in our shift-clamping method, we use another parameter

called ΔV_{RS}, which is not based on experiment. Although the $\mathrm{Na_V}1.2$ *right-shift* is not a high precision measurement ($V_{\mathrm{RS}} \sim 10{-}15\mathrm{mV}$), the *parameter* V_{RS} is kept fixed in our model for conceptual purposes: we find it helpful to distinguish empirical parameters (like V_{RS}) from exploratory parameters that intentionally deviate from experiment (like ΔV_{RS}). In fact, we use ΔV_{RS} to selectively change the model's $\mathrm{Na_V}$ kinetics to explain the effects of $\mathrm{Na_V}$ distribution on excitability in terms of the lengthwise distribution of gating properties (see Modifying the *right-shift* of $\mathrm{Na_V}1.2$ gating properties in the AIS and Shift-Clamping and the Hodgkin-Huxley model).

F.2 Notation: V_{RS}, ΔV_{RS}

In our notation, V_{RS} is *not written explicitly* in the argument of $\mathrm{Na_V}1.2$ gating variables or their time constants. Instead, we write

$$\tau_h^{\mathrm{Na_V}1.6}(V),\ \tau_h^{\mathrm{Na_V}1.2}(V),\ m_\infty^{\mathrm{Na_V}1.6}(V),\ m_\infty^{\mathrm{Na_V}1.2}(V),\ \text{et cetera,}$$

and let the superscript "$\mathrm{Na_V}1.2$" indicate that $\tau_h^{\mathrm{Na_V}1.2}$ is *right-shifted* relative to $\tau_h^{\mathrm{Na_V}1.6}$, from the fact that $\mathrm{Na_V}1.2$ channels are *right-shifted* in this model.

However, the parameter ΔV_{RS} *is* written explicitly in the argument when we model the effects of modifying the *right-shift* (Fig 6: shift-clamping). For example, when applying $\Delta V_{\mathrm{RS}} \neq 0$ to the *selected* gating properties $\tau_h^{\mathrm{Na_V}1.2}$ and $m_\infty^{\mathrm{Na_V}1.2}$, we would write

$$\begin{cases} \tau_h^{\mathrm{Na_V}1.2} = \tau_h^{\mathrm{Na_V}1.2}(V - \Delta V_{\mathrm{RS}}) \\ h_\infty^{\mathrm{Na_V}1.2} = h_\infty^{\mathrm{Na_V}1.2}(V) \\ \tau_m^{\mathrm{Na_V}1.2} = \tau_m^{\mathrm{Na_V}1.2}(V) \\ m_\infty^{\mathrm{Na_V}1.2} = m_\infty^{\mathrm{Na_V}1.2}(V - \Delta V_{\mathrm{RS}}). \end{cases} \tag{S10}$$

Using this notation, positive values of ΔV_{RS} will shift kinetic curves (gating properties) to the right in Fig P (depolarizing shift), and negative ΔV_{RS} produces a hyperpolarizing shift.

F.3 Space plots of Na_V kinetics along the AIS — steady-state

The distribution of $Na_V1.2$ and $Na_V1.6$ in the AIS creates a lengthwise distribution of gating properties. Proximal $Na_V1.2$ increases local steady-state *availability*, owing to these channels' *right-shift* (V_{RS}). In Fig Qi we visualize this effect using $\mathcal{H}(s)$: the net *availability* of Na_Vs ($\mathcal{H}$) as a function of position (s), computed by weighting $h^{Na_V1.2}$ and $h^{Na_V1.6}$ according to their respective local Na_V channel densities:

$$\mathcal{H}(s,t) = \frac{\bar{g}_{Na_V1.2}(s)h^{Na_V1.2}(s,t) + \bar{g}_{Na_V1.6}(s)h^{Na_V1.6}(s,t)}{\bar{g}_{Na_V1.2}(s) + \bar{g}_{Na_V1.6}(s)}. \tag{S11}$$

An effective local Na_V time constant of *availability* ($\boldsymbol{\mathcal{T}}$) can be computed from $\tau_h^{Na_V1.2}$ and $\tau_h^{Na_V1.6}$ as

$$\boldsymbol{\mathcal{T}}(s,t) = \frac{\bar{g}_{Na_V1.2}(s)\tau_h^{Na_V1.2}(s,t) + \bar{g}_{Na_V1.6}(s)\tau_h^{Na_V1.6}(s,t)}{\bar{g}_{Na_V1.2}(s) + \bar{g}_{Na_V1.6}(s)}. \tag{S12}$$

Above, we have abbreviated

$$f(V(s,t),t) = f(s,t) \text{ for } f = h^{Na_V1.2}, h^{Na_V1.6}, \tau_h^{Na_V1.2}, \tau_h^{Na_V1.6}. \tag{S13}$$

In Fig Qii we have selectively disabled the *right-shift* of $\tau_h^{Na_V1.2}$ by setting $\Delta V_{RS} = -V_{RS} = -13.0\text{mV}$ in Equation 3, which leaves the *right-shift* of steady-state *availability* unchanged.

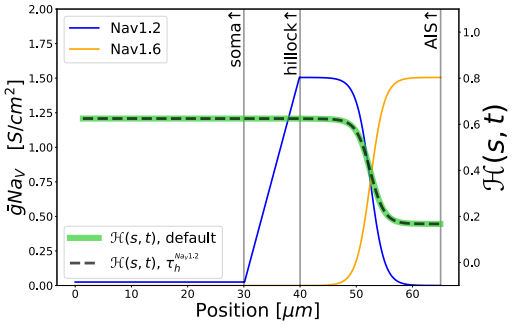

(i) Solid green curve: nominal $Na_V1.2$ *right-shift*. Travelling from left to right across the AIS, $Na_V1.6$ overtakes $Na_V1.2$ as a share of the total local Na_V density. The accompanying change in Na_V *right-shift* causes $\mathcal{H}(s)$ to drop from $\approx$ 0.6 at the soma and proximal AIS, down to $\approx$ 0.2 at the distal AIS and axon. Dashed black curve: the *right-shift* of $\tau_h^{Na_V1.2}$ has been selectively disabled without altering $h_\infty^{Na_V1.2}$, and thereby $\mathcal{H}$ is also unaffected. See (ii) to the right as well as Equation 3.

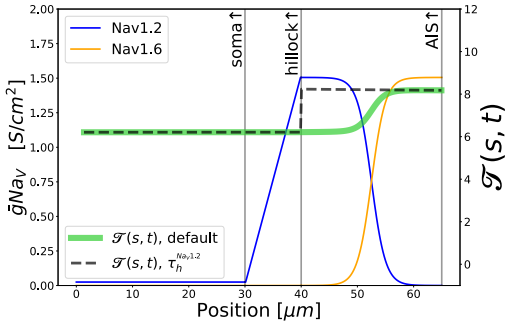

(ii) Solid green curve: nominal $Na_V1.2$ *right-shift*. Where $Na_V1.6$ overtakes $Na_V1.2$ as a share of the total local Na_V density, $\mathcal{T}(s)$ increases from $\approx$ 6ms to $\approx$ 8ms at V_{rest}. Dashed black curve: *right-shift* of $\tau_h^{Na_V1.2}$ selectively disabled by setting $\Delta V_{\text{RS}} = -V_{\text{RS}}$ in Equation 3. The effective time constant of Na_V *availability* $\mathcal{T}(s)$ is now uniform along the AIS. The abrupt transition in $\mathcal{T}$ at the AIS-hillock interface —instead of the smooth transition along the AIS in the green curve— is due to the *right-shift* of $\tau_h^{Na_V1.2}(V)$ being selectively disabled —see Equation S12. The *right-shift* of $h_\infty^{Na_V1.2}(V)$ has not been altered (see Equation S11), and the corresponding $\mathcal{H}$ (dashed black) curve in (i) is unchanged —hence the term "selective".

Fig Q: The effect of $Na_V1.2$ *right-shift* on local Na_V *availability* along the cell is visible in space plots of steady-state total *availability* $\mathcal{H}(s)$ (i) and total time constant $\mathcal{T}(s)$ (ii) at $V = V_{\text{rest}}$. See Equation S11 and Equation S12, respectively.

G Transformed backpropagation threshold data

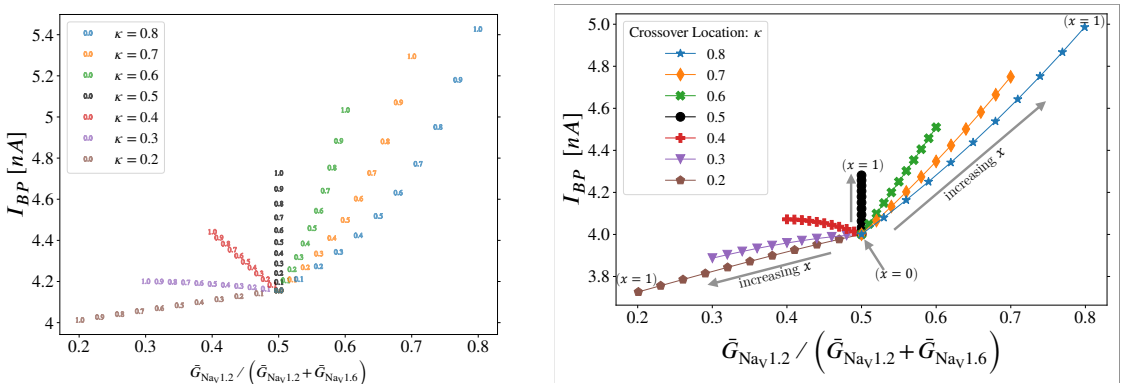

Fig R: **Backpropagation threshold plotted against the proportion of total AIS Na_V conductance allocated to $Na_V1.2$. (Somatic Stimulation.)** The data presented here are the I_{BP} measurements with somatic stimulation in the Hay-based model (left, see Fig 7A) and Hu-based model (right, see Fig 2) from the main text, transformed as follows: On the abscissa we replaced x with the ratio of $Na_V1.2$ channels —summed across all compartments in the AIS— to all Na_V channels in the AIS ($\frac{\sum_{\text{AIS segments}} \bar{g}_{Na_V1.2}}{\sum_{\text{AIS segments}} \bar{g}_{Na_V1.2} + \bar{g}_{Na_V1.6}}$). In the leftmost plot, each data point is marked by its x–value. All curves converge to a single point at 0.5 on the abscissa. That point is the I_{BP} for the flat distribution ($x = 0$), where half of the Na_V channels in the AIS are $Na_V1.2$ and the other half are $Na_V1.6$, and κ has no effect. So, $x = 0$ at the point where the curves converge, and x increases radially outward from this point, with all curves terminating at $x = 1$. The same pattern holds in the rightmost plot, in which the original markers were kept for comparison with Fig 2. These plots demonstrate that the impact on I_{BP} of spatially separating the Na_V subtypes (by increasing x) cannot be reduced to the concomitant change in total $Na_V1.2$ (or $Na_V1.6$) conductance —which only occurs when $\kappa \neq 0.5$. If the proportion of Na_V conductance contributed by each subtype in the AIS were really what determines the threshold, then every black marker would land at the same point. However, varying the spatial separation of Na_V subtypes in the AIS changes I_{BP} without any change to the ratio of total $Na_V1.2$ versus $Na_V1.6$ conductance (i.e. when $\kappa = 0.5$, the ratio is not affected by x).

H Diffusion coefficients

Diffusion coefficients for Na^+, K^+, and Cl^- in water at 25.0 ℃ are provided by [49] :

$$\begin{cases} D_{Na^+} = 1.334 \times 10^{-9} \frac{m^2}{s} \\ D_{K^+} = 1.957 \times 10^{-9} \frac{m^2}{s} \\ D_{Cl^-} = 2.032 \times 10^{-9} \frac{m^2}{s}. \end{cases} \tag{S14}$$

Our simulations are done at a warmer temperature, so these coefficients need to be adjusted. We make the adjustment using the Stokes-Einstein equation

$$D = \frac{k_B T}{\zeta(T)} = \frac{k_B T}{6\pi r \eta(T)} \; ; \tag{S15}$$

where k_B is Boltzmann's constant, T is the temperature (Kelvins K), and ζ is called the drag coefficient. ζ is given by the ion's radius r and the viscosity $\eta(T)$ of the medium (liquid water), which depends on temperature. Hence the ratio of diffusion coefficients for ion species Z at T_2 and T_1 is

$$\frac{D_Z(T_2)}{D_Z(T_1)} = \left(\frac{T_2}{T_1}\right)\left(\frac{\eta(T_1)}{\eta(T_2)}\right), \tag{S16}$$

with T_2 and T_1 converted to K. The reference values provided by [49] are measured at 298.15K (25.0℃), and the simulation temperature is 310.15K (37.0℃). Assuming the viscosity of water, we have $\eta(T_1) \cong$ 0.89 mPa s and $\eta(T_2) \cong 0.691$ mPa s. Substituting these η's into Equation S16 gives for each ionic species Z

$$\underbrace{D_Z(310.15K)}_{37.0℃} \cong 1.34 \times \underbrace{D_Z(298.15K)}_{25.0℃}, \tag{S17}$$

which yields the temperature-adjusted diffusion coefficients

$$\begin{cases} D_{Na^+} = 1.79 \times 10^{-9} \frac{m^2}{s} \\ D_{K^+} = 2.62 \times 10^{-9} \frac{m^2}{s} \\ D_{Cl^-} = 2.72 \times 10^{-9} \frac{m^2}{s}. \end{cases} \tag{S18}$$

I Tables of parameters

In Table A, we compare our Hu-based model from the main text to previous models on which it is based ([12, 26, 15]). At different locations in the cell, we tabularize parameter values from those papers alongside our own. We also include certain measurements (membrane potential, ion concentrations, Nernst potentials) taken from our model at each location once the cell has equilibrated.

The following symbols are used in Table A: (Units are given in the rightmost column.)

"×" This symbol appears when a parameter is not featured in the model corresponding to a given column.

$V_{\mathbf{rest}}$ Resting potential. The transmembrane voltage of the model neuron at steady-state with no injected current.

$V_{\mathbf{m}}^{\mathbf{location}}$ Transmembrane voltage at 'location'. In our model, the steady-state transmembrane voltage is actively maintained everywhere by Na^+/K^+-pumps and longitudinal diffusion, which control the explicit intracellular and extracellular ion concentrations. As such, the tabulated values are *recorded* from the model, not parameters per se. In the other models listed, V_{m} is identical to V_{rest}.

$R_{\mathbf{axial}}$ Axial resistance. The resistance to axial current flow across a compartment is R_{axial} multiplied by the compartment length, divided by the compartment's cross-sectional area.

$D_{\mathbf{ion}}$ Diffusion coefficient of the specified ion in water at $37°C$.

$T_{\mathbf{ref}}$ Reference temperature of experimentally developed channel properties used in the models. Past modelling, on which this paper is based, used temperature factors (described below) to adjust channel densities and speed up channel kinetics to warmer temperatures.

T Simulation temperature.

$Q_{\bar{g}_{\mathbf{V}}}^{\mathbf{Mainen}} = Q_{10,\bar{g}_{\mathbf{V}}}^{(T-T_{\mathbf{ref}})/10°C}$ To adjust for a warmer simulation temperature of $T = 37°C$ [26] scales up the maximal voltage-gated conductances, which were originally developed at $T = 23°C$ ([12]), by a factor which we denote $Q_{\mathrm{Mainen}}^{\bar{g}_{\mathrm{V}}}$. The authors warn in their model code that this scaling is valid only at $37°C$ and state that their program is not designed to model other temperatures. This internal temperature scaling can accidentally obscure parameter settings when one attempts to borrow parameters separately from the past code or from later papers that reuse these channel models. For this reason, we

have removed the temperature scaling from our own model code by setting our reference temperature equal to the simulation temperature, which sets $Q^{\bar{g}_V}_{\text{Mainen}} = 1$.

$\bar{g}^{\textbf{location}}_{\textbf{Na}_V\textbf{·Total}}$ Total combined maximal voltage-gated conductance density of $Na_V1.2$ and $Na_V1.6$ at the specified 'location' in the cell (see Equation S2). The location can be an entire Section if the membrane properties are uniform (in NEURON, Sections consist of multiple compartments). For example, this model has uniform somatodendritic channel densities, so 'soma' is sufficient to specify those parameters.

$\bar{g}^{\textbf{location}}_{\textbf{K}_V\textbf{·Total}}$ Maximal voltage-gated K^+ conductance density at the specified 'location'.

$C_{\textbf{m}}$ Membrane capacitance per unit area. Applies everywhere except at internodes.

$C^{\textbf{myelin}}_{\textbf{m}}$ Membrane capacitance of myelinated internodes.

$L_{\textbf{Section}}$ Length of the specified 'Section' (soma, hillock, AIS, etc.)

$d^{\textbf{position within Section}}_{\textbf{Section}}$ Diameter at a given normalized position $(0 \leqslant s \leqslant 1)$ within the specified Section (soma, hillock, AIS, etc.). The position is not specified when the diameter is uniform.

$R^{\textbf{Section}}_{\textbf{Passive}}$ Membrane resistivity in 'Section'.

$g^{\textbf{Section}}_{\textbf{Passive}}$ Passive generic transmembrane leak conductance density in 'Section'.

$g^{\textbf{Section}}_{\textbf{Ion, leak}}$ Specific leak conductance density of 'Ion' in 'Section'.

$I^{\textbf{Section}}_{\textbf{MaxPump}}$ Maximum Na^+/K^+-pump current density in 'Section'.

$E^{\textbf{Section}}_{\textbf{current type}}$ Nernst Potential (reversal potential) of transmembrane current 'current type' (e.g. 'leak') in 'Section' (e.g. 'soma').

$\textbf{[Ion]}^{\textbf{Section}}_{\textbf{in/out}}$ Intracellular ('in') or Extracellular ('out') concentration of 'Ion' at 'Section', with the neuron at steady-state. Because these concentrations are maintained by Na^+/K^+-pumps and longitudinal diffusion in our model, the concentrations tabulated here are measurements *recorded* from the simulation at steady-state, rather than being fixed parameters.

ranvier0, myelin0: In our model, there are 15 nodes of Ranvier and 16 myelinated internodes. The Section named 'ranvier0' is the first node of Ranvier. And 'myelin0' is the first myelinated internode of the axon, located between the distal end of the AIS (or the distal end of the bare axon when that is included) and the proximal end of ranvier0.

dend11[**22**] Main apical dendrite.

Table A: Parameters of the Hu-Based model from the main text, compared across the Hu model [15] and the original Mainen models [12, 26] upon which the Hu model was built. In the soma and dendrites of the Hu-based model, channel densities differ significantly from Hu et al. (2009) [15] to attenuate the backpropagated action potential. In the Supporting "modified Hu-based model" (Section D), those conductances match [15] closely. (We have opted to call the version in the main text the "Hu-based model" (i.e. with attenuating BAP), and the version in the Supporting Information the "modified Hu-based model" even though the parameters of the latter more closely match those of [15].) In the latter, BAP attenuation is negligible, however, the impacts on I_{BP} of varying the AIS Na_V distribution are qualitatively unchanged from the main text.

Type	Parameter Name	Hu-Based	Mainen95	Mainen96	Hu2009	units
Global						
	V_{rest}	−70.0	−70.0	−70.0	−70.0	mV
	R_{axial}	150	200	150	150	$\Omega \cdot \text{cm}$
	D_{Cl^-}	2.72	×	×	×	$10^{-9}\frac{m^2}{s}$
	D_{Na^+}	1.79	×	×	×	$10^{-9}\frac{m^2}{s}$
	D_{K^+}	2.62	×	×	×	$10^{-9}\frac{m^2}{s}$
	T_{ref}	37.0	23.0	23.0	23.0	℃
	T	37.0	23.0	37.0	37.0	℃
	$Q_{\bar{g}_V}^{\text{Mainen}} = Q_{10,\bar{g}_V}^{(T-T_{\text{ref}})/10℃}$	1.0	1.0	3.21	3.21	dimensionless
	C_m	0.75	0.75	0.75	1.0	$\frac{\mu F}{cm^2}$

	$C_{\mathrm{m}}^{\mathrm{myelin}}$	0.02	0.04	0.02	0.02	$\frac{\mu F}{\mathrm{cm}^2}$
Geometry						
	L_{soma}	30.0	25.8	30.0	30.0	µm
	L_{hillock}	10.0	10.0	10.0	10.0	µm
	L_{AIS}	25.0	15.0	15.0	50.0	µm
	$L_{\mathrm{bare\cdot axon}}$	400	×	×	400	µm
	$d_{\mathrm{soma}}^{0.5}$	19.38	15.2	19.0	19.0	µm
	$d_{\mathrm{soma}}^{1.0}$	8.62	15.2	8.6	8.6	µm
	$d_{\mathrm{hillock}}^{0.0}$	8.62	4.0	4.0	3.8	µm
	$d_{\mathrm{hillock}}^{1.0}$	1.22	1.0	1.0	2.4	µm
	d_{AIS}	1.22	1.0	1.0	1.22	µm
	$d_{\mathrm{bare\cdot axon}}$	1.22	×	×	1.02	µm
section	Parameter Name	Hu-Based	Mainen95	Mainen96	Hu2009	units
soma						
	$\bar{g}_{\mathrm{Na_V\cdot Total}}^{\mathrm{soma}}$	7.53×10^{-2}	0.003	0.002	0.008	$\frac{\mho}{\mathrm{cm}^2}$

$\bar{g}^{\text{soma}}_{\text{Na}_\text{V}\cdot\text{Total}} \times Q^{\text{Mainen}}_{\bar{g}_\text{V}}$	7.53×10^{-2}	3.00×10^{-3}	6.42×10^{-3}	2.57×10^{-2}	$\frac{\text{℧}}{\text{cm}^2}$
$\bar{g}^{\text{soma}}_{\text{K}_\text{V}}$	2.26×10^{-2}	0.01	0.02	0.002	$\frac{\text{℧}}{\text{cm}^2}$
$\bar{g}^{\text{soma}}_{\text{K}_\text{V}} \times Q^{\text{Mainen}}_{\bar{g}_\text{V}}$	2.26×10^{-2}	1.00×10^{-2}	6.42×10^{-2}	6.42×10^{-3}	$\frac{\text{℧}}{\text{cm}^2}$
$R^{\text{soma}}_{\text{Passive}}$	2.39×10^{3}	4.00×10^{4}	3.00×10^{4}	3.00×10^{4}	$\Omega \cdot \text{cm}^2$
$g^{\text{soma}}_{\text{Passive}}$	4.19×10^{-4}	2.50×10^{-5}	3.33×10^{-5}	3.33×10^{-5}	$\frac{\text{℧}}{\text{cm}^2}$
$g^{\text{soma}}_{\text{Cl}^-,\text{ leak}}$	6.27×10^{-5}	×	×	×	$\frac{\text{℧}}{\text{cm}^2}$
$g^{\text{soma}}_{\text{Na}^+,\text{ leak}}$	6.68×10^{-5}	×	×	×	$\frac{\text{℧}}{\text{cm}^2}$
$g^{\text{soma}}_{\text{K}^+,\text{ leak}}$	2.90×10^{-4}	×	×	×	$\frac{\text{℧}}{\text{cm}^2}$
$I^{\text{soma}}_{\text{MaxPump}}$	3.99×10^{-2}	×	×	×	$\frac{\text{mA}}{\text{cm}^2}$
$V^{\text{soma}}_{\text{m}}$	-70.0	-70.0	-70.0	-70.0	mV
$E^{\text{soma}}_{\text{leak}}$	×	-70.0	-70.0	-70.0	mV
$E^{\text{soma}}_{\text{Cl}}$	-70.0	×	×	×	mV
$E^{\text{soma}}_{\text{Na}}$	60.0	60.0	50.0	60.0	mV
$E^{\text{soma}}_{\text{K}}$	-90.0	-90.0	-90.0	-90.0	mV

$[Cl^-]_{in}^{soma}$	11.0	×	×	×	mM
$[Cl^-]_{out}^{soma}$	151.0	×	×	×	mM
$[Na^+]_{in}^{soma}$	15.0	×	×	×	mM
$[Na^+]_{out}^{soma}$	141.6	×	×	×	mM
$[K^+]_{in}^{soma}$	140.0	×	×	×	mM
$[K^+]_{out}^{soma}$	4.8	×	×	×	mM

section	Parameter Name	Hu-Based	Mainen95	Mainen96	Hu2009	units
AIS						
	$\bar{g}_{Na_V\cdot Total}^{AIS}$	1.505	3.0	3.0	0.32	$\frac{\mho}{cm^2}$
	$\bar{g}_{Na_V\cdot Total}^{AIS} \times Q_{\bar{g}_V}^{Mainen}$	1.505	3.0	9.628	1.027	$\frac{\mho}{cm^2}$
	$\bar{g}_{K_V}^{AIS}$	4.52×10^{-1}	×	0.2	0.1	$\frac{\mho}{cm^2}$
	$\bar{g}_{K_V}^{AIS} \times Q_{\bar{g}_V}^{Mainen}$	4.52×10^{-1}	×	6.42×10^{-1}	3.21×10^{-1}	$\frac{\mho}{cm^2}$
	$R_{Passive}^{AIS}$	4.77×10^{1}	5.00×10^{1}	5.00×10^{1}	5.00×10^{1}	$\Omega \cdot cm^2$
	$g_{Passive}^{AIS}$	2.10×10^{-2}	2.00×10^{-2}	2.00×10^{-2}	2.00×10^{-2}	$\frac{\mho}{cm^2}$
	$g_{Cl^-,\ leak}^{AIS}$	3.14×10^{-3}	×	×	×	$\frac{\mho}{cm^2}$

$g^{\mathrm{AIS}}_{\mathrm{Na^+,\,leak}}$	3.34×10^{-3}	×	×	×	$\frac{\mho}{\mathrm{cm}^2}$
$g^{\mathrm{AIS}}_{\mathrm{K^+,\,leak}}$	1.45×10^{-2}	×	×	×	$\frac{\mho}{\mathrm{cm}^2}$
$I^{\mathrm{AIS}}_{\mathrm{MaxPump}}$	1.995	×	×	×	$\frac{\mathrm{mA}}{\mathrm{cm}^2}$
$V^{\mathrm{AIS}}_{\mathrm{m}}$	−69.9	−70.0	−70.0	−70.0	mV
$E^{\mathrm{AIS}}_{\mathrm{leak}}$	×	−70.0	−70.0	−70.0	mV
$E^{\mathrm{AIS}}_{\mathrm{Cl}}$	−70.0	×	×	×	mV
$E^{\mathrm{AIS}}_{\mathrm{Na}}$	59.9	60.0	50.0	60.0	mV
$E^{\mathrm{AIS}}_{\mathrm{K}}$	−90.0	−90.0	−90.0	−90.0	mV
$[\mathrm{Cl^-}]^{\mathrm{AIS}}_{\mathrm{in}}$	11.0	×	×	×	mM
$[\mathrm{Cl^-}]^{\mathrm{AIS}}_{\mathrm{out}}$	151.0	×	×	×	mM
$[\mathrm{Na^+}]^{\mathrm{AIS}}_{\mathrm{in}}$	15.1	×	×	×	mM
$[\mathrm{Na^+}]^{\mathrm{AIS}}_{\mathrm{out}}$	141.6	×	×	×	mM
$[\mathrm{K^+}]^{\mathrm{AIS}}_{\mathrm{in}}$	139.9	×	×	×	mM
$[\mathrm{K^+}]^{\mathrm{AIS}}_{\mathrm{out}}$	4.8	×	×	×	mM

section	Parameter Name	Hu-Based	Mainen95	Mainen96	Hu2009	units
myelin0						
	$\bar{g}^{\text{myelin0}}_{\text{Na}_\text{V}\cdot\text{Total}}$	1.61×10^{-2}	0.003	×	0.002	$\frac{\text{℧}}{\text{cm}^2}$
	$\bar{g}^{\text{myelin0}}_{\text{Na}_\text{V}\cdot\text{Total}} \times Q^{\text{Mainen}}_{\bar{g}_\text{V}}$	1.61×10^{-2}	3.00×10^{-3}	×	6.42×10^{-3}	$\frac{\text{℧}}{\text{cm}^2}$
	$\bar{g}^{\text{myelin0}}_{\text{K}_\text{V}}$	4.82×10^{-3}	×	×	×	$\frac{\text{℧}}{\text{cm}^2}$
	$\bar{g}^{\text{myelin0}}_{\text{K}_\text{V}} \times Q^{\text{Mainen}}_{\bar{g}_\text{V}}$	4.82×10^{-3}	×	×	×	$\frac{\text{℧}}{\text{cm}^2}$
	$R^{\text{myelin0}}_{\text{Passive}}$	1.12×10^{4}	4.00×10^{4}	3.00×10^{4}	3.00×10^{4}	$\Omega \cdot \text{cm}^2$
	$g^{\text{myelin0}}_{\text{Passive}}$	8.94×10^{-5}	2.50×10^{-5}	3.33×10^{-5}	3.33×10^{-5}	$\frac{\text{℧}}{\text{cm}^2}$
	$g^{\text{myelin0}}_{\text{Cl}^-,\text{ leak}}$	1.34×10^{-5}	×	×	×	$\frac{\text{℧}}{\text{cm}^2}$
	$g^{\text{myelin0}}_{\text{Na}^+,\text{ leak}}$	1.43×10^{-5}	×	×	×	$\frac{\text{℧}}{\text{cm}^2}$
	$g^{\text{myelin0}}_{\text{K}^+,\text{ leak}}$	6.18×10^{-5}	×	×	×	$\frac{\text{℧}}{\text{cm}^2}$
	$I^{\text{myelin0}}_{\text{MaxPump}}$	8.51×10^{-3}	×	×	×	$\frac{\text{mA}}{\text{cm}^2}$
	$V^{\text{myelin0}}_{\text{m}}$	−69.5	−70.0	−70.0	−70.0	mV
	$E^{\text{myelin0}}_{\text{leak}}$	×	−70.0	−70.0	−70.0	mV
	$E^{\text{myelin0}}_{\text{Cl}}$	−70.0	×	×	×	mV

$E_{\mathrm{Na}}^{\mathrm{myelin0}}$	60.0	60.0	50.0	60.0	mV
$E_{\mathrm{K}}^{\mathrm{myelin0}}$	−90.0	−90.0	−90.0	−90.0	mV
$[\mathrm{Cl}^-]_{\mathrm{in}}^{\mathrm{myelin0}}$	11.0	×	×	×	mM
$[\mathrm{Cl}^-]_{\mathrm{out}}^{\mathrm{myelin0}}$	151.0	×	×	×	mM
$\left[\mathrm{Na}^+\right]_{\mathrm{in}}^{\mathrm{myelin0}}$	15.0	×	×	×	mM
$\left[\mathrm{Na}^+\right]_{\mathrm{out}}^{\mathrm{myelin0}}$	141.6	×	×	×	mM
$\left[\mathrm{K}^+\right]_{\mathrm{in}}^{\mathrm{myelin0}}$	140.0	×	×	×	mM
$\left[\mathrm{K}^+\right]_{\mathrm{out}}^{\mathrm{myelin0}}$	4.8	×	×	×	mM

section	Parameter Name	Hu-Based	Mainen95	Mainen96	Hu2009	units
ranvier0						
	$\bar{g}_{\mathrm{Na_V.Total}}^{\mathrm{ranvier0}}$	8.03×10^{-1}	3.0	3.0	0.16	$\frac{\mho}{\mathrm{cm}^2}$
	$\bar{g}_{\mathrm{Na_V.Total}}^{\mathrm{ranvier0}} \times Q_{\bar{g}_{\mathrm{V}}}^{\mathrm{Mainen}}$	8.03×10^{-1}	3.0	9.628	5.13×10^{-1}	$\frac{\mho}{\mathrm{cm}^2}$
	$\bar{g}_{\mathrm{K_V}}^{\mathrm{ranvier0}}$	2.41×10^{-1}	×	×	×	$\frac{\mho}{\mathrm{cm}^2}$
	$\bar{g}_{\mathrm{K_V}}^{\mathrm{ranvier0}} \times Q_{\bar{g}_{\mathrm{V}}}^{\mathrm{Mainen}}$	2.41×10^{-1}	×	×	×	$\frac{\mho}{\mathrm{cm}^2}$
	$R_{\mathrm{Passive}}^{\mathrm{ranvier0}}$	2.24×10^{2}	5.00×10^{1}	5.00×10^{1}	5.00×10^{1}	$\Omega \cdot \mathrm{cm}^2$

$g^{\text{ranvier0}}_{\text{Passive}}$	4.47×10^{-3}	2.00×10^{-2}	2.00×10^{-2}	2.00×10^{-2}	$\frac{\text{℧}}{\text{cm}^2}$
$g^{\text{ranvier0}}_{\text{Cl}^-,\text{ leak}}$	6.69×10^{-4}	×	×	×	$\frac{\text{℧}}{\text{cm}^2}$
$g^{\text{ranvier0}}_{\text{Na}^+,\text{ leak}}$	7.13×10^{-4}	×	×	×	$\frac{\text{℧}}{\text{cm}^2}$
$g^{\text{ranvier0}}_{\text{K}^+,\text{ leak}}$	3.09×10^{-3}	×	×	×	$\frac{\text{℧}}{\text{cm}^2}$
$I^{\text{ranvier0}}_{\text{MaxPump}}$	4.26×10^{-1}	×	×	×	$\frac{\text{mA}}{\text{cm}^2}$
$V^{\text{ranvier0}}_{\text{m}}$	-69.4	-70.0	-70.0	-70.0	mV
$E^{\text{ranvier0}}_{\text{leak}}$	×	-70.0	-70.0	-70.0	mV
$E^{\text{ranvier0}}_{\text{Cl}}$	-70.0	×	×	×	mV
$E^{\text{ranvier0}}_{\text{Na}}$	60.0	60.0	50.0	60.0	mV
$E^{\text{ranvier0}}_{\text{K}}$	-90.0	-90.0	-90.0	-90.0	mV
$[\text{Cl}^-]^{\text{ranvier0}}_{\text{in}}$	11.0	×	×	×	mM
$[\text{Cl}^-]^{\text{ranvier0}}_{\text{out}}$	151.0	×	×	×	mM
$\left[\text{Na}^+\right]^{\text{ranvier0}}_{\text{in}}$	15.0	×	×	×	mM
$\left[\text{Na}^+\right]^{\text{ranvier0}}_{\text{out}}$	141.6	×	×	×	mM

$[K^+]_{in}^{ranvier0}$	140.0	×	×	×	mM
$[K^+]_{out}^{ranvier0}$	4.8	×	×	×	mM

section	Parameter Name	Hu-Based	Mainen95	Mainen96	Hu2009	units
dend11[22]						
	$\bar{g}_{Na_V\cdot Total}^{dend11[22]}$	2.51×10^{-3}	0.003	0.00015	8.0×10^{-3}	$\frac{\mho}{cm^2}$
	$\bar{g}_{Na_V\cdot Total}^{dend11[22]} \times Q_{\bar{g}_V}^{Mainen}$	2.51×10^{-3}	3.00×10^{-3}	4.82×10^{-3}	2.57×10^{-2}	$\frac{\mho}{cm^2}$
	$\bar{g}_{K_V}^{dend11[22]}$	7.53×10^{-4}	0.01	×	1.0×10^{-3}	$\frac{\mho}{cm^2}$
	$\bar{g}_{K_V}^{dend11[22]} \times Q_{\bar{g}_V}^{Mainen}$	7.53×10^{-4}	1.00×10^{-2}	×	3.21×10^{-3}	$\frac{\mho}{cm^2}$
	$R_{Passive}^{dend11[22]}$	7.16×10^4	4.00×10^4	3.00×10^4	3.00×10^4	$\Omega \cdot cm^2$
	$g_{Passive}^{dend11[22]}$	1.40×10^{-5}	2.50×10^{-5}	3.33×10^{-5}	3.33×10^{-5}	$\frac{\mho}{cm^2}$
	$g_{Cl^-,\ leak}^{dend11[22]}$	2.09×10^{-6}	×	×	×	$\frac{\mho}{cm^2}$
	$g_{Na^+,\ leak}^{dend11[22]}$	2.23×10^{-6}	×	×	×	$\frac{\mho}{cm^2}$
	$g_{K^+,\ leak}^{dend11[22]}$	9.66×10^{-6}	×	×	×	$\frac{\mho}{cm^2}$
	$I_{MaxPump}^{dend11[22]}$	1.33×10^{-3}	×	×	×	$\frac{mA}{cm^2}$
	$V_m^{dend11[22]}$	−70.0	−70.0	−70.0	−70.0	mV

$E_{\text{leak}}^{\text{dend11[22]}}$	×	−70.0	−70.0	−70.0	mV
$E_{\text{Cl}}^{\text{dend11[22]}}$	−70.0	×	×	×	mV
$E_{\text{Na}}^{\text{dend11[22]}}$	60.0	60.0	50.0	60.0	mV
$E_{\text{K}}^{\text{dend11[22]}}$	−90.0	−90.0	−90.0	−90.0	mV
$[\text{Cl}^-]_{\text{in}}^{\text{dend11[22]}}$	11.0	×	×	×	mM
$[\text{Cl}^-]_{\text{out}}^{\text{dend11[22]}}$	151.0	×	×	×	mM
$[\text{Na}^+]_{\text{in}}^{\text{dend11[22]}}$	15.0	×	×	×	mM
$[\text{Na}^+]_{\text{out}}^{\text{dend11[22]}}$	141.6	×	×	×	mM
$[\text{K}^+]_{\text{in}}^{\text{dend11[22]}}$	140.0	×	×	×	mM
$[\text{K}^+]_{\text{out}}^{\text{dend11[22]}}$	4.8	×	×	×	mM

6.5 Tripwires: An adventure in model reproducibility

This section—roughly ten pages in length—discusses some practical aspects of multicompartmental modelling and specific issues I encountered while working with published code. Readers who are *not* working on their own modelling projects should feel free to skip ahead to ***Chapter 6 Synthesis*** on page#230.

Model code is shared to allow researchers to investigate new questions.

The construction of realistic neuron models is a multidisciplinary effort. Creating and maintaining reliable computational infrastructure (cell morphologies, adaptable biophysics, model curation) is a field in itself.

Due to the complexity of modelling conductance-based three-dimensional pyramidal neurons, I began with code and data from published studies, which constituted the ground truth of a cell's shape and the mechanisms of its excitability. It is not practical to single-handedly create a realistic multicompartmental neuron simulation from scratch—in the literal sense. Without going entirely down this rabbit hole, note that the computer language in which simulations are programmed (e.g. `Python`[4]) is itself a piece of software. Researchers in the wet lab are needed to record cell morphologies and to measure channel kinetics. Computer scientists are needed to design reliable local-variable-time-step methods to integrate nonlinear differential equations across thousands of coupled compartments.

I employed published cell morphologies, loaded via ***NEURON****.*

The software that allowed me to load the recorded morphology of pyramidal neurons and insert our biophysical transmembrane currents into them is called NEURON[5] (see Carnevale and Hines [9]). Beyond that infrastructure, we relied on experimental measurements of the properties of different ion channels in the AIS and a plethora of parameter values describing how the density of ion channels and membrane properties varies with position in the model—some of which were hand-tuned in prior studies and re-tuned for this project.

[4] `www.python.org`
[5] `https://www.neuron.yale.edu/neuron/`

I began my pyramidal cell simulations by inserting the ***CLS*** point cell model (Joós et al. [28], Boucher et al. [8]) into every compartment of the somatodendritic morphology from Hu et al. [23]. Later, I included the $Na_V1.2$, $Na_V1.6$, and K_V channel kinetics from [23] in a new version of ***T-CLS*** (Barlow et al. [2]) that featured a passive Cl^- leak current rather than the generic leak current from the original ***T-CLS*** model.

The adventure that I detail *here* arose from hidden problems in the original model code of Hu et al. [23], that made what ought to have been a straightforward programming task—adding the voltage-gated kinetics from [23] to the ***T-CLS*** simulator—into a baffling ordeal. In this thesis, the term "Hu-based model" refers to simulations that were created by adding a chloride leak current and the cell morphology and voltage-gated Na_V and K_V kinetics from [23] to the ***T-CLS*** model (Barlow et al. [4]).

Unexpected bugs in published model code caused problems, but it was important to resurrect the empirical Na_V channel kinetics from Hu et al. [23].

In their 2009 study, Hu et al. [23] used code from a 1995 paper by Mainen et al. [39] which contained bugs.[6] In one case, I found that no matter what I tried, I could not generate a plot of the Na_V channels' voltage-sensitive time constants. Without those curves, there was no way to be certain that my model would be faithful to the kinetics of the original Hu model [23]. I was also having difficulty convincing action potentials to backpropagate into the dendrites of a model that ran the channel kinetics of the ***T-CLS*** model [2], with the density of channels set to the parameters of [23]. It was desirable to match the $Na_V1.2$ and $Na_V1.6$ kinetic curves in my Hu-based model to [23] since the latter were fitted to electrophysiological recordings of sodium currents in the proximal and distal AIS. This led to several delays as I tried to figure out where *I* had made a mistake.

Out of habit, I assumed that I had made a mistake. This delayed finding the errors in multiple subprograms of the Hu et al. [23] model code.

[6] These issues are corrected in the ModelDB entry for Mainen and Sejnowski (1996) ([38], `https://modeldb.science/2488`), which was partly built on the code of Mainen et al. [39]. Despite these corrections, the code of the Hu et al. [23] model, and other papers (e.g. Kole et al. [32], Shu et al. [51] and more), had not been corrected at the time of writing this thesis.

Sifting through my simulation code, painstakingly searching for errors that would explain the problems I was having, and finding none, I tried rewriting my programs from scratch. When that did not work, I tried simulating the kinetics from Kole et al. [32] with code from their ModelDB entry[7], but alas, I could not plot gating properties in the Kole et al. model either.

With the same issues repeating in my implementation of two models, it seemed logical to assume that the problem was due to an error on my part. Another (questionable) reason for me to assume I was in error is that the simulations *did run*. That is, I could generate action potentials using code from [23], despite the difficulties in achieving backpropagation and plotting channel kinetics, etc.

Although Hu et al. [23] specify that their channel models were from Mainen et al. [39], they also explain that their pyramidal neuron morphology was taken from a different paper, Mainen and Sejnowski [38]. I recognized the similarity between the corrected Na_V channel code in [38] and other uncorrected models, including [23], and decided to copy the *parameters* from the flawed code of [23] into the corrected code of [38]. That provided a basis for comparison between the voltage-gated channel kinetics as I had implemented them in the ***T-CLS*** model with what Hu et al. [23] had done in their simulations. See Figure 6.1 below.

Hu et al. [23]'s channel models were from Mainen et al. [39], but cell morphology was from Mainen and Sejnowski [38]. Only the latter was corrected. Careful comparison across multiple published models revealed that Hu et al. [23]'s code was missing corrections present in other models.

[7] https://modeldb.science/114394

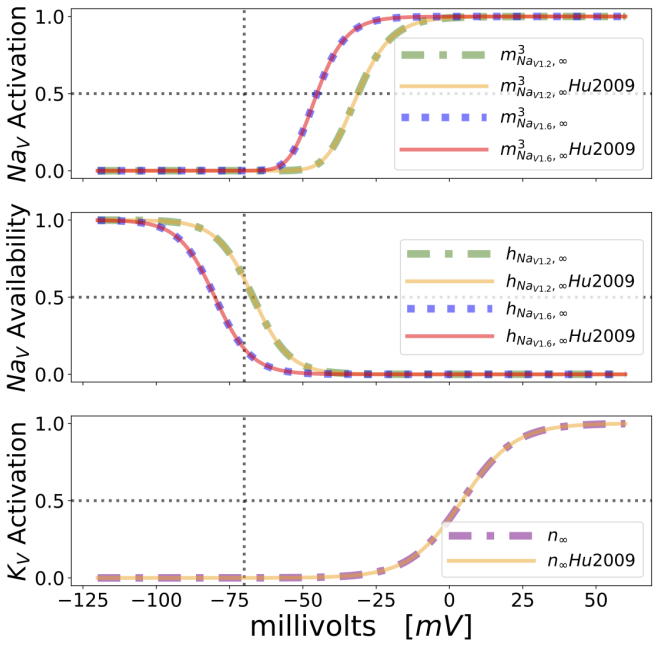

(a) Steady state activation and availability curves for $Na_V1.2$, $Na_V1.6$, and K_V.

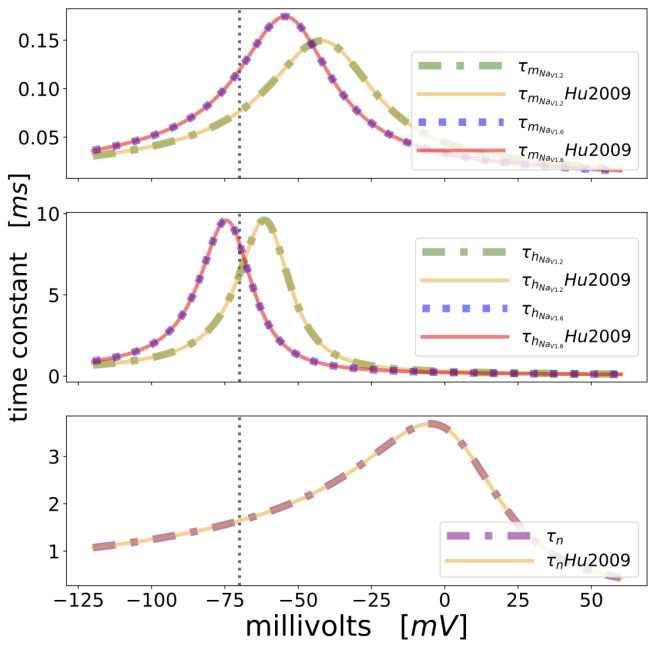

(b) Voltage sensitive time constants of $Na_V1.2$, $Na_V1.6$, and K_V.

Figure 6.1: **Resurrecting the voltage-gated channel kinetics of Hu et al. [23].** Solid curves are the modelled channel kinetics of $Na_V1.2$, $Na_V1.6$, and K_V generated from the parameters of Hu et al. [23] (`https://modeldb.science/123897`) and a corrected version of their code, which I implemented using the updated ModelDB entry for Mainen and Sejnowski [38]. Dashed lines overlaying the solid curves are the corresponding channel kinetics from my Hu-based model (Barlow et al. [4], `https://modeldb.science/267088`).

Tripwires are expected when reanimating old model code. I will only discuss the worst ones I encountered in this project.

Reinstantiating and building upon published computer models frequently involves a lot of front-loaded work, and problems are to be expected. I will not attempt to describe all of the problems that needed to be solved on the way to creating a detailed Hu-based model [4] out of the *T-CLS* point-cell model [2]. Instead, I will limit the discussion to the major tripwires in the original Hu model code[8] that I encountered when implementing the Hu-based model.

Merriam-Webster provides the following definition:

> **tripwire** | a low-placed concealed wire used especially in warfare to trip an enemy or trespasser and usually to trigger an alarm or explosive device when moved

Def^{n}: tripwire | *A piece of old code that runs unnoticed but tortures the new implementer with elusive malfunctions.*

The term is appropriate here because the code from [23] would run despite these pre-existing issues (described below), which is arguably the worst kind of problem to have as a programmer. When running simulation code from another published model, one would rather be faced with errors that crash the program since they make themselves known and can be quickly traced back to a line in the source code. The problems detailed here are tripwires because they were difficult to detect, and they halted progress through flabbergasting simulation results rather than error messages.

(Note: I must stress that I am in no way accusing Hu et al., nor anyone else, of malice or intentional omissions, as it became clear that bugs in their model originated in code they too had reused. One should assume that researchers do their utmost to avoid errors in their models. Authors should be thanked for making their code available, *not* condemned for unintended bugs. Further, I am not claiming that said bugs invalidate their research.)

[8] https://modeldb.science/123897

6.5.1 Two notable tripwires

With all of that said, the code of Hu et al. [23] contains two major tripwires:

1. A silent rescaling of the maximal conductance of voltage-gated channels (e.g. Na_V channel density) to a value that is different from what is input by the user, meaning that those parameters will not transfer to other neuron models, and
2. the mishandling of singularities that appear in the calculation of the forward and backward rate coefficients of Hodgkin-Huxley style voltage-gated channels at certain values of the membrane potential.

Disclaimer: The issues outlined herein are not intended to disparage previous works, but rather to caution future students and researchers and hopefully save them some time and effort.

In `NEURON`, it is common to include a description of a channel model at the top of its program. This is where one places helpful guidelines for future researchers who may reuse the code. It is an especially good place to warn against issues that may arise when repurposing the code. In Figure 6.2, I have included the opening comments from the $Na_V1.6$ channel model of [23].

The Hu model has a variable called `tadj = q10^((celsius - temp)/10)`. The parameter `temp` is the reference temperature for the channel model, `celsius` is the simulation temperature, and `q10` $= 2.3$ is the dimensionless temperature sensitivity. One of the effects of `tadj` in this model is to rescale the maximal conductance via `gnabar` $\longrightarrow$ `tadj*gbar`.

Hu et al. [23] make no mention of the temperature scaling, even if one checks the Na_V channel code.

Note, however, that there are no comments regarding the temperature in Figure 6.2. That is because the code they reused came from Mainen et al. [39], which was run at `celsius` $= 23$℃ ($=$ `temp`), and therefore the temperature adjustment to the maximal conductance parameter `gbar` had no effect (i.e. `tadj` $= 1$). However, Hu et al. ran their simulations at 37℃, where `tadj` *does* have an effect (i.e. `tadj` ≈ 3.21).

```
1
2  na16.mod
3
4  Sodium channel, Hodgkin-Huxley style kinetics.
5
6  Kinetics were fit to data from Huguenard et al. (1988) and Hamill et
7  al. (1991)
8
9  qi is not well constrained by the data, since there are no points
10 between -80 and -55.  So this was fixed at 5 while the thi1,thi2,Rg,Rd
11 were optimized using a simplex least square proc
12
13 voltage dependencies are shifted approximately from the best
14 fit to give higher threshold
15
16 Author: Zach Mainen, Salk Institute, 1994
17
18 ENDCOMMENT
```

Figure 6.2: **Introductory comments at top of the Na_V model code from Hu et al. [23].** There are three Na_V channel models in the ModelDB entry for this paper with the same opening comments. The channel models also contain the same *silent* temperature-rescaling of ion channel densities (discussed below) and the same error in handling singularities (see Figure 6.3). The code and comments are from the original model of Mainen et al. [39], which Hu et al. [23] later fitted to their experimentally measured Na_V currents in the AIS.

The trouble this causes is that if another researcher wishes to test the maximal conductance parameters from [23] in their own simulator, they will not be aware that the listed `gbar` values are multiplied by the factor `tadj` ≈ 3.21, because there is no parameter that stores `tadj*gbar`, which is the value that is actually used. (This problem is not unique to [23].)

Silently rescaling the maximal conductances conceals the true parameter values and impedes reproducibility.

In summary, the silent temperature adjustment that I have just described interferes with model reproducibility in two ways. First, if a researcher reuses the code, he or she may be unaware of the true values of the conductance parameters—since they are scaled within the channel model—and then publish the unscaled values. Second, if one instead opts to write their own code (as I did) and attempt to copy

parameter values from papers that used code with this hidden rescaling, they will need to multiply the parameters by the appropriate `tadj`, and there is no reason for them to know that.

When modellers modify parameters, they usually list the true values alongside the equations that contain them.

Papers that simulate the effects of temperature on transmembrane conductances (e.g. [57, 2]) typically say so explicitly, but the peculiarity of the code from Hu et al. [23]—and others reusing the code from Mainen et al. [39] and Mainen and Sejnowski [38], e.g. Kole et al. [32], Shu et al. [51]—is that while only one temperature is used, the channel density is rescaled! I removed that rescaling from my Hu-based model and made the true values explicit when tabulating parameters from previous models in the **Supporting information** (Section 6.4).

The mishandling of singularities breaks data recording within the model.

The matter of the mishandling of singularities in voltage-gated channel code in [23] is illustrated below in Figure 6.3 with orange boxes and arrows.

```
PROCEDURE rates(vm) {
        LOCAL  a, b

        a = trap0(vm,tha,Ra,qa)
        b = trap0(-vm,-tha,Rb,qa)
        mtau = 1/(a+b)
        minf = a*mtau

                :"h" inactivation

        a = trap0(vm,thi1,Rd,qi)
        b = trap0(-vm,-thi2,Rg,qi)
        htau = 1/(a+b)
        hinf = 1/(1+exp((vm-thinf)/qinf))
}


FUNCTION trap0(v,th,a,q) {
        if (fabs(v/th) > 1e-6) {
                trap0 = a * (v - th) / (1 - exp(-(v - th)/q))
        } else {
                trap0 = a * q
        }
}
```

Figure 6.3: **Error in the $Na_V1.6$ model code of Hu et al. [23].** The orange box surrounding the condition of the `if()\{\}` statement indicates the problem: The function `trap0()` fails to "trap" values of the membrane potential `v` that cause the expression inside the `if` statement to explode. At the time of writing this thesis, the bug shown above was present in **both the $Na_V1.2$ and $Na_V1.6$** channel models in Hu et al. [23] (file names "na12.mod" and "na16.mod" respectively, at ModelDB accession number 123897). The corrected code is shown below in Figure 6.4, also with an orange box.

Instead of `(v/th)`, the condition of the `if` statement in Figure 6.3 should contain `(v-th)/q`, i.e., the argument of the exponential indicated by an orange arrow. As a result, the model will evaluate an expression wherein the denominator can be arbitrarily small—a classic source of large numerical errors in computer programs. The correct code to handle this singularity is highlighted in green below in Figure 6.4, wherein the argument of the `if` statement contained in the `FUNCTION` that is named `trap0()` properly applies l'Hôpital's rule in the vicinity of the singularity.

The reader will notice that `trap0()` is commented out in the code from Mainen and Sejnowski [38] (Figure 6.4). That is because `trap0()` was eventually replaced with `efun(z)`, along with other updates to the code. These changes are explained in the comments of the Na_V channel model code "na.mod" from Mainen and Sejnowski [38], but the code of Hu et al. [23], among others, has yet to be fixed.

`trap0()` was corrected and then replaced with `efun()`, but not in Hu et al. [23], Kole et al. [32], Shu et al. [51] etc.

```
COMMENT
FUNCTION trap0(v,th,a,q) {
        if (fabs((v-th)/q) > 1e-6) {
                trap0 = a * (v - th) / (1 - exp(-(v - th)/q))
        } else {
                trap0 = a * q
        }
}
ENDCOMMENT

FUNCTION efun(z) {
        if (fabs(z) < 1e-6) {
                efun = 1 - z/2
        }else{
                efun = z/(exp(z) - 1)
        }
}
```

Figure 6.4: **Repaired Na_V channel model code in the file "na.mod" from the updated ModelDB entry for Mainen and Sejnowski [38]** (ModelDB accession number 2488). The repaired `FUNCTION trap0()` is commented out in this file, as it was later replaced with `efun()`.

In Figure 6.4, we see that as the membrane potential approaches "th" (a threshold voltage that is provided to `trap0()` when calculating the gating variables), l'Hôpital's rule is applied correctly:

$$\lim_{V \to \mathtt{th}} \mathtt{trap0} = \lim_{V \to \mathtt{th}} \left(\frac{a(V - \mathtt{th})}{1 - e^{-(V-\mathtt{th})/q}} \right) \to \left(\frac{0}{0} \right), \tag{6.1}$$

$$\implies \lim_{V \to \mathtt{th}} \mathtt{trap0} = \lim_{V \to \mathtt{th}} \left(\frac{a}{\frac{1}{q} e^{-(V-\mathtt{th})/q}} \right) = aq. \tag{6.2}$$

In light of the problems I encountered in the Hu et al. [23] model code—some of which are described above—I opted to use our existing *T-CLS* simulations to build a new Hu-based model. There are many other channel models and programs in [23]. Rather than attempt to eliminate possible errors in the rest of that code, it seemed reasonable to incorporate the repaired Na_V and K_V kinetics into our existing biophysical model. I rewrote those channels' kinetics based on the equations in Mainen et al. [39] and validated our implementation via the comparison in Figure 6.1. Parameters in our Hu-based model are compared across its ancestor models in Section 6.4.

Chapter 6 Synthesis

In this chapter, the single-compartment models of Chapters 4 and 5 are succeeded by spatially-extended pyramidal neuron models having thousands of compartments. We built upon the *CLS* model and two published pyramidal cell morphologies—a cat neuron from Hu et al. 2009 [23] and a rat neuron from Hay et al. 2011 [19]—with Hodgkin-Huxley style currents to simulate action potential initiation and backpropagation.

While multicompartmental models can hardly be described as parsimonious or computationally efficient, realistic dendritic morphology provides a rich environment for simulating backpropagation: The geometry of the dendritic tree shapes neuronal firing patterns through its interaction with nonlinear feedback from voltage-gated channels dynamics [38].

In pyramidal neurons—the majority of neurons in the cortex—the axon initial segment (AIS) contains two subtypes of voltage-gated sodium channels: $Na_V1.2$ and $Na_V1.6$, which are reported to differ in their voltage-sensitive gating properties. Past modelling studies suggested the heterogeneous pattern of $Na_V1.2$ and $Na_V1.6$ expression that is observed in early development—with $Na_V1.2$ concentrated at the proximal AIS, and $Na_V1.6$ concentrated at its distal end—evolved to "promote" or enhance backpropagation [23].

That explanation was (arguably) counterintuitive for the following reason: Electrophysiological measurements showed that $Na_V1.2$ gating kinetics are *right-shift*ed

(i.e., higher *activation* threshold) relative to $Na_V1.6$, so one might have expected that concentrating high-threshold channels proximal to the soma would inhibit backpropagation. However, the distribution of these Na_V subtypes in the AIS ought to influence backpropagation and excitability, given their shifted gating properties and the pivotal role of the AIS in triggering action potentials.

We simulated a variety of $Na_V1.2$ and $Na_V1.6$ density profiles in our pyramidal neuron models, which were based on the independent parameters, biophysics, channel distributions, and morphologies of [23, 19] (mentioned above). The published simulations—which suggested the separated Na_V distribution 'promotes' backpropagation—relied on *antidromic* stimulation (*axonal* current injection [23]). Critically, our simulations measured the threshold current-pulse amplitude (I_{BP}) required to elicit backpropagating action potentials with orthodromic *and* antidromic stimulation (somatic and axonal current injection, respectively).

Our models showed qualitative agreement with Hu et al. [23] when we emulated their axonal stimulation procedure (**Fig. 7**(B), **Fig. 4**). However, somatic current injection showed that proximal $Na_V1.2$ actually *inhibits* backpropagation with physiological, somatic stimulation (**Fig. 7**(A), **Fig. 2**). Part of the significance of this finding is that depolarizing antidromic stimulation (such as axonal current injection) is considered unphysiological. *In vivo*, pyramidal neurons receive *inhibitory* input at the AIS, but there is little biological evidence for excitatory input to the proximal axon. Pyramidal neurons do, however, have tens of thousands of excitatory (and inhibitory) synapses in their *somatodendritic* regions.[49]

In the latter case (orthodromic stimulation), we found that the separated Na_V distribution raised the backpropagation threshold, suggesting that the early (separated) $Na_V1.2$ and $Na_V1.6$ density profiles may actually serve to attenuate dendritic backpropagation and reduce neuronal excitability in the developing central nervous

system. Sensitivity analysis showed that the increased *somatic–I_{BP}* threshold with proximally-concentrated $Na_V1.2$ channels owes to their *right-shift*ed *activation* kinetics, whereas the reduced backpropagation threshold with *axonal* stimulation results from higher steady-state *activation and* a slower time-constant of *availability*—denoted h_∞ and τ_h, respectively—that follow from the *right-shift* of $Na_V1.2$.

The true role of the plastic distribution of these two Na_V subtypes must be significant, as any effect it has on backpropagation and action potential thresholds necessarily impacts the vast majority of excitatory neurons in the mammalian cortex.

6.5.2 Comparison to experimental data

At the time of writing, experimental evidence supports our Hu-based and Hay-based pyramidal neuron simulations with somatic stimulation, showing that the backpropagation threshold increased as the proportion of $Na_V1.2$ channels in the AIS rose. (See the $\kappa = 0.8$ curves in **Fig. 2** from Barlow et al. 2024 [4] (Section 6.3) and **Fig. 7**(A) from Barlow et al. 2024 [4] (Section 6.3).) In [4], we compared these results to Katz et al. [31], who observed higher spike thresholds in neurons from $Na_V1.6$-knockout mice compared to wild-type, using brief current pulses similar in amplitude and duration to those in our simulations. Since [31] exclusively stimulated their neurons at the soma—i.e., no threshold measurements were made using axonal current injection—further comparison with our axonal stimulation results was not possible. We discuss the comparison to Katz et al. [31] in Barlow et al. 2024 [4], which corresponds to Section 6.3 of this thesis.

The distributions of $Na_V1.2$ and $Na_V1.6$ are separated in the AIS early in development, but this segregation fades as pyramidal neurons mature [37]. In future experiments with improved Na_V imaging techniques, it may be possible to test more

detailed modelling predictions in Chapter 6 by performing electrophysiological measurements of the spike threshold—similar to Katz et al. [31]—in mouse neurons at P15 and P90, and record the Na_V distributions (perhaps after measuring the threshold).

Chapter 7

Additional results

7.1 Conversion of ohmic pyramidal cell model to GHK current

Our pyramidal cell simulations were originally designed with ohmic driving forces for the transmembrane ionic currents. This was done for compatibility with past models, including Mainen et al. [39], which was the basis for the model of Hu et al. [23], upon which our Hu-based model was built [4] (Section 6.3).

However, the GHK current equation (see Equation (3.58) on page #92 or Equation (7.1b) below) is more accurate across a wider range of V_{m}, and when the concentration gradient of a given voltage-gated ion 'X' depletes as a result of, e.g., sustained spiking or leaky damaged ion channels [8]. (Large changes in the intracellular or extracellular concentration of a given ion species will alter the measured conductance density of the membrane to said ions—see Section 3.5 in Background Ⅱ: Action potentials and ion channels.)

Equation (7.1a) lists the familiar ohmic approximation from the equivalent circuit model of Hodgkin and Huxley [21] (see Figure 3.6). The corresponding GHK description of voltage-gated currents with Hodgkin-Huxley style gating properties is given by Equation (7.1b) (Kotler et al. [33]):

$$I_{voltage\text{-}gated} = \begin{cases} I_{\text{ohmic}} = \bar{g}_X m^i h^j \, (V - E_X) & (7.1a) \\ I_{\text{GHK}} = \bar{P}_X m^i h^j z F \dfrac{zF}{RT} V \left(\dfrac{[X]_{\text{in}} - [X]_{\text{out}} e^{-\frac{zF}{RT}V}}{1 - e^{-\frac{zF}{RT}V}} \right). & (7.1b) \end{cases}$$

To switch the simulations over to GHK currents, the steady-state preparation of the model was calibrated to $V_{\text{rest}} = -70\text{mV}$ using the ohmic approximation. A barrier to converting the model to GHK was that, at multiple locations along the membrane, we used a variety of procedures programmed into our simulator to set and reset the densities of ion channels. Those procedures all use the Hodgkin-Huxley style $\overline{maximal\ conductance}$ parameters ($\bar{g}_{Na_V}$, $\bar{g}_{K_V}$, $\bar{g}_{\text{Cl}^-}$) to control the channel density in each compartment (i.e. segment, see Figure 3.2). This is not easy to replace because the variables x and κ are varied during simulation runs, which was implemented by scaling the $\bar{g}_X$'s at various points in the thousands of lines of simulation control code. In other words, the model is controlled by $\bar{g}_X$'s, whereas the GHK current equation has a different functional form, and currents are scaled by permeabilities ($\bar{P}_X$'s).

To calibrate the model to accept GHK current in place of the HH-style ohmic approximation without upsetting the steady state of the cell in the presence of the existing pump and leak currents, we apply the conditions:

$$I_{\text{X}}^{\text{GHK}}\Big|_{V=V_{\text{rest}}} = I_{\text{X}}^{\text{ohmic}}\Big|_{V=V_{\text{rest}}}, \tag{7.2}$$

and

$$I_{\mathrm{X}}^{\mathrm{GHK}}\Big|_{V=E_{\mathrm{X}}} = I_{\mathrm{X}}^{\mathrm{ohmic}}\Big|_{V=E_{\mathrm{X}}} \overset{\text{def}}{=} 0. \tag{7.3}$$

Equation (7.3) & Equation (7.1) give the Nernst potentials E_{X},

$$\bar{P}_X zF \frac{zF}{RT} E_{\mathrm{X}} \left(\frac{[X]_{\mathrm{in}}^{\mathrm{rest}} - [X]_{\mathrm{out}}^{\mathrm{rest}} e^{-\frac{zF}{RT}E_{\mathrm{X}}}}{1 - e^{-\frac{zF}{RT}E_{\mathrm{X}}}} \right) = 0 \Longrightarrow e^{-\frac{zF}{RT}E_{\mathrm{X}}} = \frac{[\mathrm{X}]_{\mathrm{in}}^{\mathrm{rest}}}{[\mathrm{X}]_{\mathrm{out}}^{\mathrm{rest}}}, \tag{7.4}$$

but Equation (7.4) does not solve for the permeabilities.

Similar to [46], the permeabilities were calibrated by ensuring that the Na^+, K^+, and Cl^- channel currents at V_{rest} were equal to those of our ohmic Hodgkin-Huxley style model. Plugging Equation (7.1) into Equation (7.2), we have

$$\bar{P}_X zF \frac{zF}{RT} V_{\mathrm{rest}} \left(\frac{[X]_{\mathrm{in}}^{\mathrm{rest}} - [X]_{\mathrm{out}}^{\mathrm{rest}} e^{-\frac{zF}{RT}V_{\mathrm{rest}}}}{1 - e^{-\frac{zF}{RT}V_{\mathrm{rest}}}} \right) = \bar{g}_X \left(V_{\mathrm{rest}} - E_X \right). \tag{7.5}$$

Dividing by V_{rest} and rearranging the above expression, we find

Equation (7.5) $\Longrightarrow$

$$\boxed{\bar{P}_X = \bar{g}_X \frac{1}{zF \frac{zF}{RT} [X]_{\mathrm{in}}^{\mathrm{rest}}} \underbrace{\left(\frac{1 - e^{-\frac{zF}{RT}V_{\mathrm{rest}}}}{1 - \frac{[X]_{\mathrm{out}}^{\mathrm{rest}}}{[X]_{\mathrm{in}}^{\mathrm{rest}}} e^{-\frac{zF}{RT}V_{\mathrm{rest}}}} \right)}_{\text{dimensionless}} \underbrace{\left(1 - \frac{E_X}{V_{\mathrm{rest}}} \right)}_{\text{dimensionless}}}. \tag{7.6}$$

That is, the expression for $\bar{P}_X$ in Equation (7.6) is substituted into $I_{\mathrm{GHK}}(V)$ in Equation (7.1). The permeabilities $\bar{P}_X$ needed for the conversion to GHK currents are thus obtained in terms of the $\bar{g}_X$'s and the Nernst potentials since they determine V_{rest}.

Equation (7.6) works for $X = Na^+$ and K^+, but because in our model $E_{Cl^-} = V_{\mathrm{rest}}$, it *does not work for* $X = Cl^-$. To get $\bar{P}_{Cl^-}$, one needs to take the limit as $V \longrightarrow V_{\mathrm{rest}}$ and then use l'Hôpital's rule. Here I will work out a solution to $\bar{P}_{Cl^-}(\bar{g}_{Cl^-}, V_{\mathrm{rest}})$: From

Equation (7.5) we have

$$\bar{P}_{\text{Cl}^-} zF \frac{zF}{RT} V_{\text{rest}} \left(\frac{[\text{Cl}^-]_{\text{in}}^{\text{rest}} - [\text{Cl}^-]_{\text{out}}^{\text{rest}} e^{-\frac{zF}{RT} V_{\text{rest}}}}{1 - e^{-\frac{zF}{RT} V_{\text{rest}}}} \right) = \bar{g}_{\text{Cl}^-} \underbrace{(V_{\text{rest}} - \{E_{\text{Cl}^-} = V_{\text{rest}}\})}_{=0}, \quad (7.7)$$

$$\implies \left(\frac{[\text{Cl}^-]_{\text{in}}^{\text{rest}} - [\text{Cl}^-]_{\text{out}}^{\text{rest}} e^{-\frac{zF}{RT} V_{\text{rest}}}}{1 - e^{-\frac{zF}{RT} V_{\text{rest}}}} \right) = 0. \quad (7.8)$$

This provides us with two equations:

$$\begin{cases} \bar{P}_{\text{Cl}^-} = \lim\limits_{V \to \underbrace{V_{\text{rest}}}_{=E_{\text{Cl}^-}}} \bar{g}_{\text{Cl}^-} \dfrac{1}{zF \frac{zF}{RT} [\text{Cl}^-]_{\text{in}}^{\text{rest}}} \left(\dfrac{1 - e^{-\frac{zF}{RT} V}}{1 - \frac{[\text{Cl}^-]_{\text{out}}^{\text{rest}}}{[\text{Cl}^-]_{\text{in}}^{\text{rest}}} e^{-\frac{zF}{RT} V}} \right) \left(1 - \dfrac{E_{\text{Cl}^-}}{V} \right), \text{ and} \\ e^{-\frac{zF}{RT} V_{\text{rest}}} = \dfrac{[\text{Cl}^-]_{\text{in}}^{\text{rest}}}{[\text{Cl}^-]_{\text{out}}^{\text{rest}}} \leftarrow \text{Nernst equation for Cl}^-\text{, in disguise.} \end{cases} \quad (7.9)$$

Now I will use l'Hôpital's rule in Equation (7.10) (below). From Equation (7.9), we have:

$$\bar{P}_{\text{Cl}^-} = \bar{g}_{\text{Cl}^-} \frac{1}{zF \frac{zF}{RT} [\text{Cl}^-]_{\text{in}}^{\text{rest}}} \left(1 - e^{-\frac{zF}{RT} V_{\text{rest}}} \right) \underbrace{\left\{ \begin{array}{l} \lim\limits_{V \to \underbrace{V_{\text{rest}}}_{=E_{\text{Cl}^-}}} \left(1 - \dfrac{E_{\text{Cl}^-}}{V} \right) = 0 \\ \hline \lim\limits_{V \to \underbrace{V_{\text{rest}}}_{=E_{\text{Cl}^-}}} \left(1 - \dfrac{[\text{Cl}^-]_{\text{out}}^{\text{rest}}}{[\text{Cl}^-]_{\text{in}}^{\text{rest}}} e^{-\frac{zF}{RT} V} \right) = 0 \end{array} \right\}}_{\{\} = \left\{ \lim\limits_{V \to \underbrace{V_{\text{rest}}}_{=E_{\text{Cl}^-}}} \left(\dfrac{\frac{d}{dV} \left(1 - \frac{E_{\text{Cl}^-}}{V} \right)}{\frac{d}{dV} \left(1 - \frac{[\text{Cl}^-]_{\text{out}}^{\text{rest}}}{[\text{Cl}^-]_{\text{in}}^{\text{rest}}} e^{-\frac{zF}{RT} V} \right)} \right) \right\}} . \quad (7.10)$$

Evaluating the derivatives in the numerator and denominator of the expression in $\left\{\text{curly braces}\right\}$ above, we take the new limit

$$\bar{P}_{\text{Cl}^-} = \bar{g}_{\text{Cl}^-} \frac{1}{zF\frac{zF}{RT}[\text{Cl}^-]_{\text{in}}^{\text{rest}}} \left(1 - e^{-\frac{zF}{RT}V_{\text{rest}}}\right) \left\{ \lim_{V \to \overbrace{V_{\text{rest}}}^{=E_{\text{Cl}^-}}} \left(\frac{\frac{E_{\text{Cl}^-}}{V^2}}{\frac{zF}{RT}\underbrace{\frac{[\text{Cl}^-]_{\text{out}}^{\text{rest}}}{[\text{Cl}^-]_{\text{in}}^{\text{rest}}} e^{-\frac{zF}{RT}V}}_{\to 1}} \right) \right\}, \tag{7.11}$$

Which gives the "maximal permeability" in the GHK model that satisfies the steady state in the ohmic Hu-based model:

$$\boxed{\bar{P}_{\text{Cl}^-} = \bar{g}_{\text{Cl}^-} \frac{1}{zF\left(\frac{zF}{RT}\right)^2 [\text{Cl}^-]_{\text{in}}^{\text{rest}} V_{\text{rest}}} \left(1 - e^{-\frac{zF}{RT}V_{\text{rest}}}\right)}. \tag{7.12}$$

When the maximal conductances ($\bar{g}_X$'s) are given in units of $\mathsf{mS\,/\,cm^2}$ and the ion concentrations are given in $\mathsf{mol\,/\,L}$, Equations (7.6) and (7.12) yield permeabilities with units of velocity (distance per unit time), as expected. To convert the full pyramidal cell model to GHK, all ionic currents from the original Hu-based model—Equations (15) and (16) in Barlow, Longtin, and Joós [4] (Section 6.3)—have their Omhic terms (Equation (7.1a)) replaced with a maximal permeability and a GHK driving force (Equation (7.1b)).

7.1.1 Handling singularities in GHK

```
1
2 FUNCTION GHK_Fdriving(a, cin, cout, voltage){
3   if (fabs(a*voltage) < 1e-6) {
4     GHK_Fdriving = (cin - cout*exp(-1.0*a*voltage))*(1.0/a + voltage/2.0 +
        a*voltage*voltage/12.0 - a*a*a*voltage*voltage*voltage*voltage/720.0)
5   }
6   else{
7     GHK_Fdriving = (cin - cout*exp(-1.0*a*voltage))*voltage/(1.0 -
        exp(-1.0*a*voltage))
8   }
9 }
```

Figure 7.1: **Singularities are avoided by switching to the power series for the denominator of Equation (7.1b) at small voltages.**

The above method of converting our original detailed pyramidal neuron model—which had used ohmic Hodgkin-Huxley style currents with the local channel densities being specified by maximal conductances—into a GHK-current model with channel densities set by effective permeabilities yields the currents shown in Figure 7.2.

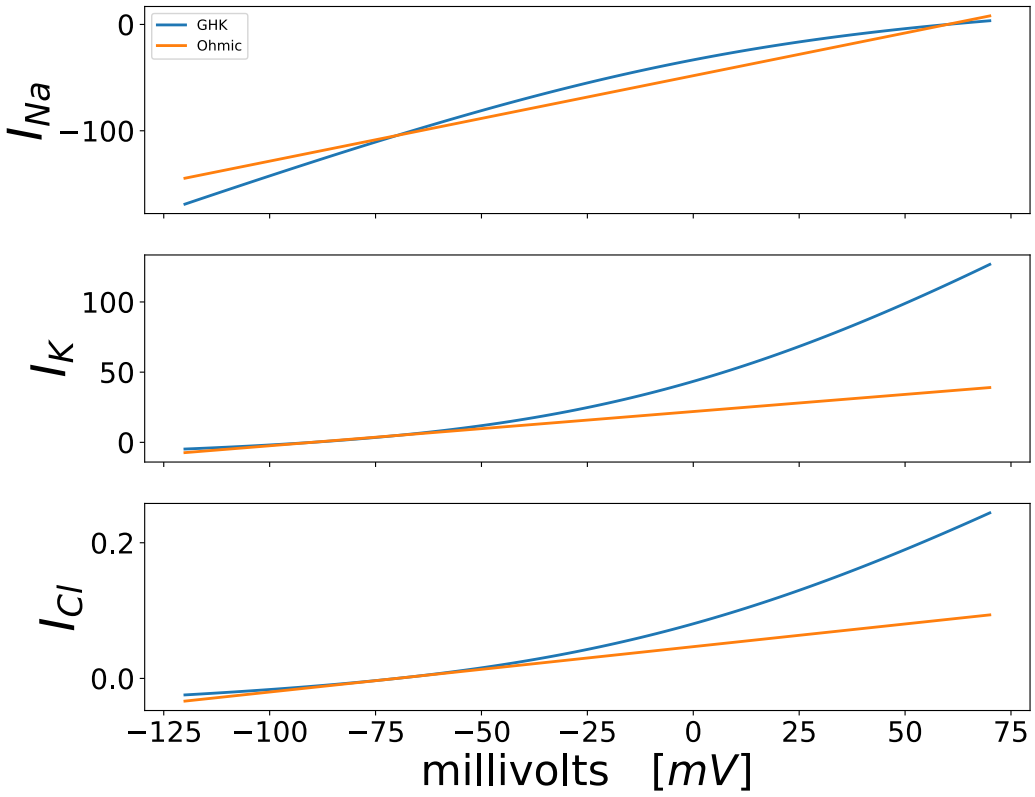

Figure 7.2: **Comparison of the GHK currents to the ohmic approximation.** The currents are plotted with arbitrary units, but with identical channel densities in both the GHK and ohmic forms. (See Figure 3.15 in Section 3.5.3.)

In Figure 7.3 we perform the same simulation procedure as in Barlow, Longtin, and Joós [4] (Section 6.3, **Fig. 2**), this time with GHK currents implemented for all ionic currents in the full pyramidal cell model. The qualitative effects of the AIS Na_V distribution seen in [4] are preserved under this change, which demonstrates that these results cannot be an artifact of the ohmic approximation. The conversion to GHK also increases Q_{BP} by $\approx$ 1pC, likely due to the increased magnitude of the hyperpolarizing potassium and chloride currents at depolarized voltages.

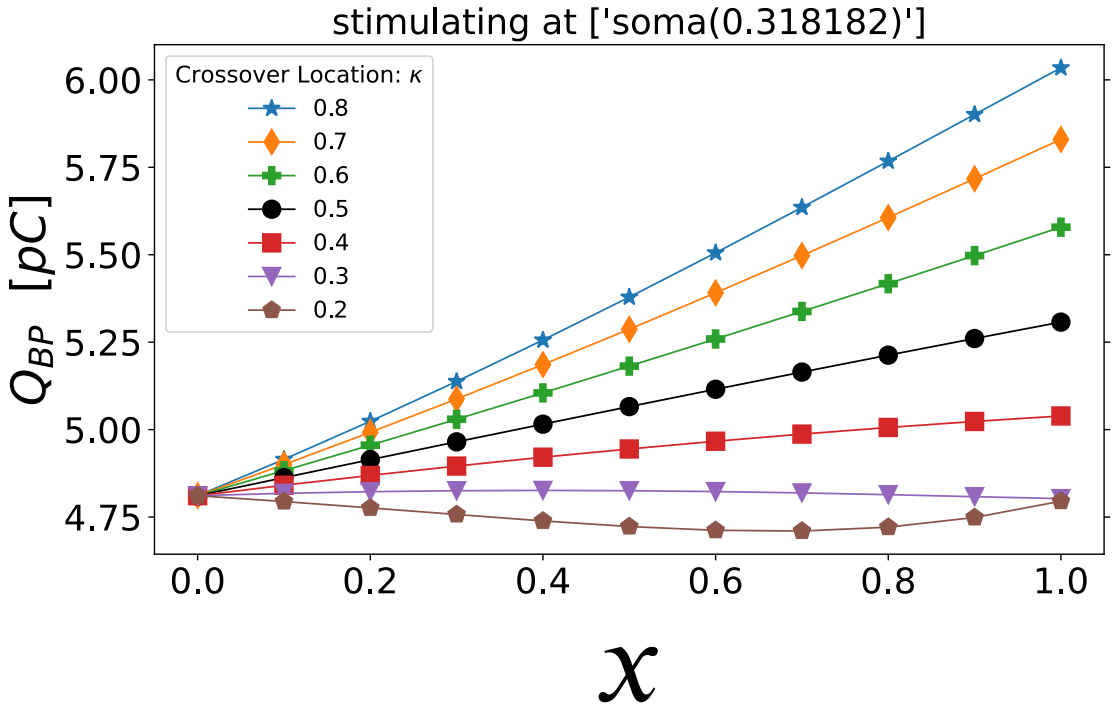

Figure 7.3: **Somatic stimulation – GHK currents.** When the GHK current equation is implemented (in place of the original Hodgkin-Huxley ohmic approximation), the effects of varying the AIS Na_V distribution on the backpropagation threshold persist. (Qualitative effects match Fig. 2 of Section 6.3, [4].) The lines have been drawn to guide the eye.

7.2 Coupled *left-shift* in the axon initial segment

Ischemic injury or mechanical damage to neurons can cause Na_V channels to become "leaky". At a given V_m, the damaged channels' *activation* and *availability* kinetics behave as though the cell were more depolarized than it actually is. That is, m and h are *left-shift*ed on the voltage axis by LS millivolts (Figure 4.1): When the membrane potential is V_m the channel behaves as though it were $V_m + LS$. For background on the CLS model, see *CLS*: Malfunctioning ion channels in a damaged membrane (Section 4.2.1) and Appendix B | Joós, Barlow, and Morris (2017) [28].

Given its proximity to the soma, the AIS may be especially vulnerable to mechanical injury when the axon is stretched, which could concentrate CLS in this region. And given the high density of Na_Vs on its membrane, any ischemia-induced CLS may have pronounced effects in the AIS. Here we use our detailed pyramidal neuron model to investigate the consequences of CLS damage to $Na_V1.2$ and $Na_V1.6$ channels in the AIS.

In this section, GHK currents replace the ohmic currents of the Hodgkin-Huxley model, as the former has advantages under the conditions imposed by CLS. The axons and dendrites of pyramidal neurons can be narrow, with diameters $\lesssim \mu m$, and their internal ion concentrations may be altered significantly by the sustained inward sodium currents that accompany CLS damage. Effective conductance densities in the ohmic approximation may thus become inaccurate, as they do not hold across large changes in ion concentration gradients [33]. As mentioned in the Background, the GHK current model is robust under changes to the concentration gradients and remains accurate over larger excursions of the membrane potential than the ohmic approximation—see Section 3.5.

Under axonal stimulation, even mild CLS ($\gtrsim 1 mV$) prevented backpropagation from occurring. This is consistent with our prior simulations of axonal stimulation in

Section 6.3 (Barlow, Longtin, and Joós [4], **Fig. 4**) as we now argue. In our sensitivity analysis of the Hu-based model (Barlow, Longtin, and Joós [4], **Fig. 6**), we showed that proximal Na_V *availability right-shift* is crucial for backpropagation to occur when the current is injected at the axon. *Left-shift*ing the AIS Na_Vs reduces proximal Na_V *availability*, which we showed to be the main determinant of the backpropagation threshold with axonal stimulation, and thereby stops backpropagation.

Under somatic stimulation, CLS modifies the relationship between the Na_V distribution and the backpropagation and forward propagation thresholds. Figure 7.4 shows in detail how CLS affects the backpropagation threshold. Top row: for smaller values of LS ($\lesssim 5\text{mV}$), the Q_{BP} is uniformly lowered by CLS damage. This is consistent with our finding in Fig. 6 of [4] (Section 6.3) that, under somatic stimulation, steady-state *activation* controls the backpropagation threshold.

As LS increases beyond 5mV, something interesting happens: The relationship between κ and Q_{BP} inverts. As the backpropagation threshold keeps falling, the constant-κ-curves having the lowest threshold appear to "reflect" off of some minimum Q_{BP} barrier. At $LS \sim 15\text{mV}$, the CLS damage has inverted the electrophysiological effect of x and κ. The vertical ordering of the constant-κ curves is the same as what was seen in **Fig. 3** of Barlow, Longtin, and Joós [4]. That is, when we model the hypothetical Na_V distributions, CLS damage in the AIS causes Q_{BP} to behave as though the AIS were put on backward. Since the *right-shift* of $Na_V1.2$ is roughly 13mV [23], this value of LS essentially converts the proximal $Na_V1.2$ into healthy $Na_V1.6$ channels, which explains why, in terms of the backpropagation threshold, the neuron behaves as if the AIS is backward.

A loss of neuronal polarity (including spines appearing in the axon and loss of Na_V clustering in the AIS (Huang and Rasband [24]) has been observed in injured neurons. With CLS, our model exhibits what might be called a loss of *electrophysiological* polarity

of the AIS, even though the distribution of Na_Vs retains its polarity (a nominal Na_V distribution with $Na_V1.2$ clustered in the proximal AIS and $Na_V1.6$ in the distal AIS).

Increasing LS still higher ($\gtrsim 11\text{mV}$), the threshold begins to rise for all constant-κ curves (Q_{BP} curves). See Figure 7.7. This may be explained by the loss of *availability* overwhelming the added *activation* of AIS Na_Vs. Additionally, the Q_{BP} curves become more tightly grouped (see the bottom right plot of Figure 7.4). That is, the spread of the $\kappa = 0.2$ and $\kappa = 0.8$ curves at $x = 1$, which we denote ΔQ, shrinks as LS grows, see Figure 7.9. This may be explained by the fact that as LS becomes large, the difference between the voltage-dependent kinetics of $Na_V1.2$ and $Na_V1.6$ over the operating voltage range of the cell becomes ever smaller.

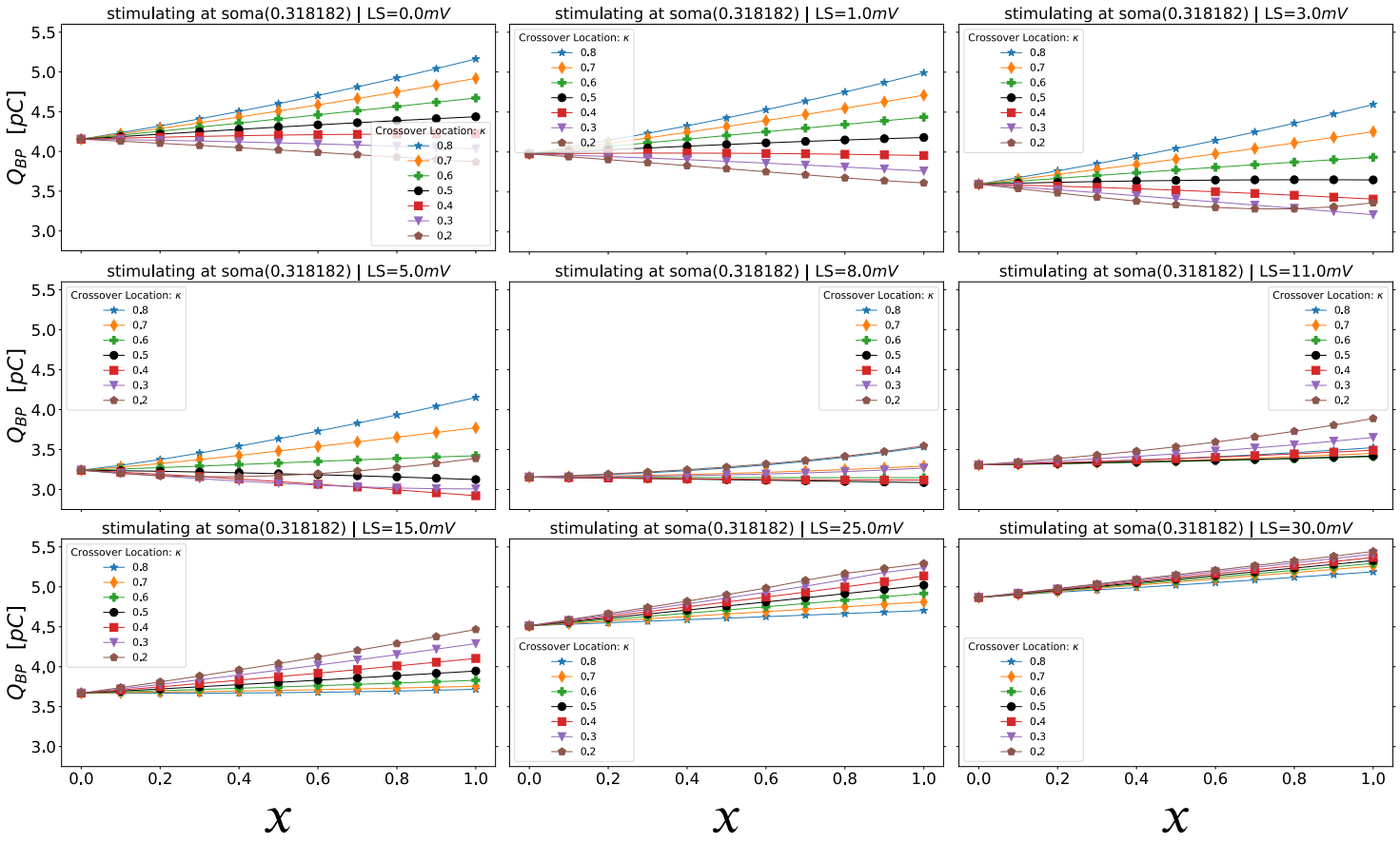

Figure 7.4: **Somatic Stimulation: Backpropagation threshold with coupled *left-shift* of $Na_V1.2$ and $Na_V1.6$ channels in the AIS.** The CLS damage inverts the relationship between the Na_V distribution and Q_{BP} as a function of x and κ. Here we show a series of plots analogous to Fig. 2 of [4] (Section 6.3), but with CLS affecting all Na_V channels in the AIS (AC =1). LS ranges from 1mV to 35mV as in Boucher et al. [8]. At first, LS lowers Q_{BP}. When LS exceeds 5mV, the constant-κ curves traverse the $x = 0.5$ line. The $\kappa = 0.8$ curve, which has the highest Q_{BP} when $LS = 0$mV, has the lowest threshold of all of the curves when $LS \gtrsim 15$mV. Likewise, the $\kappa = 0.2$ curve, which had the lowest threshold without CLS, has the highest threshold of all the constant-κ curves when $LS \gtrsim 15$mV, i.e. when the CLS exceeds the intrinsic *right-shift* of the proximal $Na_V1.2$ channels in the Hu-based model ($V_{\mathrm{RS}} = 13.0$mV), rendering their kinetics comparable to undamaged $Na_V1.6$ channels. This reversal of the Q_{BP} versus κ relationship is what is meant when we say that CLS damage inverts the electrophysiological polarity of the AIS, akin to Section 6.3, Fig. 3. The lines have been drawn to guide the eye.

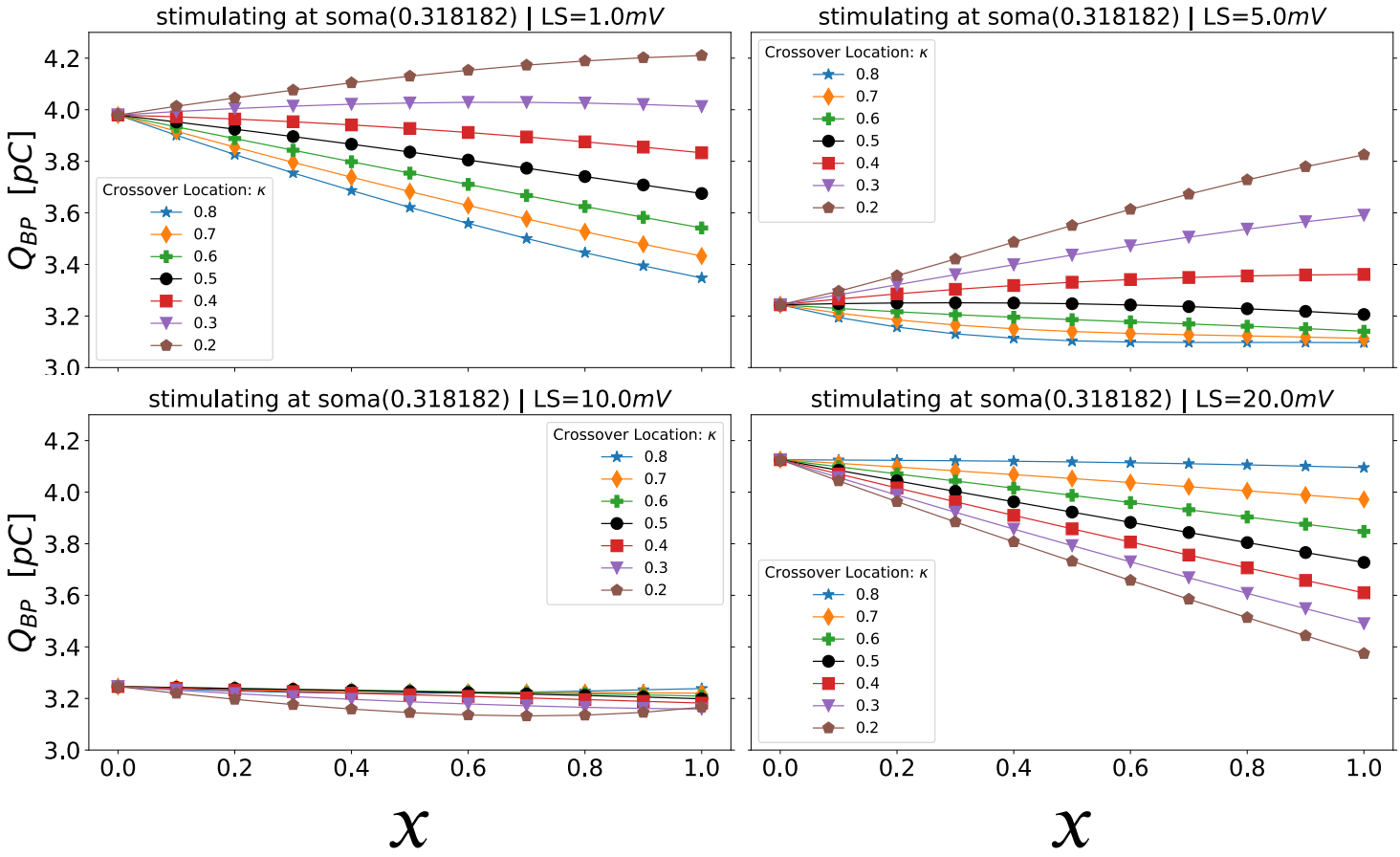

Figure 7.5: **Somatic Stimulation, Backward AIS: Backpropagation threshold with coupled *left-shift* of $Na_V1.2$ and $Na_V1.6$ channels in the AIS.** In this plot, we run the same simulations as in Figure 7.4, except with the Na_V distribution flipped longitudinally (see Section 6.3, Fig. 3). Again, as in Figure 7.4, CLS flips the vertical ordering of the constant-κ curves. This time, with regard to the effect of κ on Q_{BP}, CLS makes a backward AIS behave as though it were put on properly, at least with respect to the ordering of the constant κ-curves. In other words, the ordering is reminiscent of that with $Na_V1.2$ clustered proximally and $Na_V1.6$ clustered distally and without CLS damage. The lines have been drawn to guide the eye.

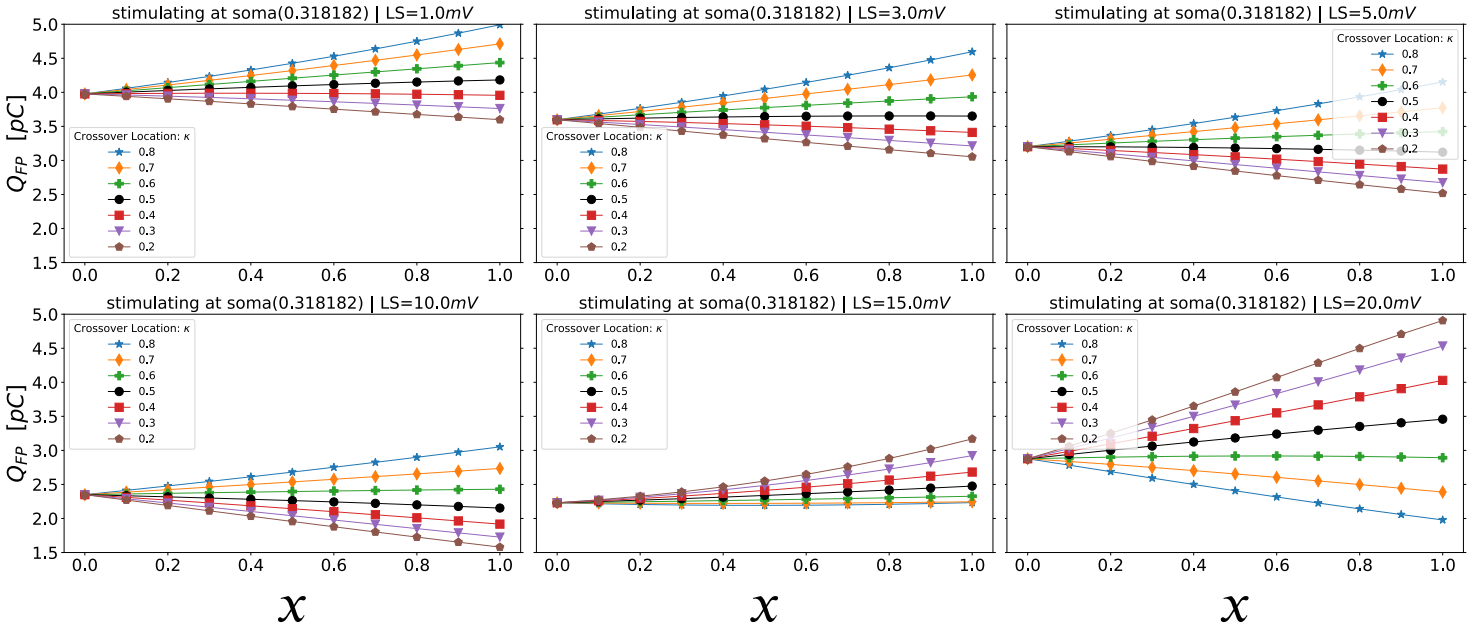

Figure 7.6: **Somatic Stimulation: Forwardpropagation threshold with coupled *left-shift* of $Na_V1.2$ and $Na_V1.6$ channels in the AIS.** The lines have been drawn to guide the eye.

The results of Figure 7.4 and Figure 7.6 are summarized in Figure 7.7. In the latter figure, we begin by discussing the $x = 0$ curves, which are marked by pink hexagons. Those curves show the effect of CLS when $Na_V1.2$ and $Na_V1.6$ are homogeneously distributed along the AIS, and hence, κ can have no effect in this case. We see that around $LS = 5\text{mV}$, Q_{FP} decouples from Q_{BP}. In contrast, without CLS damage, the two thresholds were identical—as in all of the multicompartmental models presented in this thesis thus far when they are stimulated somatically.

Initially CLS was decreasing both thresholds, but now, as the severity of the damage increases (higher LS), Q_{FP} continues to drop while Q_{BP} begins to rise. Eventually, Q_{FP} also reaches an inflection point where it begins to grow with increasing LS, until the Q_{BP} and Q_{FP} curves merge once again. This same pattern is observed in the other curves, in which $x = 1$, at all κ-values, though the inflection of the Q_{BP} and Q_{FP} thresholds occur at different LS values for those Na_V distributions.

Also notice that, among the $x = 1$ curves in Figure 7.7, there is an inversion of the ordering of the κ-values, with respect to both Q_{BP} and Q_{FP}: Without CLS damage ($LS = 0$), the highest value of κ gives the highest Q_{BP} and Q_{FP}. But once LS surpasses $\approx 13\text{mV}$ (i.e. LS exceeds the V_{RS} of $Na_V1.2$ relative to $Na_V1.6$), this ordering is inverted, i.e. with the highest value of κ giving the *lowest* Q_{BP} and Q_{FP} for all $x = 1$ curves. This inversion coincides with the point at which the CLS-damaged $Na_V1.2$ have kinetic curves approximating healthy $Na_V1.6$, and the $Na_V1.6$ curves are thoroughly *left-shift*ed, to the point that they are mostly inactivated at V_{rest}—see Fig. P in the *Supporting information* of Barlow, Longtin, and Joós [4] (Section 6.4), and Figure 4.1.

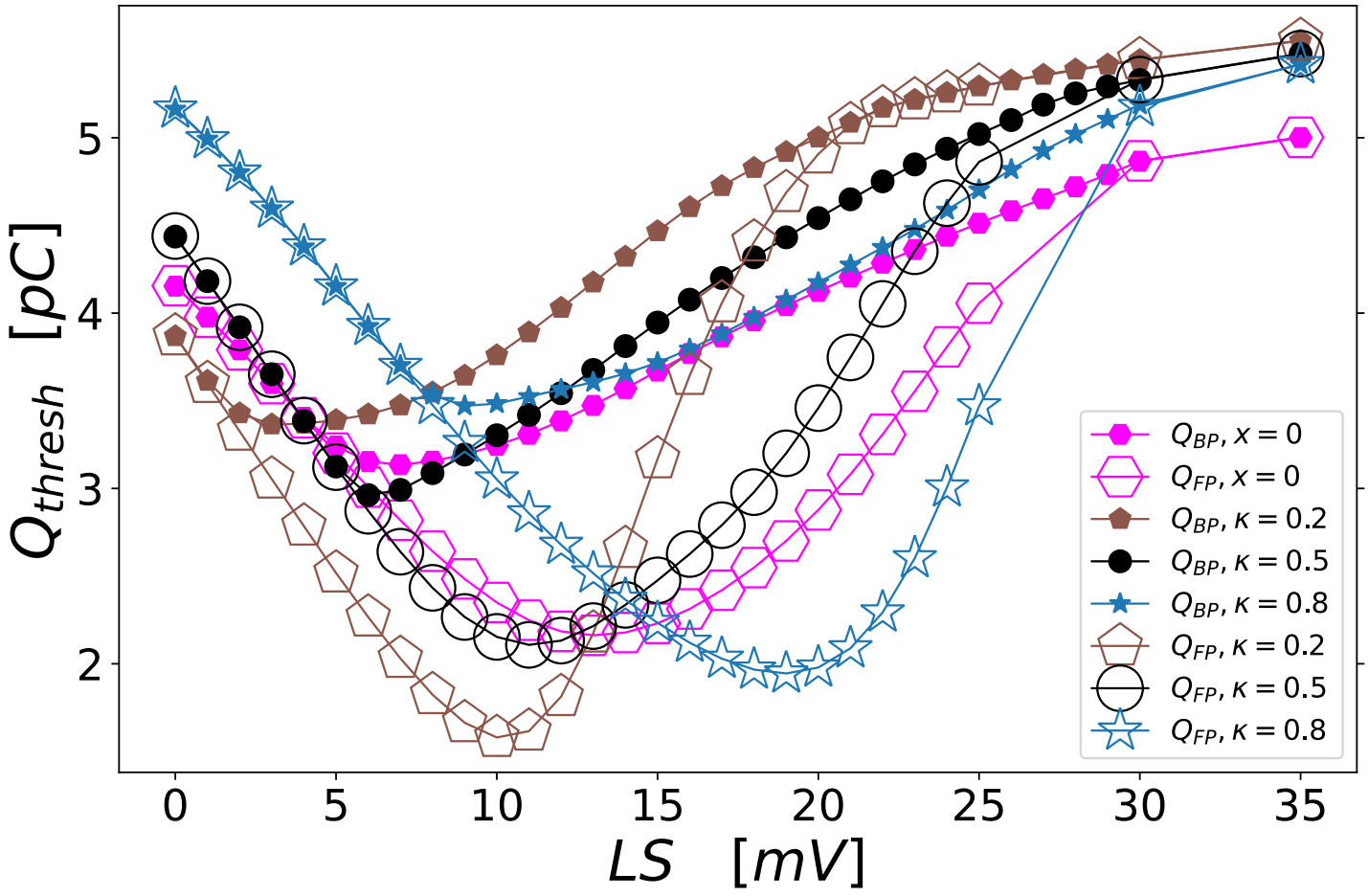

Figure 7.7: **Somatic Stimulation: CLS damage causes Q_{FP} to bifurcate away from Q_{BP}.** The crossover, κ, is undefined when $x = 0$ (the two magenta curves with hexagonal markers). In all other curves, $x = 1$. Without CLS damage, an action potential is always accompanied by backpropagation—at $LS = 0$, $Q_{BP} = Q_{FP}$. This matches our observations in the Hu-based model and the Hay-based model in Chapter 6. However, with CLS, action potentials become decoupled from backpropagation. CLS lowers the AP threshold (Q_{FP}) well below Q_{BP}, and in the region bounded by the Q_{BP} and Q_{FP} curves, the neuron loses the feedback (backpropagation) that it would normally receive following an AP. We expect this to have consequences for synaptic plasticity, which putatively relies on the information provided by the backpropagation that is normally coupled to AP generation. If the healthy neuron uses backpropagation to control excitability, for example, via STDP, then CLS could impair the neuron's ability to control ectopic spiking following trauma. The lines have been drawn to guide the eye.

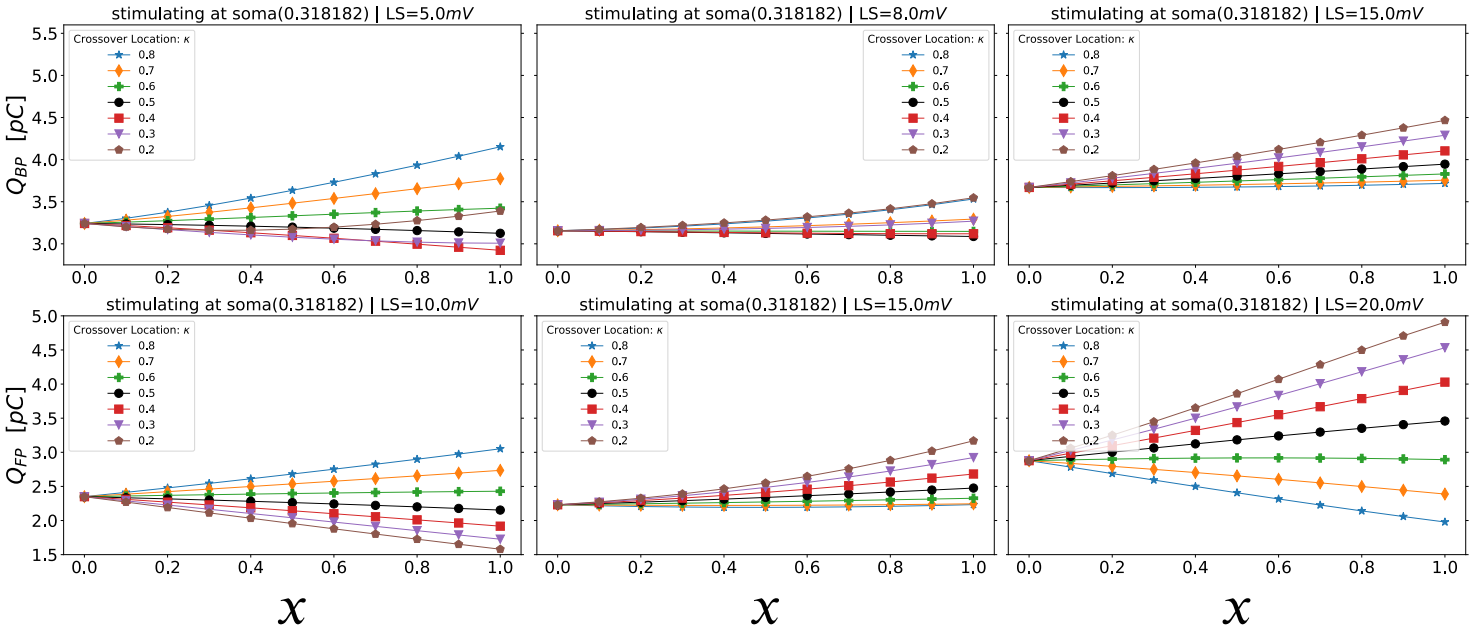

Figure 7.8: **Somatic Stimulation: Comparison of changes to the back-propagation threshold and forwardpropagation threshold due to coupled *left-shift* of $Na_V1.2$ and $Na_V1.6$ channels in the AIS.** With both Q_{BP} and Q_{FP}, CLS causes an inversion of the constant-κ curves, although the inversion occurs at a higher LS voltage for Q_{FP} than for Q_{BP}. The lines have been drawn to guide the eye.

We can track the inversion of the κ-ordering of Q_{BP} and Q_{FP} using the "spread" of the constant-κ threshold curves at $x = 1$. We calculate the spread as

$$\Delta Q(LS) = Q_{\text{thresh}}^{\kappa=0.8}(LS) - Q_{\text{thresh}}^{\kappa=0.2}(LS), \tag{7.13}$$

where Q_{thresh} is either Q_{BP} or Q_{FP}. ΔQ is defined so that it can take on negative values when the vertical ordering of the constant-κ curves is opposite to that seen with somatic stimulation and no CLS damage.

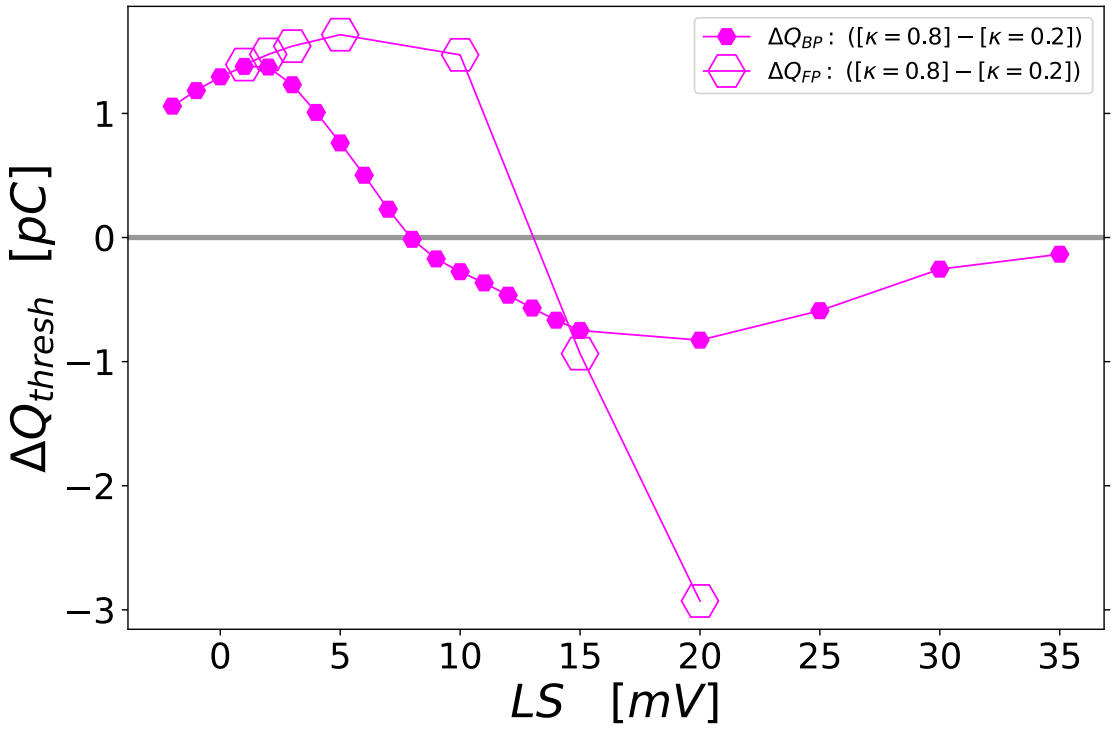

Figure 7.9: **Somatic Stimulation: Plotting the spread ΔQ of the constant-κ curves at $x = 1.0$ as a function of LS, for both Q_{BP} and Q_{FP}.** The inversion of the threshold-versus-κ relationship is visible on this plot as the point where each curve crosses the $\Delta Q = 0$ line. This occurs for the Q_{BP} and Q_{FP} curves, which remain inverted as CLS continues to rise beyond the inversion point. The lines have been drawn to guide the eye.

Chapter 7 Synthesis

We have implemented *CLS* in pyramidal neuron simulations using the morphology and empirical $Na_V1.2$ and $Na_V1.6$ channel models from Hu et al. [23], to which we added GHK current dynamics. It would be interesting to incorporate *CLS* damage into the dendritic morphology of detailed models with automatically tuned channel densities, such as that of [19] and its successors. Numerous compelling questions remain to be explored in future modelling studies applying coupled *left-shift* damage (*CLS*) to detailed pyramidal neuron models.

Thus far, we observe the x-versus-κ curves reversing their slopes with increasing *left-shift* (*LS*). This inversion occurs at values of *left-shift* that approximately cancel the 13mV intrinsic *right-shift* of the modelled $Na_V1.2$ channels (see Section 7.2 – *CLS in the AIS*).

Another persistent effect of *CLS* in the axon initial segment was the tendency of the damaged neuron to exhibit independent forward propagation and backpropagation thresholds with *orthodromic stimulation*. That is a new phenomenon, as previously, we had only observed separate thresholds with axonal (i.e. antidromic) stimulation. As the latter consequence of *CLS* damage occurs in the pyramidal neuron's quiescent-hypersensitive regime, it may interfere with spike-timing-dependent plasticity [16] and thereby impair homeostasis and learning.

Part IV

Conclusion and Future Research

Chapter 8

Conclusion

8.1 Coupled *left-shift* in point neurons

This thesis began with a detailed mapping of the regime diagram (Figure 4.4) in the single-compartment *CLS*-damage model (Chapter 4) at fixed temperature. To account for temperature changes and their effects on spontaneous, ectopic activity, we added four Q_{10} parameters (Q_{gate}, Q_{Na^+}, Q_{K^+}, Q_{pump}) to the *CLS* model code—making it a "*T-CLS*" simulator with *T* denoting *temperature*. Temperature behaved like a bifurcation parameter, similar to *LS*.

Miniature copy of Figure 4.4:

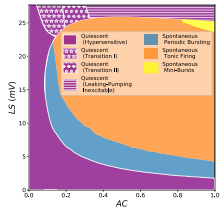

Full-size figure on page# 107.

Since I was able to generate maps of the ectopic boundaries of the *CLS* model, I used the simulation tools that I had built to create a series of regime diagrams at different temperatures and observe the movement of the quiescent-to-bursting and bursting-to-tonic firing boundaries in the *LS*–*AC* plane (Chapter 5). We found that the thresholds for ectopic bursting and spontaneous tonic firing were lowered by increased body temperature and raised by medically attainable cooling.

The predicted threshold-raising effect of cooling should protect neurons following *CLS*-type damage, which is caused by ischemia and other forms of trauma. I isolated

Raising the CLS-threshold protects injured neurons from excitotoxic spiking.

and compared several contributions of temperature to excitability through its effect on the electrogenic pump current and on HH-style ion currents via the transition rates of voltage-gated ion channels and their maximal conductances. These effects were primarily driven by Q_{Na^+}, with Q_{pump} having significant effects on excitability as well—see FIG. 4(a) and FIG. 5 in Barlow, Joós, Trinh, and Longtin [2] (Chapter 5). Although the electrogenic pump produces a hyperpolarizing current, its tendency to induce a supercritical Hopf bifurcation was analyzed in detail by Yu, Morris, Joós, and Longtin [58].

8.2 Backpropagation and the pattern of sodium channels in the AIS

Following the two successful point-cell (single-compartment) studies described above, I ventured into the perilous domain of multicompartmental neuron modelling (Chapters 6 and 7). The allure of simulating spatially extended, morphologically realistic neurons was irresistible.

The scientific motivation for this pivot was clear: The pattern of sodium channels in the axon initial segment (where action potentials begin) affects feedback sent to dendrites (called backpropagation). However the connection between backpropagation, the gating properties of the different sodium channels, and their pattern of expression in the AIS was not understood (and continues to be studied). To simulate said pattern I needed a model with many compartments, since by definition a parameter (e.g. the density of $Na_V1.2$ channels) has a single value at each compartment.

The number of compartments determines the spatial resolution of the neuron, and I needed more than one point in space to capture the pattern of sodium channels in the AIS.

Further, backpropagation happens in dendrites. Rather than introduce "simplifying" assumptions about dendritic structure—cell morphology is known to affect spiking patterns [38]—digitally reconstructed somatodendritic morphology, connected to the

Backpropagation occurs in dendrites, so I attached the AIS to digitally reconstructed dendrites from pyramidal neurons.

model AIS, provided a place to simulate backpropagation and define measurement criteria for it.

At this point it is appropriate to quote Almog and Korngreen [1], who provide a taste of what awaits those who leap into this field:

> *"Today, most compartmental models are constructed for complex cellular morphologies. They contain large numbers of voltage-gated channels, and their ion channels are not distributed along the neuronal membrane homogeneously. As a result, they contain many parameters of unknown value. And due to the limitations of modern recording techniques, we do not have experimental access to thin dendritic and axonal branches, so we are ignorant of the properties and distributions of many ion channels in the systems we are modelling. Therefore, much of the time spent making a compartmental model is dedicated to guessing parameter values, testing the model, guessing again, testing again, a cycle of hand-tuning that can loop for a depressingly long time. It should be emphasized that most of the reductions and assumptions that are commonly being made in constructing a compartmental model are due to a lack of available experimental measurements of specific parameters, rather than ignorance of such data on the modellers' part."*
>
> *"Anyone who has hand-tuned a compartmental model knows that after many tuning cycles one loses the mental capacity to improve the model: every change made, it comes to seem, is bad. This outcome, almost inevitable, is a direct consequence of the rapid parameter inflation. Malaise accompanies many scientific and engineering problems whose character is defined by their large numbers of parameters. It is a malaise which emerges from an evil curse, the curse of dimensionality."*—[1]

Despite an array of setbacks—well beyond the curse described above—some of which are detailed in Tripwires: An adventure in model reproducibility (Section 6.5), I was able to both recover and then challenge the conclusions of Hu et al. [23], using their code as a framework to build a detailed pyramidal neuron model starting from my point-cell simulations. The Hu-based model began as an expansion of the (single-compartment) *T-CLS* model code into multiple coupled compartments in a tapered linear, representing a soma and axon, and evolved into a pyramidal neuron morphology with thousands of compartments.

I replaced the Na_V and K_V kinetics embedded in the now multicompartmental *T-CLS* model—which originated from electrophysiological recordings of squid axons in Hodgkin and Huxley [21]—with the *mammalian* $Na_V1.2$, $Na_V1.6$, and K_V channel kinetics detailed in Hu et al. [23][1]. Having shifted to mammalian cell morphology, it was only logical to adopt mammalian ion channel kinetics. Otherwise, our model would have been an incongruous hybrid: a mammalian cell structure equipped with cephalopod channels. Recovering the channel kinetics of [23] became an adventure in itself, revealing persistent bugs in related model codes, see Tripwires: An adventure in model reproducibility (Section 6.5).

As stated in the text quoted above from Almog and Korngreen [1], the path from a point-cell simulator to a detailed pyramidal neuron model is not a matter of copying and connecting point cells. I rebuilt the Hu-based model multiple times with various parameter settings and backpropagation criteria to show that my findings held. During that time, most of the world was in lockdown due to a certain airborne virus. I thought I should keep pushing through. All the while, my simulations persistently showed that the distribution of sodium channels had more complicated effects on

[1] Hu et al. [23] tuned the kinetics from model code in Mainen and Sejnowski [38] to fit their recordings of Na^+ currents in the AIS.

backpropagation than previously described (and widely cited), and the Hu-based model was my only means of demonstrating that until...

With the aim of escaping the curse of dimensionality ([1]), or at least reducing its burden, I reinforced my findings (summarized below) from the Hu-based models with additional simulations built on the automatically tuned model of Hay et al. [19]. The latter simulations strengthened my findings considerably since the parameter tuning in Hay et al. [19] was achieved through an automated fitting to experimental spiking patterns, and its morphology and biophysics are independent of Hu et al. [23].

Multicompartmental models do not tend to agree with one another, or rather, minor changes can easily cause them to disagree [1]. It was compelling to see the central result (the separated Na_V distribution lowers the backpropagation threshold with axonal stimulation, but raises it with somatic stimulation [4]) confirmed in the Hay-based model, given its independent parameters, morphology, and biophysics [19].

Through the Hu-based and Hay-based models, we explained two phenomena in biophysical and dynamical detail:

1. the modulation of backpropagation by the heterogeneous spatial distribution of Na_V subtypes in the AIS, and
2. the coupling of these observations to the mode of stimulation (axonal vs somatic current injection).

The key models and experiments upon which I built my simulations defined backpropagation in terms of electrical signals in the soma (although Hay et al. [19] simulated calcium spikes in the distal dendrites). However, multicompartmental models provide omniscient access to the membrane potential at every point in the simulated neuron (one of their main advantages), and most of the interesting activity

relevant to synaptic plasticity happens in the dendrites. It seemed unreasonable to ignore the dendrites by restricting the definition of backpropagation to the voltage recorded at the soma, and I used dendritic backpropagation criteria in the Hu-based and Hay-based models.

8.3 Revealing the role of Na_V density profiles via gating-property sensitivity analysis

I also performed a sensitivity analysis by changing the *right-shift* of $Na_V1.2$ in the AIS to isolate the effects of *right-shift*ed sodium channel gating kinetics on the backpropagation threshold. In that analysis, when the *right-shift* of $Na_V1.2$ is altered, the nonlinear sodium currents are affected inhomogeneously *at every point along the AIS*. That is, *right-shift* is heterogeneously distributed in space as it interacts with the action potential initiation and backpropagation phenomena arising in the model neuron. In compartments lying outside the AIS, the *right-shift* was not modified.

Sensitivity analysis was performed by modulating the right-shift of $Na_V1.2$ channels in the AIS.

The *right-shift* of $Na_V1.2$ manifested through the voltage-dependence of those channels' *activation* and *availability* steady-states, and through their voltage-dependent time constants. By modifying the *right-shift* of one steady-state, or one time constant, in isolation, my simulations revealed that the coupling of the Na_V distributions' effects (on backpropagation) to the mode of stimulation resulted from the dominance of different Na_V gating properties when stimulation was axonal versus somatic. *Availability* properties dominated in the former, and *activation* in the latter.

Right-shift sensitivity analysis via selected $Na_V1.2$ gating properties.

8.4 Backpropagation and *CLS* damage in the AIS of a pyramidal neuron

I also modelled *CLS* damage in the AIS of the multicompartmental Hu-based model, whereas our previous studies of excitotoxic firing patterns were single-compartment

models. Since *CLS* damage can produce lasting inward Na^+ currents, these simulations used GHK-style currents. Pyramidal neurons have axonal, AIS, and dendritic processes with diameters $\lesssim$ µm, and the persistent *CLS* currents can change the local ion concentrations such that the apparent conductance densities assumed in the ohmic approximation may break down [33]. The GHK current model is robust under concentration changes and is therefore better suited to the study of *CLS* in the AIS.

The effects of *CLS* damage in the pyramidal neuron model's AIS suggest that the *left-shift*ed $Na_V1.2$ channels assume the role of healthy $Na_V1.6$ channels at values of *LS* sufficient to erase the intrinsic *right-shift* of $Na_V1.2$. I also observed an interesting decoupling of the backpropagation threshold from AP initiation (forward propagation threshold) with somatic stimulation as a result of *CLS* in the AIS. Separate thresholds for generating a strictly forward-propagating AP versus an AP accompanied by backpropagation are a feature of *axonal* stimulation, but with somatic stimulation, the two thresholds are identical under physiological (i.e. healthy) conditions.

CLS in the AIS leads to independent backpropagation and forward propagation thresholds, which are normally identical under somatic current injection in the absence of CLS damage.

This tendency of *CLS* damage to allow somatically stimulated APs to occur at currents well below the backpropagation threshold constitutes a form of hypersensitivity: The neuron is sending signals downstream without the normal regulatory feedback which backpropagation provides. Under normal conditions, that feedback helps the cell decide whether it is firing excessively or inappropriately in response to the somatodendritic input it receives.

These comments assume the putative role of backpropagation in modulating excitability via spike-timing-dependent plasticity or other forms of Hebbian learning. A related example of hypersensitivity in the form of excessive APs combined with somatodendritic hypoexcitability has been reported by Spratt et al. [52].

8.5 In defense of computer models[2]

Computer models test our theoretical understanding of natural phenomena by converting our conceptual models into explicit predictions [9].

When encountering skepticism about the utility of detailed biophysical models, as modellers are prone to do now and then, the following question must be asked: Utility compared to what? Without computational modelling, we are restricted to experimental measurements, theoretical mental models, and what can be calculated with a pencil and paper. If the physical (or biophysical) system being studied, the available experimental data about it, and the theoretical framework describing it are sufficiently complex that the behaviour of the system cannot be reliably deduced through imagination, intuition, or dead reckoning, then what better alternative is there than creating a computer model?

Experiments—or the conclusions we draw from them—often contain more assumptions than simulations. Computers crash when we miss crucial details; nature does not.

Computers can only execute the code we write, and it therefore is not possible to program a simulation without expressing its underlying assumptions in some explicit form. It is, however, possible to conduct an experiment without stating assumptions. It is a challenge, requiring imagination on the part of the experimenter, to attempt to bring into awareness all of the *latent assumptions* (e.g. when performing in vitro or in vivo electrophysiological recordings) about how the experimental conditions, including the measurement equipment, might affect their observations. One can argue that experiments contain more assumptions than models. Physical reality cannot fill in any omissions on the modeller's behalf.[3]

[2] In 2024 it feels like an odd time to be defensive on this topic, but I drafted this section before it was announced that the Nobel Prizes in Physics and Chemistry both went to modellers this year. (www.nobelprize.org/all-nobel-prizes-2024/)

[3] This is not meant to disparage experimental work. Science can exist without computer models, but there can be no science without experiments. Experimentalists diligently state their assumptions and describe their methods as clearly and comprehensively as possible. And, clearly, computer models would be powerless without experimental data to test them.

Computer simulations are powerful tools for converting our present knowledge, or conceptual models, into hypothetical data that can be objectively compared to nature. They have their limitations, but we can take heart in remembering how limited we would be without them.

Chapter 9

Future research

If the apparent tendency—reported by Hu et al. [23]—of the separated Na_V distribution to "promote" backpropagation was an artifact of antidromic stimulation[1], then we need a new hypothesis: Why might neurons express the separated Na_V pattern early in development, only to replace the proximal $Na_V1.2$ channels with $Na_V1.6$ later on?

> Specifically, how might the Na_V distribution interact with synaptic pruning and myelination in the developing central nervous system?

Perhaps the developmental remodelling of the AIS sodium channel distribution coincides with other developmental phenomena that explain its true function.

My multicompartmental simulations predict that the Na_V distribution observed in early development—with $Na_V1.2$ concentrated in the proximal AIS and $Na_V1.6$ pushed into the distal AIS[37]—actually raises the backpropagation threshold with orthodromic stimulation. Further, antidromic synapses observed at the AIS of pyramidal neurons tend to be inhibitory [49]. Lacking excitatory input to the AIS, the separated Na_V distribution would render young pyramidal neurons *less* excitable *in general*, all else being equal.[2]

[2] That is, prior to the invasion of the proximal AIS by $Na_V1.6$.

The mammalian neuron data cited in this thesis came from rats, mice, cats, and human patients who chose to donate cortical tissue that needed to be removed during brain surgery.

But all else is *not* equal. A characteristic of the young mammalian brain is the excessive connectivity of the cortex due to an abundance of (so-called) exuberant synapses. Peak synaptic density is reported to occur around postnatal day 30 ($P30$) in rat prefrontal cortex, after which the density decreases until $\approx P90$ [29]. The developmental plasticity of the AIS Na_V distribution reported by Liu et al. [37], ranging from $P15$ to $P90$, shows significant overlap with synaptic pruning, and myelination occurs during this period as well—see Fig. 6A of Liu et al. [37].

The Na_V distributions and other properties of the AIS are also known to change in response to modified presynaptic activity [34]. Hence we may hypothesize that the initially separated Na_V distribution flattens out *in concert* with synaptic pruning to lower the backpropagation threshold. That is, since $\sim 70\%$ of the synaptic input to pyramidal neurons is excitatory (Shapson-Coe et al. [49, table S7]) and our modelling predicts that concentrating $Na_V1.2$ at the proximal AIS raises the backpropagation threshold with orthodromic stimulation, we ask whether the separated Na_V distribution exists to compensate for exuberant synapses in the young brain by *inhibiting backpropagation*.

The above hypothesis, which rests on modelling with orthodromic stimulation—i.e. somatic or dendritic current injection—may have previously been obscured by the assertion from Hu et al. [23] that concentrating $Na_V1.2$ in the proximal AIS promotes backpropagation (which continues to be cited, e.g. [31, 52, 37]).

9.1 Future modelling studies

Many interesting possibilities for single-cell modelling studies arise by combining realistic synaptic input with plasticity in the AIS sodium channel distribution. The Hay-based model in Chapter 6 could be used to explore the regulation of high-amplitude backpropagation-activated calcium spikes in the distal dendrites of pyramidal neurons by the axon initial segment. Complex physiological stimulation—with many synapses spread out across the dendrites, or combined dendritic and somatic current injection—could be modelled as it interacts with the pattern of sodium channels in the AIS.

Freely available connectomic data, such as the whole fruit fly brain connectome recently completed by FlyWire[3] (Dorkenwald et al. [12]) and the reconstructed cubic millimetre of human cortex available through the H01 Release[4] (Shapson-Coe et al. [48]), could provide valuable constraints and guide the development of physiologically relevant stimulation protocols. The human connectomic data mentioned above has also revealed powerful outlier connections, where a single axon forms up to 50 synapses with one neuron.

One could similarly add inhibitory inputs at the AIS. In cortical neurons, the AIS is often densely innervated by inhibitory interneurons [48]. Concentrating inhibitory input at the trigger zone is an efficient way to stop the neuron from firing an action potential, and cortical interneurons can modulate pyramidal neurons' excitability by "vetoing" action potentials.

There is also the field of neuronal networks, which is likely to change dramatically with the growing availability of detailed connectomic data. Thus far, modellers have used the reconstructed fruit fly brain as a template for leaky integrate-and-fire

[3] https://flywire.ai
[4] https://h01-release.storage.googleapis.com/landing.html

networks [50]. It may be possible to simulate these networks with more realistic neurons, ideally preserving cell morphologies contained in the dataset, which could resurrect subtleties in each neuron's firing patterns.

Bibliography

[1] Mara Almog and Alon Korngreen. Is realistic neuronal modeling realistic? *Journal of Neurophysiology*, 116(5):2180–2209, November 2016. ISSN 0022-3077, 1522-1598. doi: 10.1152/jn.00360.2016. URL https://www.physiology.org/doi/10.1152/jn.00360.2016.

[2] B. M. Barlow, B. Joós, A. K. Trinh, and A. Longtin. Cooling reverses pathological bifurcations to spontaneous firing caused by mild traumatic injury. *Chaos: An Interdisciplinary Journal of Nonlinear Science*, 28(10):106328, October 2018. ISSN 1054-1500. doi: 10.1063/1.5040288. URL https://doi.org/10.1063/1.5040288.

[3] Ben M. Barlow, Martine Bertrand, and Béla Joós. Relaxation of a simulated lipid bilayer vesicle compressed by an atomic force microscope. *Physical Review E*, 94(5):052408, November 2016. doi: 10.1103/PhysRevE.94.052408. URL https://link.aps.org/doi/10.1103/PhysRevE.94.052408. Publisher: American Physical Society.

[4] Benjamin S. M. Barlow, André Longtin, and Béla Joós. Impact on backpropagation of the spatial heterogeneity of sodium channel kinetics in the axon initial segment. *PLOS Computational Biology*, 20(3):e1011846, March 2024. ISSN 1553-7358. doi: 10.1371/journal.pcbi.1011846. URL https://journals.plos.org/ploscompbiol/article?id=10.1371/journal.pcbi.1011846. Publisher: Public Library of Science.

[5] H. B. Barlow. Why have multiple cortical areas? *Vision Research*, 26 (1):81–90, January 1986. ISSN 0042-6989. doi: 10.1016/0042-6989(86)90072-6. URL https://www.sciencedirect.com/science/article/pii/0042698986900726.

[6] David Beniaguev, Idan Segev, and Michael London. Single cortical neurons as deep artificial neural networks. *Neuron*, 109(17):2727–2739.e3, September 2021. ISSN 0896-6273. doi: 10.1016/j.neuron.2021.07.002. URL https://www.cell.com/neuron/abstract/S0896-6273(21)00501-8.

[7] Nick Bostrom. *Superintelligence: paths, dangers, strategies*. Oxford University Press, Oxford, reprinted with corrections edition, 2017. ISBN 978-0-19-873983-8.

[8] Pierre-Alexandre Boucher, Béla Joós, and Catherine E. Morris. Coupled left-shift of Nav channels: modeling the Na+-loading and dysfunctional excitability of damaged axons. *Journal of Computational Neuroscience*, 33(2):301–319, October 2012. ISSN 1573-6873. doi: 10.1007/s10827-012-0387-7. URL https://doi.org/10.1007/s10827-012-0387-7.

[9] Nicholas T. Carnevale and Michael L. Hines. *The NEURON book*. Cambridge University Press, Cambridge, UK ; New York, 2006. ISBN 978-0-521-84321-8.

[10] J. D. Congdon, R. D. Nagle, O. M. Kinney, and R. C. van Loben Sels. Hypotheses of aging in a long-lived vertebrate, Blanding's turtle (*Emydoidea blandingii*). *Experimental Gerontology*, 36(4):813–827, April 2001. ISSN 0531-5565. doi: 10.1016/S0531-5565(00)00242-4. URL https://www.sciencedirect.com/science/article/pii/S0531556500002424.

[11] Peter Dayan and L. F. Abbott. *Theoretical neuroscience: computational and mathematical modeling of neural systems*. Computational neuroscience. Massachusetts Institute of Technology Press, Cambridge, Mass, 2001. ISBN 978-0-262-04199-7.

[12] Sven Dorkenwald, Arie Matsliah, Amy R. Sterling, Philipp Schlegel, Szi-chieh Yu, Claire E. McKellar, Albert Lin, Marta Costa, Katharina Eichler, Yijie Yin, Will Silversmith, Casey Schneider-Mizell, Chris S. Jordan, Derrick Brittain, Akhilesh Halageri, Kai Kuehner, Oluwaseun Ogedengbe, Ryan Morey, Jay Gager, Krzysztof Kruk, Eric Perlman, Runzhe Yang, David Deutsch, Doug Bland, Marissa Sorek, Ran Lu, Thomas Macrina, Kisuk Lee, J. Alexander Bae, Shang Mu, Barak Nehoran, Eric Mitchell, Sergiy Popovych, Jingpeng Wu, Zhen Jia, Manuel A. Castro, Nico Kemnitz, Dodam Ih, Alexander Shakeel Bates, Nils Eckstein, Jan Funke, Forrest Collman, Davi D. Bock, Gregory S. X. E. Jefferis, H. Sebastian Seung, and Mala Murthy. Neuronal wiring diagram of an adult brain. *Nature*, 634(8032):124–138, October 2024. ISSN 1476-4687. doi: 10.1038/s41586-024-07558-y. URL https://www.nature.com/articles/s41586-024-07558-y. Publisher: Nature Publishing Group.

[13] Aline R Dörrbaum, Lisa Kochen, Julian D Langer, and Erin M Schuman. Local and global influences on protein turnover in neurons and glia. *eLife*, 7:e34202, June 2018. ISSN 2050-084X. doi: 10.7554/eLife.34202. URL https://doi.org/10.7554/eLife.34202. Publisher: eLife Sciences Publications, Ltd.

[14] G. Bard Ermentrout and David H. Terman. The Hodgkin–Huxley Equations. In G. Bard Ermentrout and David H. Terman, editors, *Mathematical Foundations of Neuroscience*, pages 1–28. Springer, New York, NY, 2010. ISBN 978-0-387-87708-2. doi: 10.1007/978-0-387-87708-2_1. URL https://doi.org/10.1007/978-0-387-87708-2_1.

[15] G. Bard Ermentrout and David H. Terman. *Mathematical Foundations of Neuroscience*, volume 35 of *Interdisciplinary Applied Mathematics*. Springer, New York, NY, 2010. ISBN 978-0-387-87707-5 978-0-387-87708-2. doi: 10.1007/978-0-387-87708-2. URL http://link.springer.com/10.1007/978-0-387-87708-2.

[16] Daniel E. Feldman. The Spike-Timing Dependence of Plasticity. *Neuron*, 75(4): 556–571, August 2012. ISSN 08966273. doi: 10.1016/j.neuron.2012.08.001. URL https://linkinghub.elsevier.com/retrieve/pii/S0896627312007039.

[17] Richard P. Feynman, Robert B. Leighton, and Matthew L. Sands. *The Feynman lectures on physics*. Basic Books, New York, new millennium ed edition, 2011. ISBN 978-0-465-02414-8 978-0-465-02493-3 978-0-465-02416-2 978-0-465-02417-9 978-0-465-02501-5 978-0-465-02382-0. OCLC: ocn671704374.

[18] Adolph Fick. V. On liquid diffusion. *The London, Edinburgh, and Dublin Philosophical Magazine and Journal of Science*, 10(63):30–39, July 1855. ISSN 1941-5982. doi: 10.1080/14786445508641925. URL https://doi.org/10.1080/14786445508641925. Publisher: Taylor & Francis _eprint: https://doi.org/10.1080/14786445508641925.

[19] Etay Hay, Sean Hill, Felix Schürmann, Henry Markram, and Idan Segev. Models of Neocortical Layer 5b Pyramidal Cells Capturing a Wide Range of Dendritic and Perisomatic Active Properties. *PLoS Computational Biology*, 7(7):e1002107, July 2011. ISSN 1553-7358. doi: 10.1371/journal.pcbi.1002107. URL https://dx.plos.org/10.1371/journal.pcbi.1002107.

[20] Bertil Hille. *Ion channels of excitable membranes*. Sinauer, Sunderland, Mass, 3rd ed edition, 2001. ISBN 978-0-87893-321-1.

[21] A. L. Hodgkin and A. F. Huxley. A quantitative description of membrane current and its application to conduction and excitation in nerve. *The Journal of Physiology*, 117(4):500–544, 1952. ISSN 1469-7793. doi: 10.1113/jphysiol.1952.sp004764. URL https://onlinelibrary.wiley.com/doi/abs/10.1113/jphysiol.1952.sp004764.

[22] A. L. Hodgkin and B. Katz. The effect of sodium ions on the electrical activity of the giant axon of the squid. *The Journal of Physiology*, 108(1):37–77, March 1949. ISSN 1469-7793. doi: 10.1113/jphysiol.1949.sp004310. URL https://physoc.onlinelibrary.wiley.com/doi/10.1113/jphysiol.1949.sp004310. Publisher: John Wiley & Sons, Ltd.

[23] Wenqin Hu, Cuiping Tian, Tun Li, Mingpo Yang, Han Hou, and Yousheng Shu. Distinct contributions of Nav1.6 and Nav1.2 in action potential initiation and backpropagation. *Nature Neuroscience*, 12(8):996–1002, August 2009. ISSN 1546-1726. doi: 10.1038/nn.2359. URL https://www.nature.com/articles/nn.2359.

[24] Claire Yu-Mei Huang and Matthew N. Rasband. Axon initial segments: structure, function, and disease. *Annals of the New York Academy of Sciences*, 1420(1): 46–61, May 2018. ISSN 1749-6632. doi: 10.1111/nyas.13718. URL https://nyaspubs.onlinelibrary.wiley.com/doi/abs/10.1111/nyas.13718.

[25] Xinrui Huang, Kerui Li, Yiqun Liu, Chuqiao Yang, and Hongbin Han. Quantitative Measurement of Brain Extracellular Space with Three-Dimensional Electron Microscopy Imaging. *Sensing and Imaging*, 24(1):2, January 2023. ISSN 1557-2072. doi: 10.1007/s11220-022-00408-z. URL https://doi.org/10.1007/s11220-022-00408-z.

[26] Eugene M. Izhikevich. *Dynamical Systems in Neuroscience: The Geometry of Excitability and Bursting*. The MIT Press, July 2006. ISBN 978-0-262-27607-8. doi: 10.7551/mitpress/2526.001.0001. URL https://direct.mit.edu/books/monograph/2589/Dynamical-Systems-in-NeuroscienceThe-Geometry-of.

[27] Donald C Jackson. Hibernating without oxygen: physiological adaptations of the painted turtle. *The Journal of Physiology*, 543(Pt 3):731–737, September 2002.

ISSN 0022-3751. doi: 10.1113/jphysiol.2002.024729. URL https://www.ncbi.nlm.nih.gov/pmc/articles/PMC2290531/.

[28] Béla Joós, Benjamin M. Barlow, and Catherine E. Morris. Calculating the Consequences of Left-Shifted Nav Channel Activity in Sick Excitable Cells. In Mohamed Chahine, editor, *Voltage-gated Sodium Channels: Structure, Function and Channelopathies*, volume 246, pages 401–422. Springer International Publishing, Cham, 2017. ISBN 978-3-319-90283-8 978-3-319-90284-5. doi: 10.1007/164_2017_63. URL http://link.springer.com/10.1007/164_2017_63. Series Title: Handbook of Experimental Pharmacology.

[29] Janice M. Juraska and Carly M. Drzewiecki. Cortical reorganization during adolescence: What the rat can tell us about the cellular basis. *Developmental Cognitive Neuroscience*, 45:100857, October 2020. ISSN 1878-9293. doi: 10.1016/j.dcn.2020.100857. URL https://www.sciencedirect.com/science/article/pii/S1878929320301079.

[30] H. Kager, W. J. Wadman, and G. G. Somjen. Simulated Seizures and Spreading Depression in a Neuron Model Incorporating Interstitial Space and Ion Concentrations. *Journal of Neurophysiology*, 84(1):495–512, July 2000. ISSN 0022-3077. doi: 10.1152/jn.2000.84.1.495. URL https://journals.physiology.org/doi/full/10.1152/jn.2000.84.1.495. Publisher: American Physiological Society.

[31] Efrat Katz, Ohad Stoler, Anja Scheller, Yana Khrapunsky, Sandra Goebbels, Frank Kirchhoff, Michael J. Gutnick, Fred Wolf, and Ilya A. Fleidervish. Role of sodium channel subtype in action potential generation by neocortical pyramidal neurons. *Proceedings of the National Academy of Sciences*, 115(30):E7184–E7192, July 2018. ISSN 0027-8424, 1091-6490. doi: 10.1073/pnas.1720493115. URL https://www.pnas.org/content/115/30/E7184.

[32] Maarten H. P. Kole, Susanne U. Ilschner, Björn M. Kampa, Stephen R. Williams, Peter C. Ruben, and Greg J. Stuart. Action potential generation requires a high sodium channel density in the axon initial segment. *Nature Neuroscience*, 11(2):178–186, February 2008. ISSN 1546-1726. doi: 10.1038/nn2040. URL https://www.nature.com/articles/nn2040.

[33] Oron Kotler, Michael J. Gutnick, and Ilya A. Fleidervish. In computational models, action potential propagation in ultrathin axons is resilient despite considerable intracellular Na+ accumulation. *Proceedings of the National Academy of Sciences*, 119(12):e2120782119, March 2022. doi: 10.1073/pnas.2120782119. URL https://www.pnas.org/doi/full/10.1073/pnas.2120782119. Publisher: Proceedings of the National Academy of Sciences.

[34] Hiroshi Kuba, Yuki Oichi, and Harunori Ohmori. Presynaptic activity regulates Na+ channel distribution at the axon initial segment. *Nature*, 465(7301):1075–1078, June 2010. ISSN 1476-4687. doi: 10.1038/nature09087. URL https://www.nature.com/articles/nature09087. Number: 7301 Publisher: Nature Publishing Group.

[35] D. R. Lemieux, F. A. Roberge, and D. Joly. Modeling the dynamic features of the electrogenic Na,K pump of cardiac cells. *Journal of Theoretical Biology*, 154(3):335–358, February 1992. ISSN 0022-5193. doi: 10.1016/S0022-5193(05)80175-4. URL https://www.sciencedirect.com/science/article/pii/S0022519305801754.

[36] Albert Lin, Runzhe Yang, Sven Dorkenwald, Arie Matsliah, Amy R. Sterling, Philipp Schlegel, Szi-chieh Yu, Claire E. McKellar, Marta Costa, Katharina Eichler, Alexander Shakeel Bates, Nils Eckstein, Jan Funke, Gregory S. X. E. Jefferis, and Mala Murthy. Network Statistics of the Whole-Brain Connectome of Drosophila, February 2024. URL https://www.biorxiv.org/content/10.

1101/2023.07.29.551086v2. Pages: 2023.07.29.551086 Section: New Results.

[37] Hui Liu, Hong-Gang Wang, Geoffrey Pitt, and Zhe Liu. Direct Observation of Compartment-Specific Localization and Dynamics of Voltage-Gated Sodium Channels. *The Journal of Neuroscience*, 42(28):5482–5498, July 2022. ISSN 0270-6474, 1529-2401. doi: 10.1523/JNEUROSCI.0086-22.2022. URL https://www.jneurosci.org/lookup/doi/10.1523/JNEUROSCI.0086-22.2022.

[38] Zachary F. Mainen and Terrence J. Sejnowski. Influence of dendritic structure on firing pattern in model neocortical neurons. *Nature*, 382(6589):363–366, July 1996. ISSN 1476-4687. doi: 10.1038/382363a0. URL https://www.nature.com/articles/382363a0.

[39] Zachary F. Mainen, Jasdan Joerges, John R. Huguenard, and Terrence J. Sejnowski. A model of spike initiation in neocortical pyramidal neurons. *Neuron*, 15(6):1427–1439, December 1995. ISSN 0896-6273. doi: 10.1016/0896-6273(95)90020-9. URL https://www.sciencedirect.com/science/article/pii/0896627395900209.

[40] Jeremy Maitin-Shepard, Alex Baden, William Silversmith, Eric Perlman, Forrest Collman, Tim Blakely, Jan Funke, Chris Jordan, Ben Falk, Nico Kemnitz, tingzhao, Chris Roat, Manuel Castro, Sridhar Jagannathan, moenigin, Jody Clements, Austin Hoag, Bill Katz, Dave Parsons, Jingpeng Wu, Lee Kamentsky, Pavel Chervakov, Philip Hubbard, Stuart Berg, John Hoffer, Akhilesh Halageri, Christian Machacek, Kevin Mader, Lutz Roeder, and Peter H. Li. google/neuroglancer:, October 2021. URL https://doi.org/10.5281/zenodo.5573294.

[41] Robert A. McDougal, Thomas M. Morse, Ted Carnevale, Luis Marenco, Rixin Wang, Michele Migliore, Perry L. Miller, Gordon M. Shepherd, and Michael L. Hines. Twenty years of ModelDB and beyond: building essential modeling tools for the future of neuroscience. *Journal of Computational Neuroscience*, 42(1):

1–10, February 2017. ISSN 1573-6873. doi: 10.1007/s10827-016-0623-7. URL https://doi.org/10.1007/s10827-016-0623-7.

[42] Michael Mell, Lara H. Moleiro, Yvonne Hertle, Iván López-Montero, Francisco J. Cao, Peter Fouquet, Thomas Hellweg, and Francisco Monroy. Fluctuation dynamics of bilayer vesicles with intermonolayer sliding: Experiment and theory. *Chemistry and Physics of Lipids*, 185:61–77, January 2015. ISSN 0009-3084. doi: 10.1016/j.chemphyslip.2014.11.005. URL http://www.sciencedirect.com/science/article/pii/S0009308414001388.

[43] Philip Charles Nelson, David S. Goodsell, Kevin Chen, and Sarina Bromberg. *Biological physics: energy, information, life*. Chiliagon Science, Philadelphia, PA, student edition edition, 2020. ISBN 978-0-578-68702-5. OCLC: on1154771240.

[44] Charles Nicholson and Sabina Hrabětová. Brain Extracellular Space: The Final Frontier of Neuroscience. *Biophysical Journal*, 113(10):2133–2142, November 2017. ISSN 0006-3495. doi: 10.1016/j.bpj.2017.06.052. URL https://www.sciencedirect.com/science/article/pii/S0006349517307026.

[45] R. K. Pathria and Paul D. Beale. *Statistical mechanics*. Elsevier/Academic Press, Amsterdam Boston, 3rd ed edition, 2011. ISBN 978-0-12-382188-1.

[46] Ning Qian and T. J. Sejnowski. An electro-diffusion model for computing membrane potentials and ionic concentrations in branching dendrites, spines and axons. *Biological Cybernetics*, 62(1):1–15, November 1989. ISSN 1432-0770. doi: 10.1007/BF00217656. URL https://doi.org/10.1007/BF00217656.

[47] Anthony M. Rush, Sulayman D. Dib-Hajj, and Stephen G. Waxman. Electrophysiological properties of two axonal sodium channels, Na $_{v}$ 1.2 and Na $_{v}$ 1.6, expressed in mouse spinal sensory neurones: Sodium channels in sensory neurones. *The Journal of Physiology*, 564(3):803–815, May 2005. ISSN 00223751.

doi: 10.1113/jphysiol.2005.083089. URL https://onlinelibrary.wiley.com/doi/10.1113/jphysiol.2005.083089.

[48] Alexander Shapson-Coe, Michał Januszewski, Daniel R. Berger, Art Pope, Yuelong Wu, Tim Blakely, Richard L. Schalek, Peter H. Li, Shuohong Wang, Jeremy Maitin-Shepard, Neha Karlupia, Sven Dorkenwald, Evelina Sjostedt, Laramie Leavitt, Dongil Lee, Luke Bailey, Angerica Fitzmaurice, Rohin Kar, Benjamin Field, Hank Wu, Julian Wagner-Carena, David Aley, Joanna Lau, Zudi Lin, Donglai Wei, Hanspeter Pfister, Adi Peleg, Viren Jain, and Jeff W. Lichtman. A connectomic study of a petascale fragment of human cerebral cortex, November 2021. URL https://www.biorxiv.org/content/10.1101/2021.05.29.446289v4. Pages: 2021.05.29.446289 Section: New Results.

[49] Alexander Shapson-Coe, Michał Januszewski, Daniel R. Berger, Art Pope, Yuelong Wu, Tim Blakely, Richard L. Schalek, Peter H. Li, Shuohong Wang, Jeremy Maitin-Shepard, Neha Karlupia, Sven Dorkenwald, Evelina Sjostedt, Laramie Leavitt, Dongil Lee, Jakob Troidl, Forrest Collman, Luke Bailey, Angerica Fitzmaurice, Rohin Kar, Benjamin Field, Hank Wu, Julian Wagner-Carena, David Aley, Joanna Lau, Zudi Lin, Donglai Wei, Hanspeter Pfister, Adi Peleg, Viren Jain, and Jeff W. Lichtman. A petavoxel fragment of human cerebral cortex reconstructed at nanoscale resolution. *Science*, 384(6696):eadk4858, May 2024. doi: 10.1126/science.adk4858. URL https://www.science.org/doi/10.1126/science.adk4858. Publisher: American Association for the Advancement of Science.

[50] Philip K. Shiu, Gabriella R. Sterne, Nico Spiller, Romain Franconville, Andrea Sandoval, Joie Zhou, Neha Simha, Chan Hyuk Kang, Seongbong Yu, Jinseop S. Kim, Sven Dorkenwald, Arie Matsliah, Philipp Schlegel, Szi-chieh Yu, Claire E. McKellar, Amy Sterling, Marta Costa, Katharina Eichler, Alexander Shakeel

Bates, Nils Eckstein, Jan Funke, Gregory S. X. E. Jefferis, Mala Murthy, Salil S. Bidaye, Stefanie Hampel, Andrew M. Seeds, and Kristin Scott. A Drosophila computational brain model reveals sensorimotor processing. *Nature*, 634(8032): 210–219, October 2024. ISSN 1476-4687. doi: 10.1038/s41586-024-07763-9. URL https://www.nature.com/articles/s41586-024-07763-9. Publisher: Nature Publishing Group.

[51] Yousheng Shu, Alvaro Duque, Yuguo Yu, Bilal Haider, and David A. McCormick. Properties of Action-Potential Initiation in Neocortical Pyramidal Cells: Evidence From Whole Cell Axon Recordings. *Journal of Neurophysiology*, 97(1):746–760, January 2007. ISSN 0022-3077. doi: 10.1152/jn.00922.2006. URL https://journals.physiology.org/doi/full/10.1152/jn.00922.2006. Publisher: American Physiological Society.

[52] Perry W. E. Spratt, Ryan P. D. Alexander, Roy Ben-Shalom, Atehsa Sahagun, Henry Kyoung, Caroline M. Keeshen, Stephan J. Sanders, and Kevin J. Bender. Paradoxical hyperexcitability from NaV1.2 sodium channel loss in neocortical pyramidal cells. *Cell Reports*, 36(5), August 2021. ISSN 2211-1247. doi: 10.1016/j.celrep.2021.109483. URL https://www.cell.com/cell-reports/abstract/S2211-1247(21)00910-4.

[53] David Sterratt, editor. *Principles of computational modelling in neuroscience*. Cambridge University Press, Cambridge, 2011. ISBN 978-0-521-87795-4.

[54] Steven H. Strogatz. *Nonlinear dynamics and chaos: with applications to physics, biology, chemistry, and engineering*. Westview Press, a member of the Perseus Books Group, Boulder, CO, second edition edition, 2015. ISBN 978-0-8133-4910-7. OCLC: ocn842877119.

[55] Robert G. Thorne and Charles Nicholson. *In vivo* diffusion analysis with quantum dots and dextrans predicts the width of brain extracellular space. *Proceedings*

of the National Academy of Sciences, 103(14):5567–5572, April 2006. ISSN 0027-8424, 1091-6490. doi: 10.1073/pnas.0509425103. URL https://pnas.org/doi/full/10.1073/pnas.0509425103.

[56] Jun A. Wang, Wei Lin, Terence Morris, Umberto Banderali, Peter F. Juranka, and Catherine E. Morris. Membrane trauma and Na+ leak from Nav1.6 channels. *American Journal of Physiology-Cell Physiology*, 297(4):C823–C834, October 2009. ISSN 0363-6143. doi: 10.1152/ajpcell.00505.2008. URL https://journals.physiology.org/doi/full/10.1152/ajpcell.00505.2008.

[57] Mingyu Ye, Jun Yang, Cuiping Tian, Qiyu Zhu, Luping Yin, Shan Jiang, Mingpo Yang, and Yousheng Shu. Differential roles of NaV1.2 and NaV1.6 in regulating neuronal excitability at febrile temperature and distinct contributions to febrile seizures. *Scientific Reports*, 8(1):753, December 2018. ISSN 2045-2322. doi: 10.1038/s41598-017-17344-8. URL http://www.nature.com/articles/s41598-017-17344-8.

[58] Na Yu, Catherine E. Morris, Béla Joós, and André Longtin. Spontaneous Excitation Patterns Computed for Axons with Injury-like Impairments of Sodium Channels and Na/K Pumps. *PLOS Computational Biology*, 8(9): e1002664, September 2012. ISSN 1553-7358. doi: 10.1371/journal.pcbi.1002664. URL https://journals.plos.org/ploscompbiol/article?id=10.1371/journal.pcbi.1002664. Publisher: Public Library of Science.

Appendices

Table 1: Biophysical neuron models versus nodes (also called neurons) in artificial neural networks

Biophysical neuron models and neural net $\overbrace{\text{neurons}}^{\text{nodes}}$: different properties, different purposes.		
	Biophysical Neuron Models	Neurons (nodes) as defined in Artificial Neural Networks
Dynamics	Detailed empirical ion channel dynamics	Simplified abstraction
Time	Continuous* physical quantity in differential equations	iteration step
Output	Membrane potential, gating variables, ion concentrations: continuous, analog*	Activation: scalar function of summed weighted inputs
Meaning	Physical state of neuron and its surroundings	Output signal intensity
Range	Constrained and dimensional, e.g. transmembrane voltage from -80 to $+40$ mV	Arbitrary, dimensionless
$\overbrace{\text{Computational overhead}}^{\text{(per "neuron")}}$	Demanding	Efficient, but many nodes are required to emulate a single biophysical neuron simulation [6]
Parameterization	Many, often unknown parameters per neuron, "the curse of dimensionality" [1]	Fewer parameters *per neuron*
Spatial Structure	Can be spatially extended, with detailed morphology. Morphology affects firing patterns [38]	Point-like
Internal state	Complex spatiotemporal patterns	Weighted sum of local inputs
Plasticity	Local synaptic, axonal, and morphological cellular plasticity.	Connection weights are adjusted through algorithms reaching across the entire network. Many nodes.
Machine learning?	**not yet**, progressing rapidly	**YES!**

Table 1: **Biophysical neuron models vs. nodes (a.k.a. neurons) in artificial neural networks**: A by-no-means-definitive comparison of single-cell biophysical neuron models to the nodes—called neurons as well—in artificial neural networks. By necessity, this table paints with a broad brush. (*The analog models are usually simulated on *digital* computers.)

Calculating the Consequences of Left-Shifted Nav Channel Activity in Sick Excitable Cells – Joós, Barlow, and Morris (2017)

Calculating the Consequences of Left-Shifted Nav Channel Activity in Sick Excitable Cells

Bela Joos, Benjamin M. Barlow, and Catherine E. Morris

Contents

Abstract

Two features common to diverse sick excitable cells are "leaky" Nav channels and bleb damage-damaged membranes. The bleb damage, we have argued, causes a channel kinetics based "leakiness." Recombinant (node of Ranvier type) Nav1.6 channels voltage-clamped in mechanically-blebbed cell-attached patches undergo a damage intensity dependent kinetic change. Specifically, they experience a coupled hyperpolarizing (left) shift of the activation and inactivation processes. The biophysical observations on Nav1.6 currents formed the

B. Joos (✉) · B. M. Barlow
Department of Physics, University of Ottawa, Ottawa, ON, Canada
e-mail: bjoos@uottawa.ca

C. E. Morris
Neurosciences, Ottawa Hospital Research Institute, Ottawa, ON, Canada
e-mail: cmorris@uottawa.ca

M. Chahine (ed.), *Voltage-gated Sodium Channels: Structure, Function and Channelopathies*, Handbook of Experimental Pharmacology 246,
https://doi.org/10.1007/164_2017_63

basis of Nav-Coupled Left Shift (Nav-CLS) theory. Node of Ranvier excitability can be modeled with Nav-CLS imposed at varying LS intensities and with varying fractions of total nodal membrane affected. Mild damage from which sick excitable cells might recover is of most interest pathologically. Accordingly, Na^+/K^+ ATPase (pump) activity was included in the modeling. As we described more fully in our other recent reviews, Nav-CLS in nodes with pumps proves sufficient to predict many of the pathological excitability phenomena reported for sick excitable cells. This review explains how the model came about and outlines how we have used it. Briefly, we direct the reader to studies in which Nav-CLS is being implemented in larger scale models of damaged excitable tissue. For those who might find it useful for teaching or research purposes, we coded the Nav-CLS/node of Ranvier model (with pumps) in NEURON. We include, here, the resulting "Regimes" plot of classes of excitability dysfunction.

Keywords

Bleb · Ectopic · Excitability · Hyperpolarizing shift · Leaky sodium channels · Left shift · Membrane damage · Mild injury · Modeling

1 Introduction

Excitable cells express voltage-gated sodium channels (Nav) or in some cases voltage-gated calcium channels that enable them to create and propagate the voltage spikes known as action potentials (APs). For reasons that long seemed obscure, many pathological conditions that involve excitable cells included, in the list of malfunctioning parts, "leaky sodium channels." In recent reviews we have labeled such cells "sick excitable cells" and have argued that the acquired sodium channelopathies noted under these conditions almost certainly arise from the widely reported but otherwise rather overlooked bleb damage inherent to the various disease states. Specifically, it would be bleb damage to the Nav-bearing membranes that is critical for sick excitable cells (Morris et al. 2012a, b; Morris and Joós 2016). The damage can result from mechanical trauma (and the attendant intra-tissue shear stresses), ischemia, inflammation, excitotoxicity, or other conditions. Blebbing of the Nav-bearing membrane would occur progressively as, progressively, the filamentous web of actin-spectrin cytoskeleton became detached from the inner bilayer leaflet.

In ways that are only partially understood, the adherent cortical cytoskeleton contributes both to trans-leaflet asymmetry of healthy membranes and to their dynamic lateral non-random heterogeneous organization (Sheetz et al. 2006). Ischemia and inflammation lead to excessive cytoplasmic calcium, thereby hyperactivating enzymes that hydrolyze the cytoskeleton. Shear forces, by contrast, would act directly to produce detachments. The living healthy plasma membrane features not self-organized bilayer, but rather, a bilayer whose molecular structure is cell-mediated. Presumably there is a continuum between the high-entropy "self-organized" state of the outright membrane blebs observed sloughing off sick

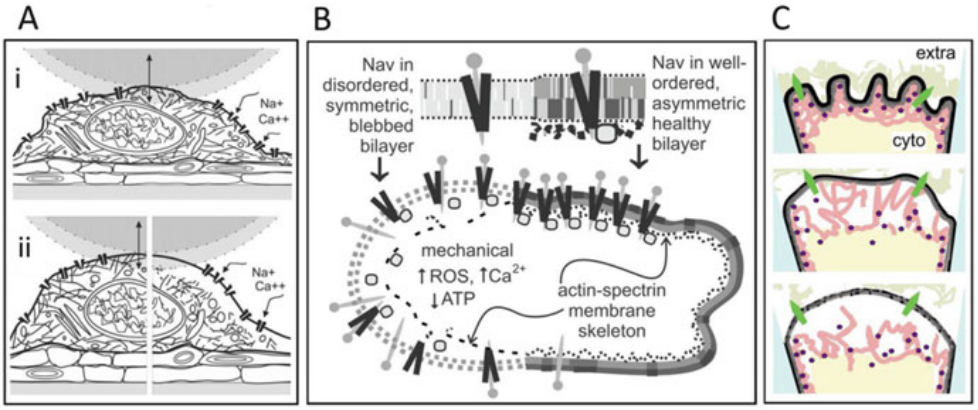

Fig. 1 Cartoon depictions of bleb damage developing in Nav-bearing plasma membranes. (**A**) Depiction of an atomic force microscopy experiment that tests the mechanical state of an excitable cell's surface/subsurface region before and after a bleb-inducing insult (Zou et al. 2013) (ii). A neuron cultured on astrocytes is depicted with a ~20 μm sphere whose maximum displacement is outlined. Excitotoxicity was mimicked with glutamate and Nav channel agonists that dissipate $[Ca^{2+}]$ and $[Na^{+}]$ gradients. Neurons inflate on exposure to hypotonic medium and to excitotoxic agonists. (ii) Early and late expected states of an enlarged neuron exposed to excitotoxic agonists is depicted: at left, once the initial channel-mediated Na^{+} influx and osmotically-obligated H_2O has hydrostatically inflated the neuron (countered to some extent by Ca^{2+}-mediated actomyosin contractility), and at right, after Ca^{2+}-toxicity has damaged the previously adherent (and contractile) neuronal membrane skeleton, allowing the plasma membrane to bleb pathologically. The bilayer in (**A**) is depicted by a simple line but the adjacent cartoon, (**B**), highlights some key changes that would be occurring in Nav channel bearing membranes as it went from healthy to blebbed (from Morris and Joós 2016). (**C**) depicts a cell-attached patch (blue (gray in print versions) is pipette walls) with extracellular, cytoplasmic, and membrane disruptions expected after a gigaohm-seal is gently formed (top) then after milder (middle) and more severe (bottom) bleb damage has occurred due to pipette aspiration. Bilayer structure denatures relative to its intact plasma membrane state, but membrane proteins (green arrow-tipped lines (light gray in print versions)) do not denature. In the case of Nav channels, a fully functional, inherently mechanosensitive voltage-gated channel finds itself in a bilayer whose mechanical state (see discussions of a bilayer's lateral pressure profile in Finol-Urdaneta et al. 2010) undergoes a major change between the healthy and fully blebbed state.

excitable cells, and the light-microscopically invisible incipient state of blebbing. As depicted in Figure 1, atomic force microscopy probing cortical neurons subjected to excitotoxic stimuli (Zou et al. 2013) suggests that during the course of blebbing, where conditions cause osmotic swelling, elevated far-field tension could be expected in the blebbed Nav-bearing membrane.

Experiments on recombinant Nav channels heterologously expressed in *Xenopus* oocytes established connection between mechanically imposed membrane damage and changes in the kinetics of the Nav channels. Channel activity was monitored as macroscopic current in cell-attached patches. The effect of membrane damage first became evident for Nav1.4 channels (Tabarean et al. 1999; Shcherbatko et al. 1999), but the irreversibly changed Nav channel kinetics observed in those experiments were not, at the time, attributed to the bleb damage per se. Subsequently,

Wang et al. (2009), doing similar experiments with Nav1.6, made the connection. They also distinguished between the large irreversible changes in Nav kinetics that were attributed to irreversible changes in membrane structure and the small (but qualitatively similar) reversible kinetic changes that arise from reversibly increased far-field membrane tension (far-field tension is used here to make it clear that we refer to a Hookean-like bilayer tension and not an interfacial surface membrane tension). Wang et al. (2009) also performed whole cell trauma experiments; Nav1.6-expressing mammalian cells subjected to traumatic-type stretch were found to exhibit a TTX-sensitive Na^+-leak. Here, our intent is to review the irreversible Nav channel kinetic changes associated mechanically induced bleb-damage, and to review our modeling of those changes in cellular contexts.

The Wang et al. (2009) patch clamp experiments form the basis of the model discussed in this review, i.e., coupled left shift (or CLS), whose properties and predictions were first presented in Boucher et al. (2012) then further explored in Yu et al. (2012) and by Lachance et al. (2014). As Morris and Joós (2016) have repeatedly emphasized, the biophysical link between blebbing and Nav channelopathy revealed by the work of Wang et al. (2009) would benefit from further experimental lines of inquiry. The issue that specifically needs to be addressed is whether it is indeed blebbed Nav-bearing membrane that should be the therapeutic target for addressing pathologies arising from abnormal Nav kinetics in sick excitable cells.

2 Experimental Basis of the Nav-CLS Model

The predominant Nav channels at nodes of Ranvier and in the distal regions of axon initial segments are Nav1.6 channels. Because Nav channel blockers are protective in cell and tissue models of mechanical, ischemic, inflammatory and other injuries, it is understood that these white matter Nav channels become lethally leaky under pathological conditions. Fast-mode gating dominates in Nav1.6 and their response to progressive bleb damage turns out to be straightforward. Reversibly applied pipette suction ("aspiration") yields irreversible and approximately equal hyperpolarizing shifts of the equilibrium conductance $g(V)$ and availability (V) as a function of the membrane voltage V. In Wang et al. (2009) (Fig. 2; Fig. 2B in Wang et al.), those quantities are shown for "pre-stretch" membrane patches and the "post-stretch" membranes. On average the cumulative applied suction produced ~20 mV of hyperpolarizing (or "left") shift. The rising curves were obtained by stepping from $V_{\text{hold}} = -110$ mV to the test potential. The g(V) curve is obtained from the normalized peak current observed at the potentials along the X-axis. At left are Nav availability curves. From V_{hold} the voltage was stepped for 210 ms to the voltages on the X-axis (210 ms is more than sufficient for fast inactivation to equilibrate) and then for 10 ms to the test voltage (0 mV) to assess availability based on peak current.

Direct evidence that both activation and fast inactivation kinetics simply "left-shift" due to membrane damage is shown in Fig. 3 (see legend) with the most

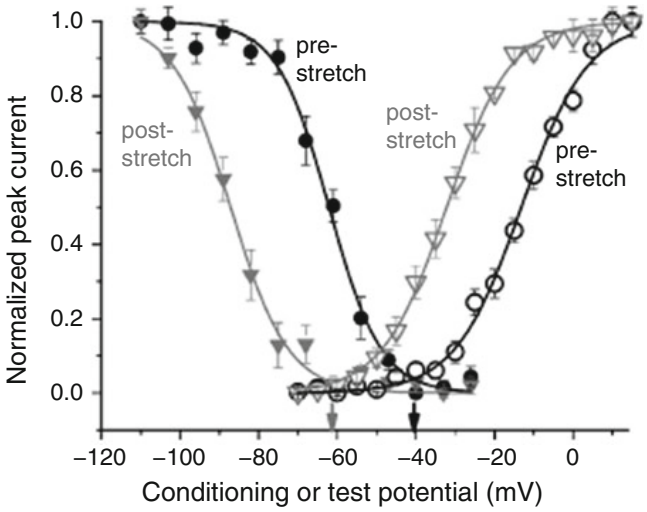

Fig. 2 Coupled-left shift (Nav-CLS). After traumatic membrane stretch, the kinetics of recombinant Nav1.6 channels expressed in oocytes are irreversibly changed. They undergo irreversible hyperpolarizing shifts of activation and steady-state fast inactivation (availability) as explained in the text. From Wang et al. (2009) where experimental details can be found

straightforward observations presented in the bottom section (*v*). Here, $I_{Na}(t)$ time courses before and after stretch at several voltages are shown for one particular cell-attached oocyte patch. Fortuitously, for this patch stretch damage produced a left-shift of exactly 20 mV. Since Nav currents were assessed at 5 mV intervals, this meant that the 20 mV left shift corresponded precisely to a membrane potential tested before and after application of membrane-traumatizing suction (stretch). Note how currents post-stretch overlap completely (over the whole activation and inactivation time course) with amplitude-normalized pre-stretch currents obtained at voltages 20 mV more hyperpolarized. This shows that after irreversible damage, both activation and inactivation are irreversibly accelerated to the same extent. Part A (i, ii) of Fig. 3 (a different patch) illustrates pre- and post-stretch currents at 0 mV in a patch whose inactivation time constant (fits not shown) shifted leftward by 16 mV. Parts iii and iv show traces for a given patch that is stepped to −15 mV pre- and post-stretch; when the currents are amplitude normalized, the slower (pre-stretch) current can then be rescaled in the time domain till it completely overlaps. This double-rescaling is another direct way in which coupled-left shift manifests itself. Figure 3B i, ii shows data from two other patches in which the observed irreversible left-shift was, fortuitously, an almost exact multiple of 5 mV (i.e., 10 and 35 mV). In the Hodgkin-Huxley formulation, fast inactivation is explicitly described as an independently voltage dependent process (i.e., it is not kinetically coupled to activation, unlike in real Nav channels; see Banderali et al. 2010 and see discussions in Morris and Joós 2016) and so the "double-rescaling" procedure does not work. However, for our modeling purposes, the consequences of this Hodgkin-Huxley departure from reality are trivial.

In some experiments irreversible stretch induced damage was taken to a point at which no further irreversible left shift occurred (this was closer to 30 mV than the ~20 of Fig. 2; approaching the "saturation" point makes membrane rupture very likely, so this was avoided usually; the ~20 mV average coupled left shift of Fig. 2 therefore underestimates left shift for these channels in fully blebbed membrane).

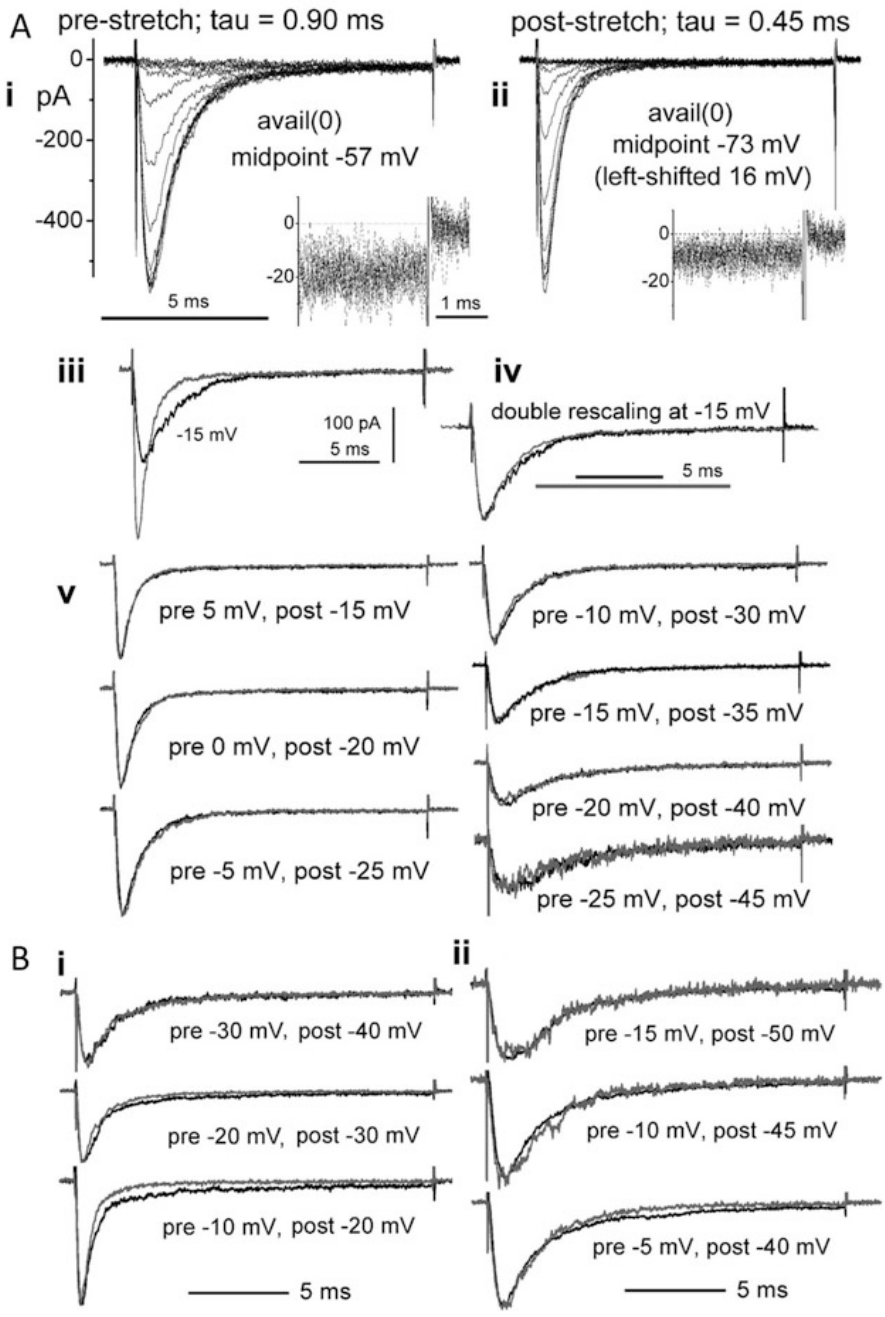

Fig. 3 Cell-attached patch clamp currents from Nav1.6 channels before and after traumatic (bleb-inducing) membrane stretch. The Nav CLS theory is based on data such as that in (**A**) i-v and in (**B**) i,ii, as explained in the text. From Wang et al. (2009) where experimental details can be found

Once "saturation" was achieved in these few experiments, it was possible to test effects of reversibly increased membrane tension. In other words, mechanosensitive (MS) gating changes could be tested. They amounted to at most a few mV of

reversible coupled left shift (this has been explored more fully in Nav1.5 channels; see Morris and Juranka 2007; Banderali et al. 2010 and the references therein). The fact that these reversible MS changes are qualitatively identical to the larger irreversible changes associated with blebbing suggests the following: from the point of view of the Nav channel's kinetic behavior, a bleb damaged membrane "looks and feels" like a bilayer that has been made to thin due to imposed stretch (for more detail and discussion see Morris and Joós 2016; Morris et al. 2012a, b). We have no information on whether blebbing Nav-bearing membrane in sick excitable cells is ever at a sufficiently elevated membrane tension to produce appreciable MS kinetic changes. We suggest, however, that even if some blebs are at elevated tension (as was suggested for the earliest stages of excitotoxicity (Fig. 1A ii)), this would be almost certainly be irrelevant since bleb damage itself impacts Nav channel gating more strongly in a kinetically identical manner.

3 The Coupled Left-Shift Model (CLS)

The experiments of Wang et al. (2009) justify a mathematically simple model of damage to nodal Nav channel function in which the kinetics are simply left-shifted by a constant voltage which we call LS and that will become a measure of the damage (Boucher et al. 2012; Morris et al. 2012a, b). As both activation and inactivation shift by the same amount, the model was called the *coupled left-shift* (CLS) model. (For discussions of the likely molecular basis of this coupling, see Banderali et al. 2010 and Morris and Joós 2016.) The voltage V_m in all expressions of the kinetics of the intact Navs is simply replaced by (V_m + LS) for the Navs in the damaged regions of the membrane.

An action potential (AP) represents a spike in the plasma membrane potential. The plasma membrane's lipid bilayer is assigned a capacitance per unit area of 1 μF/cm^2. The healthy node of Ranvier is, most of the time, in a quiescent state of readiness for firing (at its resting potential, V_{rest}) with the membrane conductance dominated by non-specific leak conductance (g_L). For computational purpose the reversal potential of g_L is set at a potential somewhat more depolarized than E_{K}. There is a low internal (axoplasmic) [Na^+] and a high external [Na^+], and vice versa for [K^+]. Depolarization of the membrane potential $V_m = V_{\text{in}} - V_{\text{out}}$ occurs when, for example a brief stimulus such as an injected current triggers Nav channels to open and support a Na^+ influx. With a brief delay, this depolarization next triggers the opening of voltage-gated K^+ channels (Kvs). The resulting outflow of K^+ drives V_m back in the hyperpolarizing direction and eventually V_m returns to V_{rest}. Homeostasis is either assumed in the CLS models that will be discussed (fixed values for the Na^+ and K^+ reversal potentials) or is explicitly included as a process by mathematically depicting the Na^+/K^+ ATPase (pumps) that continuously remove 3 Na^+ from the cell and bring in 2 K^+ per ATP consumed.

To explore qualitatively how LS might affect the excitability of nodes of Ranvier, we use the Hodgkin-Huxley (HH) model (Hodgkin and Huxley 1952) to model the Navs, Kvs and leaks, but similar calculations could be carried out using

other kinetic models. Pumps are included in much of our modeling, and for this Michaelis-Menten kinetics are used in the manner outlined by Läuger (1991). Adding the pumps acknowledges the impact of extended AP firing on excitable systems as they contend with ion homeostasis of their finite internal and external volumes.

Using the convention that ion current is positive when cations are outflowing, the differential equation governing the rate of change of V_m (written for simplicity V) is given by:

$$C\frac{\mathrm{d}V}{\mathrm{d}t} = -I_{\mathrm{Na}} - I_{\mathrm{K}} - I_{\mathrm{L}} + I_{\mathrm{stim}}, \tag{1}$$

Note that positive ion current hyperpolarizes V_m whereas negative ion current (e.g., an inflow of Na^+ ions) depolarizes V_m. In Eq. (1) I_{Na} flows through Navs and I_{K} through Kvs. I_L is the leak current and I_{stim} the injected external stimulus that, typically, is used to depolarize the membrane enough to elicit an AP.

Dividing both sides of Eq. (1) gives $\mathrm{d}V/\mathrm{d}t =$ the sum of the 4 currents divided by C; solving this differential equation yields $V(t)$, which, when all is well, takes the form of an AP. Since there is no analytical solution for $\mathrm{d}V/\mathrm{d}t$, numerical methods are used.

Expressions for each ion current and their kinetics are:

$$I_{\mathrm{Na}} = g_{\mathrm{Na}}(V - E_{\mathrm{Na}}), \quad \text{where} \quad g_{\mathrm{Na}} = \bar{g}_{\mathrm{Na}} m^3 h \tag{2}$$

$$I_{\mathrm{K}} = g_{\mathrm{K}}(V - E_{\mathrm{K}}), \quad \text{where} \quad g_{\mathrm{K}} = \bar{g}_{\mathrm{K}} n^4. \tag{3}$$

$\bar{g}_{\mathrm{Na}}$ and $\bar{g}_{\mathrm{K}}$ are the maximal conductances of the Nav and Kv channels, respectively; E_{Na} and E_{K} are the Na^+ and K^+ reversal potentials, respectively. The non-dimensional gating variables $j = m$, h and n evolve with time according to:

$$\frac{\mathrm{d}j}{\mathrm{d}t} = \alpha_j(1 - j) - \beta_j j \tag{4}$$

Each gating variable j has voltage dependent forward (α_j) and backward (β_j) rates. The variable m monitors the activation of the Nav channel whereas h describes the availability of the channel such that m^3h is the fraction of the full conductance or the open probability for the channel population. Nav channels inactivate quickly (~1 ms).

$$\alpha_m = 0.1\frac{(V + 40)}{1 - \exp[-(V + 40)/10]}, \tag{5}$$

$$\beta_m = 4\exp[-(V + 65)/18], \tag{6}$$

$$\alpha_h = 0.07\exp[-(V+65)/20], \tag{7}$$

$$\beta_h = \frac{1}{1+\exp[-(V+35)/10]}. \tag{8}$$

The Kvs, which exhibit no inactivation (at least, not on the time scale of APs) have a steady-state open probability given by n^4. The forward and backward rates of change for this variable are given by

$$\alpha_n = 0.01\frac{(V+55)}{1-\exp\left[-\frac{V+55}{10}\right]} \text{ and } \beta_n = 0.125\exp\left[-\frac{V+65}{80}\right] \tag{9}$$

Details of the kinetics can be seen in Sterratt et al. (2011).

A damaged node may have a population of Navs with a distribution of LS values. The kinetics of a Nav with a left shift of LS is modeled simply by replacing in Eqs. (5)–(9) V by V + LS. If we suppose that the node is comprised of N fractions f_i of Navs with left-shifts LS_i then with activation variables m_i ($i = 1, 2,...N$) and inactivation variables h_i ($i = 1, 2,...N$), the total Nav current will be given by Yu et al. (2012):

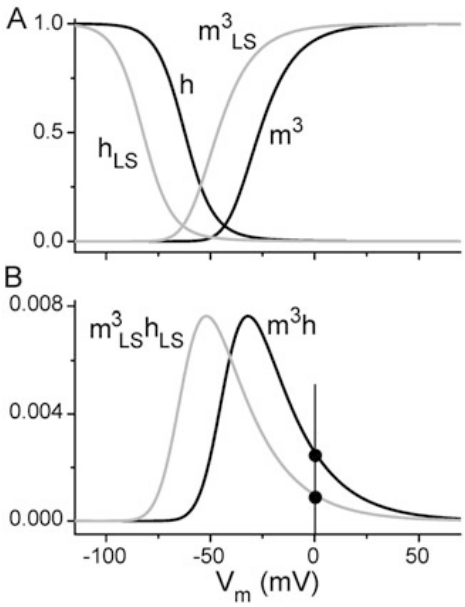

Fig. 4 Coupled left-shift (CLS) with LS = 20 mV in the Hodgkin-Huxley formulation. (**A**) Equilibrium values of activation (m^3 (V)) and inactivation ($h(V)$) variables for intact membrane (*black*) and after a 20 mV left-shift (*gray*). (**B**) The steady-state open probability, m^3h, of the intact and 20 mV left-shifted condition. Current flowing through the displaced window conductance would constitute a "Nav-leak." Note that the "window conductance" magnitude is greater at voltages nearer to normal V_{rest} and less at 0 mV (vertical line and circles). For further explanation, see Boucher et al. (2012)

$$I_{Na} = g_{Na}(V_m - E_{Na}), \text{ where } g_{Na} = \bar{g}_{Na} \sum_{i=1}^{N} f_i m_i^3 h_i \text{ and } \sum_{i=1}^{N} f_i = 1 \quad (10)$$

Figure 4 shows the impact of LS on the kinetics of a channel. The equilibrium ($t \rightarrow \infty$) values of the kinetic variables m and h shift by LS (Fig. 4A), leading to a shift in the equilibrium open probability of the channel (Fig. 4B). Consequently, the so-called window conductance operates at voltages too near the normal V_{rest} (−65.5 mV in Boucher et al. 2012). This constitutes "leaky Nav channels." A further outcome is a reduced steady-state I_{Na} at depolarized voltages (e.g., at 0 mV, as highlighted in the figure). We stress this point: when fast-mode Nav channel activity is responsible for "Nav leak," a decrease in steady-state I_{Na} near 0 mV is expected, not an increase.

The consequences of such shifts are examined next. The increased leakage near V_{rest} will tax the node requiring increased energy input to maintain the node in a resting homeostatic state. We will examine these effects when we introduce pumps.

4 CLS in a Node with Two Nav Populations (Intact and Damaged) and No Pumps

To gain insight into the effect of LS on nodal excitability we consider the simple case of two sub-populations of Nav channels, a left-shifted one with $f_1 = AC$ and an intact one with $f_2 = 1-AC$ (AC stands for "affected channels"). For parameters given in Boucher et al. (2012) Fig. 5A shows the impact of LS with perfect homeostasis assumed (i.e., Nernst potentials kept constant). Mild damage renders the node more excitable ("hypersensitive," *regime a*), lowers the threshold for initiating APs, and increases the frequency of firing. As LS increases, the node will begin to fire ectopically (i.e., without stimulus). In this idealized (perfect homeostasis) situation, the regime plot shows a large "zone" of tonic firing (*regime b*) and clearly, when a node is firing tonically, this is definitely not mild injury. Inspection of the regime plot shows that the mild damage regime (hypersensitive but not ectopically firing, *regime a*) corresponds either to any sufficiently small LS (zone along the X-axis) or to large LS/small AC (zone along the Y-axis) (see Fig. 5A). As LS and AC values push the system into the tonic firing regimes (*b* and *c*), the node also experiences increasingly greater difficulty responding to an imposed stimulus (see traces for *b* and *c*): from the $V(t)$ traces, zone *b* fires tonically but zone *c* exhibits depolarizing block. *Regime d* no longer shows tonic firing and is inexcitable. Note that the set of $V(t)$ traces illustrated are all for AC = 1 (all channels affected). AC = 1 would presumably correspond to the patch clamp experiments of Fig. 3. To provide some perspective, recall that there we saw Nav1.6 channels in damaged membranes exhibiting shifts of 16 and 20 mV. In the CLS model (for AC = 1), depolarizing block occurs around LS = 17 mV and total inexcitability near 19 mV. Experimentalists need to bear in mind the following: mild damage, though pathologically critical, would likely be extraordinarily difficult to measure biophysically. However, if CLS underlies pathological Nav leaks, mild and severe damage represent quantitatively but not

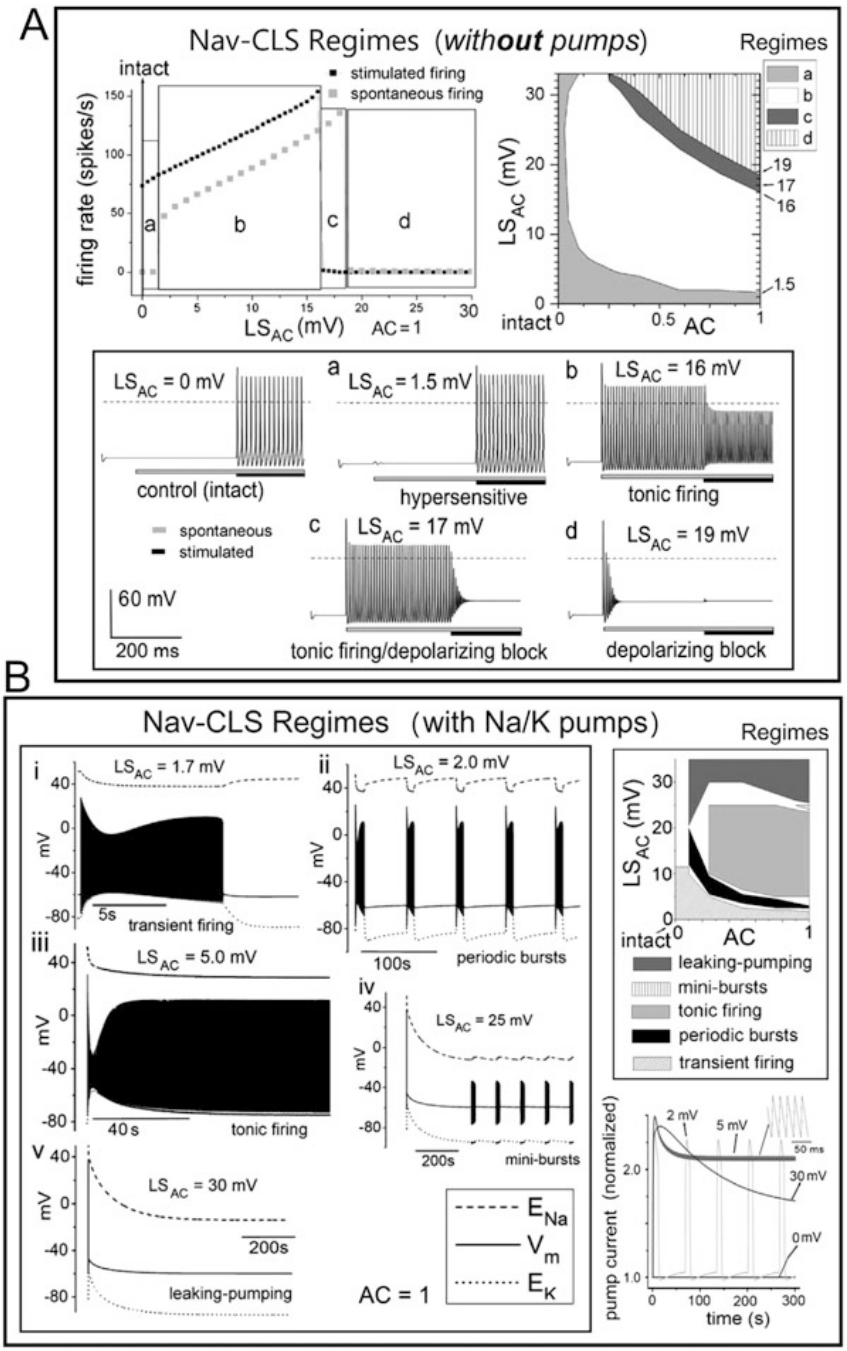

Fig. 5 Nav-CLS excitability regimes without and with pumps. (**A**) (without pumps) Computed excitability with Nav-CLS injury, as labeled. Regime plots are alluded to in the text. In voltage plots, dashed lines indicate 0 mV. (**B**) (with pumps) Na/K pumps are included with a surface s to inner volume vol_i ratio, 20 $\text{cm}^2/\mu\text{L}$, small enough to observe neuropathic behaviors over conveniently short simulation times. This ratio was used in Boucher et al. (2012), Yu et al. (2012), and Lachance et al. (2014). (Parameter Tables in Boucher et al. 2012 and Yu et al. 2012 have a typo: "m^3" instead of liters, L, for volumes. For all simulations here, $\text{vol}_i = \text{vol}_o = 3 \times 10^{-15}$ L $= 3 \times 10^{-9}$ μL). Figure modified from Boucher et al. (2012), as published in Morris and Joós (2016)

qualitatively different states. For channel neuropharmacology, it would be valid to study channels in severely damaged membrane even when the aim was eventually to target channels in mildly damaged cells.

5 Excitability and CLS Damage in a Node with Pumps

When ion fluxes are described for finite volumes of nodal axoplasm and the external volume, then whether a node is firing or quiescent, the ion gradients dissipate. When they have fuel, Na^+/K^+ ATPase pumps continuously remove 3 Na^+ from the cell and bring in 2 K^+ per ATP consumed to restore those gradients. In the Michaelis-Menten model of pump action one ATP must be hydrolyzed for each cycle of the pump. Three Na^+ ions bind the pump protein from inside and move to the external side and two K^+ ions bind from the external side and move to the inner side. Accordingly, I_{pump} depends on both $[Na^+]_i$ and $[K^+]_o$. This is the basis of the pump formulation given by Läuger (1991) and also used by Käger et al. (2000):

$$I_{\text{pump}} = I_{\text{max pump}} \left(1 + \frac{K_{M_K}}{[K^+]_o}\right)^{-2} \times \left(1 + \frac{K_{M_{Na}}}{[Na^+]_i}\right)^{-3} \tag{11}$$

The Michaelis-Menten coefficients $K_{M_{Na}}$ and K_{M_K} measure the efficiency of the process on the two sides of the pumps. $I_{\text{max pump}}$ is the maximal current generated by the pump (to a first approximation it would correspond to the pump density), and the Na^+ and K^+ currents flowing through the pump are $I_{\text{Napump}} = 3I_{\text{pump}}$ and $I_{\text{Kpump}} = -2I_{\text{pump}}$. To model the time evolution, these currents will have to be added to Eq. (1) $I_{\text{Napump}} + I_{\text{Kpump}} = I_{\text{pump}}$. To maintain homeostasis these will not suffice because to ensure $V = \text{const}$ under rest (i.e., no stimulation) conditions, pump leak currents associated with the two ions have to be included I_{Naleak} and I_{Kleak} leading to a modified Eq. (1) governing the time evolution of the voltage:

$$C\frac{dV_m}{dt} = -I_{\text{Na}} - I_{\text{K}} - I_{\text{Naleak}} - I_{\text{Kleak}} - I_{\text{leak}} - I_{\text{pump}}, \tag{12}$$

where $I_{\text{Naleak}} = g_{\text{Naleak}}(V - E_{\text{Na}})$ and $I_{\text{Kleak}} = g_{\text{Kleak}}(V - E_{\text{K}})$ (g_{Naleak} and g_{Kleak} are constants).

The ion fluxes across the membrane of the node of Ranvier lead to concentration changes:

$$\frac{d[Na^+]_i}{dt} = -\frac{(I_{\text{Na}} + I_{\text{Napump}} + I_{\text{Naleak}})A}{F\text{Vol}_i} \tag{13}$$

$$\frac{d[Na^+]_o}{dt} = \frac{(I_{\text{Na}} + I_{\text{Napump}} + I_{\text{Naleak}})A}{F\text{Vol}_o} \tag{14}$$

$$\frac{\mathrm{d}[\mathrm{K}^+]_i}{\mathrm{d}t} = -\frac{(I_\mathrm{K} + I_\mathrm{Kpump} + I_\mathrm{Kleak})A}{F\mathrm{Vol}_i} \tag{15}$$

$$\frac{\mathrm{d}[\mathrm{K}^+]_o}{\mathrm{d}t} = \frac{(I_\mathrm{K} + I_\mathrm{Kpump} + I_\mathrm{Kleak})A}{F\mathrm{Vol}_o} \tag{16}$$

where F is the Faraday constant, A is the surface area of the nodal membrane, and Vol_i (or Vol_o) is the intracellular (or extracellular) volume of the node of Ranvier under study (we take $\mathrm{Vol}_i = \mathrm{Vol}_o$ for simplicity). Ion concentration dynamics alter the reversal potentials E_Na and E_K appearing in Eqs. (2) and (3). They obey the Nernst equations:

$$E_\mathrm{Na} = -\frac{RT}{F}\ln\frac{[\mathrm{Na}^+]_i}{[\mathrm{Na}^+]_o} \quad \text{and} \quad E_\mathrm{K} = -\frac{RT}{F}\ln\frac{[\mathrm{K}^+]_i}{[\mathrm{K}^+]_o} \tag{17}$$

The key parameter determining the time evolution of the firing node is the surface area (SA) to intracellular volume (vol_i) ratio $r = \mathrm{SA}/\mathrm{vol}_i$. For a node of Ranvier of length 1 μm and radius 1 μm this would give $r = 0.5 \times 10^6\ \mathrm{m}^{-1}$, but, in reality the relevant intracellular volume includes not just the slice under the nodal membrane but the full internodal volume, which for an internode, say, 1 mm, would yield $r = 0.5 \times 10^3\ \mathrm{m}^{-1}$, i.e. a three orders of magnitude smaller. In Boucher et al. (2012) and subsequent papers (Yu et al. 2012; Lachance et al. 2014) r was set at $2 \times 10^6\ \mathrm{m}^{-1}$ to allow the different regimes of excitability to be investigated with reasonable computational resources. (As an aside, Boucher et al. (2012) erroneously gave the intracellular volume as $2 \times 10^{-15}\ \mathrm{m}^3$ instead of 2×10^{-15} L.) Consequently, the pathological changes noted in Boucher et al. (2012), Yu et al. (2012), and Lachance et al. (2014) reveal themselves more quickly than would be expected in reality. Importantly, however, the choice of volumes affects only the time scales of these slow changes and not the behaviors per se. For the resulting computations, Fig. 5B shows different patho-excitability regimes for an excitable system that pumps ions in and out of finite volumes at it attempts to maintain ion homeostasis (Boucher et al. 2012). The difficulty of maintaining ion homeostasis increases as values of LS and AC increase. With E_Na and E_K free to vary, the excitability regimes are different as seen by comparing Fig. 5A, B. In Fig. 5B, with AC = 1, increasing LS yields a range of behaviors. Mild injury elicits transient firing (just after the injury is imposed) but the mildly injured system then relaxes into a new quiescent (albeit hyperexcitable) state as homeostatic pumping catches up. With deeper injury there is ectopic firing, first in the form of periodic bursts then tonic firing, then mini-bursts or subthreshold bursts, and finally a quiescent state that is unexcitable.

6 CLS-Induced Pathological Activity for Realistically Complex Membrane Damage

The previous sections showed different regimes of excitability for nodes with a fraction of the Nav population suffering an LS. Even though a rich range of behavior was observed for mildly damaged nodes, real nodes would probably experience more complex damage patterns. In general, the regimes described above should still be relevant, but important pathological nuances could be overlooked. As an example of somewhat more realistic complexity, consider distributions of Nav population that combine both mild damage (LS = 2 mV) and heavy damage (LS > 20 mV). One such situation was examined in Yu et al. (2012). Nodes were given three Nav populations (LS_i = [26.5, 2.0, 0] mV and f_i = [0.2, 0.08, 0.72]) where f_I with $i = 1$, 2, or 3 is the fraction of the node with left shift LS_i (the Hodgkin-Huxley curves are given in Fig. 6B) and the resulting "window

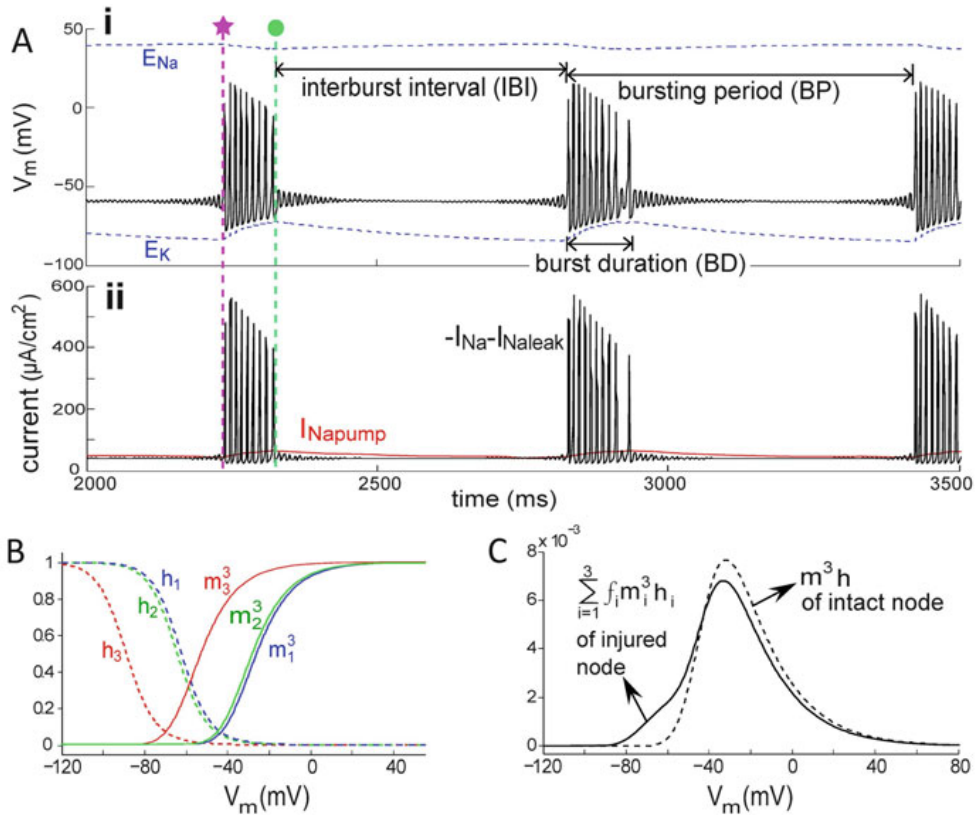

Fig. 6 Transitions between STO and burst behaviors. (**A**). Upper: V (black solid line) at an injured node and the varying E_{Ion} (E_{Na} and E_K; blue dotted lines). Three g_{Na} populations were used: LS_i = [0, 2, 26.5] mV and f_i = [0.72, 0.08, 0.2] with $Vol_i = Vol_o = 10^{-15}$ m^3. Initiation and termination times of a burst of spikes (pink star, green dot, respectively) are used in Fig. 7. Lower: corresponding Na^+ currents, as labeled. (**B**). Equilibrium values of the Nav kinetic constants for the three LS values in (**A**). (**C**) Window current for node producing bursts in (**A**) compared with intact node (from Yu et al. 2012)

conductance" is shown in Fig. 6C. We will discuss this case in some detail as it produces a pattern of behavior (i.e., $V_m(t)$) as per Fig. 6A i that is prevalent in neuropathic firing, i.e., irregularly spaced bursts of APs followed and preceded by subthreshold oscillations (STOs). Also shown is the changing Nav channel I_{Na} and a small pump I_{Na} in Fig. 6A ii. This simulation starts with the Na^+ and K^+ gradients at their maximum values (mimicking the time point immediately after an injury). Because of the damage, the node fires spontaneously, and as seen, the gradients start to deplete at a steeper pace. When depletion exceeds a certain point, the ectopic APs cease but, stimulated by the left-shifted window current (see Fig. 6B; the leftmost "shoulder" is critical here), the node produces subthreshold oscillations (STOs). Nav channel kinetics are responsible for STO frequency, but since they are associated with a reduced I_{Na} compared to actual APs, pumps are slowly able to restore the ion gradients. As this occurs, STOs decrease in amplitude. However, the interplay of Nav leak and pump current is such that the "leaky" window current eventually causes STOs to grow again and then a new ectopic AP burst occurs.

7 Dynamical Analysis of Ectopic Bursting

Performing a dynamical analysis of a Nav-CLS damaged node with mild damage and well-functioning pumps allows one to examine how the slow relentless activity of the pump interacts with the high speed non-linear kinetic properties of the AP producing channels.

Given the set of variables used for the injured system, a particular state of excitability is associated with each pair of E_{Na}, E_K values (see Fig. 5D in Yu et al. 2012). A bifurcation analysis (Fig. 7) shows how, during one ectopic burst cycle, the node goes into a spontaneous firing state, then becomes bistable, a state from which the node will switch (via a Hopf bifurcation) to a lower amplitude oscillation, then finally enter a quiescent state. It will then return via a similar pathway to the spontaneous firing state.

8 Saltatory Propagation in Axons with Mildly Damaged Nodes

The discussion thus far has concerned a single node's excitability, but damaged nodes also affect saltatory propagation of APs as shown by Boucher et al. (2012). With an emphasis largely on mild damage, Lachance et al. (2014) delved further into how CLS affects propagation, this time including the pump. For saltatory propagation each internode is represented as a single ohmic conductance κ linking two consecutive nodes of Ranvier (Ochab-Marcinek et al. 2009), on the assumption that myelinated internodes have negligible capacitance. The value of κ is chosen to ensure one-to-one propagation across the internode. Using a 10-node myelinated axon model, Lachance et al. (2014) found that quiescent, fully restabilized nodes with mild CLS damage eventually start firing ectopically if repeatedly stimulated

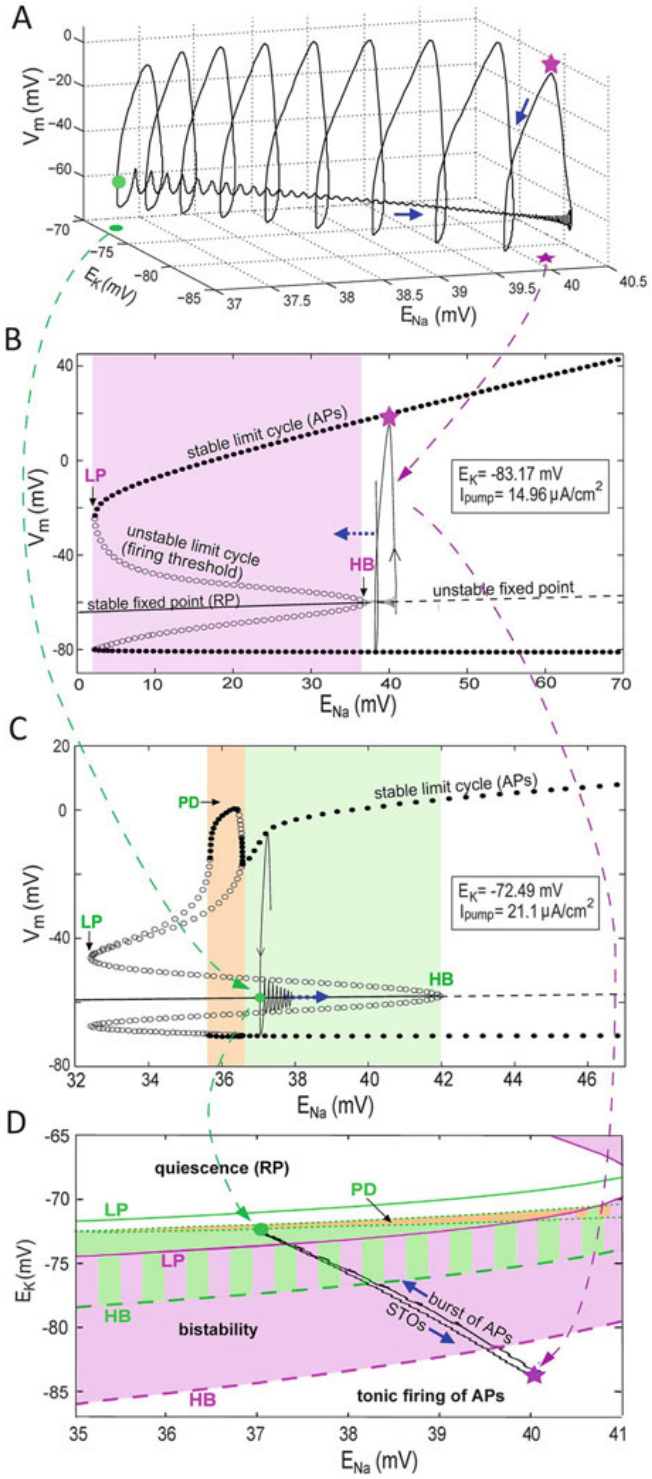

Fig. 7 Burst dynamics explained with three-dimensional V_m trajectories and bifurcation diagrams (for bursts in Fig. 6). Note: X-axis scales are different in each plot. (**A**) The first burst of APs,

by incoming APs (see Fig. 1 in Lachance et al. 2014). This outcome suggests a straightforward explanation for the well-known need to provide a relatively long low-input recovery time (i.e., stimulation of damaged tissue kept to a minimum) for those who have suffered mild traumatic brain injury.

Saltatory propagation simulations revealed another interesting phenomenon. APs can propagate with good fidelity through ectopically firing nodes, provided the frequency of the incoming APs exceeds the intrinsic frequency of the damaged node (i.e., the ectopic firing frequency of the damaged node in the absence of a stimulus). Under these conditions, the ectopic node locks its output to the frequency of the incoming stream of APs. The window of reliable propagation is robust in that it functions even when there are several consecutive ectopic nodes and even with a high level of temporal jitter in the incoming train of APs.

9 Sick Excitable Cells and Nav-CLS in Other Modeling Contexts

Various aspects of neuropathological excitability linked to neuropathic pain, epilepsy, and so on have been addressed computationally (e.g., Rotstein et al. 2006; Cressman et al. 2009; Barreto and Cressman 2011; Prescott et al. 2006; Coggan et al. 2010, 2011; Käger et al. 2000; Kovalsky et al. 2009 for dorsal root ganglion neuronal dysfunction; Choi and Waxman 2011) and discussed previously (Boucher et al. 2012; Yu et al. 2012). These works focus on simulating particular

Fig. 7 (continued) plotted in Fig. 6A as a function of time is plotted here in 3-D as a function of E_{Na} and E_K (blue arrow: direction of V_m trajectory). (**B**) The dynamical analysis of the system's transition (a bifurcation) from bursting to STOs is visualized as a diagram of the membrane potential excursions as a function of E_{Na} with fixed E_K and I_{pump} values measured at the pink star in Fig. 6A (the beginning of bursting). Such a diagram is known as a bifurcation diagram. At the pink star value the only stable solution is a periodic orbit. The pink oval loop corresponds to one cycle or one AP. Although in reality E_K also depolarizes, the graph shows how during a burst the E_{Na} decline shifts orbits leftward into the bistability regime (pink area) where two stable solutions exist. The point where a periodic orbit appears or disappears through a local change in the stability properties of a steady point is known as a Hopf bifurcation (HB). To get a more accurate representation of what happens at the transition, the analysis is repeated in (**C**) with the E_K at the green dot. (**C**) Bifurcation diagram for the fixed E_K and I_{pump} values at the green dot in (**A**). For E_{Na} at the green dot value (37.27 mV), the system (large green dot) is within the bistability regime (green area). V_m, attracted by this fixed point, has STOs until E_{Na} through the action of the pumps increases beyond the HB point and superthreshold-oscillations (APs) return. The PD region corresponds to period-doubling bifurcation (not attained during the bursting cycle). (**D**) Two-parameter bifurcation diagram for E_K and E_{Na}. Pink solid and dashed curves represent LP (saddle-node bifurcation) and HB, respectively, when I_{pump} is fixed as in (**B**). The green solid, dashed, and dash-dotted curves represent LP, HB, and PD, respectively, when I_{pump} is fixed as in *C*. With varying I_{pump} the bistability regime shifts from the pink to the green area (the zone with both colors is the overlap of these two areas). The gray area between two green dash-dotted curves is a zone with PD bifurcations. The black loop shows E_K and E_{Na} orbits during a burst (from Yu et al. 2012).

dysfunctions. As such they would not necessarily provide a more general nor cell biophysically grounded theory for dysfunctional excitability in sick excitable cells. Nav-CLS makes this connection by virtue of the commonality of bleb damage.

Jérusalem et al. (2013) incorporated Nav-CLS plus left shift of Kv activation into a multiscale model of injury to myelinated axons. Pumps were not included but in recognition of impaired ion homeostasis, E_K and E_{Na} values are moved toward 0 mV.

The Nav-*CLS* model has been applied in several contexts related to traumatic brain injury by Volman and Ng (2013, 2014, 2016). Most recently, with Ng et al. (2017) they have embedded CLS in the "mechanistic end-to-end concussion model that translates head kinematics to neurologic injury."

The involvement of neural, glial, and extracellular volume changes in dysfunctional excitability as it relates to spreading depression has been addressed computationally (Hübel and Dahlem 2014; Hübel and Ullah 2016). For cells like glia with a substantial anion conductance, including anion fluxes is mandatory. CLS, having been designed around neurons whose resting conductances are not anion based, lacks this feature, but some excitable cells have a resting anion conductances that would certainly need to be taken into account. Skeletal muscle cells and the electrocytes of various electric fish are cases in point. Ma et al. (2017) recently elaborated on dynamical issues emerging from Nav-CLS injury in excitable cells. Since their dominant interest is skeletal muscle malfunctions such as myotonia, their system could be a good platform for linking Nav-CLS to the volume regulatory and electrophysiological consequences that arise when anion fluxes are critical to the homeostatic processes.

10 The CLS Model Within NEURON, the Simulation Environment

As a simple tractable model of node damage, the *CLS* model is suitable for studying the impact of bleb damage beyond a node or series of nodes. A widely used computer environment to study neurons and networks of neurons is NEURON (www.neuron.yale.edu). NEURON was used to produce Fig. 8 which completes the regime diagram of Fig. 5B. Unlike for 5B, the responses to stimulation were tested for the part of the system corresponding to a quiescent membrane. The blue, orange, and yellow regimes represent ectopic spontaneous activity.

Nav CLS could also be adapted in the NEURON environment for regions of excitable membrane that express multiple kinetic types of Nav channels. Examples would include axon initial segments (Duménieu et al. 2017) and nociceptive nerve endings (Choi and Waxman 2011).

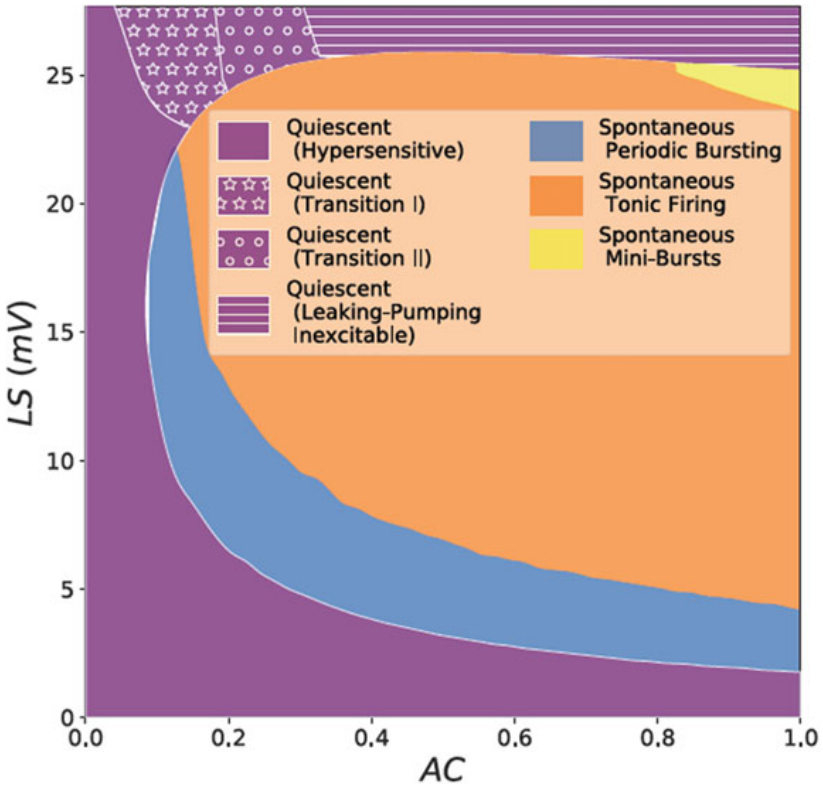

Fig. 8 Regimes of CLS obtained using NEURON Regimes of CLS induced activity for a system in which the pump remains active (damage notwithstanding) calculated for the same parameters as in Fig. 5B but using the NEURON computing environment (ModelDB). For the Quiescent regimes, excitability was tested (not shown) using a constant depolarizing I_{stim} in the same manner as in Fig. 5A (the no-pump situation). Responses to an I_{stim} were not checked for the Spontaneous regimes. In the Quiescent regimes linking the Hypersensitive and Inexcitable zones transitions I and II does not yield normal trains of APs in response to I_{stim} (the former yields complex patterns of damped voltage oscillations and quiescence and the latter exhibits highly damped small oscillations before returning to quiescence).

11 Conclusion

Inappropriately active or "leaky" Nav channels are treacherous. For clinical use, Nav channel antagonists are typically designed to target channels over-active in their slow gating mode, but the clinical efficacy of such drugs for ameliorating sick excitable cell dysfunction has been disappointing (Morris et al. 2012a, b; Morris and Joós 2016). It is well known that when a slow mode Nav leak (often referred to as excess "persistent current") develops, I_{Na} near 0 mV increases. In sick excitable cells however, we suspect that *CLS* underlies "leaky Nav channels" and if so, then the leaky channels are gating in fast, not slow mode. As Fig. 4 shows, where *CLS*-based "Nav leak" develops, a decrease (NOT an increase) in steady-state I_{Na} near

0 mV is predicted. For neuropharmacologists, this electrophysiological feature is an extremely important and straightforward practical tool arising from the *CLS* model.

More globally, several characteristics stand out with the *CLS* model. First is its foundation upon biophysical experiments on Nav channels (Wang et al. 2009). Second, a single parameter, the coupled left shift of the activation and inactivation voltages of the Nav channels, characterizes the degree of injury to the affected Nav-bearing membrane.

For those wishing to use the Yale University mathematical tool, NEURON for computational modeling of sick excitable cells, we have now made Nav-CLS available in ModelDB as described above.

The Nav-CLS model can be modified to achieve more realistic depictions in various ways. For instance, damage intensity can be made to differ in different parts of the excitable membrane using the fraction variable f. Complex damage situations can then be generated by defining a set $\{f_i, \mathrm{LS}_i\}_{i=1}^{N}$. The underlying conductances could be augmented by including a slow mode Nav with the ability to left shift with damage and by also allowing the gK(V) to left shift with damage.

A striking general outcome from our modeling to date is that mild *CLS* damage has multi-faceted pathophysiologically realistic effects on excitability. *CLS* (a rigorously observed phenomenon at the channel biophysics level (Wang et al. 2009)), has been deployed in systems that incorporate pumps, that exhibit current noise, and that take into account the abnormal intracellular and extracellular volumes that frequently accompany sick excitable cell conditions. With these characteristics included, *CLS* is sufficient to robustly explain a plethora of known but previously baffling sick excitable cell pathologies. *CLS* predicts hypersensitivity, ectopic tonic and burst firing, depolarizing block, complex subthreshold oscillations, paroxysmal bursts of activity. There is no need to invoke the expression of new channels or to suggest that cell-mediated kinetic modulation of channels must be occurring. CLS provides the only general theory we are aware of to explain dysfunctional excitability in diverse sick excitable cells. Its power, we suspect depends on the fact that *CLS* is not simply a kinetic theory, but one based on observations about the physics of bleb damage.

In summary, bleb damage to Nav-bearing membranes is a widely recognized but insufficiently studied feature of sick excitable cells that, in conjunction with Nav-CLS theory, can explain much of the pathological excitability observed in these cells.

References

Banderali U, Juranka PF, Clark RB, Giles WR, Morris CE (2010) Impaired stretch modulation in potentially lethal cardiac sodium channel mutants. Channels 4:12–21

Barreto E, Cressman JR (2011) Ion concentration dynamics as a mechanism for neuronal bursting. J Biol Phys 37:361–373

Boucher PA, Joós B, Morris CE (2012) Coupled left-shift of Nav channels: modeling the Na+-loading and dysfunctional excitability of damaged axons. J Comput Neurosci 33:301–319

Choi JS, Waxman SG (2011) Physiological interactions between Na(v)1.7 and Na(v)1.8 sodium channels: a computer simulation study. J Neurophysiol 106(6):3173–3184

Coggan JS, Prescott SA, Bartol TM, Sejnowski TJ (2010) Imbalance of ionic conductances contributes to diverse symptoms of demyelination. Proc Natl Acad Sci U S A 107:20602–20609

Coggan JS, Ocker G, Sejnowski TJ, Prescott SA (2011) Explaining pathological changes in axonal excitability through dynamical analysis of conductance-based models. J Neural Eng 8:065002

Cressman JR Jr, Ullah G, Ziburkus J, Schiff SJ, Barreto E (2009) The influence of sodium and potassium dynamics on excitability, seizures, and the stability of persistent states: I. Single neuron dynamics. J Comput Neurosci 26:159–170. Erratum in (2011) 30: 781

Duménieu M, Oulé M, Kreutz MR, Lopez-Rojas J (2017) The segregated expression of voltage-gated potassium and sodium channels in neuronal membranes: functional implications and regulatory mechanisms. Front Cell Neurosci 11:115

Finol-Urdaneta RK, McArthur JR, Juranka PF, French RJ, Morris CE (2010) Modulation of KvAP unitary conductance and gating by 1-alkanols and other surface active agents. Biophys J 98:762–772

Hodgkin AL, Huxley AF (1952) A quantitative description of membrane current and its application to conduction and excitation in nerve. J Physiol 117:500–544

Hübel N, Dahlem MA (2014) Dynamics from seconds to hours in hodgkin-huxley model with time-dependent ion concentrations and buffer reservoirs. PLoS Comput Biol 10(12):e1003941

Hübel N, Ullah G (2016) Anions govern cell volume: a case study of relative astrocytic and neuronal swelling in spreading depolarization. PLoS One 11(3):e0147060

Jérusalem A, García-Grajales JA, Merchán-Pérez A, Peña JM (2013) A computational model coupling mechanics and electrophysiology in spinal cord injury. Biomech Model Mechanobiol 14:1–14

Käger H, Wadman W, Somjen G (2000) Simulated seizures and spreading depression in a neuron model incorporating interstitial space and ion concentrations. J Neurophysiol 84:495–512

Kovalsky Y, Amir R, Devor M (2009) Simulation in sensory neurons reveals a key role for delayed Na+ current in subthreshold oscillations and ectopic discharge: implications for neuropathic pain. J Neurophysiol 102:1430–1442.

Lachance M, Longtin A, Morris CE, Yu N, Joós B (2014) Stimulation-induced ectopicity and propagation windows in model damaged axons. J Comput Neurosci 37:523–531

Läuger P (1991) Electrogenic ion pumps, distinguished lecture series of the society of general physiologists. Sinauer Associates, Sunderland, MA, p 313

Ma QX, Arneodo A, Ding GH, Argoul F (2017) Dynamical study of Nav channel excitability under mechanical stress. Biol Cybern 111(2):129–148

Morris CE, Joós B (2016) Channels in damaged membranes. In: French RJ, Noskov SY (eds) Na channels from phyla to function. Currents topics in membranes, vol 18. Elsevier, Amsterdam, pp 561–597

Morris CE, Juranka PF (2007) Nav channel mechanosensitivity: activation and inactivation accelerate reversibly with stretch. Biophys J 93:822–833

Morris CE, Boucher PA, Joós B (2012a) Left-shifted Nav channels in injured bilayer: primary targets for neuroprotective Nav antagonists? Front Pharmacol 3:19

Morris CE, Juranka PF, Joós B (2012b) Perturbed voltage-gated channel activity in perturbed bilayers: implications for ectopic arrhythmias arising from damaged membrane. Prog Biophys Mol Biol 110:245–256

Ng LJ, Volman V, Gibbons MM, Phohomsiri P, Cui J, Swenson DJ, Stuhmiller JH (2017) A mechanistic end-to-end concussion model that translates head kinematics to neurologic injury. Front Neurol 8:269

Ochab-Marcinek A, Schmid G, Goychuk I, Hänggi P (2009) Noise-assisted spike propagation in myelinated neurons. Phys Rev. E 79(1):011904

Prescott SA, Sejnowski TJ, De Koninck Y (2006) Reduction of anion reversal potential subverts the inhibitory control of firing rate in spinal lamina I neurons: towards a biophysical basis for neuropathic pain. Mol Pain 2:32–51

Rotstein HG, Oppermann T, White JA, Kopell N (2006) The dynamic structure underlying subthreshold oscillatory activity and the onset of spikes in a model of medial entorhinal cortex stellate cells. J Comput Neurosci 21:271–292

Shcherbatko A, Ono F, Mandel G, Brehm P (1999) Voltage-dependent sodium channel function is regulated through membrane mechanics. Biophys J 77:1945–1959

Sheetz MP, Sable JE, Döbereiner HG (2006) Continuous membrane cytoskeleton adhesion requires continuous accommodation to lipid and cytoskeleton dynamics. Annu Rev. Biophys Biomol Struct 35:417–434

Sterratt D, Graham B, Gillies A, Willshaw D (2011) Principles of computational modelling in neuroscience. Cambridge Univ Press, Cambridge

Tabarean IV, Juranka P, Morris CE (1999) Membrane stretch affects gating modes of a skeletal muscle sodium channel. Biophys J 77:758–774

Volman V, Ng LJ (2013) Computer modeling of mild axonal injury: implications for axonal signal transmission. Neural Comput 25:2646–2681

Volman V, Ng LJ (2014) Primary paranode demyelination modulates slowly developing axonal depolarization in a model of axonal injury. J Comput Neurosci 37:439–457

Volman V, Ng LJ (2016) Perinodal glial swelling mitigates axonal degradation in a model of axonal injury. J Neurophysiol 115:1003–1017

Wang JA, Lin W, Morris T, Banderali U, Juranka PF, Morris CE (2009) Membrane trauma and Na + leak from Nav1.6 channels. Am J Physiol Cell Physiol 297:C823–C834

Yu N, Morris CE, Joós B, Longtin A (2012) Spontaneous excitation patterns computed for axons with injury-like impairments of sodium channels and Na/K pumps. PLoS Comput Biol 8: e1002664

Zou S, Chisholm R, Tauskela JS, Mealing GA, Johnston LJ, Morris CE (2013) Force spectroscopy measurements show that cortical neurons exposed to excitotoxic agonists stiffen before showing evidence of bleb damage. PLoS One 8:e73499

T-CLS model: Graphical summary of Chapter 5

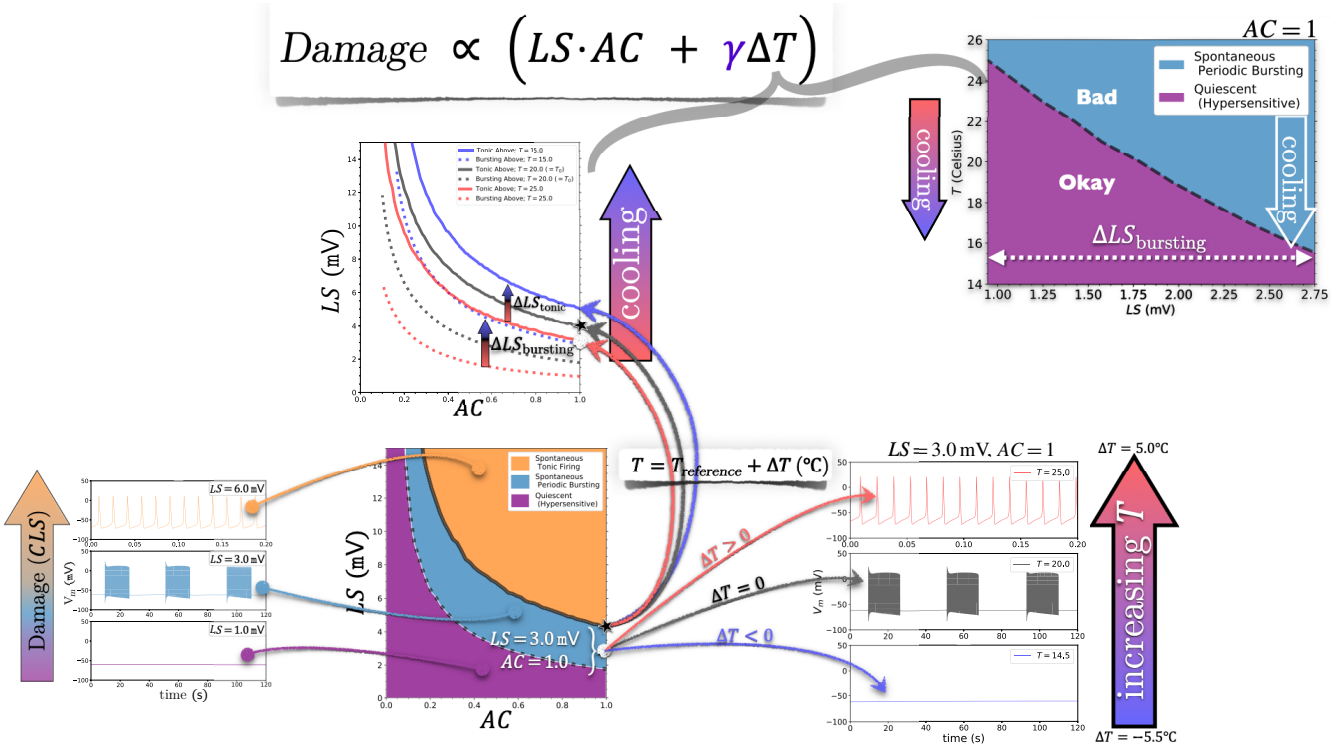

Figure 1: **Graphical summary of Chapter 5 results.** Here we connect the key plots from Chapter 5 together in one figure. Starting from the upper left: FIG. 2(b), FIG. 3, FIG. 1(a), FIG. 1(b), and FIG. 2(a) of Barlow et al. 2018 [2] (Section 5.3). The phenomenological formula—$Damage \propto (AC \cdot LS + \gamma \Delta T)$—breaks down for $AC \lesssim 0.2$, or where the ectopic LS-thresholds grow asymptotically.

Unedited pages #3 & #5 from Barlow, Joós, Trinh, and Longtin (2018)

For clarity, I made a cosmetic edit to the PDF copy of Barlow et al. 2018 [2] included in Section 5.3 of the main text. The edit occurred in *FIG. 1.*(a) on page#136 and *FIG. 2.*(a) on page#140—i.e. the third and seventh pages of Barlow et al. 2018, respectively.

Both figures plot time series of the membrane potential (V_m) in three panels, however, **the timescale on the abscissa varies among the panels**. Specifically, ~ 200ms of tonic firing is shown in the top panel of *FIG. 1.*(a) and the bottom panel of *FIG. 2.*(a), whereas the other two panels in each figure span ~ 120s.

- To help readers notice the shorter duration plotted with tonic firing, the ms–timescale tick marks have their labels highlighted in colour on page#136 and page#140.
- The original as-published figures are included in this Appendix, below.

generic conditions, as *LS* increases, a bifurcation first occurs from quiescence to a bursting firing pattern in which APs are arranged in clusters separated by quiescent phases. The bursting involves a rapidly firing phase, followed by a quiescent phase, and the whole pattern repeats. As *LS* increases even more, another bifurcation occurs, this time from bursting to tonic firing. At this transition, the quiescent interval between the clusters of spikes has shrunk such that only the rapidly firing "tonic" phase remains. These bifurcations are summarized in Fig. 1 for the more detailed HH model we present below. It is in fact a phase diagram illustrating the position of the tonic and bursting solutions in the two-dimensional subspace spanned by the *LS* parameter and the *AC* parameter that quantifies the fraction of channels affected by CLS.

A dynamical analysis of these solutions and their bifurcations at a single node of Ranvier was reported in Ref. 4. There, a numerical bifurcation tool was used as well as a slow-fast analysis: the fast sub-system generates the rapid limit cycle associated with the spikes during the active phase of the burst, while the dynamics of the Nernst potentials form the slow one (see Sec. II). In the context of transmission down an axon, CLS has negative consequences on information transmission, especially at low frequencies.[5] Bursting is also associated with the presence of subthreshold oscillations, which have been implicated in neuropathic pain, i.e., pain signals that outlast the injury.[6–8] In fact, it appears that the joint effect of such oscillations and noise, associated with channel conductance fluctuations and other sources of cellular stochasticity, produces firing patterns that highly resemble those seen in the context of neuropathic pain.

These "injured" ectopic dynamics set the stage for investigating the role played by temperature in injured cells. Temperature (T) is part of the original HH formalism,[3] which includes a temperature factor in the equations for the three gating variables: m and h for the voltage-gated Na^+ channel (or Nav), and n for the voltage-gated K^+ channel (or Kv) (see below). But the effect of temperature extends beyond simply speeding up kinetics. It is generally assumed that increases in temperature also lead to higher conductances and to stronger ionic pump activity.[9]

If T is too high, the standard HH axon loses its ability to generate APs altogether, i.e., it undergoes conduction block (see Ref. 10 for a more recent survey). In therapeutic applications, it is also known that the ability of a neuron to respond to high frequency biphasic stimulation is temperature dependent.[11] Beyond a certain threshold frequency, the nerve conduction is blocked, but this threshold increases with temperature. At some point, the smaller refractory period at higher T loses to inactivation and repolarizing forces. But before this point is reached, T changes can significantly alter firing patterns. In the majority of cells in the CNS, this is bad news, but for non-noxious thermoreceptors in the periphery as well as in specialized areas of the CNS (hypothalamus), the variation in firing pattern encodes the information about T changes, and the body can adapt by, e.g., sweating to remove heat or shivering to generate heat.

It has been shown that, upon cooling a nerve, its axons conduct more slowly. Given that there is already a distribution of propagation velocities due to heterogeneity in axon diameters, the cooling will cause a bigger "dispersion" in time delays of propagation down the nerve, as predicted in model studies.[12] One consequence of this enhanced temporal dispersion is thought to be the loss of synchrony of activation of postsynaptic targets, with possible clinical manifestations.

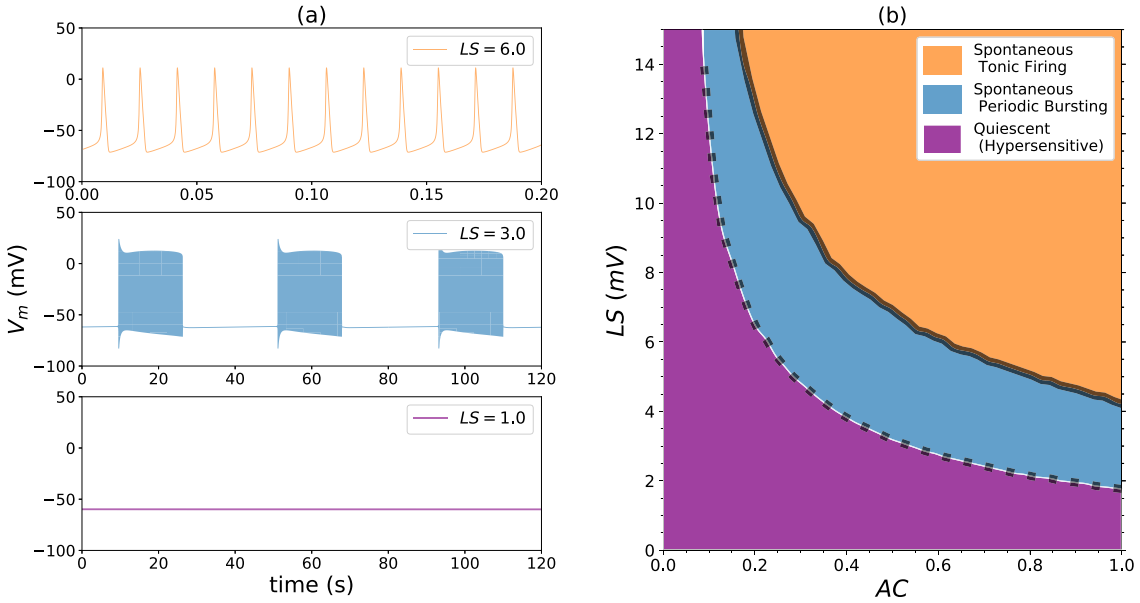

FIG. 1. As the left-shift (*LS*) voltage increases, the system becomes ectopic. In (a), time series of the membrane potential are shown with all channels left-shifted by the amount indicated; in other words, the fraction of affected channels (*AC*) equals 1. Damage increases from the bottom plot upward. The regime diagram (b) features two boundaries. The lower boundary (dashed black line) is the bursting threshold. Below it, the node remains stable (quiescent regime). Above this threshold, the node becomes ectopic: at first bursting spontaneously and then firing tonically above the upper boundary.

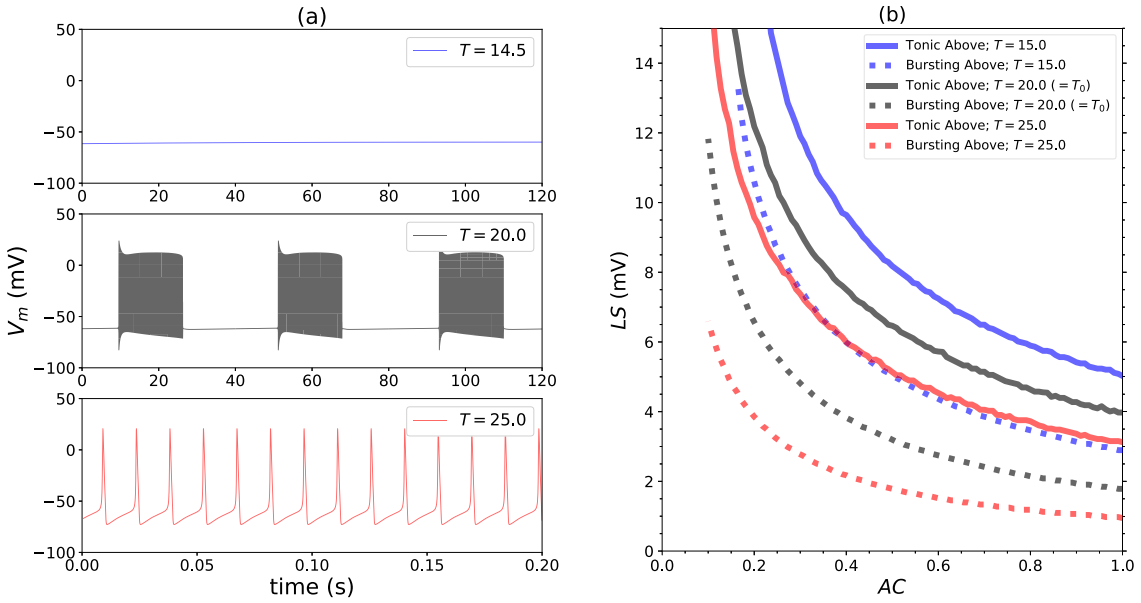

FIG. 2. T-CLS: (a) As *temperature* is varied, the system moves from quiescent, to bursting, to tonic firing; at fixed left-shift (here $LS = 3.0$ mV, $AC = 1$). This effect can be understood in terms of the regime diagram: Temperature moves the ectopic boundary. (b) The dashed and solid lines have the same meaning as in Fig. 1(b). Temperature increases from the top downward.

have been chosen. For example, we could have decided to calibrate our model at 37 °C. Given the dependence of the Nernst potentials on absolute temperature, this simply implies that we would have been working with slightly different ratios of internal to external concentrations. We would expect qualitatively similar results to Fig. 2(b) by increasing/decreasing the temperature by 5 °C.

The Nernst potentials are directly proportional to T as we can see in their definitions above. Their increase with T expresses the fact that the strength of the diffusion of the ions to dissipate their gradients also increases with T. However, for simplicity, the Nernst potential for the weaker leak current, made up mostly of chloride, is given a T-independent value. The same goes for the (weak) maximal leak conductance g_{leak}. The consequences of these choices are highlighted in the Discussion section. Note that the magnitude of the Nernst potentials is directly proportional to temperature, although with temperature being in Kelvins, this is a limited effect for 5°-10° changes. However, their dependence on the effect of T on ionic concentration ratios, due to the pump, is more significant as we will see below.

As mentioned above, there is a more intimate link between our CLS model and cold receptor models on which our temperature analysis is built: both involve bursting oscillations, and their associated subthreshold oscillations (see, e.g., Refs. 20, 21, 26, and 29). However, there are some important dynamical differences. Models of cold receptors burst for a different reason than the CLS model above. They typically possess an endogenous slow-wave oscillation that causes parabolic bursting. The slow wave goes on even if spikes are not present, a clear slow-fast decomposition of the full dynamics. The cold receptor models burst due to a slow subsystem that involves an inward current (such as persistent Na^+) and a slow subthreshold outward current. The latter, although generally thought to involve K^+, has been assigned a more generic mechanism for its activation (see Ref. 26 and references therein), or been given a specific calcium dependence and accompanying calcium buffering dynamics.[20,32] In contrast, leaking Nav channels initiate ectopic firing in the CLS model. This can lead to bursts because the slow dynamics of the Na^+/K^+ pump struggle to restore ion gradients during the active firing phase of ectopic firing. Thus, during the active phase, the Nernst potentials become depleted, and firing stops at some point; the gradients are restored by the pump during this quiescent phase. This CLS burst oscillation does not persist in the absence of firing.

All numerical integrations were carried out using the NEURON simulation environment (www.neuron.yale.edu) running on an Apple laptop computer. The code is based on a Python script stored on ModelDB (http://modeldb.yale.edu/234111).[24] This code allows users to explore the phase diagram in Fig. 1(b) by selecting (AC, LS) coordinates and running simulations. NEURON's built in adaptive time step method (CVode) was used.

III. RESULTS

We will discuss the effect of temperature in terms of the phase diagram of the original coupled left shift (CLS) model. Figure 1(a) shows the behavior observed as the damage is increased at a node with all Nav's left-shifted. The node stays quiescent for small damage up to a critical value, then as LS is increased further the Na^+ current flowing in triggers a burst of APs which lasts for a finite time. In that phase, APs are produced spontaneously until the ion gradients are too depleted to maintain firing with the stimulating I_{Na} current. As LS is